1-1-2012

Development of an electrospary ionization source and vacuum interface for guided ion beam tandem mass spectrometry experiments: structural and energetic effects in the molecular recognition of amino acids by 18-crown-6

Yu Chen
Wayne State University,

DEVELOPMENT OF AN ELECTROSPARY IONIZATION SOURCE AND VACUUM INTERFACE FOR GUIDED ION BEAM TANDEM MASS SPECTROMETRY EXPERIMENTS: STRUCTURAL AND ENERGETIC EFFECTS IN THE MOLECULAR RECOGNITION OF AMINO ACIDS BY 18-CROWN-6

by

YU CHEN

DISSERTATION

Submitted to the Graduate School

of Wayne State University,

Detroit, Michigan

in partial fulfillment of the requirements

for the degree of

DOCTOR OF PHILOSOPHY

2012

MAJOR: CHEMISTRY (Analytical)

Approved by:

_____

Advisor Date

_____

_____

_____

_____

ACKNOWLEDGMENTS

First, I would like to take this opportunity to express my deepest gratitude to my Ph. D mentor, Professor Mary T. Rodgers, of the faculty of the Department of Chemistry at Wayne State University. Her enthusiasm and dedication to science significantly influences me and inspires me to take on the challenges of my future professional career. Her earnest working attitude sets a great example for me to approach science and solve scientific problems in the future. With her intelligent guidance, and continuous support, I have found the way to become a great researcher.

I would also like to thank Dr. Cliff Frieler for providing high-performance computational resources and networking systems. I really appreciate his lead during the move of our lab and guidance in making our newly renovated lab function. My appreciation also goes to Professor P. B. Armentrout and his group (University of Utah) for providing me the opportunity to work on their instrument and gain hands-on experience with an electrospray ionization source. I would like to thank Professor Arthur Suits and Dr. Vasiliy Goncharov for the excellent collaborative project, where I learned more instrumentation skills.

I also thank all previous and present members of the Rodgers' group for their kind cooperation. I appreciate S. D. M. Chinthaka and Chunhai Ruan for training me in the usage of our guided ion beam tandem mass spectrometer, and David Nie and Calvin Austin for helping me maintain the instrument and share other lab duties.

I thank all members of the Wayne State University Computing & Information Technology Center for providing and maintaining computational resources. Thanks to Nestor Ocampo for his continuous support and help with computer service.

Finally, I would like to thank my parents for their encouragement, patience, and endless support.

TABLE OF CONTENTS

LIST OF TABLES

LIST OF FIGURES

LIST OF SCHEMES

CHAPTER 1

INTRODUCTION

1.1. Protein Structure Elucidation Techniques

Protein structures and protein-protein interactions play critical roles in biological processes. As a result, studies aimed at the characterization and improved understanding of the three-dimensional structure of proteins and the intra- and intermolecular interactions that stabilize their structures and complexes are ubiquitous throughout the biological and chemical disciplines. X-ray crystallography[1] and NMR spectroscopy[2,3] are well-established analytical techniques for protein structure elucidation. However, NMR requires a large quantity of the protein in a specific solvent, while X-ray crystallography requires sample crystallization. Mass spectrometry (MS) has become an increasingly important tool for protein structure determination due to its speed, sensitivity, and specificity.[4-6]

1.2. Mass Spectrometric Techniques to Study Protein Structures

A variety of MS approaches have been used to characterize protein structure and intra- and intermolecular protein interactions. Hydrogen/deuterium exchange (H/D exchange)[7-14] is an effective mass spectrometric technique based on either gas phase or solution phase exchange of backbone amide hydrogen atoms with deuterium to explore protein structure. Amide hydrogen atoms on the surface of a protein undergo exchange reactions with deuterium rapidly. In contrast, amide hydrogen atoms that are involved in intramolecular hydrogen bonds exchange very slowly. In solution, the exchange rate is primarily determined by solvent accessibility, and whether the amine

hydrogen atoms are involved in hydrogen bonding interactions. Therefore, protein structural information can be correlated to the rates of H/D exchange, making H/D exchange a useful technique for studying protein structure and dynamics.

Chemical cross-linking is another approach employed for the study of protein three-dimensional structures and protein-protein interactions.[15-23] Cross-linking reactions are generally carried out using homo- or heterobifunctional cross-linking reagents, binding to specific functional targets, to impose a distance constraint on the respective protein side chains. The length and conformation of the cross-linking reagent is controlled, therefore, intramolecular cross-linking can provide further insight into how proteins fold. In contrast, intermolecular cross-linking facilitates the determination of reactive components and protein surface contacts.

1.3. Selective Noncovalent Adduct Protein Probing

Selective noncovalent adduct protein probing (SNAPP) has been developed to exploit protein structure and folding states in solution.[24-33] SNAPP relies on the selective binding of a crown ether to basic amino acids residues, and in particular lysine (Lys) residues, to facilitate rapid identification and characterization of protein sequence, structure, and conformational changes, such that it can be used to provide information that is key to understanding functional behavior in biological systems at the molecular level. 18-Crown-6 (18C6) is most commonly employed as a protein side chain tag because of its enzyme-like specificity in its interactions with Lys side chains. The extent of 18C6 attachment to Lys is determined by the degree of accessibility to the Lys side chains. When Lys engages in intramolecular interactions such as a hydrogen bond or

salt bridge, the intramolecular interaction generally prevents the attachment of 18C6. Therefore, the number of 18C6 ligands that bind to a protein is also directly correlated to its structure. Because the number of 18C6 ligands that bind to a protein can be easily determined by MS due to the appreciable mass shift (264 Da per 18C6 ligand bound), protein structure and folding information under varying solution conditions can be extrapolated.

The SNAPP method have been applied to a variety of systems to elucidate the effects of metal ion binding on the structure of proteins. For example, attachment of 18C6 to Calmodulin-Ca^{2+} induces substantial conformation rearrangement as reflected by the number and extent of 18C6 binding to the protein detected by MS.[30] The number of 18C6 ligands that bind to α-synuclein, a protein associated with the pathology of Parkinson's disease, changes significantly in the presence of Al^{3+}, suggesting that Al^{3+} binding induces dramatic conformational changes. In contrast, the binding of Cu^{2+} does not cause a dramatic change in the 18C6 SNAPP distribution, suggesting that the structural rearrangement induced by the presence of Cu^{2+} is minimal.[30]

Julian and coworkers applied a site-directed mutagenesis approach, in which Lys residues of a series of ubiquitin mutants were exchanged for asparagine one at a time, to investigate the mechanism of the SNAPP method.[31] They found that Lys reactivity follows the order, free or noninteracting Lys > Lys engaged in hydrogen bonds > Lys engaged in a salt bridge. Surface availability does not ensure the attachment of 18C6. However, lack of surface accessibility will constrain the attachment of 18C6. Interestingly, they observed SNAPP distributions with complexation of up to six 18C6 ligands although the ubiquitin mutants possess only five Lys residues, indicating that the

N-terminal amino group or residues other than Lys may also contribute to the SNAPP distribution. Our previous study of protonated peptidomimetic base–18C6 complexes found that the N-terminal amino group mimic, isopropylamine (IPA), exhibits a higher 18C6 binding affinity than that of the Lys mimic, n-butylamine (NBA).[34] Similarly, our study of protonated amino acid–18C6 complexes found that the protonated backbone amino group is the most favorable 18C6 binding site for the amino acids glycine (Gly), alanine (Ala), histidine (His), and arginine (Arg), whereas the protonated side chain amino group is slightly favored over the protonated backbone amino group for Lys. Thus, our results suggest that binding to the N-terminal amino group may also contribute to the SNAPP distribution.

1.4. Molecular Recognition Applications

The use of molecular recognition of various protein sequences and structures by crown ethers has also been pursued in other groups. Brodbelt and coworkers reported a method using 18C6 derivatized with a chromophore, to study fragmentation patterns of peptides.[35] The chromophore tag noncovalently binds to a Lys side chain via the 18C6 moiety. The chromophore facilitates peptide fragmentation by absorbing UV radiation and transferring it to the peptide via intramolecular vibrational redistribution (IVR).

Schneider and coworkers developed a strategy, using crown ethers as scaffolds for protein surface target recognition to explore protein folding and the mechanism of ligand binding. They designed a peptide receptor with 18C6 at one binding site for interaction with the peptide N-terminus and a peralkylammonium group as the other binding site for interaction with the C-terminus, via binding to the zwitterionic form of the

unprotected tripeptide, Gly-Trp-Gly, to develop a peptide differentiation method based on length, amino acid composition, sequence, and the configuration of the peptide and protein.[36, 37]

Griebenow and coworkers colyophilized subtilisin Carlsberg, a protein digesting enzyme, with 18C6 in organic solvent to investigate how enzyme structure and stability are correlated to catalytic properties.[38] They found that colyophilization of subtilisin with 18C6 substantially improves enzyme activity in organic solvents. They concluded that the active site structure is locally preserved by the presence of the crown ether. Exposure to organic solvents leads to the release of the crown ether but the active site structure remains intact, preserving the activity of the enzyme.

Schalley and coworkers applied molecular recognition between 18C6 and oligolysine peptides to investigate molecular mobility,[39] which has attracted considerable attention in supramolecular chemistry and biochemistry. They utilized H/D exchange methods to investigate whether 18C6 moves along an oligolysine scaffold by hopping from one Lys side chain to the next. They observed highly dynamic motion of 18C6 along oligolysine peptide chains, suggesting that other biological noncovalent complexes may exhibit dynamic behavior that had previously not been recognized. They proposed a mechanism for the dynamic motion of 18C6 along oligolysine peptide chains that proceeds by simultaneous transfer of 18C6 from its ammonium ion binding site to a nearby amino group together with a proton.

Robinson and coworkers reported a novel charge reduction approach that is based on the collision-induced removal of noncovalently attached aza-18C6 from the charged side chain of tetrameric human transthyretin (TTR).[40] The selective binding of

the crown ether to the protein contributes to the low quantity of aza-18C6 required, and reduces unintended side reactions in solution. Reduction of the charge state by using molecular recognition of aza-18C6 does not cause dramatic structural change. Therefore, it significantly improves the stability of protein complexes, and protects the native states of proteins.

Oshima and coworkers applied dicyclohexano-18C6 (DCH18C6) as an affinity ligand to extract the lysine-rich protein Cytochrome *c* in the Li_2SO_4/polyethylene glycol (PEG) aqueous two-phase system.[41] Cytochrome *c* was quantitatively extracted into the PEG-rich phase in the presence of DCH18C6 within 5 minutes.

1.5. Amino Acids for Molecular Recognition

The charged amino acids (AAs), Lys, His, Arg, glutamic acid (Glu), and aspartic acid (Asp) offer the best targets for molecular recognition of specific side chains in peptides or proteins. As a result of the structural similarity of the acidic AAs, Glu and Asp, which differ only in number of methylenes groups in the side chain, differentiation of the acidic AAs is very challenging. The basic AAs, Lys, His, and Arg offer a greater possibility of achieving specificity due to the different chemical functionalities of their side chains. Gly and Ala are good models for molecular recognition of the N-terminal amino group in peptides and proteins because the backbone amino group is the only favorable binding site for 18C6 complexation to these two AAs.

Lysine is one of the most common AAs in proteins, and is almost always found at protein surfaces. Lys comprises 9.19% of the protein in catfish,[42] 8.11% of the protein in chicken,[43] and 8.31% of the protein in beef.[44] Welfle and coworkers used maleic

anhydride covalently bound to Lys residues to determine the relative reactivity of Lys residues in HIV-1 capsid protein p24.[45] They concluded that an epitope binding affinity for the antibody strongly increased after maleic anhydride modification of the Lys residue of rp24 due to the induced change in protein conformation. D'Ambrosio and coworkers investigated the structure of porcine aminoacylase 1 (ACY1), a zinc-binding metalloenzyme using acetylation with acetic anhydride.[46] MALDI-MS analyses found eight out of 17 Lys residues acetylated, indicating that these residues are solvent-exposed.

Arginine has the largest p*K*a among all AAs. Therefore, Arg is almost always protonated under physiological conditions. Julian and Beauchamp tested various macrocycles to determine which are best suited to host the side chain of Arg.[27] They found that dibenzo-30-crown-10 (DB30C10) forms a strongly bound complex with the alkyl-guanidinium side chain of Arg, such that it can be used as a reagent for selectively identifying the presence of Arg in peptides or proteins.

Histidine is commonly involved in protein biochemistry and a common target for the study of protein surface structure. Glocker and coworkers applied diethyl pyrocarbonate (DEPC) modification of recombinant human macrophage colony-stimulating factor (rhM-CSF) protein to determine regions structurally important to ligand-receptor interactions.[47] They found that DEPC selectively modifies solvent-accessible His residues in rhM-CSF, abolishing binding and receptor activation. However, no noncovalent side chain tags have been identified thus far for selective binding of His residues.

1.6. Motivation and Systems Investigated

Although the protonated side chain of Lys has been shown to be the primary binding site for 18C6 complexation, the protonated side chains of His, Arg, and the N-terminal amino group may also compete for 18C6 complexation. Therefore, knowledge of the 18C6 binding affinities of the protonated side chains of AAs would provide insight into the selectivity of the complexation process. Other factors such as relative PA and possible binding modes between 18C6 and the AAs also play critical roles in the molecular recognition of 18C6 to peptides and proteins.

The relative PAs of 18C6 and AAs significantly affect the binding and CID behavior of the proton bound complexes between 18C6 and guest species. Therefore, an accurate PA of 18C6 would enhance our understanding of the 18C6 selectivity for the side chains of AAs. In addition, the binding modes between 18C6 and guest cations significantly affect their binding strength. Therefore, structural information regarding the proton bound complexes between 18C6 and relevant guest cations will help to visualize the binding modes and better understand trends in the 18C6 binding affinities.

In the present work, three major factors that affect the 18C6 selectivity for various binding sites in peptides and proteins were investigated: (1) The 18C6 binding affinities of a series of peptidomimetic bases (Bs), AAs, and acetylated amino acids (AcAAs) were measured using guided ion beam tandem mass spectrometry (GIBMS) techniques. The Bs serve as mimics of N-terminal amino group and the side chains of the basic AAs. The Bs examined here include: Isopropylamine (IPA), imidazole (Imid), 4-methylimidazole (4MeImid), 1-methylguanidine (MGD), methylamine (MA), ethylamine (EA), n-propylamine (NPA), n-butylamine (NBA) and 1,5-diamino pentane (DAP). The

AAs examined here include: Gly, Ala, Lys, His, and Arg. The AcAAs examined include the backbone acetylated forms of Lys, Arg, and His, as well as the side chain acetylated form of Lys, (2) The PA of 18C6 was re-evaluated using competitive threshold collision-induced dissociation techniques, and (3) infrared multiple photon dissociation (IRMPD) action spectroscopy of protonated peptidomimetic base–18C6 complexes were examined to provide experimental evidence for the structures derived from theoretical studies of the proton bound base–18C6 complexes.

1.6.1. 18C6 Binding Affinities of Bs, AAs, and AcAAs

In the present work, energy-resolved collision-induced dissociation experiments and theoretical electronic structure calculations are used to examine the 18C6 binding affinities of favorable 18C6 binding sites in peptides and proteins, i.e. the N-terminal amino group and the side chains of the basic amino acids. 18C6 binding affinities of these sites were investigated in a pedagogic fashion. First, the 18C6 binding affinities of a series of peptidomimetic bases (B) that serve as mimics for the side chains of Lys, Arg, His and the N-terminal amino group are examined to determine the intrinsic 18C6 binding affinities of the N-terminal amino group and the associated side chain functionalities.[34] These studies were extended to include several AAs,[48] and further extended to include four AcAAs[49] to determine the 18C6 binding affinities of the N-terminal amino group and side chains of the basic AAs.

The peptidomimetic bases examined here include: isopropylamine (IPA) chosen as a mimic for the N-terminal amino group, imidazole (Imid) and 4-methylimidazole (4MeImid) chosen as mimics for the side chain of His, 1-methylguanidine (MGD) chosen

as a mimic for the side chain of Arg, and several primary amines including methylamine (MA), ethylamine (EA), n-propylamine (NPA), n-butylamine (NBA) and 1,5-diamino pentane (DAP) as mimics for the side chain of Lys. In order to examine the 18C6 binding affinities of AA residues in peptides and proteins, including backbone effects, these studies were extended to include five AAs, where AA = Gly, Ala, Lys, His, and Arg. In order to determine 18C6 binding affinities of the N-terminal amino group and side chains of AAs in peptides and proteins, theses studies were further extended to include four AcAAs to control the 18C6 binding site, either to the backbone amino group or to the side chains of the AAs. The AcAAs examined here include: backbone acetylated Lys, (N_α–AcLys), side chain acetylated Lys, (N_ε–AcLys), backbone acetylated Arg, (N_α–AcArg), and backbone acetylated His, (N_α–AcHis).

1.6.2. Re-evaluation of the Proton Affinity of 18C6

The proton affinity (PA) of 18C6 plays a critical role in the binding and CID behavior of proton bound complexes between 18C6 and guest cations. An accurate determination of the PA of 18C6 can improve our current understanding and ability to control the molecular recognition between 18C6 and related molecules and guest cations. However, very limited thermochemical data has thus far been reported in the literature. Two separate determinations of the PA of 18C6 have previously been reported. Both Meot-Ner[50] and Kebarle and coworkers[51] used high pressure mass spectrometry (HPMS) techniques to determine the PA 18C6. The PA of 18C6 was determined to be 920.5 ± 8.4 kJ/mole by Meot-Ner[50] based on the proton transfer equilibrium reactions between two reference bases, 1,2-diazine and pyridine, and 18C6.

The PA of 18C6 determined by Kebarle and coworkers[51] was derived using ammonia as a reference base as 962.3 ± 8.4 kJ/mole. In their PA database evaluation, Hunter and Lias made use of the PA of 18C6 reported by Kebarle and coworkers and adjusted it to 967.0 ± 8.4 kJ/mol based on adjustments and temperature corrections to the PAs of the relevant reference bases.[52,53]

In the current study, the PA of 18C6 is re-evaluated by examining the threshold collision-induced dissociation (TCID) behavior of four proton bound heterodimers, $(B)H^+(18C6)$, which dissociate to produce $H^+(B)$ + 18C6 and $H^+(18C6)$ + B in competition, where B = Gly, Ala, Imid, and 4MeImid.[54] Based on the literature PAs of the reference Bs and the measured relative PAs of B and 18C6 using TCID techniques, the PA of 18C6 is re-evaluated. The TCID thresholds for the two CID pathways provide the $(B)H^+$–18C6 and $(18C6)H^+$–B BDEs as well as the relative PAs of B and 18C6. The measured $(B)H^+$–18C6 and $(18C6)H^+$–B BDEs and evaluated PA of 18C6 are compared to theoretical estimates determined using M06 and B3LYP theories. The PA of 18C6 determined here is compared to measured values reported by Meot-Ner,[50] Kebarle and coworkers,[51] and evaluated by Lias and Hunter for the NIST Webbook.[52,53]

1.6.3. IRMPD Action Spectroscopy of $(B)H^+(18C6)$ Complexes

Structural effects play a critical role in the molecular recognition of peptides and proteins by crown ethers. In order to experimentally characterize the ground-state and low-energy conformers of the $(B)H^+(18C6)$ complexes, and to validate the structural information extracted from theoretical calculations, the interactions of 18C6 with five protonated peptidomimetic bases are examined by IRMPD action spectroscopy

techniques.[55] The peptidomimetic bases examined here include: IPA, NBA, DAP, 4MeImid, and MGD. In order to determine the ground-state and stable low-energy conformers of the $(B)H^+(18C6)$ complexes, the measured IRMPD action spectra of these complexes are compared with linear IR spectra derived from theoretical calculations performed at the B3LYP/6-31G* level of theory.

1.7. References

(1) Matthews, B. W. *Annu. Rev. Phys. Chem.* **1976**, *27*, 493.

(2) Dyson, H. J.; Wright, P. E. *Chem. Rev.* **2004,** *104,* 3607.

(3) Palmer, A. G. *Chem. Rev.* **2004,** *104,* 3623.

(4) Mendoza, V. L.; Vachet, R. W. *Mass Spectrom. Rev.* **2009**, *28*, 785.

(5) Wales, T. E.; Engen, J. R. *Mass Spectrom. Rev*. **2006**, *25*, 158.

(6) Sinz, A. *Mass Spectrom. Rev.* **2006**, *25*, 663.

(7) Wales, T. E.; Engen, J. R. *Mass Spectrom. Rev*. **2006**, *25*, 158.

(8) Smith, D. L.; Deng, Y.; Zhang, Z. *J. Mass Spectrom*. **1997**, *32*, 135.

(9) Engen, J. R.; Smith, D. L. *Anal. Chem.* **2001**, *73*, 256A.

(10) Kaltashov, I. A.; Eyles, S. J*. Mass Spectrom. Rev.* **2002**, *21*, 37.

(11) Kaltashov, I. A.; Eyles, S. J*. Mass Spectrom. Rev.* **2002**, *37*, 557.

(12) Hoofnagle, A. N.; Resing, K. A.; Ahn, N. G. *Annu. Rev. Biophys. Biomol. Struct.* **2003**, *32*, 1.

(13) Eyles, S. J.; Kaltashov, I. A. *Methods* **2004***, 34*, 88.

(14) Garcia, R. A.; Pantazatos, D.; Villarreal, F. J. *Assay Drug Dev. Technol.* **2004**, *2*, 81.

(15) Sinz, A. *J. Mass Spectrom*. **2003**, *38*, 1225.

(16) Brunner, J. *Annu. Rev. Biochem.* **1993**, *62*, 483.

(17) Kluger, R.; Alagic, A. *Bioorg. Chem.* **2004**, *32*, 451.

(18) Melcher, K. *Curr. Prot. Pept. Sci.* **2004**, *5*, 287.

(19) Kodadek, T.; Duroux-Richard, I.; Bonnafous, J. C. *Trends Pharmacol. Sci.* **2005**, *26*, 210.

(20) Back, J. W.; de Jong, L.; Muijsers, A.O.; de Koster, C. G. *J. Mol. Biol.* **2003**, *331*, 303.

(21) Friedhoff, P. *Anal. Bioanal. Chem.* **2005**, *381*, 78.

(22) Trakselis, M. A.; Alley, S. C.; Ishmael, F. T. *Bioconjugate. Chem.* **2005**, *16*, 741.

(23) Petrotchenko, E. V.; Pedersen, L. C.; Borchers, C. H.; Tomer, K. B.; Negishi, M. *FEBS Lett.* **2001**, *490*, 39.

(24) Julian, R. R.; Beauchamp, J. L. *Int. J. Mass Spectrom.* **2001**, *210/211*, 613.

(25) Julian, R. R.; Beauchamp, J. L. *J. Am. Soc. Mass Spectrom.* **2002**, *13*, 493.

(26) Julian, R. R.; Beauchamp, J. L. *J. Am. Soc. Mass Spectrom.* **2004**, *15*, 616.

(27) Julian, R. R.; Akin, M.; May, J. A.; Stoltz, B. M.; Beauchamp, J. L. *Int. J. Mass Spectrom.* **2002**, *220*, 87.

(28) Julian, R. R.; May, J. A.; Stoltz, B. M.; Beauchamp, J. L. *Int. J. Mass Spectrom.* **2003**, *228*, 851.

(29) Ly, T.; Julian, R. R. *J. Am. Soc. Mass Spectrom.* **2006**, *17*, 1209.

(30) Ly, T.; Julian, R. R. *J. Am. Soc. Mass Spectrom.* **2008**, *19*, 1663.

(31) Liu, Z.; Cheng, S.; Gallie, D. R.; Julian, R. R. *Anal. Chem.* **2008**, *80*, 3846.

(32) Ly, T.; Liu, Z.; Pujanauski, B. G.; Sarpong, R.; Julian, R. R. *Anal. Chem.* **2008**, *80*, 5059.

(33) Yeh, G. K.; Sun, Q.; Meneses, C.; Julian, R. R. *J. Am. Soc. Mass Spectrom.* **2009**, *20*, 385.

(34) Chen, Y; Rodgers, M. T. *J. Am. Chem. Soc.*. **2012**, *134*, 2313.

(35) Wilson, J. J.; Kirkovits, G. J.; Sessler, J. L.; Brodbelt, J. S. *J. Am. Soc. Mass Spectrom.* **2008**, *19*, 257.

(36) Hossain, M. A.; Schneider, H. J. *J. Am. Chem. Soc.* **1998**, *120*, 11208.

(37) Peczuh, M. W.; Hamilton, A. D. *Chem. Rev.* **2000**, *100*, 2479.

(38) Santos, A. M.; Vidal, M.; Pacheco, Y.; Frontera, J.; Báez, C.; Ornellas, O.; Barletta, G.; Griebenow, K. *Biotechnol*. *Bioeng*. **2001**, *74*, 295.

(39) Weimann, D. P.; Winkler, H. D. F.; Falenski, J. A.; Koksch, B.; Schalley, C. A. *Nature Chem.*, **2009**, *1*, 573.

(40) Pagel, K.; Hyung, S. J.; Ruotolo, B. T.; Robinson, *Anal. Chem*. **2010**, *82*, 5363.

(41) Oshima, T.; Suetsugu, A.; Baba, Y. *Anal. Chim. Acta.* **2010**, *674*, 211.

(42) Helena Kloosterman; USDA National Nutrient Database for Standard Reference. "Essential Amino Acids Search, Catfish Farmed" Retrieved 2010-10-10.

(43) Helena Kloosterman; USDA National Nutrient Database for Standard Reference. "Essential Amino Acids Search, Chicken Roasting Meat Skin". Retrieved 2010-10-10.

(44) Helena Kloosterman; USDA National Nutrient Database for Standard Reference. "Essential Amino Acids Search, Beef Ground 90, 10 Cooked". Retrieved 2010-10-10.

(45) Ehrhardm, B.; Misselwitz, R.; Welfle, K.; Hausdorf, G.; Glaser, R. W.; Schneider-Mergener, J.; Welfle, H. *Biochemistry* **1996**, *35*, 9097.

(46) D'Ambrosio, C.; Talamo, F.; Vitale, R. M.; Amodeo, P.; Tell, G.; Ferrara, L.; Scaloni, A. *Biochemistry* **2003**, *42*, 4430.

(47) Glocker, M. O.; Kalkum, M.; Yamamoto, R.; Schreurs, J. *Biochemistry* **1996**, *35*, 14625.

(48) Chen, Y; Rodgers, M. T. *J. Am. Chem. Soc.*. **2012**, *134*, 5863.

(49) Chen, Y.; Rodgers, M. T. *J. Am. Soc. Mass Spectrom.* **2012**, submitted.

(50) Meot-Ner, M. *J. Am. Chem. Soc.* **1983**, *105*, 4906.

(51) Sharma, R. B.; Blades, A. T.; Kebarle, P. *J. Am. Chem. Soc.* **1984**, *106*, 510.

(52) Hunter, E. P.; Lias, S. G. *J. Phys. Chem. Ref. Data,* **1998**, *27*, 413.

(53) NIST Chemistry Webbook, NIST Standard Reference Database Number 69, http://webbook.nist.gov/chemistry/.

(54) Chen, Y.; Rodgers, M. T. *Anal. Chem.* **2012**, ac-2012-01804j, submitted.

(55) Chen, Y.; Rodgers, M. T. *J. Am. Soc. Mass Spectrom.* **2012**, submitted.

CHAPTER 2

EXPERIMENTAL AND THEORETICAL METHODS

2.1. GIBMS Instrument Overview

Figure 2.1 shows a schematic diagram of the guided ion beam tandem mass spectrometer (GIBMS). The vacuum system consists of six regions that are independently pumped: (1) ESI source–rf ion funnel–hexapole ion guide interface, (2) the first differentially pumped chamber, (3) the second differentially pumped chamber, (4) the magnetic sector flight tube and third differentially pumped chamber, (5) the reaction chamber, and (6) the detector chamber. The ESI source–rf ion funnel–hexapole ion guide interface region is pumped by a roots blower, whereas other regions are pumped by diffusion pumps with integral water baffles. Details of each region of the apparatus are provided below.

2.2. ESI Source- RF Ion Funnel-Hexapole/Collision Cell Interface

An electrospray ionization (ESI) source has been developed for the guided ion beam tandem MS, as shown in **Figure 2.2**. Coupled to the ESI source, a vacuum interface that ensures the production of thermal ions was also developed that includes an rf ion funnel and hexapole ion guide/collision cell assembly. The rf ion funnel-hexapole ion guide interface significantly improves the ion transmission efficiency and generates thermal ion beams with a narrow well-defined kinetic energy distribution.

2.2.1. ESI Source

Ions are generated using a home-built ESI source similar in design to that developed by Moison et al.[1] The relevant peptidomimetic base (B), amino acid (AA), or acetylated amino acid (AcAA) as well as 18C6 are dissolved in a 50%:50% by volume MeOH:H_2O mixture to produce a solution that is ~0.2 mM in each species. The solution is delivered to a 35 gauge stainless steel (SS) ESI needle (Small Parts) via a syringe pump (Harvard Apparatus, PHD 22/2000) at a flow rate of ~1.0 μL/min. The ESI needle is biased at ~1.7–2.0 kV provided by a high voltage dc power supply (Glassman, model EQ5R240). The ESI needle is mounted on an XYZ translation stage (Line Tool Co, model A RH- ½" travel) for fine tuning of the needle location relative to the capillary tubing.

The fine spray of droplets emanating from the ESI needle is visualized using a fiber optic illuminator (Cole-Parmer, WU-41723-00) and a Light Pipe (Cole-Parmer, EW-41720-75), and monitored with a CCTV camera (Panasonic, WV-BP330), and displayed on a CCTV monitor (Videology, 40VM9). Droplets emanating from the spray are transferred into the vacuum region through a 0.030" ID, and 0.063 OD SS capillary (McMaster-Carr), that is held within a capillary tubing holder (CTH). The CTH is machined from 0.063" ID, 0.375" OD SS tubing (Small Parts) and reamed out to an ID of 0.067" to allow easy insertion of the 0.063" OD capillary tubing. The entrance of the 0.063" capillary tubing is further restricted using an entrance limiting orifice (ELO) that is machined into a cap that slides over the entrance end of the CTH. A small-diameter (0.006", 0.009, and 0.012") hole is drilled at the center of the ELO. Under normal operating conditions, a 0.009" opening is used to achieve good signal stability. The ELO

serves to throttle the gas load into the vacuum, such that the diameter of the ELO is directly correlated with the pressure in the source interface region.

The CTH is electrically isolated using PEEK thermoplastic material to allow the entire capillary to be biased at 20–50 V independently, and heated to 90–200^{o}C if necessary. The dc voltage is provided by a dc power supply (BK Precision, model 1623 A). The capillary is heated by a heating tape (Omega, HTC-030) that is controlled by a variable autotransformer (Staco, 3PN1010). The capillary temperature is monitored using a K type thermocouple through a thermocouple feedthrough (MDC, TC PWR K). The K type thermocouple is connected to a digital multimeter (Omega, HHM57B) for temperature readout. The capillary is ~4.0” long and its exit is flush with the first plate of the rf ion funnel.

2.2.2. RF Ion Funnel

The rf ion funnel, similar in design to that developed by Smith and coworkers,[2,3] is a focusing device that facilitates efficient transfer of ions from the high pressure source region to the low pressure region of the mass spectrometer. The ion funnel consists of 88 0.020” thick brass ring electrodes. Each electrode is separated by a 0.020” thick Teflon sheet. The first 44 electrodes have a constant ID of 1.000”, while the latter 44 electrodes have IDs that decrease from 1.000” to 0.094” to form a linear taper. A linear dc gradient is applied across the ion funnel by applying a dc voltage to the first and last plates of the ion funnel with a resistor chain connecting all intervening plates. The entrance plate is biased at ~25 V, while the exit plate is held at ~5 V for the systems investigated here. Adjacent electrodes receive equal and opposite phases of

an rf signal with a peak-to-peak voltage in the range between 10 and 30 V, and is operated at a frequency in the range between 0.6 and 1.2 MHz. This oscillating field on the plates and the tapering of the lenses focuses ions radially to the center of the ion funnel.

A jet disrupter (JD), a 0.25” diameter metal disc, is located ~1.0” from the entrance of the ion funnel to prevent large droplets from the spray from depositing downstream on the hexapole ion guide. The JD is biased at 15–25 V. A dc-only hexapole injection lens (HIL) with a 0.140” ID follows the last plate of the ion funnel to prevent ions that have entered the hexapole from diffusing back upstream toward the ion funnel. The HIL is biased at a voltage that lies between the voltage on the final ion funnel plate and the hexapole dc voltage, which is typically held at ground potential.

The circuit board that provides the dc and rf signals to the ring electrodes was designed using an internet vendor (www.ExpressPCB.com). The circuit board provides both rf and dc outputs, such that it requires only one electrical connection per plate. Surface-mount resistors (200 kOhm, 1/8 Watt, Size 1206, Allied Electronics) and capacitors (0.01 μF, 100 V, Size 1206, Allied Electronics) are used on the circuit board. Two dc voltages, (dc^+, on the entrance lens, dc^- on the exit lens) are applied across the ion funnel to define the linear voltage gradient. Normal operating conditions for the ion funnel are dc^+ = ~25 V and dc^- = ~5 V.

A home-built dc voltage divider that consists of a 75 V dc linear regulated power supply (Acopian Technical, model B75GT05) and a four-channel circuit provides four dc voltages for dc^+, dc^-, JD, and HIL, respectively. The rf signal is applied to the ion funnel using a 20 MHz sweep function generator (B&K Precision, model 4040A), and is

amplified with an rf amplifier (Electronics & Innovation, model 240 L). The signal from the amplifier is split into equal and opposite phases with a 100-ohm trifilar-wound ferrite-core balun transformer. The home-built balun consists of two stacked ferrite toroids (Amidon Inc. FR-290-77) wrapped with 14-gauge magnet wire.

2.2.3. RF Hexapole Ion Guide/Collision Cell

Ions emanating from the ion funnel are thermalized in the hexapole ion guide by collisions with the background gases. The hexapole ion guide consists of six 0.125" diameter $\times$ 6.0" long SS rods (Small Parts), equally spaced on a 0.375" BC. Adjacent rods receive equal and opposite phases of rf signal. The hexapole is operated in the rf only mode with a peak to peak voltage of ~300 V and a frequency of 5.5 MHz. The rf signal is generated using an rf generator described by Jones et al.[45] The dc offset of the hexapole was held at ground potential. Therefore, the ions pass through the hexapole region primarily by diffusion.

The hexapole ion guide spans two vacuum regions, the ESI source vacuum interface region and the differential region. While running the ESI source, the pressure in the source region is ~50 mTorr, and 5–8 $\times$ 10^{-5} Torr in the differential region. These pressures ensure a high number of ion/neutral collisions in the hexapole ion guide for thermalization. The center of the hexapole ion guided is surrounded by a collision cell. When necessary, collision gas, i.e. argon, helium, and nitrogen, can be introduced into the cell to facilitate thermalization of the ions emanating from the ESI source. Other gases can be introduced into the collision cell to react with ions produced by the ESI

source, generally by adduction or ligand exchange to generate complexes not produced directly by the ESI source.

2.3. Differential Focusing Stage

Ions are effusively sampled from the ESI source–rf ion funnel–hexapole ion guide interface and are gently focused by a series of aperture lenses in the differential focusing stage (DFS). Low dc voltages are applied to the differential lenses to avoid energetic collisions that could internally excite the ions. The DFS lenses have an open design to maximize gas conductance, which reduces the probability of energetic collisions in this region. The pressure in the differential region is maintained at 5–8 $\times$ 10^{-5} Torr during ESI operation by a 2000 Ls^{-1} diffusion pump with integral water cooled baffles (Edwards Diffstak MK 2250/2000P). Differential pumping of the following region is maintained by a 5.0 mm diameter exit aperture.

2.4. Ion Beam Formation (Momentum Analyzer and FS1, FS2, and FS3)

The ion beam emanating from the DFS is re-shaped from cylindrical to ribbon shape and accelerated for momentum analysis in focusing state 1 (FS1). The ions are extracted from the first differential region and collimated by a double aperture immersion lens, focused by an einzel lens, and then accelerated to the momentum analysis potential. An electrostatic quadrupole doublet lens converts the beam from cylindrical symmetry to a ribbon shape appropriate for momentum analysis. The ion beam is introduced into the flight tube through the entrance slit of the momentum analyzer. The source end of the instrument is isolated by a gate valve mounted on the flight tube of

the analyzer to allow cleaning of the heated capillary inlet, rf ion funnel, and hexapole ion guide without venting the entire instrument. The pressure in the FS1 region is maintained at 1–2 $\times$ 10^{-6} Torr during ESI operation by a 700 Ls^{-1} diffusion pump with integral water cooled baffles (Edwards Diffstak MK2 160/700P).

Differential pumping of the magnetic sector flight tube is maintained by the entrance slit of the momentum analyzer. The magnetic momentum analyzer consists of a magnetic sector (Nuclide Corporation) with a 30.5 cm radius ion flight path and a 90° deflection angle. The entrance and exit slit widths are 1 mm. The flight tube is biased at -2800 V dc. The momentum analyzer serves as a mass filter with a mass range from 1 to 1500 Da, and a mass resolution of ~500 ($m/\Delta m$ fwhm) for ions with a kinetic energy distribution narrower than 1 eV (E/ΔE fwhm).

After passing through the exit slit of the momentum analyzer, the ion beam is reconverted to cylindrical symmetry by a second electrostatic quadrupole doublet lens and focused by an einzel lens in focusing stage 2 (FS2). A set of horizontal and vertical deflectors allows centering of the ion beam on the entrance to the reaction vacuum chamber through a 2 mm aperture. This aperture also serves to separate vacuum regions for differential pumping. The pressure in the flight tube and FS2 region is maintained by a 300 Ls^{-1} diffusion pump with integral water baffles (Edwards Diffstak MK2 100/300P). The ion beam is decelerated by an exponential retarder, which consists of 31 evenly spaced stainless steel plates and is 9.8 cm long. The potentials on the retarder plates are determined by internally connected resistors that establish an exponentially decreasing field.[6] The last three plates are connected and biased to a potential controlled externally. These final plates act as the first lens in a four element

lens sequence, focusing stage 3 (FS3), that focuses and injects the ions into the octopole ion beam guide.

2.5. Reaction Region

The reaction region comprises an octopole ion guide surrounded by a gas reaction cell. Equal and opposite phases of a radio frequency voltage are applied to the octopole rods to provide a radial effective potential well for highly efficient collection of ionic reaction products.[7] The octopole ion guide consists of eight rods of 3.2 mm diameter $\times$ 27.9 cm long, equally spaced on a circle of 11.7 mm diameter. The rf signal is generated by a high voltage rf generator described by Jones et al.[5] The peak-to-peak amplitude of the rf potential is typically 300 V, which provides a trapping well of 2.83 V.[8] The dc potential on the octopole ion guide and surrounding collision gas cell is controlled by a bipolar operation power supply (Kepco BOP100-M) under computer control in order to vary the kinetic energy of the ions during experiments.

The octopole passes through a gas reaction cell midway along its length. The gas cell consists of a 51 mm long $\times$ 51 mm diameter central body with smaller diameter extension tubes, 32 mm long $\times$ 17 mm diameter, extending from each end of the gas cell along the octopole rods, designed to limit gas conductance from the cell.[9] Two SS tubes emanating perpendicularly from the gas reaction cell for introducing collision gas and monitoring the gas cell pressure are electrically isolated from ground via glass to metal seals. The gas pressure introduced into the collision cell is controlled by a leak valve and measured by a capacitance manometer (MKS Baratron 690A). The estimated effective cell length is 8.3 cm with a 10% uncertainty assuming a trapezoidal pressure

profile.[9] In order to ensure that multiple ion-neutral collisions are improbable, the collision gas pressure is typically varied between 0.05 to 0.2 mTorr for cross section measurements. Xe is used as the collision gas because it is heavy and polarizable and therefore leads to more efficient kinetic to internal energy transfer in the CID process.[10-12] A pressure difference ratio of approximately 70:1 between the collision gas cell and the reaction vacuum chamber is maintained during operation by continuous pumping using a 2000 L s^{-1} diffusion pump with integral water cooled baffles (Edwards Diffstak MK2 250/2000P). The gas in can be diverted from the reaction cell directly to the reaction vacuum chamber by switching remotely controlled electropneumatic valves on the gas inlet lines to measure the background signals arising from collisions that occur outside of the collision gas cell. In this configuration, the background pressure in the reaction chamber is the same as when the gas is flowing to the collision gas cell. The effective length for background reactions is approximately twice as long as the collision gas cell path length, resulting in a measured foreground/background ion intensity ratio of nearly 40:1.

2.6. Quadrupole Mass Filter and Ion Detector

After passing through the collision gas cell, ions drift to the end of the octopole ion guide and are extracted and injected into the quadrupole mass filter by five lenses of cylindrical symmetry in focusing stage 4 (FS4). The quadrupole mass filter (Extrel, ¾" Tri-Filter Quadrupole Mass Filter, 150 QC RF/DC Power Supply) is composed of rods that are 19 mm diameter × 22.9 cm long. The quadrupole rods consist of three segments, pre-rods, center-rods, and post-rods. The pre-rods and post-rods work as ion

guides and are shorted to receive a single dc voltage. The center-rods work as a mass filter and are controlled by a 150 QC power supply. The 880 kHz rf voltage is generated by 150 QC power supply with which the quadrupole mass filter can provide a mass range of 1–1000 Da. To achieve maximum transmission of ions, the quadrupole is ordinarily operated at fairly low mass resolution.

Ions emanating from the quadrupole mass filter are focused by three lenses of cylindrical symmetry in the detector focusing stage. Ions are detected using a secondary electron scintillation detector of the Daly type,[13] operated at a target potential of 28 kV. Combined with pulse counting electronics, the detector provides high counting efficiency and low mass discrimination. The scintillation photons are detected using a photomultiplier tube (Hamamatsu R329 SEL). The output pulses of the photomultiplier are directly discriminated from noise using a constant fraction discriminator (Canberra model 2126) and counted using a dual counter timer (Canberra model 2071 A) for digital data acquisition. A linear ratemeter (EG&G Ortec model 661) is used for visual display during tuning of the ion beam. The counting response of the ion detection system is linear up to ~ 2×10^7 s^{-1}, and the counting noise background is less than 10 s^{-1}, providing a dynamic range in excess of 6 orders of magnitude.

2.7. Data Acquisition System

The guided ion beam apparatus is controlled by a personal computer equipped with a Pentium 133 MHz processor. Hardware control functions are provided by a commercial GPIB interface board (Keithley PCI-488) and a custom digital I/O board. The GPIB board has 12-bit resolution and controls a Canberra dual counter timer 2071

A (used in ion detection) and a Kepco BOP 100-1M power supply (used to control the dc voltage applied to the reaction region). The BOP has two modes with high (0 to ± 100 eV) and low (0 to ± 10 eV) ranges, such that the 12-bit resolution of the GPIB results in a minimum energy step size of 0.002eV below 10 eV and 0.024 eV above 10 eV. The digital I/O board contains a 16-bit optically isolated DAC used to set the m/z of the quadrupole mass filter. The minimum step size is 0.0153 Da. The digital I/O board also has two digital outputs connected to solid-state relays, which control electropneumatic valves that direct the neutral reactant gas to the collision gas cell or reaction chamber. The I/O board also interfaces to the Baratron through a SCSI cable such that the pressure output is read digitally. All other ion lens potentials in the instrument and gas flow rates in the source and interaction regions need not vary with the ion interaction energy and are therefore not automated. Lens potentials are provided by custom-built voltage dividers powered by standard dc power supplies. Collision gas flow rates are controlled manually with variable leak valves (Granville Phillips, model 203).

Two fully 32-bit multithreaded graphical user interface (GUI) programs have been developed to control the instrument and acquire data during experiments. The programs are written using Compaq Vision Fortran Version 6.1A with lower level device interfaces written in C. The first program, MSCAN, allows the quadrupole mass filter to be scanned at a fixed octopole interaction energy and records the intensity of detected ions as a function of mass. The second program, EMP (energy, mass, and pressure) allows the octopole interaction energy to be scanned and records the intensity of the specified reactant and product ions as a function of this energy. These programs have several

features in common. Each program has a real-time graphical display and I/O windows, a control panel, and a color and symbol palette. The control panel provides several functions: (1) it requires user input for instrument control and set up of a desired experiment, (2) in real time, it reports details and progress of the current experiment, and (3) allows changes to be made in the graphical display window during data acquisition.

2.8. General Procedures

Ion intensities are converted to absolute cross sections using Beer's law. The experimental total reaction cross section, σ_{tot}, is determined by the relation,

$$I_R = \left(I_R + \sum I_p\right) e^{-\sigma_{tot} n L} \tag{2.1}$$

where I_R and I_P are the measured transmitted intensities of the reactant and product ions, respectively, n is the gas density, and L is the effective collision gas cell length. Individual product cross sections are calculated using the following formula

$$\sigma_p = \sigma_{tot} \left(I_p \Big/ \sum I_p \right) \tag{2.2}$$

Equations 2.1 and 2.2 presume that sum of the transmitted reactant and product ions is equal to the incident ion intensity, i.e., $I_0 = I_R + \sum I_P$. Due to the 4π collection characteristics of the octopole, this is valid as long as all significant product channels are monitored.

Absolute uncertainties in cross section magnitudes are estimated to be ± 20%, which are largely the result of errors in the pressure measurement and the length of the interaction region. Relative uncertainties are approximately ± 5%.

Ion kinetic energies in the laboratory frame, E_{lab}, are converted to energies in the center of mass frame, E_{CM}, using the formula $E_{CM} = E_{lab}\, m/(m + M)$, where M and m are the masses of the ionic and neutral reactants, respectively. All energies are reported in the CM frame unless otherwise noted. The absolute zero and distribution of the ion kinetic energies are determined using the octopole ion guide as retarding potential analyzer as previously described.[9] The potential difference between the ESI capillary and the interaction region (i.e., the dc voltage of the octopole) establishes the nominal laboratory ion kinetic energy. The octopole ion guide itself serves as a highly efficient retarding energy analyzer. The ion beam intensity, I_0, is monitored as the dc voltage of the octopole is swept through the ion energy zero, producing a retardation curve such as that shown in **Figure 2.3.** This figure shows the ion intensity of the (methylamine)H^+(18C6) complex as a function of the laboratory kinetic energy. The trapping characteristics of the octopole prevent dispersion of low energy ions due to space charge. Further, because reactions take place in the same region as the energy analysis, there is no ambiguity in the interaction determination due to contact potential differences. For the ESI source, the experimental primary ion kinetic energy distribution, as determined by the retarding energy analysis, is nearly Gaussian. A Gaussian curve fitted to the experimental distribution from the retarding energy analysis is shown in **Figure 2.4**, where the ion beam energy distribution was obtained by taking the derivative with respect to energy of the retarding energy analysis curve. The solid line is a Gaussian curve fitted to the data points. The apparent full-width-at-half-maximum (fwhm) from the retardation curve adequately describes the width of the Gaussian fit. For most of the experiments performed here, the distribution of ion kinetic energies is

nearly Gaussian with a fwhm typically between 0.2 and 0.6 eV (lab). The uncertainty in the absolute energy scale is ± 0.05 eV (lab).

Even when the pressure of the reactant neutral is low, it has previously been demonstrated that the effect of multiple collisions can significantly influence the shape of CID cross sections.[14] Because the presence and magnitude of these pressure effects are difficulty to predict, we have performed pressure-dependent studies of all cross sections examined in this work. Data free from pressure effects are obtained by extrapolating to zero reactant pressure, as described previously.[14] Thus, results reported in these studies are due to single bimolecular encounters.

2.9. Thermochemical Analysis

The threshold regions of the CID cross sections were modeled using an empirical threshold energy law, equation 2.3

$$\sigma(E) = \sigma_0 \sum_i g_i (E + E_i - E_0)^n / E \qquad (2.3)$$

where σ_0 is an energy independent scaling factor, E is the relative translational energy of the reactants, E_0 is the threshold for reaction of the ground electronic and ro-vibrational state, and n is an adjustable parameter that describes the efficiency of kinetic to internal energy transfer.[8] The summation is over the ro-vibrational states of the reactant ions, i, where E_i is the excitation energy of each state and g_i are the populations of those states ($\Sigma g_i = 1$). The relative reactivity of all ro-vibrational states, as reflected by σ_0 and n, is assumed to be equivalent.

Several systems investigated here result in two CID reactions occurring in parallel and competing with each other. To examine the effects of competition on the

measured CID cross sections and extract accurate threshold values from the experimental data, the modified model of equation 2.4 based on equation 2.3 was used to simultaneously analyze the thresholds for these systems.

$$\sigma_j(E) = \frac{n\sigma_{0,j}}{E}\sum_i g_i \int_0^{E+E_i-E_0} \frac{k_j(E^*)}{k_{tot}(E^*)}[1-e^{-k_{tot}(E^*)\tau}](\Delta E)^{n-1}d(\Delta E) \qquad (2.4)$$

The indices j refer to a particular product channel, $k_{tot} = \sum k_j$, and all rate constants are calculated using Rice-Ramsperger-Kassel-Marcus (RRKM) theory. The ratio of dissociation rates k_j/k_{tot} introduces the coupling between product channels j. The scaling factors $\sigma_{0,j}$ are ideally the same for all product channels, however, independent scaling is needed to accurately reproduce the cross section magnitudes in theses systems. E^* is the internal energy of the energized molecule after collision, $E^* = E + E_i - \Delta E$, where E and E_i are as defined in equation 2.3 and ΔE is the energy that remains in translation after collision between the reactant ions and Xe.

The density of ro-vibrations states, i, is determined using the Beyer-Swinehart algorithm,[15-17] and the relative populations, g_i, are calculated for a Maxwell-Boltzmann distribution at 298 K, the internal temperature of the reactants. The calculated frequencies are scaled by ±10% to estimate the sensitivity of our analysis to the deviations from the true frequencies as suggested by Pople.[18,19] The corresponding change in the average vibrational energy is assumed to provide a good estimate of one standard deviation of the uncertainty in the vibrational energy.

All CID reactions that occur faster than the experimental time scale, ~10^{-4} s, should be observed. However, as the size of the reactant ions increases, there is an increased probability that the CID reaction will not take place within the experimental

time scale. Once the lifetime of the energized molecule (EM) approaches this limit, the CID threshold shifts to higher energies, resulting in a kinetic shift. Therefore, statistical theories for unimolecular dissociation were included in the analysis, specifically Rice-Ramsperger-Kassel-Marcus (RRKM) theory, as described in detail elsewhere[20,21] to quantify and correct for the kinetic shift. This requires sets of ro-vibrational frequencies appropriate for the EM and the transition states (TSs) leading to dissociation. The TSs are expected to be loose and product-like and thus are modeled using the ro-vibrational frequencies of the products for these systems. This treatment corresponds to a phase space limit (PSL) in which the TS occurs at the centrifugal barrier for dissociation as described in detail elsewhere.[20]

The models represented by equations 2.3 and 2.4 are expected to be appropriate for translationally driven reactions[22] and have been found to reproduce cross sections well in numerous previous studies of CID processes.[23-34] The model is convoluted with the kinetic and internal energy distributions of the reactants, and a nonlinear least-squares analysis of the data is performed to give optimized values for the parameters σ_0, E_0, and n. The errors associated with the measurement of E_0 are estimated from the range of threshold values determined for the zero-pressure-extrapolated data sets for each complex, variations associated with uncertainties in the vibrational frequencies, and the error in the absolute energy scale, ±0.05 eV (lab). For analyses that include the RRKM lifetime analysis, the uncertainties in the reported E_0(PSL) values also include the effects of increasing and deceasing the time assumed available for dissociation (~ 10^{-4} s) by a factor of 2.

Equations 2.3 and 2.4 explicitly include the internal energy of the reactant, E_i. All energy available is treated statistically because the ro-vibrational energy of the reactants is redistributed throughout the reactant upon interaction with Xe. Because the CID processes examined here are simple noncovalent bond cleavage reactions, the E_0(PSL) values determined from analysis with equations 2.3 and 2.4 can be equated to 0 K BDEs.[35,36] The accuracy of the thermochemistry obtained by this modeling procedure has been verified for many systems by comparing values derived from other experimental techniques and to ab initio calculations. Absolute BDEs in the range from ~10 to 400 kJ/mol have been accurately determined using threshold collision-induced dissociation (TCID) techniques.[37]

2.10. Conversion from 0 to 298 K

To allow comparison to commonly employed experimental conditions, the 0 K BDEs are converted to 298 K bond enthalpies and free energies. The enthalpy and entropy conversions are calculated using standard formulas (assuming harmonic oscillator and rigid rotor models) and vibrational and rotational constants determined for the B3LYP/6-31G* optimized geometries.

2.11. FT–ICR MS–FEL Instrument Overview

Infrared multiple photon dissociation (IRMPD) action spectroscopy experiments are performed using a Fourier transform ion cyclotron resonance mass spectrometer (FTICR MS) coupled to the free electron laser (FEL). A schematic diagram of the FT–ICR MS coupled to the FEL is shown in **Figure 2.5**.

2.11.1. Free Electron Laser (FEL)

Electrons generated by an electron gun are accelerated in a linear accelerator to relativistic speeds and injected into an undulator. The oscillating trajectory of the electron beam in the magnetic field results in the irradiation of infrared beam. An optical cavity captures the light, therefore, freshly injected electrons can interact with the circulating light pulses to generate stimulated emission. The wavelength of the stimulated radiation is controlled by the FEL resonance condition. The deviation from the straight path of the electron beam is determined by the magnetic field strength in the undulator. Higher magnetic field induces greater electron deviation from the straight path, resulting in a longer resonance wavelength.

The output wavelength of the FEL depends on the strength of the magnetic field. Adjustment of the gap between the two arrays of magnets forming the undulator allows the strength of the magnetic field to be varied, and the wavelength of the irradiation to be tuned. The FEL has been described in detail elsewhere.[38–40]

2.11.2. Fourier Transform Ion Cyclotron Resonance Mass Spectrometer

IRMPD action spectra of five (B)H^+(18C6) complexes were measure using 4.7 T Fourier transform ion cyclotron resonance mass spectrometer (FT-ICR MS) coupled to the free electron laser (FEL) that is housed at the FOM Institute for Plasma Physics, Rijnhuizen and has been described in detail elsewhere.[38-40] The protonated complexes were generated using a micromass “Z-spray” electrospray ionization (ESI) source from solutions containing 1 mM 18C6, 2 mM peptidomimetic base and 1–4 mM acetic acid in an approximately 50%/50% MeOH/H_2O mixture. The solution was introduced to the ESI

needle at a flow rate of 10 μL/min, and the ESI needle was generally held at ~3 kV. Ions emanating from the ESI source were accumulated in a hexapole trap for several seconds followed by pulsed extraction through a quadrupole bender and injected into the ICR cell via an rf octopole ion guide. Potential switching of the dc bias of the octopole was applied where a negative dc bias was superimposed on the full length of the octopole rods with relative ground potential on the ICR cell. Therefore, ions were decelerated by climbing the potential difference between the octopole ion guide and the ICR cell, and are easily captured by a gated trapping technique in the ICR cell.[39] The precursor ions were mass selected using stored waveform inverse Fourier transform (SWIFT) techniques and irradiated by the FEL at pulse energies of ~40 mJ per macropulse of 5 μs duration for 3 s at a repetition rate of 5 Hz, corresponding to interaction of the (B)H^+(18C6) complexes with 15 macropulses.

The IRMPD yield was determined from the precursor ion intensity (I_p) and the sum of the fragment ion intensities (I_{fi}) after laser irradiation at each frequency as shown in equation 2.5.

$$\text{IRMPD yield} = \left(\sum_i I_{f_i}\right) \Big/ \left(I_p + \sum_i I_{f_i}\right) \tag{2.5}$$

2.12. Theoretical Calculations

To obtain stable geometries, vibrational frequencies, and energetics for the reactants and their CID products, theoretical calculations were performed using HyperChem[41] and the Gaussian 03[42] and 09[43] suites of programs. The reactants may exhibit many stable low-energy structures, therefore potential low-energy candidate structures were obtained via a 300 cycle simulated annealing procedure employing the

Amber force field. A three phase annealing process was used, with each cycle beginning and ending at 0 K, lasting for 0.8 ps, and achieving a simulation temperature of 1000 K. Heating and cooling times for each cycle were 0.3 ps each, allowing 0.2 ps for the ions to sample conformational space at the simulation temperature. Relative energies were computed using molecular mechanics methods every 0.001 ps. The most stable conformers accessed at the end of each annealing cycle were subjected to additional analysis. All structures within 30 kJ/mol of the lowest-energy structure found via the simulated annealing procedure, as well as others representative and encompassing the entire range of structures found were further optimized using density function theory.

Geometry optimizations for the reactants and their CID products were performed using density functional theory at the B3LYP/6-31G* level.[44,45] Vibrational analyses of the geometry-optimized structures were performed to determine the vibrational frequencies of the optimized species for use in modeling of the CID data and generation of theoretical linear IR spectra. The frequencies calculated were scaled by a factor of 0.9804.[46] Single-point energy calculations were performed at the B3LYP/6-311+G(2d,2p) and M06/6-311+G(2d,2p) levels of theory using the B3LYP/6-31G* optimized geometries for all systems examined in the present work. Single-point energy calculations were also performed at MP2(full)/6-311+G(2d,2p) level of theory using B3LYP/6-31G* and B3LYP/6-311+G(d,p) optimized geometries for neutral and protonated peptidomimetic bases and 18C6 as well as the (B)H^+(18C6) complexes. To obtain accurate energetics, zero-point energy (ZPE) and basis set super position error

(BSSE) corrections are included in the computed BDEs using the counterpoise approach.[47, 48]

Polarizability is one of the key factors that contribute to the strength of noncovalent interactions. Thus, the isotropic molecular polarizabilities of the ground-state conformations of the CID products are calculated using the PBE0 hybrid functional and the 6-311+G(2d,2p) basis set using the B3LYP/6-31G* optimized geometries. This level of theory was chosen because polarizabilities determined using the PBE0 functional[49] exhibit very good agreement with experimentally determined polarizabilities.[50]

Theoretical linear IR spectra of five $(B)H^+(18C6)$ complexes, where B = IPA, NBA, DAP, 4MeImid, and MGD were generated using the calculated harmonic vibrational frequencies (scaled by a factor of 0.97 in this case) and IR intensities. The theoretical linear IR spectra were broadened using a 20 cm^{-1} fwhm Gaussian line shape to account for the effects of multiple photon excitation and to allow for meaningful comparison to the experimental IRMPD spectra.

2.13. References

(1) Moison, R. M.; Armentrout, P. B. *J. Am. Soc. Mass Spectrom.* **2007**, *18*, 1124.

(2) Shaffer, S. A.; Prior, D. C.; Anderson, G. A.; Udseth, H. R.; Smith, R. D. *Anal. Chem.* **1998**, *70,* 4111.

(3) Shaffer, S. A.; Tolmachev, A.; Prior, D. C.; Anderson, G. A.; Udseth, H. R.; Smith, R. D. *Anal. Chem.* **1999**, *71,* 2957.

(4) Jones, R. M.; Anderson, S. L. *Rev. Sci. Instrum.* **2000**, *71*, 4335.

(5) Jones, R. M.; Gerlich, D.; Anderson, S. L. *Rev. Sci. Instrum.* **1997**, *68*, 3357.

(6) Vestal, M. L.; Blakly, C. R.; Ryan, P. B.; Futrell, J. H. *Rev. Sci. Instrum.* **1976**, *47*, 15.

(7) Teloy, E.; Gerlich, D. *Chem. Phys*. **1974**, *4*, 417.

(8) Muntean, F.; Armentrout, P. B. *J. Chem. Phys*. **2001**, *115*, 1213.

(9) Ervin, K. M.; Armentrout, P. B. *J. Chem. Phys*. **1985**, *83*, 166.

(10) Rodgers, M. T.; Armentrout, P. B. *J. Am. Chem. Soc.* **2002**, *124*, 2678.

(11) Aristov, N.; Armentrout, P. B. *J. Phys. Chem*.**1986**, *90*, 5135.

(12) Hales, D. A.; Armentrout, P. B. *J. Cluster Sci.* **1990**, *1*, 127.

(13) Daly, N. R. *Rev. Sci. Instrum*. **1959**, *31*, 264.

(14) Rodgers, M. T.; Armentrout, P. B. *Int. J. Mass Spectrom*. **1999**, *185/186/187*, 359.

(15) Beyer, T. S.; Swinehart, D. F. *Commun. ACM* **1979**, *16*, 379.

(16) Stein, S. E.; Rabinovitch, B. S. *J. Chem. Phys*. **1973**, *58*, 2438.

(17) Stein, S. E.; Rabinovitch, B. S. *Chem. Phys. Lett***. 1977**, *49*, 183.

(18) Pople, J. A.; Schlegel, H. B.; Raghavachari, K.; DeFrees, D. J.; Binkley, J. F.; Frisch, M. J.; Whitesides, R. F.; Hout, R. F.; Hehre, W. J. *Int. J. Quantum Chem. Symp*. **1981**, *15*, 269.

(19) DeFrees, D. J.; McLean, A. D. *J. Chem. Phys*. **1985**, *82*, 333.

(20) Rodgers, M. T.; Ervin, K. M.; Armentrout, P. B. *J. Chem. Phys*. **1997**, *106*, 4499.

(21) Khan, F. A.; Clemmer, D. E.; Schultz, R. H.; Armentrout, P. B. *J. Phys. Chem*. **1993**, *97*, 7978.

(22) Chesnavich, W. J.; Bowers, M. T. *J. Phys. Chem.* **1979**, *83*, 900.

(23) Yang, Z.; Rodgers, M. T. *Phys. Chem. Chem. Phys.* **2004**, *6*, 2749.

(24) Yang, Z.; Rodgers, M. T. *J. Am. Chem. Soc.* **2004**, *126,* 16217.

(25) Rannulu, N. S.; Rodgers, M. T. *Phys. Chem. Chem. Phys.* **2005**, *7*, 1014.

(26) Ruan, C.; Rodgers, M. T. *J. Am. Chem. Soc.* **2004**, *126,* 14600.

(27) Ruan, C.; Rodgers, M. T. *J. Am. Chem. Soc.* **2009**, *131*, 10918.

(28) Ruan, C.; Yang, Z.; Rodgers, M. T. *Phys. Chem. Chem. Phys.* **2007**, *9*, 5902.

(29) Chinthaka, S. D. M.; Chu, Y.; Rannulu, N. S.; Rodgers, M. T. *J. Phys. Chem. A* **2007**, *110*, 1426.

(30) Chinthaka, S. D. M.; Rodgers, M. T. *J. Phys. Chem. A* **2006**, *111*, 8152.

(31) Rannulu, N. S.; Rodgers, M. T. *Phys. Chem. Chem. Phys*. **2005**, *7*, 1014.

(32) Rannulu, N. S.; Amunugama, R.; Yang, Z.; Rodgers, M. T. *J. Phys. Chem. A* **2004**, *108*, 6385.

(33) Amunugama, R.; Rodgers, M. T. *Int. J. Mass. Spectrom*. **2003**, *227*, 1.

(34) Amunugama, R.; Rodgers, M. T. *J. Phys. Chem. A* **2002**, *106*, 9718.

(35) Dalleska, N. F.; Honma, K.; Armentrout, P. B. *J. Am. Chem. Soc*. **1993**, *115*, 12125.

(36) Armentrout, P. B.; Simons, J. *J. Am. Chem. Soc.* **1992**, *114*, 8627.

(37) Rodgers, M. T.; Armentrout, P. B. *Mass Spectrom. Re*v. **2000**, *19*, 215.

(38) Valle, J. J.; Eyler, J. R.; Oomens, J.; Moore, D. T.; van der Meer, A. F. G.; von Heldon, G.; Meijer, G.; Hendrickson, C. L.; Marshall, A. G.; Blakney, G. T. *Rev. Sci. Instrum*. **2005**, *76*, 023103.

(39) Polfer, N. C.; Oomens, J.; Moore, D. T.; von Helden, G.; Meijer, G.; Dunbar, R. C. *J. Am. Chem. Soc.* **2006**, *128*, 517.

(40) Polfer, N. C.; Oomens, J. *Phys. Chem. Chem. Phys*. **2007**, *9*, 3804.

(41) *HyperChem Computational Chemistry Software Package*, Version 5.0; Hypercube Inc: Gainsville, FL, 1997.

(42) Gaussian 03, Revision C.02, Frisch, M. J.; Trucks, G. W.; Schlegel, H. B.; Scuseria, G. E. ; Robb, M. A.; Cheeseman, J. R.; Montgomery, Jr., J. A.; Vreven, T.; Kudin, K. N.; Burant, J. C.; Millam, J. M.; Iyengar, S. S.; Tomasi, J.; Barone, V.; Mennucci, B.; Cossi, M.; Scalmani, G.; Rega, N.; Petersson, G. A.; Nakatsuji, H.; Hada, M.; Ehara, M.; Toyota, K.; Fukuda, R.; Hasegawa, J.; Ishida, M.; Nakajima, T.; Honda, Y.; Kitao, O.; Nakai, H.; Klene, M.; Li, X.; Knox, J. E.; Hratchian, H. P.; Cross, J. B.; Bakken, V.; Adamo, C.; Jaramillo, J.; Gomperts, R.; Stratmann, R. E.; Yazyev, O.; Austin, A. J.; Cammi, R.; Pomelli, C.; Ochterski, J. W.; Ayala, P. Y.; Morokuma, K.; Voth, G. A.; Salvador, P.; Dannenberg, J. J.; Zakrzewski, V. G.; Dapprich, S.; Daniels, A. D.; Strain, M. C.; Farkas, O.; Malick, D. K.; Rabuck, A. D.; Raghavachari, K.; Foresman, J. B.; Ortiz, J. V.; Cui, Q.; Baboul, A. G.; Clifford, S.; Cioslowski, J.; Stefanov, B. B.; Liu, G.; Liashenko, A.; Piskorz, P.; Komaromi, I.; Martin, R. L.; Fox, D. J.; Keith, T.; Al-Laham, M. A.; Peng, C. Y.; Nanayakkara, A.; Challacombe, M.; Gill, P. M. W.; Johnson, B.; Chen, W.; Wong, M. W.; Gonzalez, C.; Pople, J. A. Gaussian, Inc., Wallingford CT, 2004.

(43) Frisch, M. J.; Trucks, G. W.; Schlegel, H. B.; Scuseria, G. E.; Robb, M. A.; Cheeseman, J. R.; Scalmani, G.; Barone, V.; Mennucci, B.; Petersson, G. A.;

Nakatsuji, H.; Caricato, M.; Li, X.; Hratchian, H. P.; Izmaylov, A. F.; Bloino, J.; Zheng, G.; Sonnenberg, J. L.; Hada, M.; Ehara, M.; Toyota, K.; Fukuda, R.; Hasegawa, J.; Ishida, M.; Nakajima, T,; Honda, Y.; Kitao, O.; Nakai, H.; Vreven, T,; Montgomery, J. A.; Jr., Peralta, J. E.; Ogliaro, F.; Bearpark, M.; Heyd, J. J.; Brothers, E.; Kudin, K. N.; Staroverov, V. N.; Kobayashi, R.; Normand, J.; Raghavachari, K.; Rendell, A.; Burant, J. C.; Iyengar, S. S.; Tomasi, J.; Cossi, M.; Rega, N.; Millam, J. M.; Klene, M.; Knox, J. E.; Cross, J. B.; Bakken, V.; Adamo, C.; Jaramillo, J.; Gomperts, R.; Stratmann, R. E.; Yazyev, O.; Austin, A. J.; Cammi, R.; Pomelli, C.; Ochterski, J. W.; Martin, R. L.; Morokuma, K.; Zakrzewski, V. G.; Voth, G. A.; Salvador, P.; Dannenberg, J. J.; Dapprich, S.; Daniels, A. D.; Farkas, Ö.; Foresman, J. B.; Ortiz, J. V.; Cioslowski, J.; Fox, D. J. Gaussian 09, Revision A.1, Gaussian, Inc., Wallingford CT (2009).

(44) Becke, A. D. *J. Chem. Phys.* **1993**, *98*, 5648.

(45) Lee, C.; Yang, W.; Parr, R. G. *Phys. Rev. B* **1988**, *37*, 785.

(46) Foresman, J. B.; Frisch, Æ. *Exploring Chemistry with Electronic Structure Methods*, 2nd ed.; Gaussian: Pittsburgh, PA, 1996; p. 64.

(47) Boys, S. F.; Bernardi, R. *Mol. Phys.* **1979**, *19*, 553.

(48) van Duijneveldt, F. B.; van Duijneveldt-van de Rijdt, J. G. C. M.; van Lenthe, J. H. *Chem. Rev.* **1994**, *94*, 1873.

(49) Adamo, C.; Barone, V. *J. Chem. Phys.* **1999**, *110*, 6158.

(50) Smith, S. M; Markevitch, A. N.; Romanov, D. A.; Li, X.; Levis, R. J.; Schlegel, H. B. *J. Phys. Chem. A* **2004**, *108*, 11063.

2.14. Figure Captions

Figure 2.1. Schematic diagram of the guided ion beam tandem mass spectrometer.

Figure 2.2. Schematic diagram of the electrospray ionization source-rf ion funnel-hexapole ion guide/collision cell interface.

Figure 2.3. Retarding potential analysis of the (MA)H^+(18C6) complex ion beam as a function of the laboratory ion kinetic energy.

Figure 2.4. Kinetic energy distribution of the (MA)H^+(18C6) complex ion beam.

Figure 2.5. Schematic diagram of the Fourier transform ion cyclotron resonance mass spectrometer coupled to the FELIX free electron laser.

Figure 2.1.

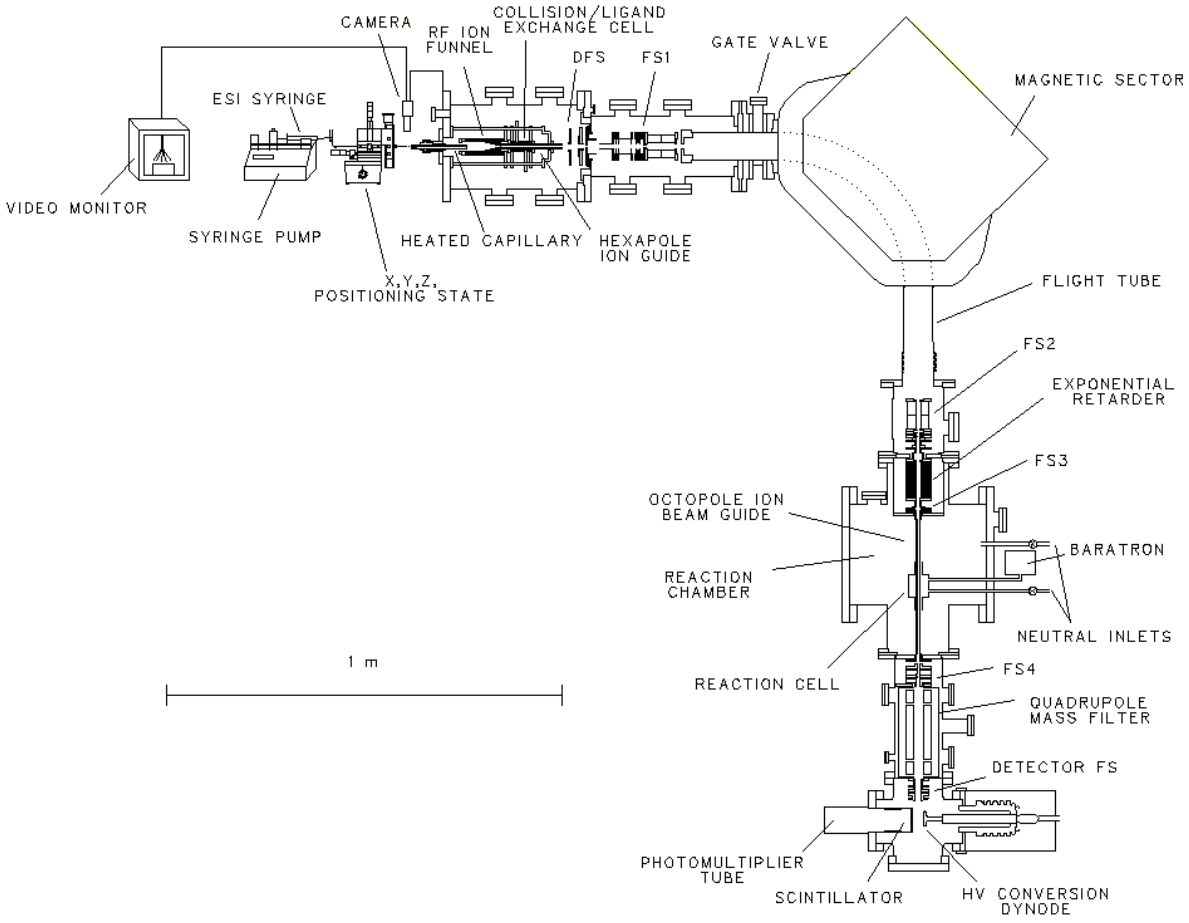
CAMERA
COLLISION/LIGAND EXCHANGE CELL
RF ION FUNNEL
DFS
FS1
GATE VALVE
MAGNETIC SECTOR
ESI SYRINGE
VIDEO MONITOR
SYRINGE PUMP
HEATED CAPILLARY
HEXAPOLE ION GUIDE
X,Y,Z, POSITIONING STATE
FLIGHT TUBE
FS2
EXPONENTIAL RETARDER
FS3
OCTOPOLE ION BEAM GUIDE
BARATRON
REACTION CHAMBER
NEUTRAL INLETS
1 m
REACTION CELL
FS4
QUADRUPOLE MASS FILTER
DETECTOR FS
PHOTOMULTIPLIER TUBE
SCINTILLATOR
HV CONVERSION DYNODE

Figure 2.2.

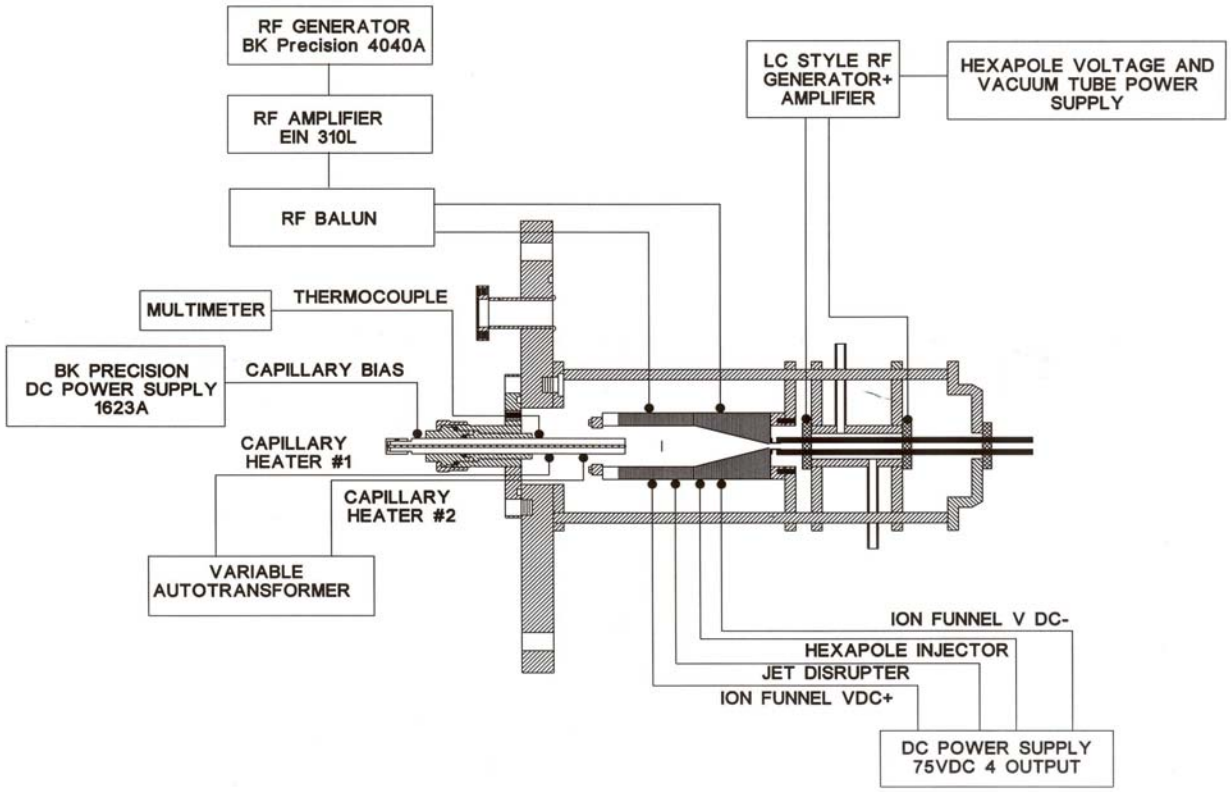
RF GENERATOR
BK Precision 4040A
RF AMPLIFIER
EIN 310L
RF BALUN
LC STYLE RF
GENERATOR+
AMPLIFIER
HEXAPOLE VOLTAGE AND
VACUUM TUBE POWER
SUPPLY
MULTIMETER
THERMOCOUPLE
BK PRECISION
DC POWER SUPPLY
1623A
CAPILLARY BIAS
CAPILLARY
HEATER #1
CAPILLARY
HEATER #2
VARIABLE
AUTOTRANSFORMER
ION FUNNEL V DC-
HEXAPOLE INJECTOR
JET DISRUPTER
ION FUNNEL VDC+
DC POWER SUPPLY
75VDC 4 OUTPUT

Figure 2.3.

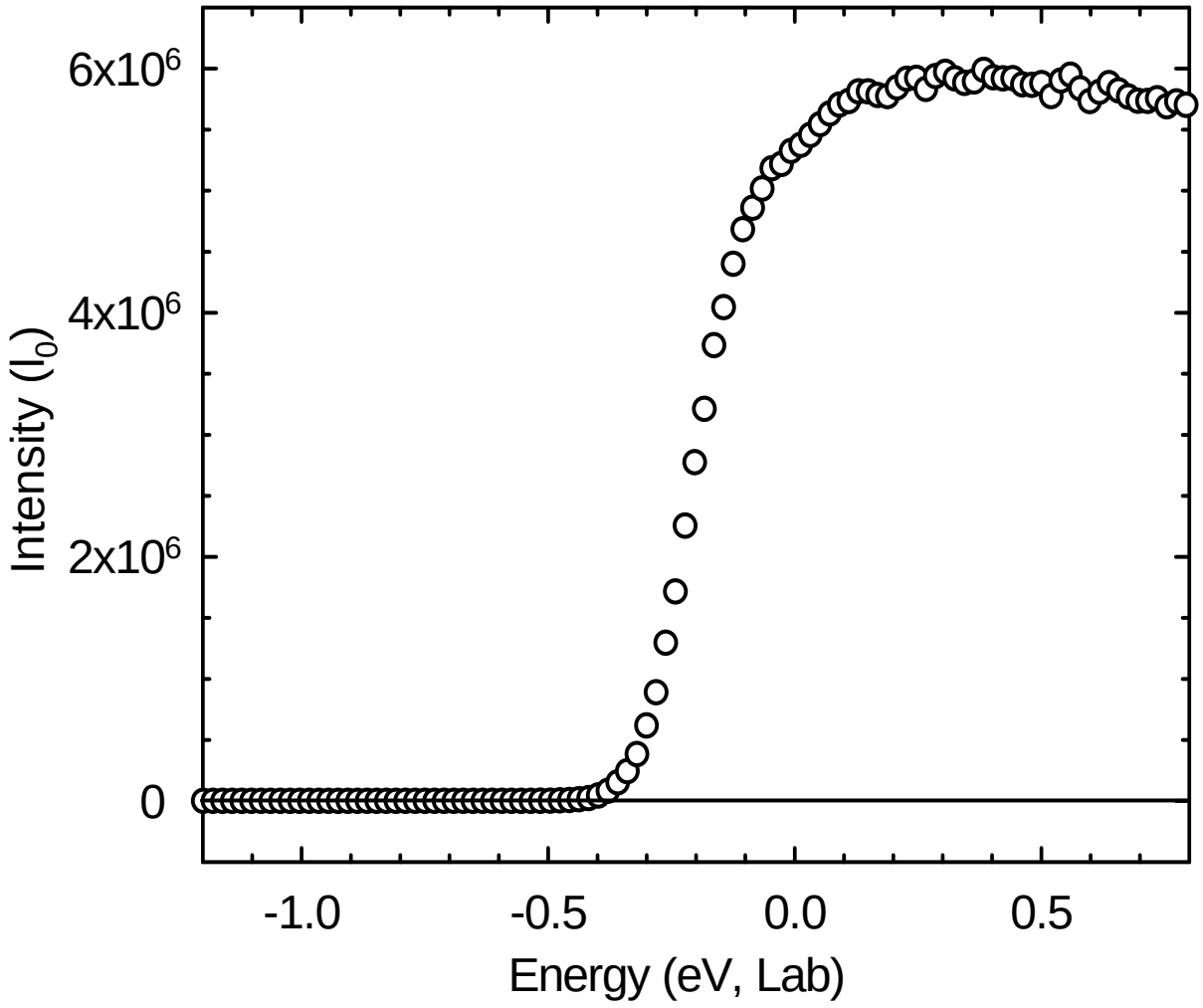

Figure 2.4.

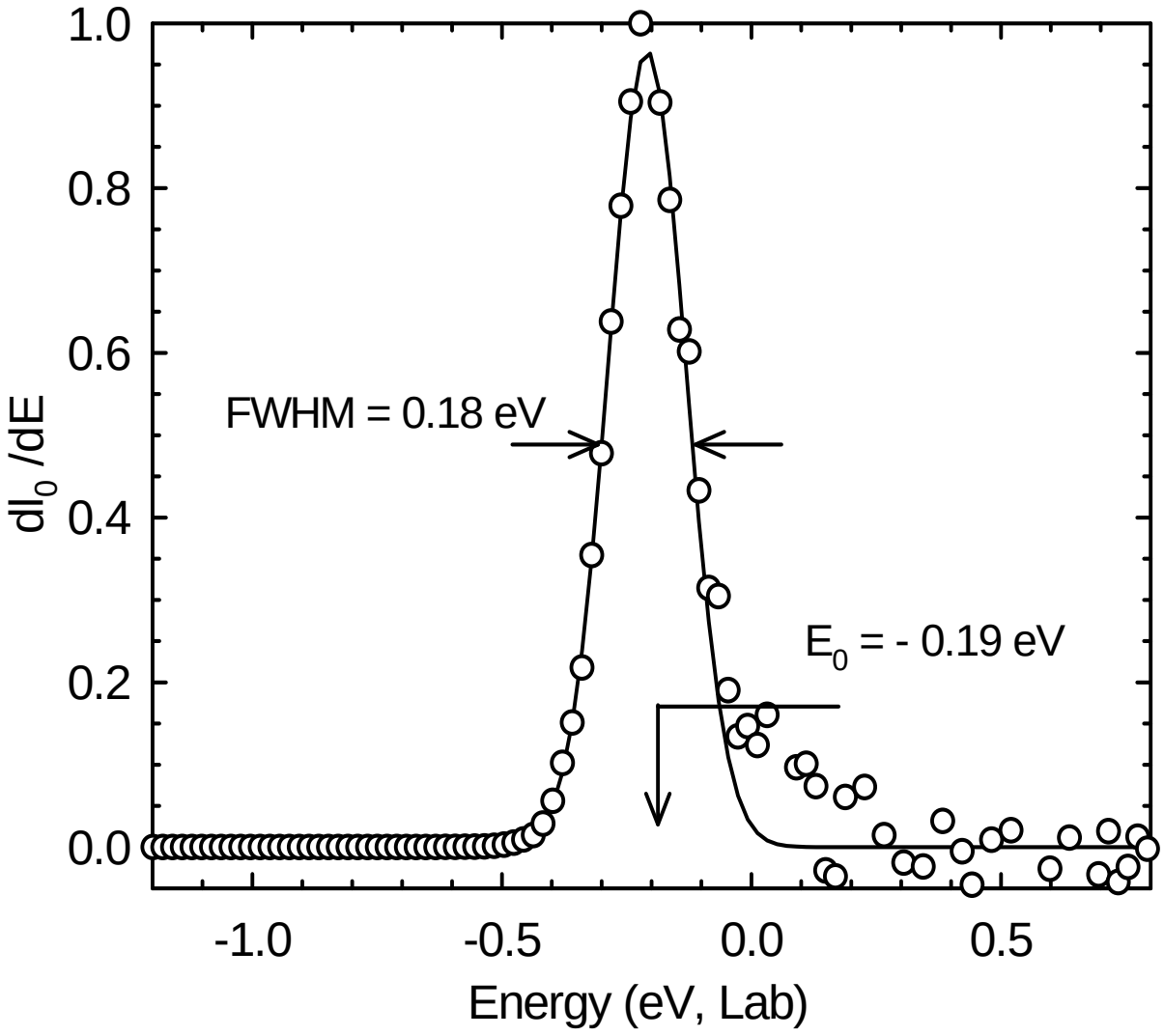
1.0
0.8
0.6
0.4
0.2
0.0
dI0 /dE
FWHM = 0.18 eV
E0 = - 0.19 eV
-1.0
-0.5
0.0
0.5
Energy (eV, Lab)

Figure 2.5.

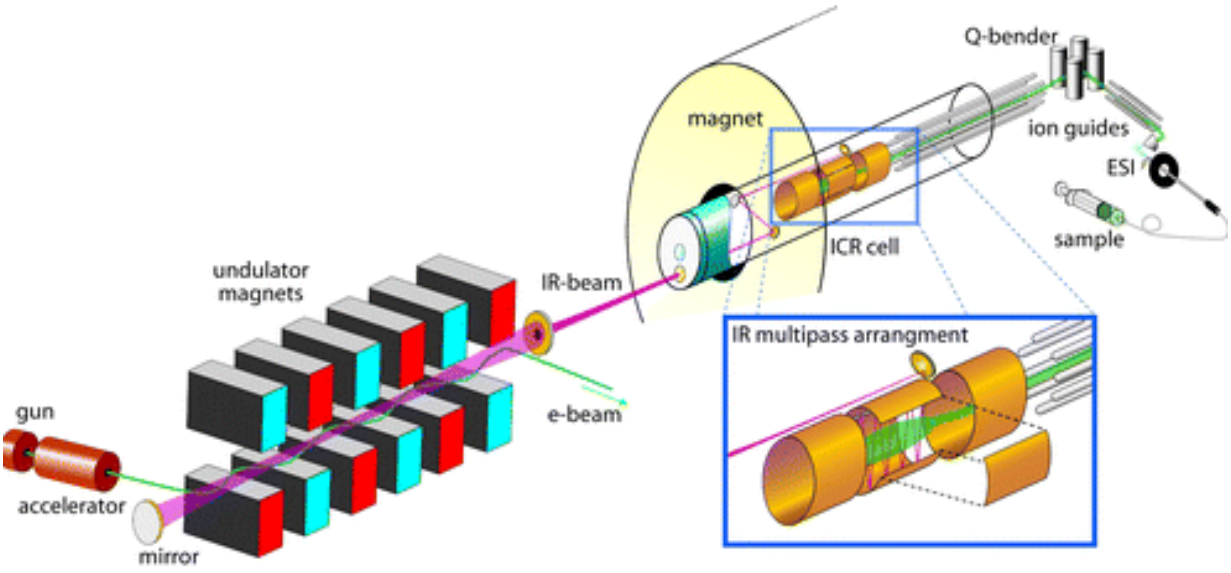
Q-bender
magnet
ion guides
ESI
sample
ICR cell
undulator
magnets
IR-beam
IR multipass arrangment
gun
e-beam
accelerator
mirror

CHAPTER 3

STRUCTURAL AND ENERGETIC EFFECTS IN THE MOLECULAR RECOGNITION OF PROTONATED PEPTIDOMIMETIC BASES BY 18-CROWN-6

Portions of this chapter were reprinted with permission from Chen, Y. and Rodgers, M. T. Structural and Energetic Effects in the Molecular Recognition of Protonated Peptidomimetic Bases by 18-Crown-6. *J. Am. Chem. Soc.*, **2012**, *134*, 2313.

3.1. Introduction

Structure-function relationships are well established for biological polymers, and in particular, proteins. As a result, studies aimed at the characterization and improved understanding of the three-dimensional structure of proteins and the intra- and intermolecular interactions that stabilize their structures and complexes are ubiquitous throughout the biological and chemical disciplines. X-ray crystallography[1] and NMR spectroscopy[2,3] are well-established analytical techniques for protein structure elucidation. However, NMR requires a large quantity of the protein in a specific solvent, while X-ray crystallography requires sample crystallization, which can be difficult to achieve.

Mass spectrometry (MS) has become an increasingly important tool for protein structure determination due to its speed, sensitivity, and specificity.[4-6] H/D exchange[7-13] and chemical cross-linking[14-22] have been used to characterize protein structure and intra- and inter-molecular protein interactions.

Beauchamp, Julian, and coworkers have developed a third approach, selective noncovalent adduct protein probing (SNAPP)[23-32] that utilizes noncovalent recognition of

amino acid residues, and in particular lysine (Lys) residues, to facilitate rapid identification and characterization of protein sequence, structure and conformational changes, and provides information key to understanding functional behavior in biological systems at the molecular level. The extent of 18C6 adduction is determined by the number of accessible Lys side chains, i.e., those that are not involved in intramolecular interactions such as hydrogen bonds or salt bridges. Intramolecular interactions generally prevent the attachment of 18C6 and are directly correlated to the structure of the protein. Therefore, binding of 18C6 can be employed as a sensitive probe of protein structure. Because the number of 18C6 ligands that bind to a protein can be easily determined by MS due to the large mass shift (264 Da per 18C6 ligand bound), information relevant to protein folding under varying solution conditions can be extrapolated.

Although the protonated side chain of Lys has been shown to be the primary binding site for 18C6 complexation, the protonated side chains of His, Arg, and the N-terminal amino group may also compete for 18C6. Therefore, accurate thermochemical information regarding the binding between 18C6 and the basic amino acids may provide insight into the selectivity of the complexation process. However, very limited thermochemical data has thus far been reported in the literature.

In this chapter, absolute 18C6 affinities of nine protonated peptidomimetic bases are determined using guided ion beam tandem mass spectrometry techniques. Peptidomimetic bases that serve as models for the N-terminal amino group and the side chains of Lys, His, and Arg are examined here. Isopropylamine (IPA) is chosen as a mimic for the N-terminal amino group, imidazole (Imid) and 4-methylimidazole

(4MeImid) are chosen as mimics for the side chain of His, 1-methylguanidine (MGD) is chosen as a mimic of the side chain of Arg, and several primary amines including: methylamine (MA), ethylamine (EA), n-propylamine (NPA), n-butylamine (NBA) and 1,5-diamino pentane (DAP) as mimics for the side chain of Lys, as shown in the multiply protonated model peptide of **Figure 3.1**. The energy-dependent cross sections for collision-induced dissociation (CID) of the protonated peptidomimetic base–18C6 complexes are analyzed using methods previously developed that explicitly include the effects of the kinetic and internal energy distributions of the reactants, multiple ion-neutral collisions, and the kinetics of unimolecular dissociation. Absolute $(B)H^+$–18C6 bond dissociation energies (BDEs) for nine $(B)H^+(18C6)$ complexes are derived and compared to theoretical estimates for these BDEs computed here.[33]

3.2. Collision-Induced Dissociation Experiments

Cross sections for CID of nine protonated peptidomimetic base-18C6 complexes, $(B)H^+(18C6)$ with Xe, where B = Imid, 4MeImid, MA, EA, NPA, NBA, IPA, DAP, and MGD are measured using a guided ion beam tandem mass spectrometer that has been described in detail previously.[34] The $(B)H^+(18C6)$ complexes are generated by electrospray ionization (ESI).[35] The ions are effusively sampled from the source region, focused, accelerated, and focused into a magnetic sector momentum analyzer for mass analysis. Mass-selected ions are decelerated to a desired kinetic energy and focused into an octopole ion guide. The octopole passes through a static gas cell containing Xe at low pressure (~0.05–0.20 mTorr) to ensure that multiple ion-neutral collisions are improbable. Products and unreacted beam ions drift to the end of the octopole, are

focused into a quadrupole mass filter for mass analysis, and are subsequently detected with a secondary electron scintillation detector and standard pulse counting techniques. Details of the experimental procedures and thermochemical analysis of the experimental data are given in **Chapter 2**.

3.3. Theoretical Calculations

A simulated annealing methodology using HyperChem[36] and the AMBER force field was used to generate starting structures of neutral and protonated 18C6 for higher level optimization. All structures determined within 30 kJ/mol of the lowest-energy structure were optimized using the Gaussian 03 [37] and 09 [38] suites of programs.

Geometry optimizations for the neutral and protonated peptidomimetic bases as well as the proton bound (B)H^+(18C6) complexes were performed using density functional theory at the B3LYP/6-31G* level.[39,40] The frequencies calculated were scaled by a factor of 0.9804.[41] Because all systems examined here involve hydrogen bonds, we also performed geometry optimization of the ground-state structures of the nine (B)H^+(18C6) complexes at the B3LYP/6-311+G(d,p) level of theory, adding a polarized p function on the hydrogen atoms and a diffuse function on heavy atoms, to assess the dependence of the theoretical results on the level of theory employed for geometry optimization. Single-point energy calculations were performed at the B3LYP/6-311+G(2d,2p), MP2(full)/6-311+G(2d,2p), and M06/6-311+G(2d,2p) levels of theory using the B3LYP/6-31G* and B3LYP/6-311+G(d,p) optimized geometries, respectively. To obtain accurate BDEs, zero-point energy (ZPE) and basis set super position error (BSSE) corrections are included in the computed BDEs using the

counterpoise approach.[42, 43] Additional details regarding procedures employed for the theoretical calculations are given in **Chapter 2**.

3.4. Results

3.4.1. Cross Sections for Collision-Induced Dissociation

Experimental cross sections were obtained for the interaction of Xe with nine $(B)H^+(18C6)$ complexes, where B = Imid, 4MeImid, MA, EA, NPA, NBA, IPA, DAP and MGD. **Figure 3.2** shows representative data for the $(NBA)H^+(18C6)$ and $(MGD)H^+(18C6)$ complexes. Experimental cross sections for the other $(B)H^+(18C6)$ complexes are shown in **Figure S1** of the Supporting Information of reference 33. The most favorable process for all complexes is loss of an intact 18C6 ligand in the CID reactions 3.1.

$$(B)H^+(18C6) + Xe \rightarrow H^+(B) + 18C6 + Xe \quad (3.1)$$

Loss of the neutral base, B, to produce $H^+(18C6)$ was also observed as a minor product in competition with $H^+(B)$ for all complexes except those where B = MGD and DAP, CID reactions 3.2.

$$(B)H^+(18C6) + Xe \rightarrow H^+(18C6) + B + Xe \quad (3.2)$$

The magnitude of the $H^+(18C6)$ product cross section is the largest for the $(Imid)H^+(18C6)$ complex, a factor of four higher than that in the $(NBA)H^+(18C6)$ and $(IPA)H^+(18C6)$ systems, and a factor of 25 higher than that in the $(4MeImid)H^+(18C6)$ system. The same trend was also found for branching ratio between $H^+(18C6)$ and $H^+(B)$ in these systems: 4MeImid < IPA ≈ NBA < Imid. In contrast, the relative thresholds between $H^+(18C6)$ and $H^+(B)$ in these systems follow the reverse trend. The

difference between the threshold for H^+(18C6) and H^+(B) in the (Imid)H^+(18C6) system is the smallest, ~0.6 eV, indicating that competition between the formation of H^+(18C6) and H^+(B) in this system is the most significant. As a result, the magnitude of the H^+(18C6) product cross section in the (Imid)H^+(18C6) system is the greatest. The difference between the H^+(18C6) and H^+(B) threshold increases to ~1.1 eV for complexes involving NBA and IPA, and increases to ~1.5 eV for the complexes involving 4MeImid. At elevated energies, products corresponding to the sequential dissociation of H^+(18C6) were also observed for all complexes, reactions 3.3, except the (4MeImid)H^+(18C6) complex.

$$H^+(18C6) + Xe \rightarrow H^+(C_2H_4O)_n + (6\text{-}n)\, C_2H_4O + Xe \qquad (3.3)$$

It is likely that this process also occurs in the (4MeImid)H^+(18C6) system, but that the signal-to-noise in those experiments was not sufficient to differentiate the $H^+(C_2H_4O)_n$ fragments from background noise (~10^{-3} $Å^2$). For the (DAP)H^+(18C6) and (MGD)H^+(18C6) complexes, the H^+(18C6) competitive dissociation pathway was not observed due to the relatively large difference in the PAs of these bases and 18C6. At elevated energies, fragments such as 1-pentanamine (NPenA) and guanidine (GD) corresponding to sequential dissociation of H^+(DAP) and H^+(MGD) were observed, reactions 3.4 and 3.5.

$$H^+(DAP) + Xe \rightarrow H^+(NPenA) + NH_3 + Xe \qquad (3.4)$$

$$\rightarrow H^+(MA) + NBA + Xe$$

$$\rightarrow C_5H_{11}^+ + 2\, NH_3 + Xe$$

$$H^+(MGD) + Xe \rightarrow H^+(GD) + CH_3 + Xe \qquad (3.5)$$

More detailed analyses of the fragments corresponding to the sequential dissociation of H^+(18C6) and H^+(B) were not pursued here, and thus will not be discussed further.

3.4.2. Theoretical Results

The ground-state structures of the (4MeImid)H^+(18C6), (MGD)H^+(18C6) and (NBA)H^+(18C6) complexes are shown in **Figure 3.3**, while the structures for the other six (B)H^+(18C6) complexes are shown in **Figure S2** of the Supporting Information of reference 33. The ground-state structures of the neutral and protonated 18C6 are shown in **Figure 3.4**, and bases are shown in **Figure 3.5**, while the results for the stable low-energy conformations of the neutral and protonated bases are shown in **Figure S3** of reference 33. Structures of several representative low-energy conformations of neutral and protonated 18C6 are shown in **Figures S4** and **S5** of reference 33, respectively. The (B)H^+–18C6 BDEs at 0 K calculated at the MP2(full), B3LYP, and M06 levels of theory using a 6-311+G(2d,2p) basis set for both levels of geometry optimization B3LYP/6-31G* and B3LYP/6-311+G(d,p) including ZPE and BSSE corrections, are listed in **Table 3.1**, while values listed in **Table S3** of reference 33 provide details of the ZPE and BSSE corrections. Comparison of the measured and calculated values suggests that the MP2(full) results are most reliable and that surprisingly the agreement is very slightly better for structures optimized at the B3LYP/6-31G* level of theory. Therefore, the following discussion will focus on the geometries and relative energies calculated at MP2(full)/6-311+G(2d,2p)//B3LYP/6-31G* level of theory unless otherwise specified.

3.4.2.1. 18C6

The ground-state conformation of neutral 18C6 is of C_i symmetry; four of its six ether oxygen atoms are directed inward from the ether backbone, while the other two are directed outward as seen in **Figure 3.4**. A weak intramolecular CH···O interaction helps stabilize the ground-state conformer. A stable conformer with D_{3d} symmetry was also found that lies 14.8 kJ/mol higher in energy than the ground-state structure (**Figure S4** of reference 33). In this conformation, each of the oxygen atoms are directed inward from the ether backbone, forming a nucleophilic cavity for very favorable interaction with guest cations. These structures are consistent with the lowest-energy conformers identified by Feller and Glendening.[44, 45] In their study, the D_{3d} conformer was computed to lie 18.4 kJ/mol (RHF/6-31+G*//RHF/6-31+G*) and 22.6 kJ/mol (MP2/6-31+G*//RHF/6-31+G*) higher in energy than the ground-state conformation.

In the ground-state conformation of H^+(18C6), the proton binds to an O atom and is stabilized by an O1···H^+···O3 hydrogen bond (**Figure 3.4**). The ground-state of H^+(18C6) exhibits a boat-like conformation. A relatively flat conformation of H^+(18C6) with the proton stabilized between the O1 and O3 oxygen atoms was also found that lies 30.6 kJ/mol higher in energy than the ground-state structure (**Figure S5** of reference 33). The conformer where the proton binds to an oxygen atom and maintains the ~D_{3d} symmetry of the 18C6 backbone lies 65.6 kJ/mol higher in energy than the ground-state structure.

3.4.2.2. Peptidomimetic Bases

Details of the optimized geometries of the ground-state conformations of the neutral and protonated bases are provided in the **Figure 3.5**. The preferred site of protonation for all bases is to the lone pair of electrons on the nitrogen atom. For Imid and 4MeImid, the proton binds at the N3 position of the imidazole ring to form conformers with C_{2V} and C_s symmetry, respectively. In the ground-state structure of H^+(IPA), H^+(MA), H^+(EA), H^+(NPA), and H^+(NBA), the proton binds to the amino group. The hydrocarbon backbones of the ground-state conformers of H^+(EA), H^+(NPA) and H^+(NBA) exhibit zigzag conformations. In its ground-state conformation, H^+(DAP) forms an eight-membered ring conformer that is stabilized by a hydrogen bonding interaction between the protonated and neutral amino groups. The extended zigzag conformer of H^+(DAP) in which the proton is attached to a single amino group is 69.2 kJ/mol less favorable than the ground-state hydrogen bonded ring conformer. For MGD, the proton could bind to the primary or secondary amine or the primary imine to form a stable protonated conformer. The most favorable protonation site is the imine nitrogen atom, which is 148.9 and 150.1 kJ/mol more favorable than the primary and secondary amine binding sites, respectively.

3.4.2.3. (B)H^+(18C6) Complexes

In the ground-state conformations of the (B)H^+(18C6) complexes, the proton binds to the peptidomimetic base to form a protonated structure very similar to that of the isolated protonated base that interacts with 18C6 via two, three, or four N–H···O hydrogen bonds. The preferred site of proton binding remains the base even when the

PA of 18C6 exceeds that of the base. The conformation of 18C6 in these complexes bears great similarity to the D_{3d} structure of the neutral crown with a nucleophilic cavity in the center for interaction with the protonated base.

In the ground-state conformations of the $(IPA)H^+(18C6)$, $(DAP)H^+(18C6)$, $(MA)H^+(18C6)$, $(EA)H^+(18C6)$, $(NPA)H^+(18C6)$ and $(NBA)H^+(18C6)$ complexes (**Figures 3.3** and **S2** of reference 33), the proton binds to the nitrogen atom of the base resulting in a protonated amino group that interacts with 18C6 via three nearly ideal (i.e., nearly linear) N–H···O hydrogen bonds. The conformation of 18C6 in these complexes bears great similarity to the D_{3d} structure of the neutral crown with a nucleophilic cavity in the center for the interaction with the protonated base. Complexation to the protonated base causes the 18C6 cavity to contract, resulting in the oxygen to center-of-mass distance to decrease from 2.880 Å in the D_{3d} conformation of neutral 18C6 to 2.860 Å for $(IPA)H^+(18C6)$, 2.857 Å for $(DAP)H^+(18C6)$ and $(NBA)H^+(18C6)$, 2.854 Å for $(NPA)H^+(18C6)$ and $(EA)H^+(18C6)$, and 2.847 Å for $(MA)H^+(18C6)$ in the ground-state conformations of these complexes. Complexation to 18C6 also induces electron redistribution from the methylene groups toward the oxygen atoms as evidenced by an increase in the Mulliken charges on the oxygen (-) and carbon (+) atoms in the $(B)H^+(18C6)$ complexes as compared to free 18C6. Another stable conformer was found for the $(DAP)H^+(18C6)$ complex that lies 11.7 kJ/mol higher in energy than the ground-state conformation. In this excited conformer, $H^+(DAP)$ bears similarity to the ground-state ring structure, where the two amino groups share the proton and interact with the O1 and O4 atoms of 18C6 via two N–H···O hydrogen bonds instead of three

hydrogen bonding interactions with the free protonated amino group as in the ground-state conformer, as shown in **Figure S6** of the Supporting Information of reference 33.

For the (Imid)H^+(18C6) and (4MeImid)H^+(18C6) complexes, the proton binds to the neutral base to form H^+(Imid) and H^+(4MeImid), which bind to a distorted D_{3d} conformer of 18C6 via two N–H···O hydrogen bonds similar to the excited ring conformer of (DAP)H^+(18C6). The O1 and O4 atoms of 18C6 are tilted above the nearly planar ring structure forming hydrogen bonds with the hydrogen atoms of the secondary amines. Another low-energy conformer that lies 3.3 and 2.5 kJ/mol higher in energy, respectively, is found for both the (Imid)H^+(18C6) and (4MeImid)H^+(18C6) complexes as shown in **Figure S6** of the Supporting Information of reference 33. Compared to the ground-state structures, these conformers differ primarily in the conformations of 18C6, which are flattened somewhat relative to the ground-state conformers. For the (MGD)H^+(18C6) system, protonated MGD binds to a distorted D_{3d} conformer of 18C6 via four N–H···O hydrogen bonds to the O1, O2, and O4 (2) atoms. A stable conformer of H^+(MGD) where the proton is bound to the primary amine also binds to 18C6 to form a stable complex, as shown in **Figure S6** of the Supporting Information of reference 33. However, this latter structure is 43.4 kJ/mol less stable than the ground-state conformer. 18C6 exhibits an approximately D_{3d} conformation where the six oxygen atoms are oriented toward the interior of the ring and interact with the primary amine H atoms via three N–H···O hydrogen bonds.

3.4.3. Threshold Analysis

The model of equation 2.3 (**Chapter 2**) was used to analyze the thresholds for reactions 3.1 in nine $(B)H^+(18C6)$ complexes. The results of these analyses are provided in **Table 3.2**. Representative results are shown in **Figure 3.6** for the $(NBA)H^+(18C6)$ and $(MGD)H^+(18C6)$ complexes. The analyses for the other seven $(B)H^+(18C6)$ complexes are shown in **Figure S7** of the Supporting Information of reference 33. In all cases, the experimental cross sections for reactions 3.1 are accurately reproduced using a loose PSL TS model.[46] Previous work has shown that this model provides the most accurate assessment of the kinetics shifts for CID process for electrostatically bound ion-molecule complexes.[47-55] Good reproduction of the data is obtained over energy ranges exceeding 3.0 eV and cross section magnitudes of at least a factor of 100. **Table 3.2** also lists E_0 values obtained without including the RRKM lifetime analysis. Comparison of these values with the E_0(PSL) values shows that the kinetic shifts are the largest for the most strongly bound systems, such that the kinetic shift for the $(MA)H^+(18C6)$, $(EA)H^+(18C6)$, $(NPA)H^+(18C6)$, $(NBA)H^+(18C6)$ and $(IPA)H^+(18C6)$ complexes vary between 1.98 and 2.26 eV. No simple correlation among these systems is found as the strength of binding decreases, while the number of modes available increases, with the size of B. The kinetic shift decreases for the $(DAP)H^+(18C6)$ complex to 1.59 eV, and becomes even smaller, 1.34 to 1.22 eV, for the $(4MeImid)H^+(18C6)$, $(Imid)H^+(18C6)$, and $(MGD)H^+(18C6)$ complexes. These trends are consistent with expectations that the observed kinetic shift should directly correlate with the density of states of the activated complex at threshold, which increases with energy and the number of modes available to the system.

The entropy of activation, $\Delta S^{\dagger}$, is a measure of the looseness of the TS and the complexity of the system. It is determined from the molecular parameters used to model the EM and TS for dissociation as listed in **Table S1** and **S2** of reference 33. The $\Delta S^{\dagger}$(PSL) values at 1000 K are listed in **Table 3.2** and vary between 69 to 123 J/K mol across the these systems. These values are consistent with the noncovalent nature of the binding in these systems. The $\Delta S^{\dagger}$(PSL) values are the smallest for the complexes to Imid and 4MeImid, 69 and 85 J/K mol, where only two hydrogen bonds are cleaved in the CID process, and larger for the remaining complexes 103 to 123 J/K mol, where three or four hydrogen bonds are broken.

3.5. Discussion

3.5.1. Comparison of Theory and Experiment

The measured and calculated 18C6 binding affinities of Imid, 4MeImid, MA, EA, NPA, NBA, IPA, DAP, and MGD at 0 K are summarized in **Table 3.1**. The agreement between MP2(full)/6-311+G(2d,2p)//B3LYP/6-31G* theory and experiments is illustrated in **Figure 3.7**. The mean absolute deviation (MAD) between theory and experiment for all nine complexes is 12.1 $\pm$ 9.7 kJ/mol. For the Imid, 4MeImid, IPA, DAP, and MGD systems, the measured BDEs exhibit excellent agreement with MP2(full) theory with a MAD of 4.4 $\pm$ 3.8 kJ/mol. Although a nice linear correlation between the TCID measured and calculated $(B)H^{+}$–18C6 is found for the MA, EA, NPA, and NBA systems, MP2(full) theory systematically overestimates the BDEs in these complexes by 21.7 ± 2.9 kJ/mol.

The BDEs calculated using M06 theory are consistent with those calculated using MP2(full) theory with deviations between 2 and 8 kJ/mol across these systems.

The MAD between M06/6-311+G(2d,2p)//B3LYP/6-31G* theory and experiments is slightly poorer than for MP2 results, 15.8 ± 13.3 kJ/mol. The BDEs calculated using M06 theory excluding the Lys mimics exhibit excellent agreement with the measured BDEs with a MAD similar to that found for MP2(full) theory, 4.9 ± 4.0 kJ/mol. However, for the MA, EA, NPA, and NBA systems, M06 theory overestimates the BDEs by almost 8 kJ/mol more than MP2(full) theory, with a MAD of 29.4 ± 3.0 kJ/mol. M06 theory reproduces the MP2(full) observed trends in the binding and achieves a similar, albeit reduced, accuracy for the energetics of these systems, but requires significantly less computing time. Thus, M06 is potentially suitable for describing the energetics of larger related hydrogen bound systems, where computational effort becomes increasingly important.

The agreement between B3LYP theory and the measured BDEs is less satisfactory with a MAD of 25.2 ± 14.6 kJ/mol. B3LYP theory systematically underestimates the measured BDEs for the Imid, 4MeImid, MGD, DAP, and IPA systems by 36.4 ± 7.2 kJ/mol. For the MA, EA, NPA, and NBA systems, B3LYP theory only underestimates the BDEs by 11.3 ± 5.6 kJ/mol. Indeed for these systems B3LYP theory performs better than MP2(full) theory and may be more suitable for describing the binding to primary amines.

As described in the Theoretical Calculations section, geometry optimizations were also performed at B3LYP/6-311+G(d,p) level of theory. The additional polarization function on the hydrogen atoms and diffuse function on the heavy atoms does not dramatically alter the optimized geometry, suggesting that the B3LYP/6-31G* theory is sufficient to describe the structures of these complexes. In addition, the MP2(full)/6-

311+G(2d,2p) BDEs for the structures optimized with the extended basis set changed by less than 1.8 kJ/mol in all systems. In fact, the MAD between MP2(full) theory and experiment actually degrades very slightly to 12.5 ± 10.1 kJ/mol (versus 12.1 ± 9.7 kJ/mol). The M06/6-311+G(2d,2p) BDEs for the structures optimized with the extended basis set changed by less than 3.4 kJ/mol in all systems. The MAD between M06 theory and experiment improves slightly to 15.4 ± 12.9 kJ/mol (versus 15.8 ± 13.3 kJ/mol). The B3LYP/6-311+G(2d,2p) BDEs for the structures optimized with the extended basis set changed by less than 3.2 kJ/mol in all systems. The MAD between B3LYP theory and experiment improves slightly to 24.2 ± 14.4 kJ/mol (versus 25.2 ± 14.6 kJ/mol). This is less than a 1 kJ/mol change on average, suggesting that the additional cost of the calculations using the larger basis set is not justified.

3.5.2. Trends in the 18C6 Binding Affinities

The measured $(B)H^+$–18C6 BDEs determined here follow the order: IPA ≥ MA > EA > NPA ≥ NBA > DAP > IMID ≥ MGD > 4MeImid. The interactions of 18C6 with IPA, MA, EA, NPA, NBA and DAP all involve three nearly ideal N–H···O hydrogen bonds, which result in the strongest noncovalent interactions between 18C6 and the bases investigated here. 18C6 interacts with MGD via four less than ideal (nonlinear) hydrogen bonds with three oxygen atoms to form a low symmetry conformer. 4MeImid and Imid interact with 18C6 via two nonideal hydrogen bonds to alternate oxygen atoms (O1 and O4) to form relatively weakly bound complexes. These trends in the $(B)H^+$–18C6 BDEs confirm that the geometry, even more importantly than the number of hydrogen bonding interactions, is critical to the strong binding necessary for molecular

recognition. The trends in the measured and computed $(B)H^+$–18C6 BDEs differ somewhat. MP2 and M06 theories overestimate the strength of binding to the primary alkyl amines, MA, EA, NPA, and NBA, whereas values for all of the other peptidomimetic bases are within experimental error of the measured values. This discrepancy is not well understood, but is not the result of the basis set size used for optimization as discussed in the previous section.

3.5.3. Binding Sites of Amino Acid Side Chains

Julian and Beauchamp applied the SNAAP method to exploit noncovalent interactions between crown ethers and the side chains of the amino acids in peptides and proteins. Their results suggest that 18C6 exhibits a strong binding preference for the side chain of Lys residues. In a study by Julian and Beauchamp,[23] a mixture of NBA, guanidine (GD), and Imid was sprayed with 18C6. They observed that the $(NBA)H^+(18C6)$ complex completely dominates the spectrum and is the base peak (100% relative abundance); while the relative intensity of the $(GD)H^+(18C6)$ and $(Imid)H^+(18C6)$ complexes is 3.5% and 1%, respectively. Although 18C6 exhibits a binding preference for Lys side chains, the side chains of Arg, His, and the N-terminal amino group may serve as competitive binding sites for 18C6 complexation. This result is consistent with the trends in the measured binding affinities examined here. Our measure BDEs suggest that the 18C6 affinity for the Lys mimics is ~50 kJ/mol higher than that for the His and Arg mimics. Therefore, the competition between the Lys residues and His or Arg residues for 18C6 is not severe. Based on the measured CID thresholds, IPA exhibits a greater binding affinity for 18C6 than MA, EA, NPA, and NBA.

Therefore, the N-terminal amino group could serve as a favorable alternative binding site for 18C6. The X-ray study of Krestov and coworkers suggests that steric interactions with the N-terminal amino acid side chain could constrain its complexation to 18C6.[56] They found that the "depth of penetration" of the ammonium group into the 18C6 cavity for complexation is significantly different for diglycine and dialanine. The ammonium group in diglycine is much closer to the crown than that of dialanine during complexation. Steric interactions with the methyl side chain in proximity to the amino group in dialanine do not allow 18C6 to approach as closely and therefore bind as strongly. Thus, the 18C6 binding affinity of the N-terminal amino group should depend on the nature of the side chain. Binding should be the strongest when glycine is the N-terminal amino acid and should decrease with increasing size/polarizability of the side chain. Thus, the ability of the N-terminal amino group to compete with the Lys side chains will depend upon the identity of the N-terminal amino acid.

3.5.4. Measured BDEs versus Polarizability of the Bases

As discussed above, the measured BDEs for the primary alkyl amine bases MA, EA, NPA, and NBA deviate systematically from the MP2(full)/6-311+G(2d,2p)//B3LYP/6-31G* calculated BDEs by 21.7 ± 2.9 kJ/mol. The measure BDEs exhibit a reverse linear correlation with the calculated polarizability of the bases as illustrated in **Figure 3.8a**. Theoretical calculations indicate that the binding between 18C6 and the bases involves N-H···O hydrogen bonds (or proton-lone pair electron interactions). Therefore, the strength of binding between 18C6 and the bases should be controlled by the nature of the interactions, ion-dipole and ion-induced dipole interactions. The polarizability of MA

is 3.6 Å^3, increases to 5.5 Å^3 for EA, to 7.3 Å^3 for NPA, and to 9.1 Å^3 for NBA. The more polarizable bases bind the proton more strongly and distribute the excess charge more evenly throughout the protonated base resulting in greater stabilization. The reduced charge on the protons of the amino group leads to weaker binding to 18C6.

The reverse linear correlation between the measured BDEs and the calculated polarizability of the bases was also observed for the Imid and 4MeImid systems, also shown in **Figure 3.8a**. The polarizability of Imid is 7.0 Å^3 and increases to 8.9 Å^3 for 4MeImid. In contrast, the measured BDE for the (Imid)H$^+$–18C6 complex is 175.0 kJ/mol and decreases to 167.6 kJ/mol for the (4MeImid)H$^+$–18C6 complex. The correlation line between the measured BDEs and the calculated polarizability for the two groups of bases are highly parallel, suggesting that the effects of additional methylene groups are additive. Each additional methylene group contributes to a decrease in the measured BDE of ~5 kJ/mol, and increases the polarizability by ~1.8 Å^3 for both the primary amine and imidazolic bases.

3.5.5. Measured BDEs versus PA of the Bases

Because the nitrogen bases investigated in this study involve different types of hydrogen bonding interactions with 18C6, the correlation between the proton affinity (PA) of the base and the measured BDEs are examined among bases that exhibit similar binding geometries to 18C6.

Among the Lys mimics, MA, EA, NPA and NBA, the measured 18C6 binding affinity exhibits a reverse linear correlation with the PA of these bases, as shown in **Figure 3.8b**. The PA of NBA is 921.5 kJ/mol, decreases to 917.8 kJ/mol for NPA, 912.0

kJ/mol for EA, and 899.0 kJ/mol for MA.[57] In contrast, the measured $(B)H^+$–18C6 BDEs increase from 223.8 kJ/mol for NBA to 224.2 kJ/mol for NPA, 233.2 kJ/mol for EA, and 238.0 kJ/mol for MA. This reverse linear correlation was previously explained based on the N–H bond lengths and the charge retained on the amino protons. Bases with higher PAs bind the proton tighter and lead to weaker interactions with 18C6, resulting in lower dissociation thresholds.

As discussed above, the PAs of the primary amines are anti-correlated with the 18C6 binding affinities. The analogous correlation was also observed between Imid and 4MeImid, as shown in **Figure 3.8b**. The PA of 4MeImid is 952.8 kJ/mol, ~ 10 kJ/mol greater than that of Imid. In contrast, the threshold for loss of 18C6 is 7.4 kJ/mol lower for 4MeImid than that of Imid.

The reverse correlation between PA and the measured $(B)H^+$–18C6 BDEs was also found for the complex to MGD. Although there is no PA reported in the literature, MGD is expected to exhibit a higher PA than all of the other bases based on MP2(full) and B3LYP calculations. MP2(full) theory finds that the PA of MGD exceeds that of all of the other bases examined here by 23.2 to 108.1 kJ/mol, whereas B3LYP theory finds slightly larger differences, 31.8 to 120.7 kJ/mol, respectively. In addition, Arg is known to be the most basic amino acid. Therefore, MGD as the mimic of Arg, is expected to exhibit a higher PA than all of the other mimics examined. MGD exhibits a much weaker binding interaction with 18C6 as compared to the MA, EA, NPA, NBA, and IPA systems as a result of the substantial PA difference relative to the other systems, and the very nonideal hydrogen bonding interactions in the $(MGD)H^+(18C6)$ complex.

Although DAP exhibits different interactions with 18C6 as compared to IPA and MGD, the reverse trend between measured BDEs and PA still loosely holds. DAP has a PA of 999.6 kJ/mol, 75.8 kJ/mol higher than that of IPA. Therefore, the measured BDE for DAP is expected to be lower than that of the N-terminal amino group mimic. Although the PA of MGD has not been reported, MP2(full) calculations suggest that the PA of DAP is 23.2 kJ/mol lower than that of MGD. Therefore, DAP is expected to exhibit a higher affinity for 18C6 than MGD. This reverse correlation was also observed for these systems. The measured BDE of DAP is 52.5 kJ/mol lower than that of IPA and 11.0 kJ/mol higher than that of MGD, consistent with expectations for the measured BDE of DAP.

3.5.6. Competitive Reaction Pathways

In most systems examined here, H^+(18C6) was observed in competition with formation of the protonated base. Because the cross sections for this product are small compared to the most favorable dissociation product, H^+(B), and the thresholds are higher, it does not significantly influence the kinetics of dissociation for the primary CID pathway. Therefore, a PSL TS was used to analyze the H^+(B) cross sections in this study. In principle, simultaneous competitive analysis of the H^+(B) and H^+(18C6) product cross section may also provide the relative PAs of 18C6 and the bases. However, attempts to analyze the data competitively using a loose PSL TS produced poor fits for all systems except Imid and 4MeImid, indicating that there is likely a tight TS barrier resulting from conformational changes that must occur to produce the H^+(18C6) product. Thus, competitive analyses of these systems will not provide the desired

relative PAs except in the cases of Imid and 4MeImid and therefore were not pursued further here. Competitive analyses of the CID cross sections of (Imid)H^+(18C6) and (4MeImid)H^+(18C6) will be discussed in **Chapter 6**.

3.5.7. Entropy Effects

The NIST webbook suggests that the PA of 18C6 is 967.0 kJ/mol, higher than the PAs of 4MeImid (952.8 kJ/mol), Imid (942.8 kJ/mol), IPA (923.8 kJ/mol), MA (899.0 kJ/mol), EA (912.0 kJ/mol), NPA (917.8 kJ/mol), and NBA (921.5 kJ/mol). Therefore, the threshold for production of H^+(18C6) might be expected to be lower than the threshold for dissociation to produce H^+(B). However, in all of the systems investigated here, the H^+(B) product was observed as the major CID product and the lowest energy dissociation pathway. This phenomenon can be understood by considering the change in entropy associated with the dissociation pathways. Entropy effects on CID results have been addressed by McLuckey and Cooks.[58-61] Wesdemiotis reported that entropy changes involved in the fragmentation of heterodimers can play a critical role in determining the preferred dissociation pathway.[59] For all of the systems examined here, the reaction pathway that involves the formation of H^+(B) exhibits a greater increase in entropy than the H^+(18C6) pathway. In the ground-state structure of H^+(18C6), the proton is bound to one oxygen atom and stabilized by a hydrogen bonding interaction with another oxygen atom, which results in more constrained rotational and vibration degrees of freedom in the protonated complex of 18C6. Therefore, the relatively favorable entropy change compared to the formation of H^+(18C6) facilitates the formation of H^+(B), making the "***apparent***" PA of these bases higher than that of 18C6.

Therefore, the kinetics of dissociation are severely slowed down, resulting in a more significant kinetic shift as compared to the H^+(B) pathway. As a result, despite the fact that the reported PA of NBA is 45.5 kJ/mol lower than that of 18C6, the dissociation pathway that forms H^+(NBA) is still more favorable. Therefore, the H^+(NBA) and the H^+(18C6) branching ratio does not accurately reflect the relative PAs of NBA and 18C6 as a result of entropic effects. The same holds true for all of the other primary amines investigated.

The magnitudes of the CID product cross sections for H^+(B) and H^+(18C6) are the result of competition between enthalpy and entropy: entropy favors the formation of H^+(B), while enthalpy favors the formation of the protonated species that exhibits a higher PA. In the MGD and DAP containing systems, the base exhibits a higher PA than 18C6. Therefore, enthalpy favors the formation of H^+(B). The relatively favorable entropy change as compared to the formation of H^+(18C6) also favors the formation of H^+(B). As a result, H^+(B) was observed as the only CID product. In contrast, in the complexes involving Imid, 4MeImid, MA, EA, NPA, NBA, and IPA, the PA of the base is lower than that of 18C6. Therefore, enthalpy favors the formation of H^+(18C6). However, entropy effects dominate and favor the formation of H^+(B). As a result, H^+(B) was observed as the major CID product and the lowest energy dissociation pathway, while H^+(18C6) was observed as a very minor competitive CID product.

3.6. Conclusions

The kinetic energy dependence for CID of nine (B)H^+(18C6) complexes, where B = Imid, 4MeImid, MA, EA, NPA, NBA, IPA, DAP, and MGD with Xe is examined by

guided ion beam tandem mass spectrometry techniques. For all nine systems, the primary dissociation pathway observed for these noncovalently bound complexes is loss of neutral 18C6. Thresholds for these CID processes are determined after consideration of the effects of the kinetic and internal energy distributions of the reactants, multiple collisions with Xe, and the lifetimes for unimolecular dissociation. $(B)H^+$–18C6 BDEs at 0 K are calculated at the MP2(full), B3LYP, and M06 levels of theory using a 6-311+G(2d,2p) basis set for both levels of geometry optimization, B3LYP/6-31G* and B3LYP/6-311+G(d,p). Good agreement between MP2(full) and M06 theoretically calculated and TCID experimentally determined BDEs was found in most cases. Compared to MP2(full) theory, M06 theory provides similar (albeit somewhat reduced) accuracy, but requires significantly less computing time, suggesting that M06 theory may be a good choice for calculations of larger noncovalently bound systems. The agreement between B3LYP theory and experiment is less satisfactory in these cases, but is better for the primary amines. Geometry optimization with an extended basis set, B3LYP/6-311+G(d,p) does not change the optimized structures, or the computed BDEs significantly, suggesting that the B3LYP/6-31G* level of theory is sufficient for describing the noncovalently bound systems examined here.

The 18C6 binding affinities determined here combined with structural information obtained from theoretical calculations provides useful insight into the processes that occur in the molecular recognition of 18C6 by peptides and proteins for protein structure and sequence investigation. In the MGD and DAP systems, both enthalpy and entropy favor the formation of $H^+(B)$. Therefore, $H^+(B)$ was observed as the major CID product, and $H^+(18C6)$ was not observed. In the other $(B)H^+(18C6)$ complexes, entropy effects

strongly influence the dissociation behavior, resulting in the observation of H^+(B) as the major and lowest energy CID pathway. However, enthalpy favors the formation of H^+(18C6). Therefore, H^+(18C6) was observed in competition with the primary CID pathway. As a result of the significant difference in entropy for these competitive dissociation pathways, the apparent cross section thresholds of the two products do not necessarily reflect the relative PAs of these bases and 18C6.

The Lys mimic, NBA, and the smaller primary amine analogs exhibit higher binding affinities for 18C6 than the His mimics, 4MeImid and Imid, and the Arg mimic, MGD, suggesting that amongst all basis amino acids, the side chains of Lys residues are the preferred binding sites for 18C6 complexation. These results suggest that competition between Arg or His and Lys for 18C6 is not significant. The mimic for the N-terminal amino group, IPA, exhibits a greater 18C6 binding affinity than the Lys mimic, NBA, suggesting that the N-terminus could serve as a favorable alternative binding site for 18C6. Based on correlations between the PA and polarizability of the bases and the measured (B)H^+–18C6 BDEs, binding to the N-terminal amino group should be the most competitive with the Lys side chains when the N-terminal amino acid is glycine and should become decreasingly less competitive as the size/polarizability of the side chain increases. This conclusion is being examined further in **Chapter 4** by investigating the analogous 18C6 complexes to glycine, alanine, Lys, His and Arg.

3.7. References

(1) Matthews, B. W. *Annu. Rev. Phys. Chem.* **1976**, *27*, 493.

(2) Dyson, H. J.; Wright, P. E. *Chem. Rev.* **2004,** *104,* 3607.

(3) Palmer, A. G. *Chem. Rev.* **2004,** *104,* 3623.

(4) Mendoza, V. L.; Vachet, R. W. *Mass Spectrom. Rev.* **2009**, *28*, 785.

(5) Wales, T. E.; Engen, J. R. *Mass Spectrom. Rev*. **2006**, *25*, 158.

(6) Sinz, A. *Mass Spectrom. Rev.* **2006**, *25*, 663.

(7) Smith, D. L.; Deng, Y.; Zhang, Z. *J. Mass Spectrom*. **1997**, *32*, 135.

(8) Engen, J. R.; Smith, D. L. *Anal. Chem.* **2001**, *73*, 256A.

(9) Kaltashov, I. A.; Eyles, S. J*. Mass Spectrom. Rev.* **2002**, *21*, 37.

(10) Kaltashov, I. A.; Eyles, S. J. *Mass Spectrom. Rev.* **2002**, *37*, 557.

(11) Hoofnagle, A. N.; Resing, K. A.; Ahn, N. G. *Annu. Rev. Biophys. Biomol. Struct.* **2003**, *32*, 1.

(12) Eyles, S. J.; Kaltashov, I. A. *Methods* **2004***, 34*, 88.

(13) Garcia, R. A.; Pantazatos, D.; Villarreal, F. J. *Assay Drug Dev. Technol.* **2004**, *2*, 81.

(14) Sinz, A. *J. Mass Spectrom*. **2003**, *38*, 1225.

(15) Brunner, J. *Annu. Rev. Biochem.* **1993**, *62*, 483.

(16) Kluger, R.; Alagic, A. *Bioorg. Chem.* **2004**, *32*, 451.

(17) Melcher, K. *Curr. Prot. Pept. Sci.* **2004**, *5*, 287.

(18) Kodadek, T.; Duroux-Richard, I.; Bonnafous, J. C. *Trends Pharmacol. Sci.* **2005**, *26*, 210.

(19) Back, J. W.; de Jong, L.; Muijsers, A. O.; de Koster, C. G. *J. Mol. Biol.* **2003**, *331*, 303.

(20) Friedhoff, P. *Anal. Bioanal. Chem.* **2005**, *381*, 78.

(21) Trakselis, M. A.; Alley, S. C.; Ishmael, F. T. *Bioconjug. Chem.* **2005**, *16*, 741.

(22) Petrotchenko, E. V.; Pedersen, L. C.; Borchers, C. H.; Tomer, K. B.; Negishi, M. *FEBS Lett.* **2001**, *490*, 39.

(23) Julian, R. R.; Beauchamp, J. L. *Int. J. Mass Spectrom.* **2001**, *210/211*, 613.

(24) Julian, R. R.; Beauchamp, J. L. *J. Am. Soc. Mass Spectrom.* **2002**, *13*, 493.

(25) Julian, R. R.; Beauchamp, J. L. *J. Am. Soc. Mass Spectrom.* **2004**, *15*, 616.

(26) Julian, R. R.; Akin, M.; May, J. A.; Stoltz, B. M.; Beauchamp, J. L. *Int. J. Mass Spectrom.* **2002**, *220*, 87.

(27) Julian, R. R.; May, J. A.; Stoltz, B. M.; Beauchamp, J. L. *Int. J. Mass Spectrom.* **2003**, *228*, 851.

(28) Ly, T.; Julian, R. R. *J. Am. Soc. Mass Spectrom.* **2006**, *17*, 1209.

(29) Ly, T.; Julian, R. R. *J. Am. Soc. Mass Spectrom.* **2008**, *19*, 1663.

(30) Liu, Z.; Cheng, S.; Gallie, D. R.; Julian, R. R. *Anal. Chem.* **2008**, *80*, 3846.

(31) Ly, T.; Liu, Z.; Pujanauski, B. G.; Sarpong, R.; Julian, R. R. *Anal. Chem.* **2008**, *80*, 5059.

(32) Yeh, G. K.; Sun, Q.; Meneses, C.; Julian, R. R. *J. Am. Soc. Mass Spectrom.* **2009**, *20*, 385.

(33) Chen, Y.; Rodgers, M. T. *J. Am. Chem. Soc.*, **2012**, *134*, 2313.

(34) Rodgers, M. T. *J. Phys. Chem. A* **2001**, *105*, 2374.

(35) Moison, R. M.; Armentrout, P. B. *J. Am. Soc. Mass Spectrom.* **2007**, *18*, 1124.

(36) *HyperChem Computational Chemistry Software Package*, Version 5.0; Hypercube Inc: Gainsville, FL, 1997.

(37) Frisch, M. J.; et al. *Gaussian 03*, Revision A.1; Gaussian, Inc.: Wallingford, CT, 2004. See **Chapter 2** for full reference.

(38) Frisch, M. J.; et al. *Gaussian 09*, Revision C.01; Gaussian, Inc.: Wallingford, CT, 2009. See **Chapter 2** for full reference.

(39) Becke, A. D. *J. Chem. Phys.* **1993**, *98*, 5648.

(40) Lee, C.; Yang, W.; Parr, R. G. *Phys. Rev. B* **1988**, *37*, 785.

(41) Foresman, J. B.; Frisch, Æ. *Exploring Chemistry with Electronic Structure Methods*, 2nd ed.; Gaussian: Pittsburgh, PA, 1996; p 64.

(42) Boys, S. F.; Bernardi, R. *Mol Phys.* **1979**,*19*, 553.

(43) van Duijneveldt, F. B.; van Duijneveldt-van de Rijdt, J. G. C. M.; van Lenthe, J. H. *Chem. Rev.* **1994**, *94*, 1873.

(44) Glendening, E. D.; Feller, D. *J. Am. Chem. Soc.* **1996**, *118*, 6052.

(45) Glendening, E. D.; Feller, D.; Thompson, M. A. *J. Am. Chem. Soc.* **1994**, *116*, 10657.

(46) Rodgers, M. T.; Ervin, K. M.; Armentrout, P. B. *J. Chem. Phys*. **1997**, *106*, 4499.

(47) Rodgers, M. T.; Armentrout, P. B. *J. Phys. Chem. A* **1997**, *101*, 1238.

(48) Rodgers, M. T.; Armentrout, P. B. *J. Phys. Chem. A* **1997**, *101*, 2614.

(49) Rodgers, M. T.; Armentrout, P. B. *Int. J. Mass Spectrom.* **1999**, *185/186/187*, 359.

(50) Rodgers, M. T.; Armentrout, P. B. *J. Phys. Chem. A* **1999**, *103*, 4955.

(51) Armentrout, P. B.; Rodgers, M. T. *J. Phys. Chem. A* **1999**, *104*, 2238.

(52) Amunugama, R.; Rodgers, M. T. *Int. J. Mass Spectrom.* **2000**, *195/196*, 439.

(53) Rodgers, M. T.; Armentrout, P. B. *J. Am. Chem. Soc.* **2000**, *122*, 8548.

(54) Rodgers, M. T.; Armentrout, P. B. *J. Chem. Phys*. **1998**, *109*, 1787.

(55) Rodgers, M. T. *J. Phys. Chem. A* **2001**, *105*, 8145.

(56) Kulikov, O. V.; Krestov, G. A. *Pure & Appl. Chem*. **1995**, 67,1103.

(57) Hunter, E. P.; Lias, S. G. *J. Phys. Chem. Ref. Data***, 1998**, *27*, 413.

(58) McLuckey, S. A.; Cooks, R. G.; Fulford, J. E. *Int. J. Mass Spectrom. Ion Phys.* **1983**, *52*, 165.

(59) Cerda, B. A.; Wesdemiotis, C. *J. Am. Chem. Soc.* **1996**, *118*, 11884.

(60) Cheng, X.; Wu, Z.; Fenselau, C. *J. Am. Chem. Soc.* **1993**, *115*, 4844.

(61) Bliznyuk, A. A.; Schaefer, H. F.; Amster, I. J. *J. Am. Chem. Soc.* **1993**, *115*, 5149.

Table 3.1. $(B)H^+$–18C6 Bond Dissociation Enthalpies at 0 K in kJ/mol[a]

B	TCID[b]	MP2 (full)	M06	B3LYP
4MeImid	167.6 (6.9)	167.1 (167.7)	162.7 (164.0)	136.8 (136.7)
MGD	174.3 (6.3)	165.7 (165.6)	167.7 (166.5)	133.6 (134.5)
Imid	175.0 (9.3)	177.1 (178.1)	174.8 (176.2)	148.2 (148.4)
DAP	185.8 (9.8)	177.8 (179.6)	183.8 (185.4)	142.0 (145.2)
NBA	223.8 (9.5)	247.4 (248.1)	256.4 (253.0)	210.5 (211.7)
NPA	224.2 (9.3)	248.1 (248.8)	255.1 (254.6)	212.4 (213.4)
EA	233.2 (10.4)	250.8 (251.3)	258.9 (258.3)	216.7 (217.6)
MA	238.0 (10.6)	259.8 (261.2)	266.4 (266.9)	234.6 (235.6)
IPA	238.3 (10.1)	240.8 (241.6)	248.6 (249.4)	199.0 (200.1)
AEU/MAD[c]	9.1 ± 1.5	12.1 ± 9.7 (12.5 ± 10.1)	15.8 ± 13.3 (15.4 ± 12.9)	25.2 ± 14.6 (24.2 ± 14.4)

[a]Single-point energies are calculated at the indicated level of theory using the 6-311+G(2d,2p) basis set and geometries optimized at the B3LYP/6-31G* level of theory. Single-point energies calculated at the indicated level of theory using the 6-311+G(2d,2p) basis set and geometries optimized at the B3LYP/6-311+G(d,p) level of theory are listed in parentheses. [b]Uncertainties are listed in parentheses. [c]Average experimental uncertainty (AEU) and mean absolute deviation (MAD) between theory and experiment for geometries optimized with the 6-31G* basis set. MAD using geometries optimized with the 6-311+G(d,p) basis set are listed in parentheses.

Table 3.2. Threshold Dissociation Energies at 0 K and Entropies of Activation at 1000 K of (B)H^+(18C6) Complexes[a]

B	σ_o[b]	n[b]	E_0 (eV)[c]	E_0 (PSL) (eV)[b]	Kinetic Shift (eV)	ΔS (PSL) (J mol^{-1} K^{-1})
4MeImid	117.5 (5.9)	0.8 (0.1)	3.08 (0.08)	1.74 (0.07)	1.34	69 (5)
MGD	94.5 (4.2)	0.9 (0.1)	3.03 (0.1)	1.81 (0.07)	1.22	109 (4)
Imid	61.9 (4.8)	1.0 (0.1)	3.12 (0.11)	1.81 (0.10)	1.31	85 (4)
DAP	94.6 (10.4)	1.3 (0.1)	3.52 (0.1)	1.93 (0.10)	1.59	113 (4)
NBA	68.9 (5.7)	1.0 (0.1)	4.58 (0.13)	2.32 (0.10)	2.26	109 (4)
NPA	3.5 (0.4)	1.2 (0.1)	4.36 (0.04)	2.32 (0.10)	2.04	116 (4)
EA	4.8 (0.4)	1.3 (0.1)	4.40 (0.10)	2.42 (0.11)	1.98	115 (4)
MA	44.6 (4.3)	1.3 (0.1)	4.57 (0.08)	2.47 (0.11)	2.10	103 (4)
IPA	62.5 (4.2)	0.8 (0.1)	4.65 (0.14)	2.47 (0.10)	2.18	123 (2)

[a]Present results, uncertainties are listed in parentheses. [b]Average values for loose PSL transition state. [c]No RRKM analysis.

3.8. Figure Captions

Figure 3.1. Structures of the peptidomimetic nitrogen bases examined as mimics for the N-terminal amino group and the side chains of the basic amino acids, histidine, arginine and lysine.

Figure 3.2. Cross sections for CID of the $(NBA)H^+(18C6)$ and $(MGD)H^+(18C6)$ complexes with Xe as a function of collision energy in the center-of-mass frame (lower *x*-axis) and laboratory frame (upper *x*-axis). Data are shown for a Xe pressure of 0.2 mTorr.

Figure 3.3. B3LYP/6-31G* optimized geometries of the ground-state conformers of the $(4MeImid)H^+(18C6)$, $(MGD)H^+(18C6)$, and $(NBA)H^+(18C6)$ complexes.

Figure 3.4. B3LYP/6-31G* optimized geometries of the ground-state conformers of the neutral and protonated 18C6.

Figure 3.5. B3LYP/6-31G* optimized geometries of the ground-state conformers of the neutral and protonated peptidomimetic bases.

Figure 3.6. Zero-pressure-extrapolated cross sections for CID of $(NBA)H^+(18C6)$ and $(MGD)H^+(18C6)$ complexes in the threshold region as a function of collision energy in the center-of-mass frame (lower *x*-axis) and laboratory frame (upper *x*-axis). The solid lines show the best fits to the data using equation 2.3 convoluted over the neutral and ion kinetic and internal energy distributions. The dotted lines show the model cross sections in the absence of experimental kinetic energy broadening for reactants with an internal energy corresponding to 0 K.

Figure 3.7. Comparison of the MP2(full) calculated and TCID measured $(B)H^+$–18C6 0 K BDEs. Theoretical BDEs determined from single point energy calculations at the MP2(full)/6-311+G(2d,2p)//B3LYP/6-31G* level of theory including ZPE and BSSE corrections.

Figure 3.8. TCID measured $(B)H^+$–18C6 BDEs at 0 K (kJ/mole) versus PBE1PBE calculated polarizability of B, where B = MA, EA, NPA, NBA, Imid, and 4MeImid (part a). TCID measured $(B)H^+$–18C6 BDEs at 0 K (kJ/mole) versus PA of B, where B = MA, EA, NPA, NBA, Imid and 4MeImid (part b). PAs taken from the NIST Webbook.[57]

Figure 3.1.

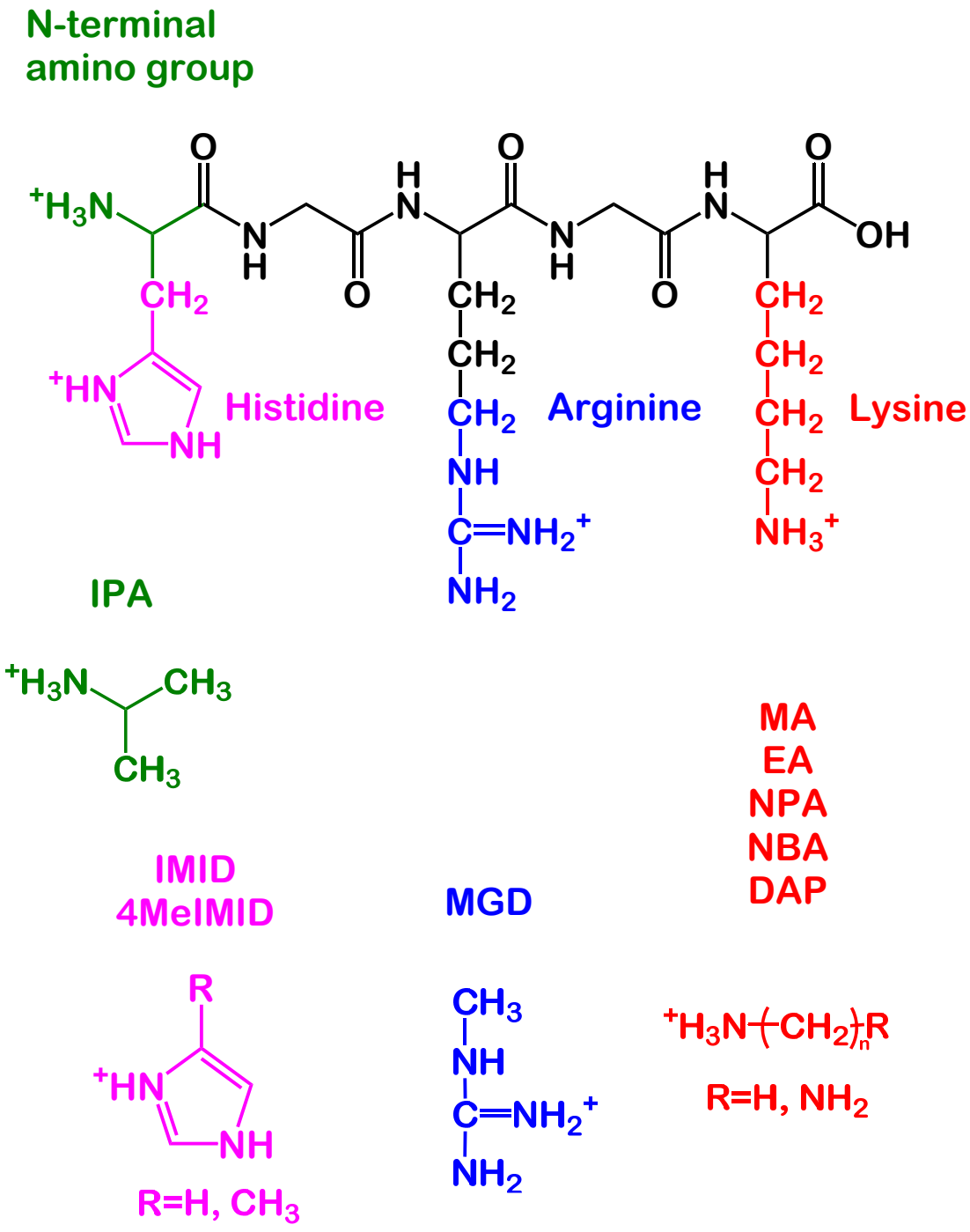
N-terminal
amino group
Histidine
Arginine
Lysine
IPA
IMID
4MeIMID
R=H, CH3
MGD
MA
EA
NPA
NBA
DAP
R=H, NH2

Figure 3.2.

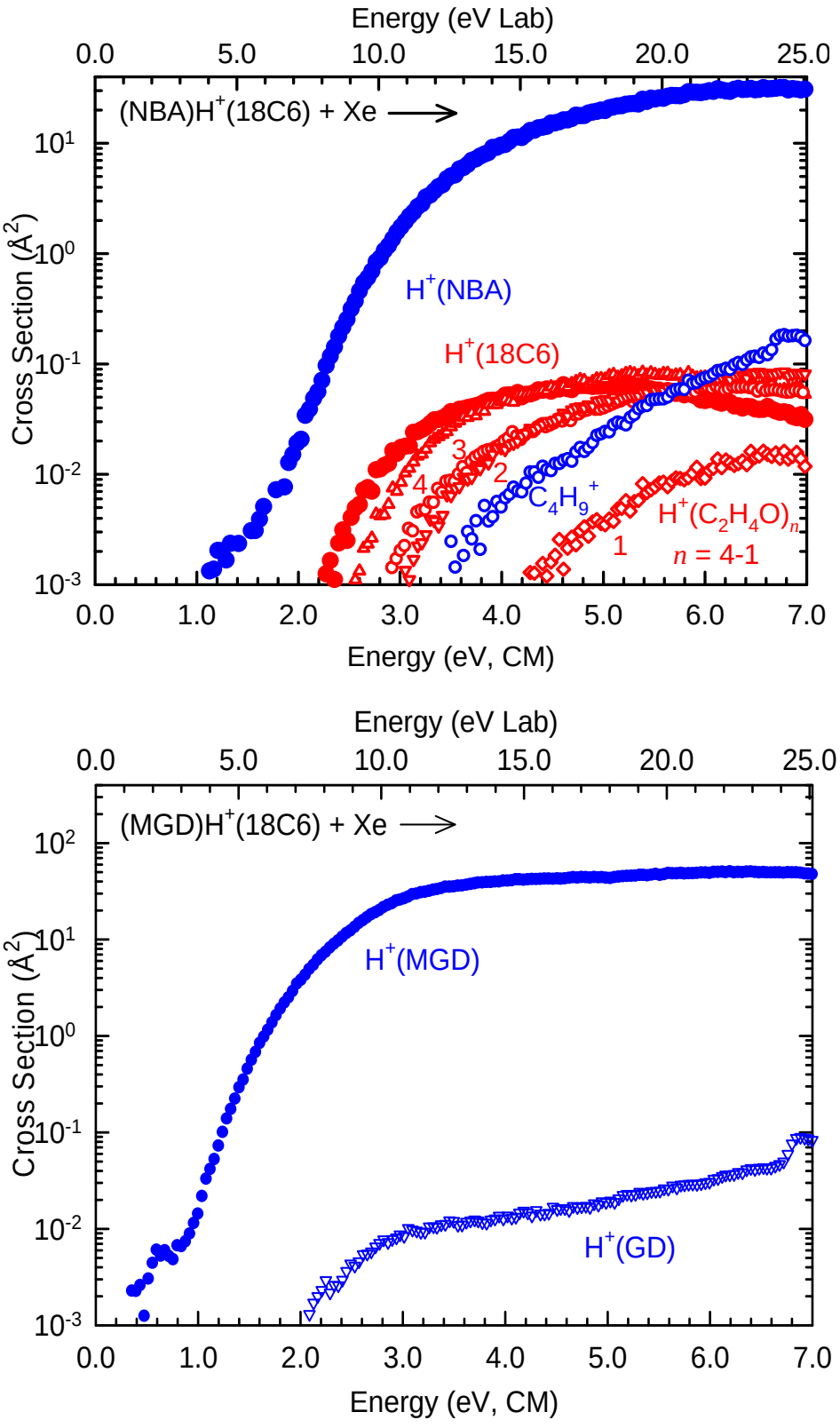
Energy (eV Lab)
0.0
5.0
10.0
15.0
20.0
25.0
(NBA)H+(18C6) + Xe
Cross Section (Å2)
10^1
10^0
10^-1
10^-2
10^-3
H+(NBA)
H+(18C6)
3
4
2
C4H9+
H+(C2H4O)n
n = 4-1
1
0.0
1.0
2.0
3.0
4.0
5.0
6.0
7.0
Energy (eV, CM)
Energy (eV Lab)
0.0
5.0
10.0
15.0
20.0
25.0
(MGD)H+(18C6) + Xe
Cross Section (Å2)
10^2
10^1
10^0
10^-1
10^-2
10^-3
H+(MGD)
H+(GD)
0.0
1.0
2.0
3.0
4.0
5.0
6.0
7.0
Energy (eV, CM)

Figure 3.3.

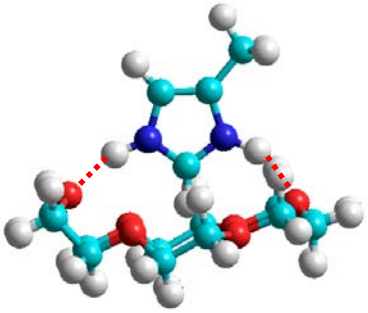

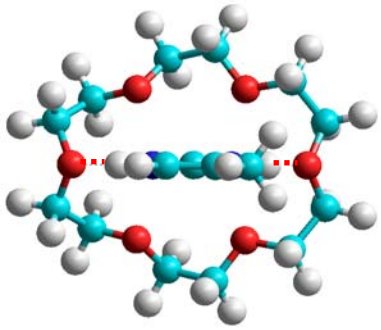

$(IMID)H^{+}(18C6)$

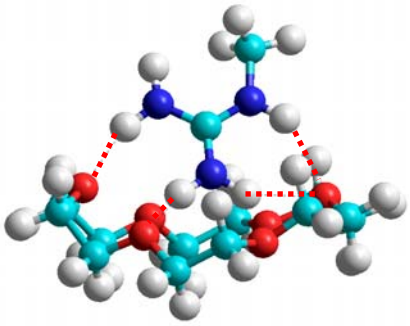

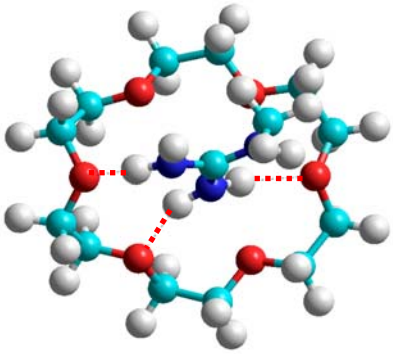

$(MGD)H^{+}(18C6)$

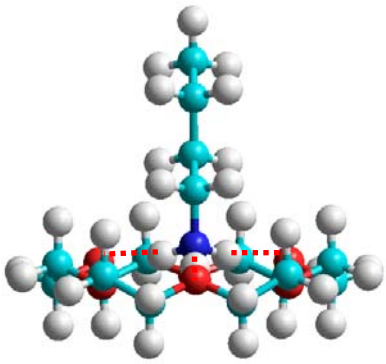

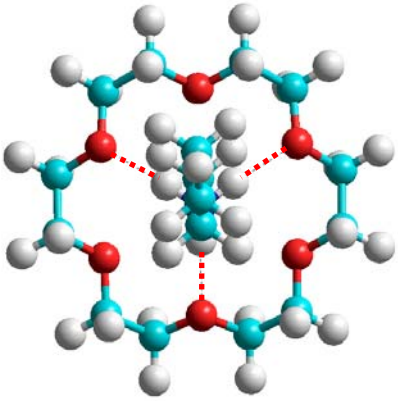

$(NBA)H^{+}(18C6)$

Figure 3.4.

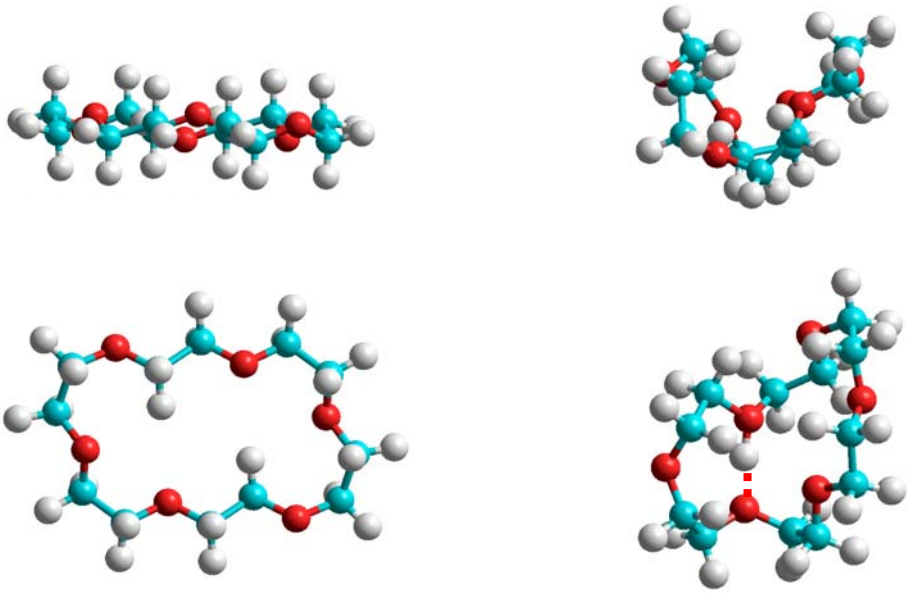

18C6 H^+(18C6)

Figure 3.5.

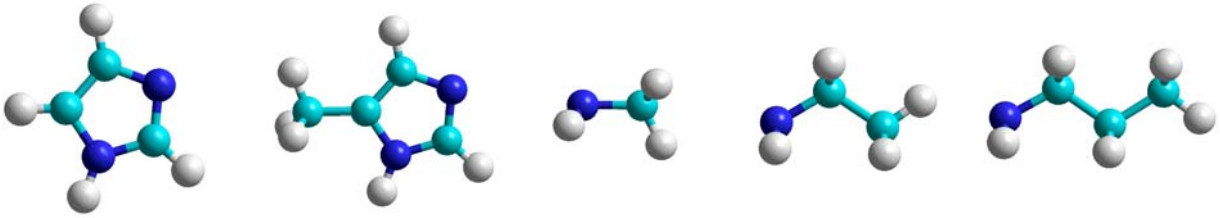

Imid 4MeImid MA EA NPA

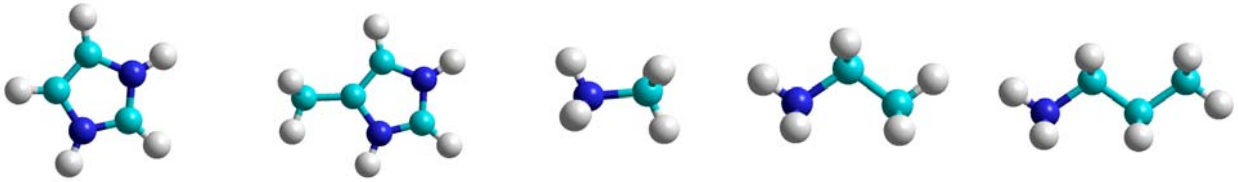

H^+(Imid) H^+(4MeImid) H^+(MA) H^+(EA) H^+(NPA)

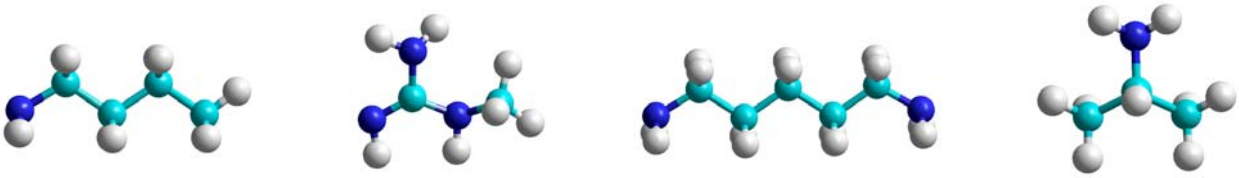

NBA MGD DAP IPA

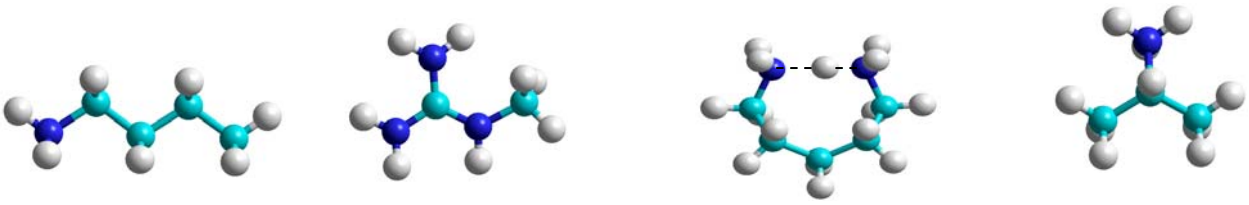

H^+(NBA) H^+(MGD) H^+(DAP) H^+(IPA)

Figure 3.6.

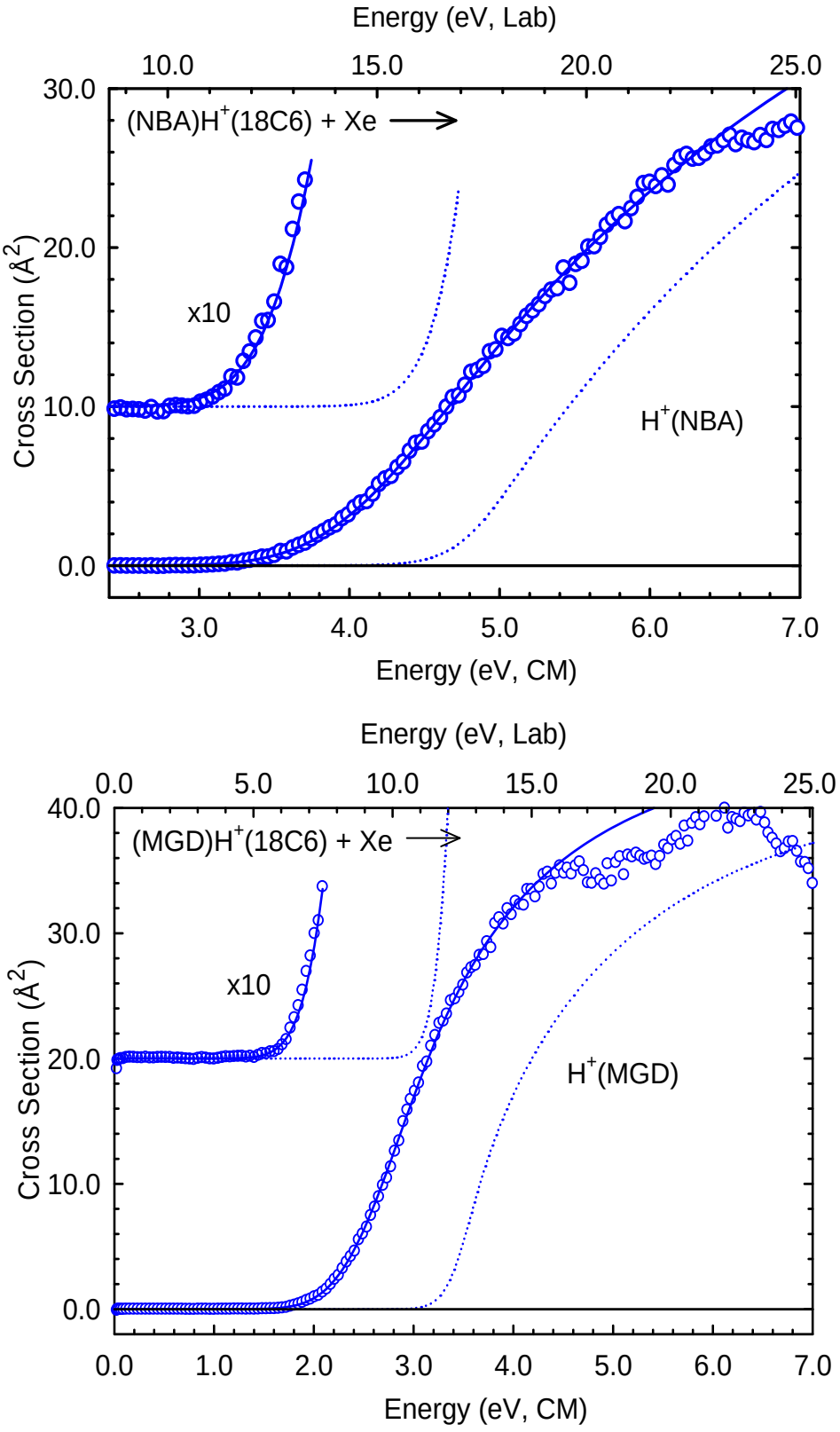
Energy (eV, Lab)
10.0
15.0
20.0
25.0
30.0
(NBA)H+(18C6) + Xe
Cross Section (Å2)
20.0
x10
10.0
H+(NBA)
0.0
3.0
4.0
5.0
6.0
7.0
Energy (eV, CM)
Energy (eV, Lab)
0.0
5.0
10.0
15.0
20.0
25.0
40.0
(MGD)H+(18C6) + Xe
30.0
Cross Section (Å2)
x10
20.0
H+(MGD)
10.0
0.0
0.0
1.0
2.0
3.0
4.0
5.0
6.0
7.0
Energy (eV, CM)

Figure 3.7.

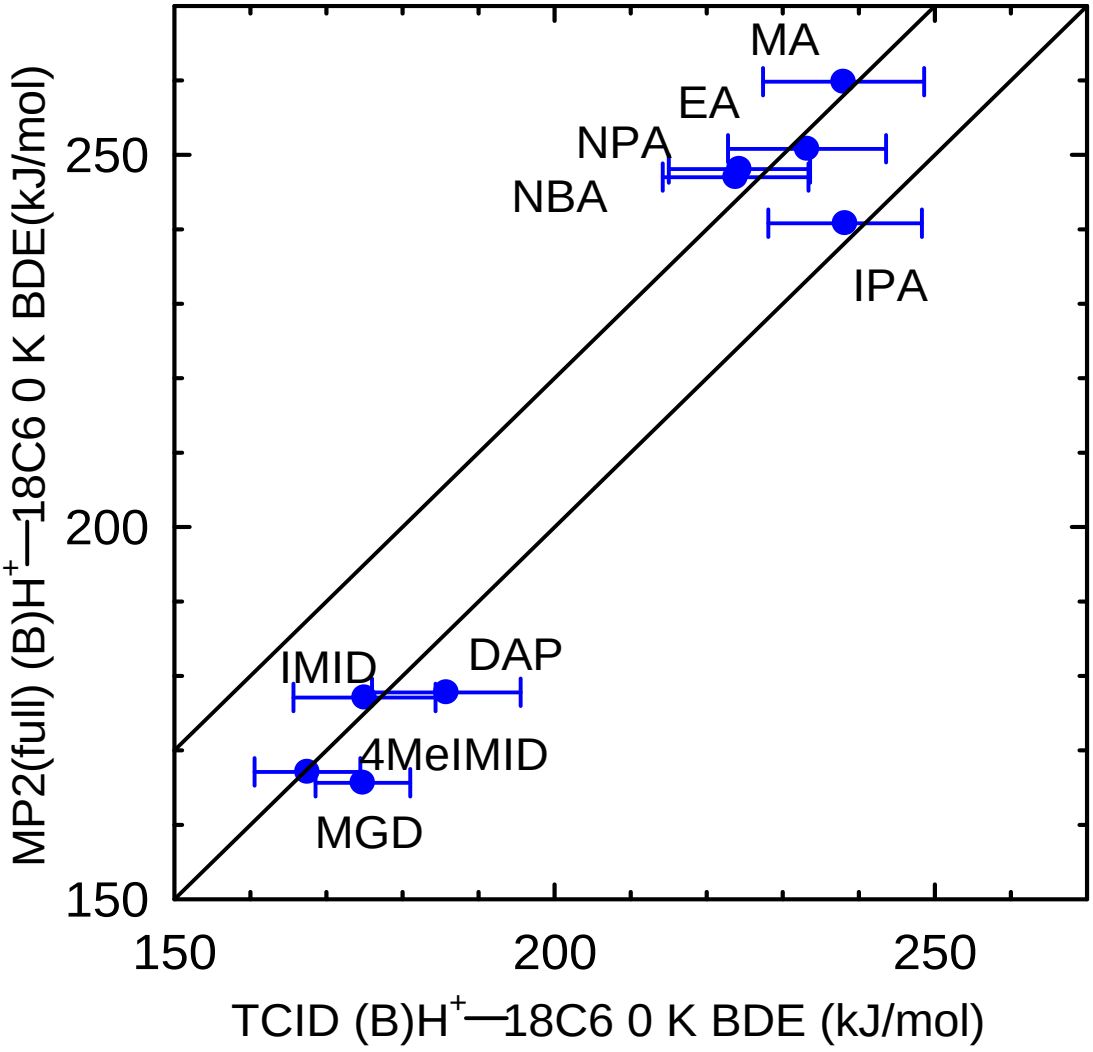
MA
EA
NPA
NBA
IPA
IMID
DAP
4MeIMID
MGD
150
200
250
150
200
250
MP2(full) (B)H+—18C6 0 K BDE(kJ/mol)
TCID (B)H+—18C6 0 K BDE (kJ/mol)

Figure 3.8.

(a)

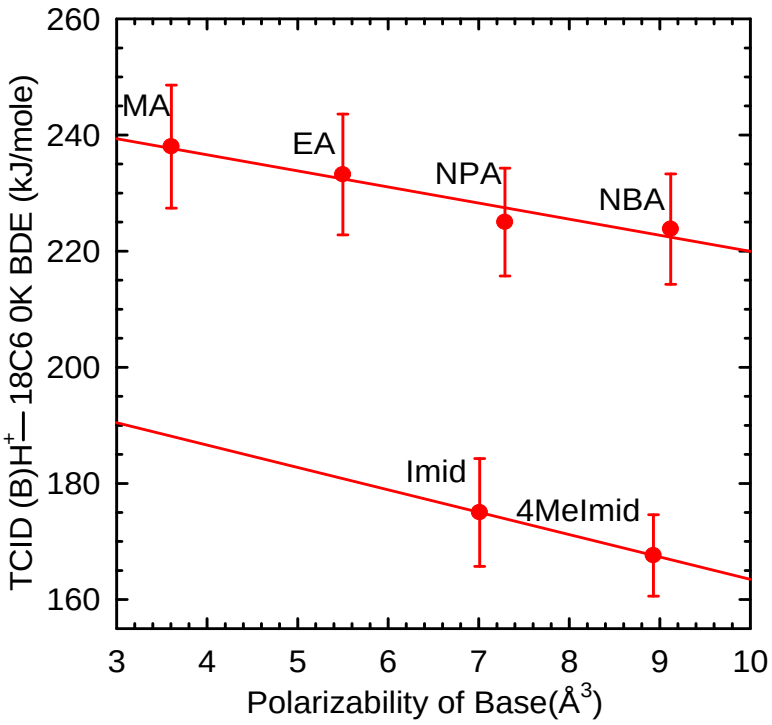
260
240
220
200
180
160
TCID (B)H+— 18C6 0K BDE (kJ/mole)
MA
EA
NPA
NBA
Imid
4MeImid
3
4
5
6
7
8
9
10
Polarizability of Base(Å3)

(b)

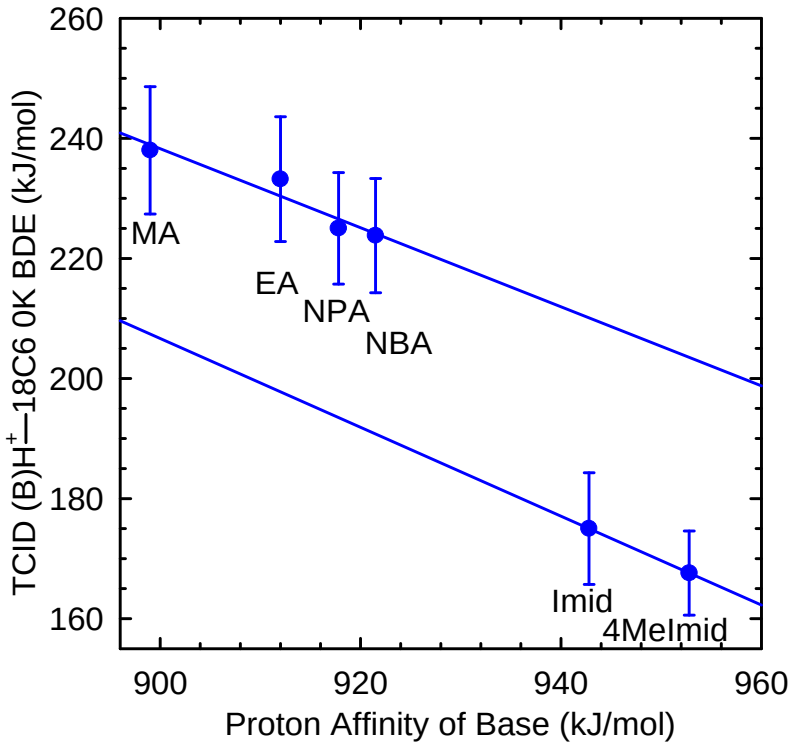
260
240
220
200
180
160
TCID (B)H+—18C6 0K BDE (kJ/mol)
MA
EA
NPA
NBA
Imid
4MeImid
900
920
940
960
Proton Affinity of Base (kJ/mol)

CHAPTER 4

STRUCTURAL AND ENERGETIC EFFECTS IN THE MOLECULAR RECOGNITION OF AMINO ACIDS BY 18-CROWN-6

Portions of this chapter were reprinted with permission from Chen, Y. and Rodgers, M. T. Structural and Energetic Effects in the Molecular Recognition of Amino Acids by 18-Crown-6. *J. Am. Chem. Soc.*, **2012**, *134*, 5863.

4.1. Introduction

Protein structures and protein-protein interactions play critical roles in biological processes. Binding "hot spots" typically refer to an ~600 $Å^2$ region on the surface of a protein at or near the geometric center of the protein-protein interface, and have been identified in a number of protein interfaces.[1-4] These "hot spots" are absolutely essential for protein-protein interactions and contribute significantly to the stability of protein-protein complexes. Therefore, protein structure elucidation and protein surface recognition may provide insight into how proteins interact with each other.

X-ray crystallography[5] and NMR spectroscopy[6,7] are well-established techniques that have been implemented to study protein structures. However, X-ray analyses require sample crystallization, while NMR studies require a large quantity of the protein in a specific solvent.

In contrast, mass spectral analyses are not subject to these limitations. Therefore, mass spectrometry (MS) has become an increasingly important tool for protein structure determination due to its speed, sensitivity, and specificity.[8,9] A variety

of mass spectrometric techniques have been applied to study protein structures, such as hydrogen/deuterium exchange (H/D exchange)[9-16] and chemical cross-linking.[17-26]

Selective noncovalent adduct protein probing (SNAPP) has been developed to exploit protein structure and folding states in solution.[27-36] SNAPP relies on the selective binding of a crown ether to basic amino acid (AA) residues, and in particular lysine (Lys) residues, to facilitate rapid identification and characterization of protein sequence, structure, and conformational changes. 18-crown-6 (18C6) is most commonly employed as a protein side chain tag because of its enzyme-like specificity in its interactions with Lys side chains. The extent of 18C6 attachment to a protein is determined by the degree of accessibility to its Lys side chains. When a Lys side chain engages in intramolecular interactions such as a hydrogen bond or salt bridge, the intramolecular interaction generally prevents the attachment of 18C6. Therefore, the number of 18C6 ligands that bind is also directly correlated to the protein structure. Because the number of 18C6 ligands that bind to a protein can be easily determined by MS due to the large mass shift (264 Da per 18C6 bound), protein structure and folding information under varying solution conditions can be extrapolated.

Accurate structural and thermochemical information regarding the binding between 18C6 and the AAs may provide insight into the selectivity of the complexation process. However, very limited thermochemical data has thus far been reported in the literature.[37] In this chapter, we extend this work to explicitly include five AAs using both guided ion beam tandem mass spectrometry techniques and theoretical electronic structure calculations. We characterize the structures of protonated amino acid-18C6 complexes and measure the absolute 18C6 binding affinities of the protonated AAs to

provide further insight into the molecular recognition of AAs, and by inference, peptides and proteins by 18C6. The AAs examined in the present study include: glycine (Gly), alanine (Ala), Lys, His, and Arg as shown schematically in the multiply protonated model peptide of **Figure 4.1**. The energy-dependent CID cross sections are analyzed using methods previously developed that explicitly include the effects of the kinetic and internal energy distributions of the reactants, multiple ion-neutral collisions, and the kinetics of unimolecular dissociation. Absolute $(AA)H^+$–18C6 bond dissociation energies (BDEs) for five $(AA)H^+(18C6)$ complexes are derived and compared to theoretical estimates determined using M06 and B3LYP theory. Absolute $(18C6)H^+$–AA BDEs are also determined for the complexes to Gly and Ala and compared with theory.[38]

4.2. Collision-Induced Dissociation Experiments

Cross sections for CID of five protonated amino acid-18C6 complexes, $(AA)H^+(18C6)$ with Xe, where AA = Gly, Ala, Lys, His, and Arg, are measured using a guided ion beam tandem mass spectrometer that has been described in detail previously.[39] The $(AA)H^+(18C6)$ complexes are generated by electrospray ionization (ESI).[40] The ions are effusively sampled from the source region, focused, accelerated, and focused into a magnetic sector momentum analyzer for mass analysis. Mass-selected ions are decelerated to a desired kinetic energy and focused into an octopole ion guide. The octopole passes through a static gas cell containing Xe at low pressure (~0.05–0.20 mTorr) to ensure that multiple ion-neutral collisions are improbable. Products and unreacted beam ions drift to the end of the octopole, are focused into a quadrupole mass filter for mass analysis, and are subsequently detected with a

secondary electron scintillation detector and standard pulse counting techniques. Details of the experimental procedures and thermochemical analysis are given in **Chapter 2**.

4.3. Theoretical Calculations

A simulated annealing procedure using HyperChem[41] and the AMBER force field was used to generate starting structures of neutral and protonated 18C6 and the AAs for higher level optimization. All structures found within 30 kJ/mol of the lowest-energy structure were further optimized using the Gaussian 09 [42] suites of programs.

Geometry optimizations for neutral and protonated 18C6 and the AAs as well as the proton bound $(AA)H^+(18C6)$ complexes were performed using density functional theory at the B3LYP/6-31G* level of theory.[43,44] Vibrational analyses of the geometry-optimized structures were performed to determine the vibrational frequencies of the optimized species for use in modeling of the CID data. The frequencies calculated were scaled by a factor of 0.9804.[45] Single-point energy calculations were performed at the B3LYP/6-311+G(2d,2p) and M06/6-311+G(2d,2p) levels of theory using the B3LYP/6-31G* optimized geometries. To obtain accurate energetics, zero-point energy (ZPE) and basis set super position error (BSSE) corrections are included in the computed BDEs using the counterpoise approach.[46, 47] The polarizability of neutral and protonated AAs are calculated at the Perdew, Burke, and Ernzerhof (PBE1PBE, also known as PBE0) level of theory, with the PBE1PBE/6-311+G(2d,2p) basis set. Further details of the theoretical calculations are given in **Chapter 2**.

4.4. Results

4.4.1. Cross Sections for Collision-induced Dissociation

Experimental cross sections were obtained for the interaction of Xe with five $(AA)H^+(18C6)$ complexes, where AA = Gly, Ala, Lys, His, and Arg. **Figure 4.2** shows representative data for the $(Lys)H^+(18C6)$ and $(Gly)H^+(18C6)$ complexes. Experimental cross sections for the other $(AA)H^+(18C6)$ complexes are shown in **Figure S1** of the Supporting Information of reference 38. Loss of the intact 18C6 ligand is observed for all five complexes, CID reactions 4.1,

$$(AA)H^+(18C6) + Xe \rightarrow H^+(AA) + 18C6 + Xe \quad (4.1)$$

and corresponds to the most favorable process for the complexes to Lys, His, and Arg. The apparent thresholds for the $H^+(AA)$ product decreases in the order Gly > Ala > Lys > His > Arg, suggesting that the binding of 18C6 follows that same order. The magnitude of the $H^+(AA)$ cross section increases in nearly the reverse order, Gly < Ala < Arg < His < Lys.

For the complexes to Gly and Ala, loss of the intact AA is observed in competition with loss of 18C6, and corresponds to the lowest-energy CID pathway for these complexes, CID reactions 4.2.

$$(AA)H^+(18C6) + Xe \rightarrow H^+(18C6) + AA + Xe \quad (4.2)$$

The apparent threshold for the $H^+(18C6)$ product increases from Gly to Ala, whereas the difference in the apparent threshold for $H^+(AA)$ and $H^+(18C6)$ decreases from Gly to Ala, indicating that Ala competes more effectively than Gly for the proton. Thus, the magnitude of the $H^+(AA)$ product cross section is greater for the complex to Ala. At

elevated energies, products corresponding to the sequential dissociation of H^+(18C6) were also observed in the complexes to Gly and Ala, reactions 4.3.

$$H^+(18C6) + Xe \rightarrow H^+(C_2H_4O)_n + (6\text{-}n)\ C_2H_4O + Xe, \quad n = 1 - 4 \qquad (4.3)$$

At elevated energies, products corresponding to sequential dissociation of H^+(AA) were also observed for the complexes to Lys, His, and Arg. Sequential dissociation of the H^+(Lys) primary product results in the loss of NH_3 and sequential concomitant loss of CO and H_2O. At elevated energies, direct loss of ethylamine is also observed.[48,49] Sequential dissociation of H^+(His) results in simultaneous loss of CO and H_2O and sequential loss of NH_3.[48] Sequential dissociation of H^+(Arg) results in the loss of NH_3 or guanidine (GD), or the fragmentation of protonated guanidine, H^+(GD), as well as the simultaneous loss of NH_3, CO, H_2O and CN_2H_2.[49] These results are consistent with CID results for the H^+(Lys), H^+(His), and H^+(Arg) complexes previously reported by Siu, Hopkinson, and coworkers.[49] Ligand exchange to produce XeH^+(AA) is only observed for the complex to Arg at elevated energies.

4.4.2. Theoretical Results

The ground-state structures of the (AA)H^+(18C6) complexes are shown in **Figure 4.3**. Structures of several representative low-energy conformations of the (AA)H^+(18C6) complexes are shown in **Figure S2** of the Supporting Information of reference 38. The ground-state structures of neutral and protonated 18C6 are shown in **Figure 3.4** and in **Chapter 3**. Results for the stable low-energy conformations of the neutral and protonated AAs and 18C6 are shown in **Figure S3** of the Supporting Information of reference 38. The (AA)H^+–18C6 BDEs at 0 K calculated at the M06/6-

311+G(2d,2p)//B3LYP/6-31G* and B3LYP/6-311+G(2d,2p)//B3LYP/6-31G* levels of theory including ZPE and BSSE corrections, are listed in **Table 4.1**. Comparison of the measured and calculated values suggests that the M06 results are most reliable. Therefore, the following discussion will focus on the relative energies calculated at M06/6-311+G(2d,2p) level of theory using the B3LYP/6-31G* optimized structures unless otherwise specified.

4.4.2.1. Amino Acids

The ground-state structures of the neutral and protonated AAs are shown in **Figure 4.4**. Details of the optimized geometries for the stable low-energy conformations of the neutral and protonated AAs are provided in **Figure S3** of the Supporting Information of reference 38. The backbone N–terminal amino group is the preferred site of protonation to Gly and Ala. In contrast, protonation of the side chain substituent is preferred for the basic AAs, Lys, His, and Arg.

The ground-state conformers of Gly and H^+(Gly) are shown in **Figure 4.4**, and several stable low-energy conformers are shown in **Figure S3** of the Supporting Information of reference 38. In the ground-state structure of neutral Gly, the N-terminal amino group points away from the CH_2 group, consistent with the structure found by Cassady and coworkers.[50] The ground-state structure of Ala exhibits a similar conformation to that of Gly. In the ground-state structure of H^+(Gly), one of the N-terminal amino hydrogen atoms points toward the carbonyl oxygen atom forming an intramolecular hydrogen bond. However, geometry optimization of the ground-state structure found by Cassady and coworkers using HF/6-31G* theory corresponds to a

transition state (TS) structure at the B3LYP/6-31G* level of theory, as shown in **Figure S3** of the Supporting Information of reference 38. The ground-state structure of H^+(Gly) found in the present study was also reported by Armentrout and coworkers.[51] The ground-state structure of H^+(Ala) exhibits a conformation similar to that of H^+(Gly) with the backbone hydrogen atom substituted by a methylene group.

The ground-state conformers of Lys and H^+(Lys) are shown in **Figure 4.4**, and several stable low-energy conformers are shown in **Figure S3** of the Supporting Information of reference 38. The ground-state structures of Lys and H^+(Lys) found in the present study are consistent with the structures reported by Williams and coworkers.[52] The ground-state structure of Lys is stabilized by two intramolecular hydrogen bonds, one between the amino nitrogen atom of the side chain and the backbone hydroxyl hydrogen atom, and the other between the carbonyl oxygen atom and one of the amino hydrogen atoms of the backbone. The ground-state structure of H^+(Lys) is also stabilized by two intramolecular hydrogen bonds. The protonated amino group of the side chain forms two intramolecular hydrogen bonds with the backbone amino nitrogen and carbonyl oxygen atoms.

The ground-state conformers of His and H^+(His) are shown in **Figure 4.4**, and several stable low-energy conformers are shown in **Figure S3** of the Supporting Information of reference 38. The ground-state structure of His is stabilized by two intramolecular hydrogen bonds between the imine hydrogen and the carbonyl oxygen atoms and between the hydroxyl hydrogen and the backbone amino nitrogen atom, consistent with the structure found by Dunbar, Siu, and coworkers.[53] The ground-state structure of H^+(His) is also stabilized by two intramolecular hydrogen bonds, one

between the protonated side chain amino hydrogen and backbone amino nitrogen atoms, and the other between the backbone amino hydrogen and carbonyl oxygen atoms. The ground-state structure found in the present work was also reported by Kovacevic and coworkers.[54] The ground-state structure reported by Amster and coworkers involves a hydrogen bond between the protonated side chain and the carbonyl oxygen atom.[55] However, present calculations suggest that this conformer lies 4.8 kJ/mol higher in energy than the most stable (ground-state) conformer determined here.

The ground-state conformers of Arg and H^+(Arg) are shown in **Figure 4.4**, and several stable low-energy conformers are shown in **Figure S3** of the Supporting Information of reference 38. The ground-state structures of neutral and protonated Arg determined here are consistent with structures previously reported by Gutowski, Williams, and Jockusch.[56,57] The ground-state structure of Arg is stabilized by three intramolecular hydrogen bonds, one between the backbone amino nitrogen and the hydroxyl hydrogen atoms, one between one of the side chain primary amine hydrogen atoms and the backbone carboxyl oxygen atom, and the third between one of the backbone primary amine hydrogen atoms and the side chain imine nitrogen atom.[56] In the ground-state conformer of H^+(Arg), the protonated side chain forms two intramolecular hydrogen bonds with the backbone amino nitrogen and the carbonyl oxygen atoms.[57]

4.4.2.2. $(AA)H^+(18C6)$ Complexes

The ground-state conformations of the $(AA)H^+(18C6)$ complexes are shown in **Figure 4.3**, while select excited low-energy conformers are shown in **Figure S2** of the Supporting Information of reference 38. 18C6 binds to the protonated backbone amino group in the complexes to Gly, Ala, Arg, and His, whereas binding to the protonated side chain substituent is preferred for the complex to Lys. In all cases, binding occurs via three nearly ideal N–H···O hydrogen bonds. The conformation of 18C6 in all of these complexes bears great similarity to the D_{3d} excited conformer of the neutral crown with a nucleophilic cavity in the center for interaction with the protonated AA.

In the ground-state conformations of the $(Gly)H^+(18C6)$ and $(Ala)H^+(18C6)$ complexes, the conformations of $H^+(Gly)$ and $H^+(Ala)$ are remarkably similar to the conformations of the isolated ground-state species. In both cases, the protonated backbone amino group interacts with 18C6 via three nearly ideal N–H···O hydrogen bonds. In the ground-state conformation of the $(Lys)H^+(18C6)$ complex, the $H^+(Lys)$ moiety is stabilized by an intramolecular hydrogen bond between a backbone amino hydrogen and carbonyl oxygen atoms. The $H^+(Lys)$ moiety exhibits an extended conformation, resulting in the protonated side chain amino group interacting with 18C6 via three nearly ideal N–H···O hydrogen bonds. Several excited conformers where 18C6 also interacts with the protonated side chain amino group, but that differ in the conformation of the AA backbone were also found; an example is shown in **Figure S2** of the Supporting Information of reference 38. Likewise, excited conformers where 18C6 binds to the protonated backbone amino group were also found, but the most stable of these conformers is 4.2 kJ/mol less stable than the ground-state conformer determined

here. Thus, binding to the side chain of Lys is favored over binding to the backbone by at least 4.2 kJ/mol. Attempts to calculate salt bridge structures in which 18C6 binds to the either the protonated side chain or the protonated backbone always converged to one of the low-energy non-salt bridge structures shown in **Figure S2** of reference 38 except when open structures with no hydrogen bond stabilization between the protonated amino and carboxylate groups are computed. However, all such zwitterionic complexes found are at least 179 kJ/mol less stable than the ground-state conformer.

In the ground-state conformation of the (His)H^+(18C6) complex, the proton binds to the backbone amino group of His to form H^+(His), which binds to a distorted D_{3d} conformer of 18C6 via three nearly ideal N–H···O hydrogen bonds. The conformation of the H^+(His) moiety in this complex is stabilized by an intramolecular hydrogen bond between the backbone carboxyl hydrogen and side chain imine nitrogen atoms. Stable conformations are also found where the proton binds to the side chain of His and the H^+(His) moiety binds to 18C6 via two N–H···O hydrogen bonds as shown in **Figure S2** of the Supporting Information of reference 38. However, these conformers are calculated to be at least 36.9 kJ/mol less stable than the ground-state conformer. Again attempts to calculate salt bridge structures (where both the backbone amino group and side chain are protonated and the carboxyl group is deprotonated) in which 18C6 binds to the protonated backbone amino group always converged to the ground-state conformation. Attempts to calculate salt bridge structures in which 18C6 binds to the either the protonated side chain or the protonated backbone always converged to one of the low-energy non-salt bridge structures shown in **Figure S2** of reference 38.

The ground-state conformation of the $(Arg)H^+(18C6)$ complex is a salt bridge structure in which both the backbone amino group and side chain are protonated, while the carboxyl group is deprotonated, and the protonated backbone amino group of the $H^+(Arg)$ moiety binds to a distorted D_{3d} conformer of 18C6 via three nearly ideal N–H···O hydrogen bonds. The $H^+(Arg)$ moiety is stabilized by two intramolecular hydrogen bonds between the amine and imine hydrogen atoms of the protonated side chain and one of the backbone carboxylate oxygen atoms. Stable conformations are also found where only the side chain is protonated, and the protonated side chain of the $H^+(Arg)$ moiety binds to 18C6 via three N–H···O hydrogen bonds to the O1, O2, and O4 atoms of 18C6 as shown in **Figure S2** of the Supporting Information of reference 38. However, the most stable conformer of this nature is calculated to be 13.9 kJ/mol less stable than the ground-state conformer. Stable conformations are also found where only the backbone is protonated, and the protonated backbone amino group of the $H^+(Arg)$ moiety binds via three nearly ideal N–H···O hydrogen bonds. However, the most stable conformer of this nature is calculated to be 42.7 kJ/mol less stable than the ground-state conformer. Other salt bridge conformations involving 18C6 binding to the protonated side chain were also investigated. However, these structures always converged to non-salt bridge conformations.

4.4.3. Threshold Analysis

The model of equation 2.3 was used to analyze the thresholds for reactions 4.1 in five $(AA)H^+(18C6)$ complexes, where AA = Gly, Ala, Lys, His, and Arg. The results of these analyses are provided in **Table 4.2** and representative results are shown in

Figure 4.5 for the $(Lys)H^+(18C6)$ and $(Gly)H^+(18C6)$ complexes. The analyses for the other $(AA)H^+(18C6)$ complexes are shown in **Figure S4** of the Supporting Information of reference 38. For the complexes to Lys, His, and Arg, the data were analyzed in two ways. First, the CID cross sections were analyzed assuming that the most stable backbone binding conformations of the $(AA)H^+(18C6)$ complexes were accessed in the experiments, i.e., the ground-state conformations of the complexes to His and Arg and an excited conformation of the complex to Lys. Second, the data were analyzed assuming that the most stable side chain binding conformations of the $(AA)H^+(18C6)$ complexes were accessed in the experiments, i.e., the ground-state conformation of the complex to Lys, and excited conformations of the complexes to His and Arg. In all cases, the experimental cross sections for reaction 4.1 are accurately reproduced using a loose PSL TS model.[58] Previous work has shown that this model provides the most accurate assessment of the kinetics shifts for CID process for electrostatically bound ion-molecule complexes.[59-67] Good reproduction of the data is obtained over energy ranges exceeding 3.0 eV and cross section magnitudes of at least a factor of 100. **Table 4.2** lists values of the E_0 obtained without including the RRKM lifetime analysis. Comparison of these values with the E_0(PSL) values where lifetime effects are included shows that the kinetic shifts are the largest for the most strongly bound systems. The kinetic shifts observed for the $(AA)H^+(18C6)$ complexes decrease in the order Gly > Ala > Lys > His > Arg. The same trend is found for the measured thresholds for loss of 18C6 from these complexes. Thus, the trend in the kinetic shifts is consistent with expectations that the observed kinetic shift should directly correlate with the density of states of the activated complex at the threshold, which increases with energy.

For the $(Gly)H^+(18C6)$ and $(Ala)H^+(18C6)$ systems, the threshold determination is influenced by the competition among reactions 4.1 and 4.2. Therefore, the cross sections for reactions 4.1 and 4.2 were analyzed competitively using the model of equation 2.4 for these systems. The results of these analyses are provided in **Table 4.2** and shown in **Figure S4** of the Supporting Information of reference 38. The $(AA)H^+$–18C6 BDEs obtained from competitive fits are larger than the values obtained from independent fits, and are in better agreement with the theoretical results for both the $(Gly)H^+(18C6)$ and $(Ala)H^+(18C6)$ systems. The difference in the thresholds obtained from competitive and independent analyses generally allows the competitive shifts to be assessed. Determined in the usual way as the difference between the threshold determined for independent versus simultaneous analysis of the competitive CID thresholds, the competitive shifts for the $(AA)H^+$–18C6 BDEs are –0.35 and –0.21 eV for the complexes to Gly and Ala, respectively. The competitive shifts for the $(18C6)H^+$–AA BDEs are –0.19 and –0.20 eV for the Gly and Ala systems, respectively. The negative competitive shifts suggest that the competition sped up both pathways rather than retarding the less favorable dissociation pathway. This clearly makes no sense. In both systems, the independent fits to the $H^+(AA)$ and $H^+(18C6)$ product cross sections require larger *n* values (and therefore lead to lower threshold energies) in order to reproduce the slowly rising cross sections. In contrast, when competition is included, the slow rising behavior is shown to be a consequence of the competition and is properly handled by the model of equation 2.4, resulting in larger thresholds and lower *n* values. Thus, reliable thermochemistry can only be extracted from the CID thresholds for these systems when competitive effects are included.

The entropy of activation, $\Delta S^{\dagger}$, is a measure of the looseness of the TS and the complexity of the system. It is determined from the molecular parameters used to model the EM and TS for dissociation as listed in **Table S1** and **S2** of the Supporting Information of reference 38. The $\Delta S^{\dagger}$(PSL) values at 1000 K are listed in **Table 4.2** and vary between 61 to 138 J/K mol across the these systems. The variation in the $\Delta S^{\dagger}$ values is found to correlate directly with the size of the system and inversely with the strength of binding. For the (Gly)H^+(18C6) and (Ala)H^+(18C6) complexes, the entropy of activation is larger for the production of H^+(AA) as compared to H^+(18C6), indicating that the formation of H^+(AA) is entropically favored over the formation of H^+(18C6).

4.5. Discussion

4.5.1. Comparison of Theory and Experiment

The measured and calculated (AA)H^+–18C6 BDEs for the complexes to Gly, Ala, Lys, His, and Arg and the (18C6)H^+–AA BDEs for the complexes to Gly and Ala at 0 K are summarized in **Table 4.1**. The agreement between theory and experiment is illustrated in **Figure 4.6**. Values for the complexes to Lys, His, and Arg include the most stable conformers involving 18C6 binding to the protonated backbone as well as 18C6 binding to the protonated side chain. The measured (AA)H^+–18C6 BDEs exhibit excellent agreement with M06 theory assuming that the ground-state conformations are accessed in the experiments for all systems except the (His)H^+(18C6) complex. The mean absolute deviation (MAD) between M06 theory and experiment is 7.7 $\pm$ 10.9 kJ/mol when all five complexes are included, and decreases to 2.8 $\pm$ 2.1 kJ/mol when the (His)H^+(18C6) complex is not included. The agreement between B3LYP theory and

the measured BDEs is less satisfactory. B3LYP theory systematically underestimates the measured $(AA)H^+$–18C6 BDEs by 39.2 ± 12.8 kJ/mol. In contrast, when the $(His)H^+$(18C6) complex is not included, the MAD becomes even worse, 43.4 ± 10.1 kJ/mol. However, the trend in the B3LYP calculated $(AA)H^+$–18C6 BDEs, Gly > Ala > Lys > His > Arg, parallels the measured values, whereas M06 theory reverses the relative affinities of His and Lys and finds Gly > Ala > His > Lys > Arg. This suggests that M06 theory may be overestimating the $(His)H^+$–18C6 BDE. If the most stable conformer involving 18C6 binding to the protonated side chain of His were accessed in the experiments rather than the calculated ground-state conformation, the MAD between M06 theory and experiment improves to 4.0 ± 3.2 kJ/mol, but degrades for B3LYP theory to 44.3 ± 9.0 kJ/mol. This suggests that an alternative explanation for the measured 18C6 affinities is that the side chain protonated species is accessed in measureable abundance in the ESI of these species. The average experimental uncertainty (AEU) for the measured $(AA)H^+$–18C6 BDEs is 7.2 ± 3.0 kJ/mol, is approximately equal to (or larger) than the MAD for M06 theory, but significantly smaller than that of B3LYP theory. Thus, M06 theory is clearly able to describe the hydrogen bonding interactions in these complexes much more accurately than B3LYP. The agreement is much better for the $(Lys)H^+$(18C6) complex when it is assumed that the ground-state side chain binding conformer is accessed in the experiments, and degrades significantly when it is assumed that an excited backbone binding conformer is accessed. In contrast, the agreement between theory and experiments for the $(Arg)H^+$(18C6) complex is excellent regardless of which structure is assumed to be accessed in the experiments.

The measured and calculated $(18C6)H^+$–AA BDEs of Gly and Ala at 0 K are also summarized in **Table 4.1**. Excellent agreement between M06 theory and the measured BDEs is also observed with a MAD of 7.9 ± 8.1 kJ/mol. Again, the agreement between B3LYP theory and the measured BDEs is less than satisfactory. B3LYP theory systematically underestimates the measured $(18C6)H^+$–AA BDEs by 40.8 ± 1.8 kJ/mol. The AEU for the measured $(18C6)H^+$–AA BDEs is 9.6 ± 1.3 kJ/mol, is larger than the MAD for M06 theory, but also significantly smaller than that of B3LYP theory. Thus, M06 theory is clearly able to describe the hydrogen bonding interactions in these complexes much more accurately than B3LYP.

4.5.2. Trends in the 18C6 Binding Affinities

The measured $(AA)H^+$–18C6 BDEs determined here follow the order: Gly > Ala > Lys > His > Arg. Based on the ground-state conformations computed for these five $(AA)H^+(18C6)$ complexes (see **Figure 4.3**), 18C6 binds to the protonated backbone amino group in the complexes to Gly, Ala, Arg, and His, whereas binding to the protonated side chain substituent is preferred for the complex to Lys. In all cases, binding occurs via three nearly ideal N–H···O hydrogen bonds. The trends in the measured $(AA)H^+$–18C6 BDEs can be understood by examining steric interactions between 18C6 and the amino acid side chains. Gly and Ala bind most strongly because they possess the smallest side chain substituents, H and CH_3, and thus experience the least steric repulsion with 18C6. Lys exhibits the highest 18C6 affinity amongst the basic AAs examined here. Theoretical calculations indicate that binding to the protonated backbone amino group is favored over binding to the protonated side chain

of His by 40.9 and 25.1 kJ/mol and of Arg by 13.9 and 5.8 kJ/mol (M06 and B3LYP theories, respectively). Thus, 18C6 binding to Lys side chains is clearly preferred over side chain binding to His and Arg. However, the present experimental results do not establish the relative preferences for side chain binding to His and Arg.

The analogous trend was also observed in **Chapter 3** for the protonated peptidomimetic base–18C6 complexes. The peptidomimetic bases that involve three N–H···O hydrogen bonds exhibit the greatest binding affinities for 18C6. The Lys mimic, n-butylamine (NBA), exhibits a higher 18C6 binding affinity than the His mimics, imidazole (Imid) and 4-methylimidazole (4MeImid), and the Arg mimic, 1-methylguanidine (MGD). The trend in the 18C6 binding affinity between His and Arg is not readily predictable from the previous study because the 18C6 binding affinity of the Arg mimic lies between that of the two His mimics, Imid and 4MeImid. The 18C6 binding affinity of the Arg mimic, MGD, is 0.2 kJ/mol lower than that of the His mimic, Imid, but is 8.2 kJ/mol higher than the other His mimic, 4MeImid.

Unfortunately the peptidomimetic bases employed in that study were not chosen in an entirely consistent fashion. 4MeImid is a better mimic for the side chain of His than Imid, but rather than 1-methylguanidine, the best mimic for Arg would be 1-propylguanidine. The inverse correlation between the strength of binding in the $(B)H^+(18C6)$ complexes with the size/polarizability of the peptidomimetic base found suggests that 1-propylguanidine would bind less strongly than MGD by ~16 kJ/mol, or ~8 kJ/mol less strongly than 4MeImid. This analysis suggests that His should bind 18C6 more strongly than Arg. While consistent with the trend measured here for His and Arg,

theory suggests that the present results characterize the relative backbone affinities of these AAs, not the side chain affinities.

4.5.3. Binding Sites of Amino Acid Side Chains

The measured 18C6 binding affinity for Lys is 11.4 kJ/mol higher than that of His, and 26.1 kJ/mol higher than that of Arg, suggesting that Lys is the preferred binding site for 18C6 complexation amongst the basic AAs in proteins or peptides. Much larger differences in the 18C6 binding preferences of the basic AAs are expected because the measured 18C6 binding affinities of His and Arg provide a measure of the binding to the protonated backbone amino group, which is calculated to be 40.9 and 13.9 kJ/mol (M06) more favorable than side chain binding, respectively. These results suggest that the Lys side chains are the preferred binding site for 18C6 complexation amongst the basic AAs in peptides and proteins. Similar results were also found in our study of protonated peptidomimetic bases–18C6 complexes in **Chapter 3**. The 18C6 binding affinity of the Lys mimic, NBA, is 48.8 kJ/mol higher than that of the His mimic, Imid and 49.0 kJ/mol higher than that of the Arg mimic, MGD. The same general trend was also reported by Julian and Beauchamp[27] when a 1:1:1 mixture of NBA, guanidine (GD), and Imid was sprayed with 18C6. They found that the (NBA)H^+(18C6) complex dominates the spectrum and is the base peak (100% relative abundance), while the relative intensity of the (GD)H^+(18C6) and (Imid)H^+(18C6) complexes is 3.5% and 1%, respectively, suggesting that H^+(NBA) binds 18C6 more strongly than H^+(GD) and H^+(Imid).

Gly and Ala exhibit higher 18C6 binding affinities than the other AAs examined here, suggesting that the N-terminal amino group could serve as an alternative binding site for 18C6 complexation. The methyl group of the Ala side chain increases the steric hindrance and constrains its complexation to 18C6. As a result, the 18C6 binding affinity of Ala is 7.4 kJ/mol lower than that of Gly. The X-ray study of Krestov and coworkers suggests that steric interactions with the N-terminal amino acid side chain could constrain its complexation with 18C6.[68] They found that the “depth of penetration” of the ammonium group into the 18C6 cavity for complexation exhibits a significant difference between diglycine and dialanine. The ammonium group in diglycine is much closer to the crown than that of dialanine during complexation. Steric interactions with the methyl side chain in proximity to the amino group in dialanine do not allow 18C6 to approach as closely and therefore bind as strongly. These and the present results suggest that the 18C6 binding affinity of the N-terminal amino group decreases as the size/polarizability of its side chain increases as a result of steric hindrance.

4.5.4. Measured $(AA)H^+$–18C6 BDEs versus Polarizability of the AAs

In our study of the binding in protonated peptidomimetic base–18C6 complexes, $(B)H^+(18C6)$, in **Chapter 3**, an inverse correlation between the 18C6 binding affinity and the polarizability of the base, B, was found. As can be seen in **Figure 4.7a**, an inverse correlation between the measured 18C6 binding affinities and the polarizability of the neutral and protonated AAs is also found. Because the binding between 18C6 and the protonated AAs involves N–H···O hydrogen bonding interactions, the strength of binding should be controlled by ion-dipole and ion-induced dipole interactions. The polarizability

of H^+(Gly) is 5.5 $Å^3$, increases to 7.2 $Å^3$ for H^+(Ala), 13.5 $Å^3$ for Lys, 13.9 $Å^3$ for His, and 16.0 Å for Arg. The more polarizable AAs bind the proton more strongly and distribute the excess charge more evenly throughout the protonated base resulting in greater stabilization. The reduced charge on the protons of the amino group leads to weaker binding to 18C6. As a result, the 18C6 binding affinity decreases from 262.4 kJ/mol for Gly to 255.0 for Ala, to 167.7 kJ/mol for Lys, to 156.3 kJ/mol for His, and to 141.1 kJ/mol for Arg. A parallel correlation between the measured BDEs and the polarizability of the neutral AAs is also obviously found, as protonation merely results in a small decrease in the polarizability.

4.5.5. Measured BDEs versus PA of the AAs

The measured 18C6 binding affinities were also shown to exhibit an inverse linear correlation with the PA of the peptidomimetic base as a result of the shorter N–H bonds and the decreased charge retained on the amino protons. An inverse correlation between the measured 18C6 binding affinity and the PA of the AAs is also observed in the systems examined here, as shown in **Figure 4.7b**. The PA of Gly is 886.5 kJ/mol, increases to 901.6 kJ/mol for Ala, 996.0 kJ/mol for Lys, 999.6 kJ/mol for His,[69] and 1051.0 kJ/mol for Arg.[70-72] Accordingly, the measured (AA)H^+–18C6 BDEs decrease from 262.4 kJ/mol for Gly, to 255.0 kJ/mol for Ala, 167.7 kJ/mol for Lys, 156.3 kJ/mol for His, and 141.1 kJ/mol for Arg. This inverse correlation can be easily understood because the AA with a higher PA binds the proton tighter and leads to weaker hydrogen-bonding interactions with 18C6, resulting in lower dissociation thresholds.

That is, the binding is strongest when the PAs of the AA and 18C6 are similar such that the proton is more equally shared.

4.5.6. Competitive Reaction Pathways

In the $(Gly)H^+(18C6)$ and $(Ala)H^+(18C6)$ complexes, $H^+(AA)$ was observed in competition with the formation of $H^+(18C6)$. The cross sections for these products are large enough to significantly influence the kinetics of dissociation for the primary CID pathway. Therefore, a loose PSL TS was used to simultaneously analyze the $H^+(AA)$ and $H^+(18C6)$ product cross sections. The results of the competitive analyses of the cross sections of the $H^+(AA)$ and $H^+(18C6)$ products exhibit excellent agreement with M06 theory indicating that the loose PSL TS model accurately describes the binding in theses systems.

4.5.7. Entropy Effects

The NIST Chemistry WebBook suggests that the PA of 18C6 is 967.0 kJ/mol, higher than the PAs of both Gly and Ala, 886.5 and 901.6 kJ/mol, respectively.[70] Therefore, $H^+(18C6)$ was observed as the lowest energy CID product in the $(Gly)H^+(18C6)$ and $(Ala)H^+(18C6)$ complexes. Interestingly, $H^+(AA)$ is also observed as a competitive CID product. This phenomenon can be understood by considering the change in entropy associated with the dissociation pathways. Entropy effects on CID results have been addressed by McLuckey and Cooks.[73-75] Wesdemiotis reported that entropy changes involved in the fragmentation of heterodimers play a critical role in determining the preferred dissociation pathway.[74] For the $(Gly)H^+(18C6)$ and

(Ala)H^+(18C6) systems, the reaction pathway that involves formation of H^+(AA) exhibits a greater increase in entropy than the H^+(18C6) pathway. In the ground-state structure of H^+(18C6), the proton is bound to one oxygen atom and is stabilized by a hydrogen bonding interaction with another oxygen atom, which results in more constrained rotational and vibration degrees of freedom in the protonated complex of 18C6. Therefore, the relatively favorable entropy change as compared to the formation of H^+(18C6) facilitates the formation of H^+(AA), making the formation of H^+(AA) as a CID product feasible even though the AA exhibits a much lower PA than 18C6. For example, in the (Gly)H^+(18C6) and (Ala)H^+(18C6) systems, elimination of H^+(AA) leads to a large gain in rotational and vibrational degrees of freedom of 18C6, resulting in a substantial increase in entropy for this competitive reaction pathway. In contrast, the formation of H^+(18C6) results in entropic loss as compared to the H^+(AA) competitive dissociation pathway. Therefore, the kinetics of dissociation are slowed down, resulting in a more significant kinetic shift as compared to the H^+(AA) pathway. As a result, despite the fact that the PAs of Gly and Ala are 80.5 kJ/mol and 65.4 kJ/mol lower than that of 18C6, respectively, the dissociation pathway that forms H^+(AA) is still observed and dominates at elevated energies.

The magnitudes of the CID product cross sections for H^+(AA) and H^+(18C6) are the result of competition between enthalpy and entropy: entropy favors the formation of H^+(AA), while enthalpy favors the formation of the species that exhibits the higher PA. In the Lys, His, and Arg containing systems, the AA exhibits a higher PA than 18C6. Therefore, enthalpy favors the formation of H^+(AA). The relatively favorable entropy change as compared to the formation of H^+(18C6) also favors the formation of H^+(AA).

As a result, H^+(AA) and its fragments were observed as the only CID products. In contrast, in the complexes involving Gly and Ala, the PA of 18C6 exceeds that of the AA. Therefore, enthalpy favors the formation of H^+(18C6). As a result, H^+(18C6) was observed as the lowest energy CID product. However, because entropy favors the formation of H^+(AA), it is observed as a competitive CID product.

4.6. Conclusions

The kinetic energy dependence for CID of five (AA)H^+(18C6) complexes, where AA = Gly, Ala, Lys, His, and Arg, with Xe is examined by guided ion beam tandem mass spectrometry techniques. Loss of the intact 18C6 ligand is observed for all five complexes, and corresponds to the most favorable process for the complexes to Lys, His, and Arg. For the complexes to Gly and Ala, loss of the intact AA is observed in competition with loss of 18C6 and corresponds to the lowest-energy pathway for these complexes. Thresholds for these CID processes are determined after consideration of the effects of the kinetic and internal energy distributions of the reactants, multiple collisions with Xe, and the lifetimes for unimolecular dissociation. The ground-state structures and theoretical estimates for the CID thresholds are determined from density functional theory calculations performed at the B3LYP/6-311+G(2d,2p)//B3LYP/6-31G* and M06/6-311+G(2d,2p)//B3LYP/6-31G* levels of theory. Excellent agreement between M06 theoretically calculated and TCID experimentally determined BDEs was found for all systems except (His)H^+(18C6), where either theory overestimates the strength of binding or excited conformers are accessed in these experiments. In

contrast, B3LYP theory systematically underestimates the strength of binding in all of these systems.

The 18C6 binding affinities determined here combined with structural information obtained from theoretical calculations provides useful insight into the processes that occur in the molecular recognition of AAs by 18C6 and implications for binding to peptides and proteins. Amongst the basic AAs, Lys exhibits the highest binding affinity for 18C6, suggesting that the side chains of Lys residues are the preferred binding sites for 18C6. Gly and Ala exhibit greater 18C6 binding affinities than Lys, suggesting that the N-terminal amino group could also serve as a favorable binding site for 18C6. The 18C6 binding affinity exhibits an inverse correlation with the polarizability and PA of the AA. Thus, the ability of the N-terminal amino group to serve as a binding site for 18C6 requires that it be protonated and accessible in the peptide or protein. Binding of 18C6 to the N-terminal amino group will be most effective for Gly and becomes increasingly less favorable as the size and proton affinity of the AA increases.

4.7. References

(1) Clackson, T.; Ultsch, M. H.; Wells, J. A.; Vos, A. M. D. *J. Mol. Biol.* **1998**, *277*, 1111.

(2) Wells, J. A. *Proc. Natl. Acad. Sci. U.S.A.* **1996**, 93, 1.

(3) Bogan, A. A.; Thorn, K. S. *J. Mol. Biol.* **1998**, *280*, 1.

(4) Clackson, T.; Wells, J. A. *Science* **1995**, *267*, 383.

(5) Matthews, B. W. *Annu. Rev. Phys. Chem.* **1976**, *27*, 493.

(6) Dyson, H. J.; Wright, P. E. *Chem. Rev.* **2004**, *104,* 3607.

(7) Palmer, A. G. *Chem. Rev.* **2004**, *104,* 3623.

(8) Mendoza, V. L.; Vachet, R. W. *Mass Spectrom. Rev.* **2009**, *28*, 785.

(9) Wales, T. E.; Engen, J. R. *Mass Spectrom. Rev*. **2006**, *25*, 158.

(10) Smith, D. L.; Deng, Y.; Zhang, Z. *J. Mass Spectrom*. **1997**, *32*, 135.

(11) Engen, J. R.; Smith, D. L. *Anal. Chem.* **2001**, *73*, 256A.

(12) Kaltashov, I. A.; Eyles, S. J*. Mass Spectrom. Rev.* **2002**, *21*, 37.

(13) Kaltashov, I. A.; Eyles, S. J*. Mass Spectrom. Rev.* **2002**, *37*, 557.

(14) Hoofnagle, A. N.; Resing, K. A.; Ahn, N. G. *Annu. Rev. Biophys. Biomol. Struct.* **2003**, *32*, 1.

(15) Eyles, S. J.; Kaltashov, I. A. *Methods* **2004***, 34*, 88.

(16) Garcia, R. A.; Pantazatos, D.; Villarreal, F. J. *Assay Drug Dev. Technol.* **2004**, *2*, 81.

(17) Sinz, A. *J. Mass Spectrom*. **2003**, *38*, 1225.

(18) Sinz, A. *Mass Spectrom. Rev.* **2006**, *25*, 663.

(19) Brunner, J. *Annu. Rev. Biochem.* **1993**, *62*, 483.

(20) Kluger, R.; Alagic, A. *Bioorg. Chem.* **2004**, *32*, 451.

(21) Melcher, K. *Curr. Prot. Pept. Sci.* **2004**, *5*, 287.

(22) Kodadek, T.; Duroux-Richard, I.; Bonnafous, J. C. *Trends Pharmacol. Sci.* **2005**, *26*, 210.

(23) Back, J. W.; de Jong, L.; Muijsers, A. O.; de Koster, C. G. *J. Mol. Biol.* **2003**, *331*, 303.

(24) Friedhoff, P. *Anal. Bioanal. Chem.* **2005**, *381*, 78.

(25) Trakselis, M. A.; Alley, S. C.; Ishmael, F. T. *Bioconjug. Chem.* **2005**, *16*, 741.

(26) Petrotchenko, E. V.; Pedersen, L. C.; Borchers, C. H.; Tomer, K. B.; Negishi, M. *FEBS Lett.* **2001**, *490*, 39.

(27) Julian, R. R.; Beauchamp, J. L. *Int. J. Mass Spectrom.* **2001**, *210/211*, 613.

(28) Julian, R. R.; Beauchamp, J. L. *J. Am. Soc. Mass Spectrom.* **2002**, *13*, 493.

(29) Julian, R. R.; Beauchamp, J. L. *J. Am. Soc. Mass Spectrom.* **2004**, *15*, 616.

(30) Julian, R. R.; Akin, M.; May, J. A.; Stoltz, B. M.; Beauchamp, J. L. *Int. J. Mass Spectrom.* **2002**, *220*, 87.

(31) Julian, R. R.; May, J. A.; Stoltz, B. M.; Beauchamp, J. L. *Int. J. Mass Spectrom.* **2003**, *228*, 851.

(32) Ly, T.; Julian, R. R. *J. Am. Soc. Mass Spectrom.* **2006**, *17*, 1209.

(33) Ly, T.; Julian, R. R. *J. Am. Soc. Mass Spectrom.* **2008**, *19*, 1663.

(34) Liu, Z.; Cheng, S.; Gallie, D. R.; Julian, R. R. *Anal. Chem.* **2008**, *80*, 3846.

(35) Ly, T.; Liu, Z.; Pujanauski, B. G.; Sarpong, R.; Julian, R. R. *Anal. Chem.* **2008**, *80*, 5059.

(36) Yeh, G. K.; Sun, Q.; Meneses, C.; Julian, R. R. *J. Am. Soc. Mass Spectrom.* **2009**, *20*, 385.

(37) Chen, Y.; Rodgers, M. T. *J. Am. Chem. Soc.*, **2012**, *134*, 2313.

(38) Chen, Y.; Rodgers, M. T. *J. Am. Chem. Soc.*, **2012**, *134*, 5863.

(39) Rodgers, M. T. *J. Phys. Chem. A* **2001**, *105*, 2374.

(40) Moison, R. M.; Armentrout, P. B. *J. Am. Soc. Mass Spectrom.* **2007**, *18*, 1124.

(41) *HyperChem Computational Chemistry Software Package*, Version 5.0; Hypercube Inc: Gainsville, FL, 1997.

(42) Frisch, M. J.; et al. *Gaussian 09*, Revision C.01; Gaussian, Inc.: Wallingford, CT, 2009. See **Chapter 2** for full reference.

(43) Becke, A. D. *J. Chem. Phys.* **1993**, *98*, 5648.

(44) Lee, C.; Yang, W.; Parr, R. G. *Phys. Rev. B* **1988**, *37*, 785.

(45) Foresman, J. B.; Frisch, Æ. *Exploring Chemistry with Electronic Structure Methods*, 2nd ed.; Gaussian: Pittsburgh, PA, 1996; p 64.

(46) Boys, S. F.; Bernardi, R. *Mol*. *Phys*. **1979**, *19*, 553.

(47) van Duijneveldt, F. B.; van Duijneveldt-van de Rijdt, J. G. C. M.; van Lenthe, J. H. *Chem. Rev.* **1994**, *94*, 1873.

(48) Yalcin, T.; Harrison, A. G. *J. Mass Spectrom*. **1996**, *31*, 1237.

(49) Iris Shek, P. Y.; Zhao, J.; Ke, Y.; Siu, K. W. M.; Hopkinson, A. C. *J. Phys. Chem. A* **2006**, *110*, 8282.

(50) Zhang, K.; Zimmerman, D. M.; Chung-Phillips, A.; Cassady, C. J. *J. Am. Chem. Soc.* **1993**, *115*, 10812.

(51) Armentrout, P. B.; Heaton, A. L.; Ye, S. J. *J. Phys. Chem. A* **2011**, *115*, 11144.

(52) Lemoff, A. S.; Bush, M. F.; O'Brien, J. T.; Williams, E. R. *J. Phys. Chem. A* **2006**, *110*, 8433.

(53) Dunbar, R. C.; Hopkinson, A. C.; Oomens, J.; Siu, C. K.; Siu, K. W. M.; Steill, J. D.; Verkerk, U. H.; Zhao, J. *J. Phys. Chem. B* **2009,** *113,* 10403.

(54) Kovacevic, B.; Rozman, M.; Klasinc, L.; Srzic, D.; Maksic, Z. B.; Yanez, M. *J. Phys. Chem. A* **2005**, *109*, 8329.

(55) Bliznyuk, A. A.; Schaefer III, H. F.; Amster, I. J. *J. Am. Chem. Soc.* **1993**, *115*, 5149.

(56) Ling, S.; Yu, W.; Huang, Z.; Lin, Z.; Haranczyk, M.; Gutowski, M. *J. Phys. Chem. A* **2006**, *110,* 12282.

(57) Forbes, M. W.; Bush, M. F.; Polfer, N. C.; Oomens, J.; Dunbar, R. C.; Williams, E. R.; Jockusch, R. A. *J. Phys. Chem. A* **2007,** *111,* 11759.

(58) Rodgers, M. T.; Ervin, K. M.; Armentrout, P. B. *J. Chem. Phys*. **1997**, *106*, 4499.

(59) Rodgers, M. T.; Armentrout, P. B. *J. Phys. Chem. A* **1997**, *101*, 1238.

(60) Rodgers, M. T.; Armentrout, P. B. *J. Phys. Chem. A* **1997**, *101*, 2614.

(61) Rodgers, M. T.; Armentrout, P. B. *Int. J. Mass Spectrom.* **1999**, *185/186/187*, 359.

(62) Rodgers, M. T.; Armentrout, P. B. *J. Phys. Chem. A* **1999**, *103*, 4955.

(63) Armentrout, P. B.; Rodgers, M. T. *J. Phys. Chem. A* **1999**, *104*, 2238.

(64) Amunugama, R.; Rodgers, M. T. *Int. J. Mass Spectrom.* **2000**, *195/196*, 439.

(65) Rodgers, M. T.; Armentrout, P. B. *J. Am. Chem. Soc.* **2000**, *122*, 8548.

(66) Rodgers, M. T.; Armentrout, P. B. *J. Chem. Phys*. **1998**, *109*, 1787.

(67) Rodgers, M. T. *J. Phys. Chem. A* **2001**, *105*, 8145.

(68) Kulikov, O. V.; Krestov, G. A. *Pure & Appl. Chem*. **1995**, *67*, 1103.

(69) Bouchoux, G.; Bussson, D. A.; Colas, C.; Sablier, M. *Eur. J. Mass Spectrom*. **2004**, *10*, 977.

(70) Hunter, E. P.; Lias, S. G. *J. Phys. Chem. Ref. Data,* **1998**, *27*, 413.

(71) Bouchoux, G.; Salpin, J. Y. *Eur. J. Mass Spectrom.* **2003**, *9*, 391.

(72) Meot-Ner, M.; Hunter, E.; Field, F. H. *J. Am. Chem. Soc.* **1979**, *101*, 686.

(73) McLuckey, S. A.; Cooks, R. G.; Fulford, J. E. *Int. J. Mass Spectrom. Ion Phys.* **1983**, *52*, 165.

(74) Cerda, B. A.; Wesdemiotis, C. *J. Am. Chem. Soc.* **1996**, *118*, 11884.

(75) Cheng, X.; Wu, Z.; Fenselau, C. *J. Am. Chem. Soc.* **1993**, *115*, 4844.

Table 4.1. Bond Dissociation Enthalpies of $(AA)H^+(18C6)$ at 0 K in kJ/mol[a]

AA	Ionic product	TCID	M06[b]			B3LYP[c]		
			D_e	D_0[d]	$D_{0,BSSE}$[d,e]	D_e	D_0[d]	$D_{0,BSSE}$[d,e]
Gly	$H^+(18C6)$	222.9 (10.6)[f]	232.8	217.5	209.3	203.8	188.5	180.9
	$H^+(Gly)$	262.4 (10.6)[f]	285.6	274.8	262.5	242.6	231.7	221.4
Ala	$H^+(18C6)$	216.5 (8.7)[f]	239.4	223.2	214.4	201.6	185.2	177.0
	$H^+(Ala)$	255.0 (9.8)[f]	276.9	264.4	251.4	223.8	211.3	200.5
Lys	$H^+(Lys)$	167.7 (7.1)	190.1	184.3	172.8	152.2	146.5	137.0
His	$H^+(His)$	156.3 (4.6)	208.5	196.4	183.3	157.2	145.1	133.9
Arg	$H^+(Arg)$	141.1 (4.0)	171.3	157.3	143.7	119.6	105.6	93.7
AEU / MAD		7.2 (3.0)[g] 9.6 (1.3)[h]		18.9 (12.2)[g] 6.0 (0.9)[h]	7.7 (10.9)[g] 7.9 (8.1)[h]		28.5(12.6)[g] 32.8 (2.2)[h]	39.2 (12.8)[g] 40.8 (1.8)[h]

[a]Present results, uncertainties are listed in parentheses. [b]Calculated at M06/6-311+G(2d,2p)//B3LYP/6-31G* level of theory. [c]Calculated at B3LYP/6-311+G(2d,2p)//B3LYP/6-31G* level of theory. [d]Including ZPE corrections with frequencies scaled 0.9804. [e]Also includes basis BSSE corrections. [f]TCID bond dissociation enthalpies obtained from competitive analyses. [g]Values for $(AA)H^+$–18C6. [h]Values for $(18C6)H^+$–AA.

Table 4.2. Fitting Parameters of Equations 4.1 and 4.2, Threshold Dissociation Energies at 0 K, and Entropies of Activation at 1000 K of (AA)H^+(18C6) Complexes[a]

AA	Ionic product	σ_o[b]	n[b]	E_0[c] (eV)	E_0 (PSL)[b] (eV)	Kinetic shift (eV)	$\Delta S^{\dagger}$(PSL) (J mol^{-1} K^{-1})
Gly[d]	H^+(18C6)	28.5 (7.4)	0.8 (0.1)	4.10 (0.14)	2.13 (0.11)	1.97	86 (4)
	H^+(Gly)	7.0 (1.4)	1.5 (0.1)	4.54 (0.07)	2.37 (0.10)	2.17	101 (4)
Gly[e]	H^+(18C6)	37.0 (11)	0.6 (0.1)	-	2.32 (0.11)	-	85 (4)
	H^+(Gly)	0.9 (0.2)	0.6 (0.1)	-	2.72 (0.12)	-	113 (4)
Ala[d]	H^+(18C6)	10.8 (2.6)	1.2 (0.2)	3.74 (0.11)	2.04 (0.09)	1.70	105 (4)
	H^+(Ala)	14.8 (2.7)	1.2 (0.1)	4.59 (0.08)	2.43 (0.09)	2.16	130 (4)
Ala[e]	H^+(18C6)	1.2 (0.3)	0.5 (0.1)	-	2.24 (0.10)	-	105 (4)
	H^+(Ala)	16.7 (5.6)	0.5 (0.1)	-	2.64 (0.10)	-	129 (4)
Lys	H^+(Lys)[f]	108.0(12)	0.8 (0.1)	3.79 (0.09)	1.98 (0.07)	1.81	122 (4)
	H^+(Lys)[g]	122.0 (12)	0.7 (0.1)	3.83 (0.09)	1.74 (0.07)	2.09	61 (4)
His	H^+(His)[f]	15.7 (1.2)	1.7 (0.1)	2.68 (0.09)	1.62 (0.05)	1.06	128 (4)
	H^+(His)[g]	16.3 (1.5)	1.7 (0.1)	2.69 (0.09)	1.61 (0.05)	1.08	114 (4)
Arg	H^+(Arg)[f]	10.1 (0.9)	1.6 (0.1)	2.37 (0.09)	1.46 (0.04)	0.91	138 (4)
	H^+(Arg)[g]	9.9 (1.0)	1.6 (0.1)	2.37 (0.09)	1.36 (0.05)	1.01	101 (4)

[a]Present results, uncertainties are listed in parentheses. [b]Average values for loose PSL transition state. [c]No RRKM analysis. [d] Values obtained for independent fits to the CID product channels. [e] Values obtained for competitive fits to the CID product channels. [f]Values obtained for fits using parameters derived from the most stable backbone binding conformation. [g]Values obtained for fits using parameters derived from the most stable side chain binding conformation.

4.8. Figure Captions

Figure 4.1. Multiply protonated model peptide showing the structures of the amino acids examined here including: Gly, Ala, Lys, His, and Arg.

Figure 4.2. Cross sections for CID of the $(Lys)H^+(18C6)$ and $(Gly)H^+(18C6)$ complexes with Xe as a function of collision energy in the center-of-mass frame (lower *x*-axis) and laboratory frame (upper *x*-axis). Data are shown for a Xe pressure of 0.2 mTorr.

Figure 4.3. B3LYP/6-31G* optimized geometries of the ground-state conformers of the $(AA)H^+(18C6)$ complexes, where AA = Gly, Ala, Lys, His, and Arg.

Figure 4.4. B3LYP/6-31G* optimized geometries of the ground-state conformers of the neutral and protonated AAs, where AA = Gly, Ala, Lys, His, and Arg.

Figure 4.5. Zero-pressure-extrapolated cross sections for CID of $(Lys)H^+(18C6)$ and $(Gly)H^+(18C6)$ complexes in the threshold region as a function of collision energy in the center-of-mass frame (lower *x*-axis) and laboratory frame (upper *x*-axis). The solid lines show the best fits to the data using equation 2.3 convoluted over the neutral and ion kinetic and internal energy distributions. The dotted lines show the model cross sections in the absence of experimental kinetic energy broadening for reactants with an internal energy corresponding to 0 K.

Figure 4.6. Theoretical versus experimental 0 K BDEs of $(AA)H^+(18C6)$ complexes. All values are taken from **Table 4.1**. Values assuming that 18C6 binds to the protonated backbone amino group are plotted as circles, while values for 18C6 binding to the protonated side chain are plotted as triangles. Theoretical values include ZPE and BSSE corrections.

Figure 4.7. Measured $(AA)H^+$–18C6 BDE at 0 K (kJ/mol) versus PBE0/6-311+G(2d,2p) calculated polarizability of AA and $H^+(AA)$, part a, versus the PA of AA, part b, where AA = Gly, Ala, Lys, His, and Arg. PAs taken from the NIST Webbook.[70]

Figure 4.1.

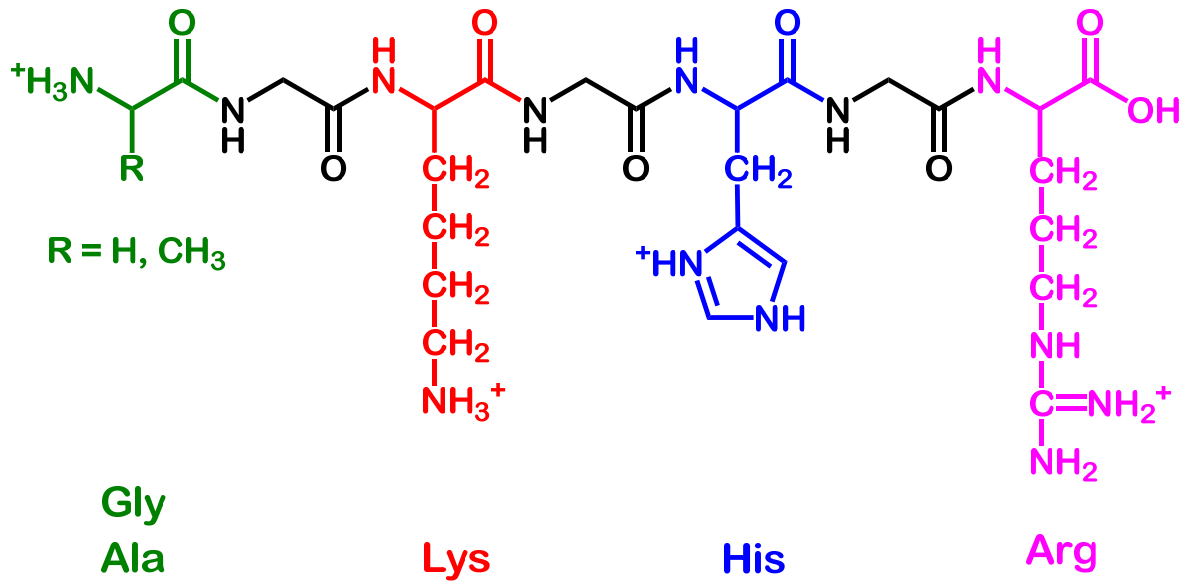
+H3N
O
N
H
R
R = H, CH3
H
N
CH2
CH2
CH2
CH2
NH3+
+HN
NH
OH
NH
C=NH2+
NH2
Gly
Ala
Lys
His
Arg

Figure 4.2.

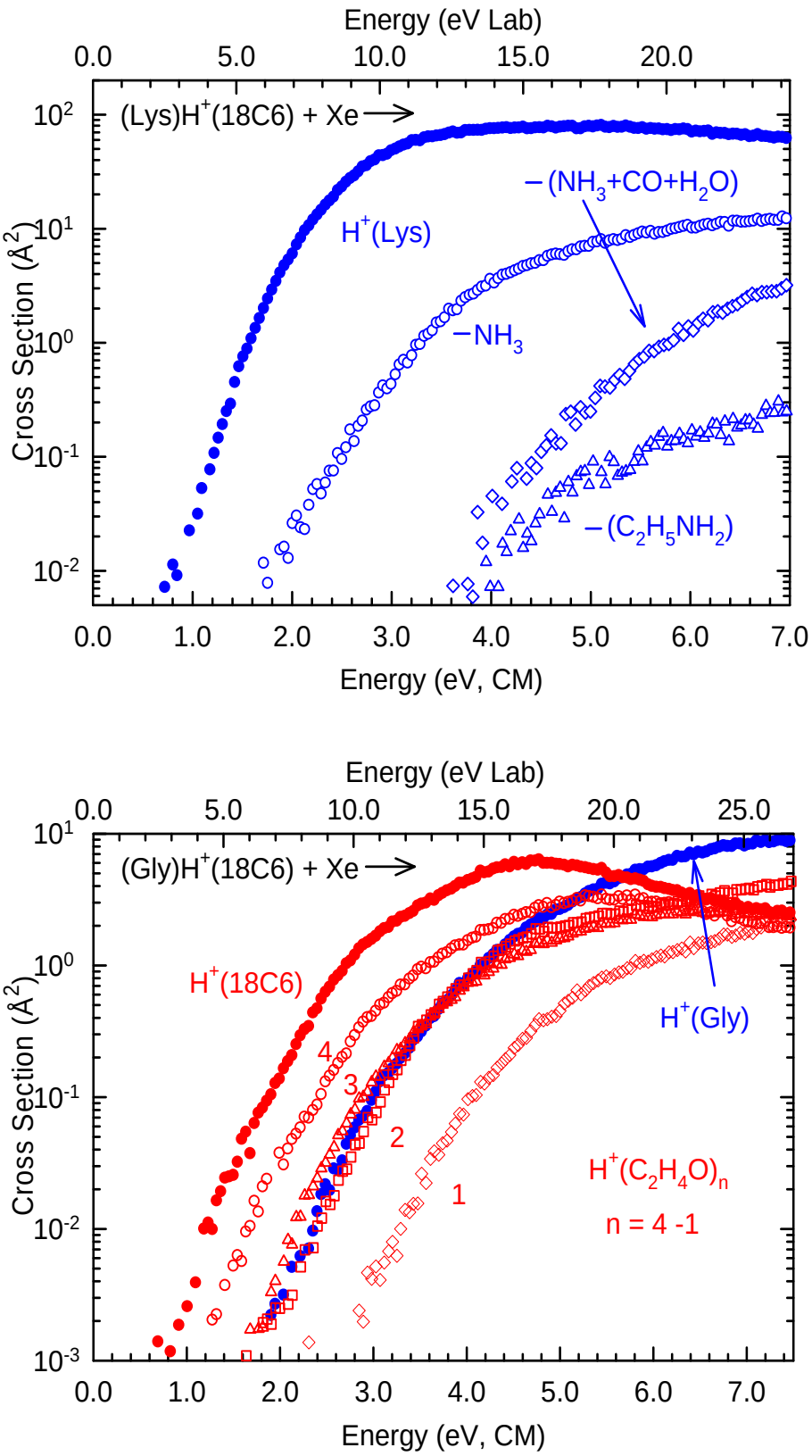
Energy (eV Lab)
0.0
5.0
10.0
15.0
20.0
(Lys)H+(18C6) + Xe
−(NH3+CO+H2O)
H+(Lys)
−NH3
−(C2H5NH2)
Cross Section (Å2)
Energy (eV, CM)
Energy (eV Lab)
0.0
5.0
10.0
15.0
20.0
25.0
(Gly)H+(18C6) + Xe
H+(18C6)
H+(Gly)
4
3
2
1
H+(C2H4O)n
n = 4 -1
Cross Section (Å2)
Energy (eV, CM)

Figure 4.3.

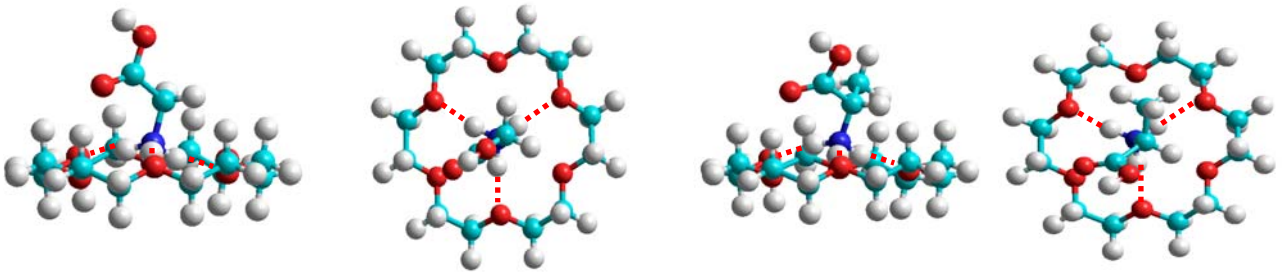

$(Gly)H^+(18C6)$ $(Ala)H^+(18C6)$

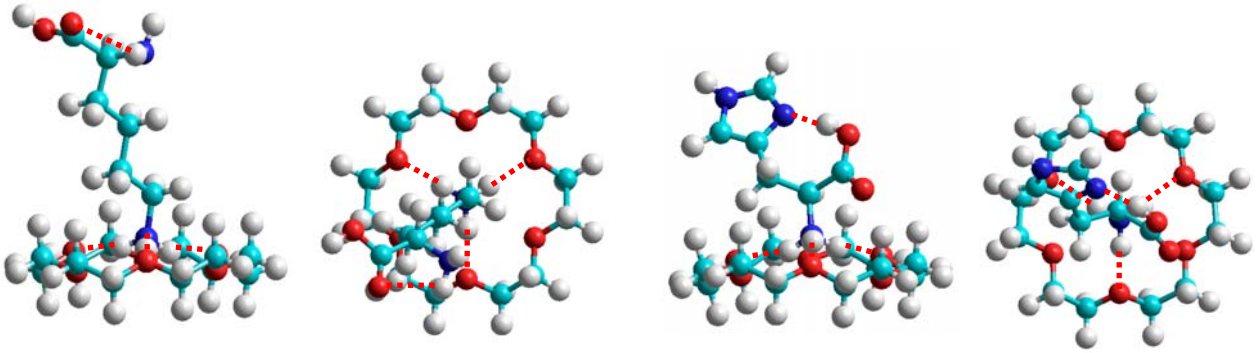

$(Lys)H^+(18C6)$ $(His)H^+(18C6)$

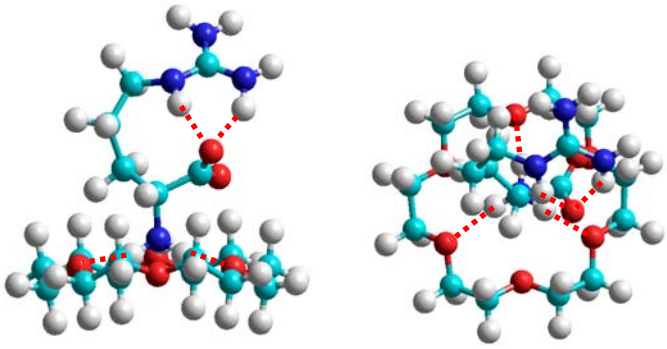

$(Arg)H^+(18C6)$

Figure 4.4.

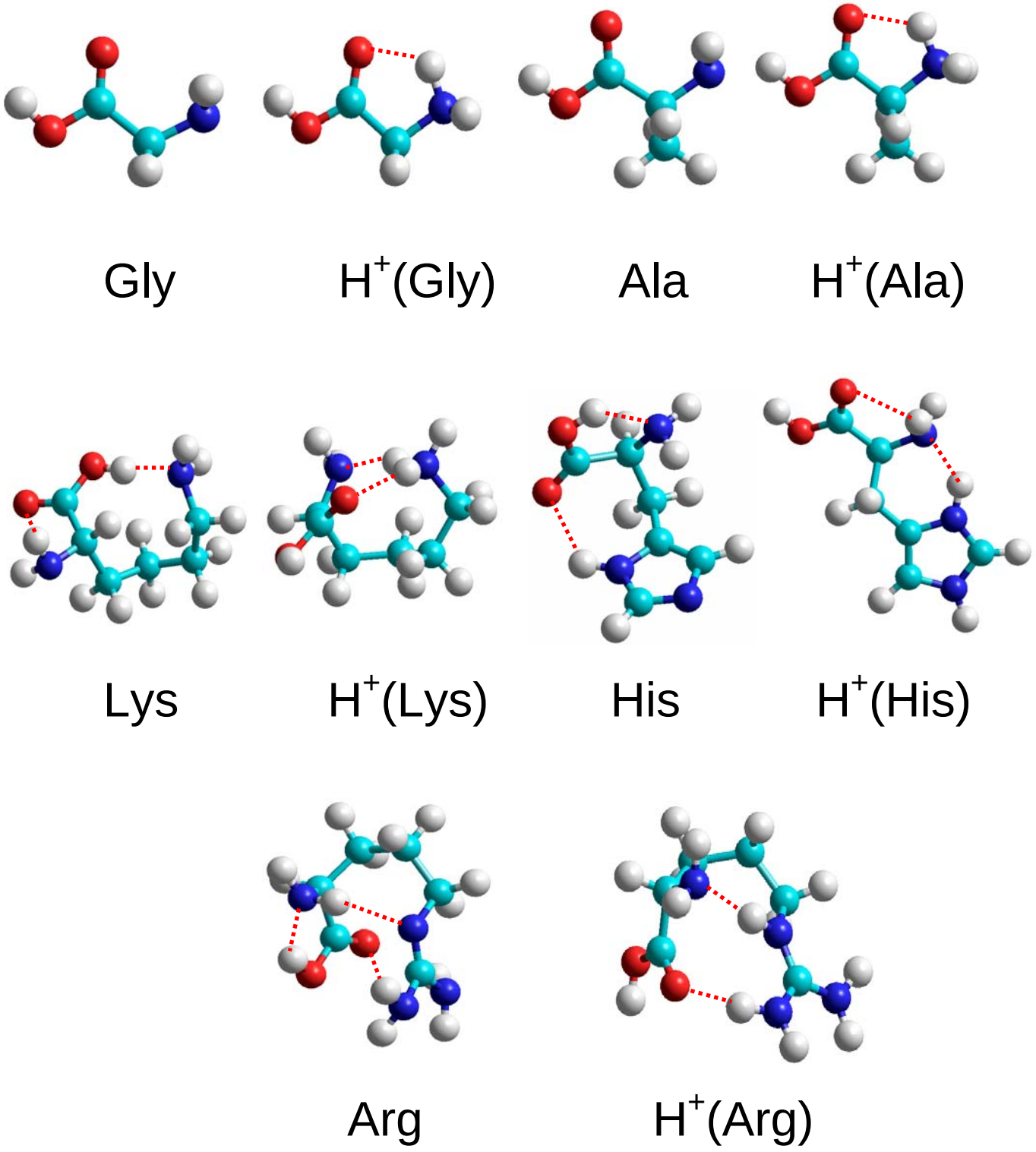

Figure 4.5.

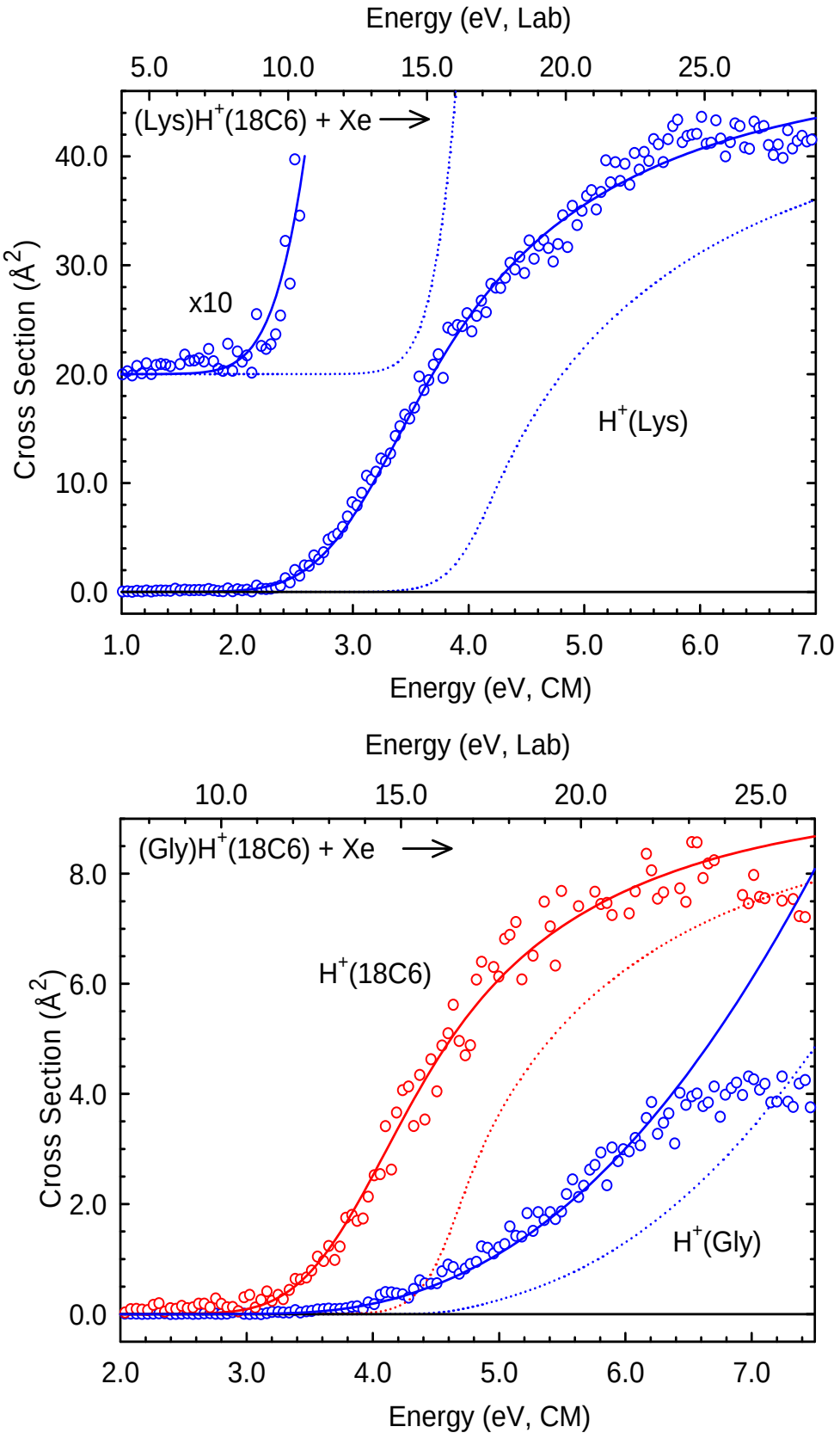
Energy (eV, Lab)
5.0
10.0
15.0
20.0
25.0
(Lys)H+(18C6) + Xe
40.0
30.0
20.0
10.0
0.0
Cross Section (Å2)
x10
H+(Lys)
1.0
2.0
3.0
4.0
5.0
6.0
7.0
Energy (eV, CM)
Energy (eV, Lab)
10.0
15.0
20.0
25.0
(Gly)H+(18C6) + Xe
8.0
6.0
4.0
2.0
0.0
Cross Section (Å2)
H+(18C6)
H+(Gly)
2.0
3.0
4.0
5.0
6.0
7.0
Energy (eV, CM)

Figure 4.6.

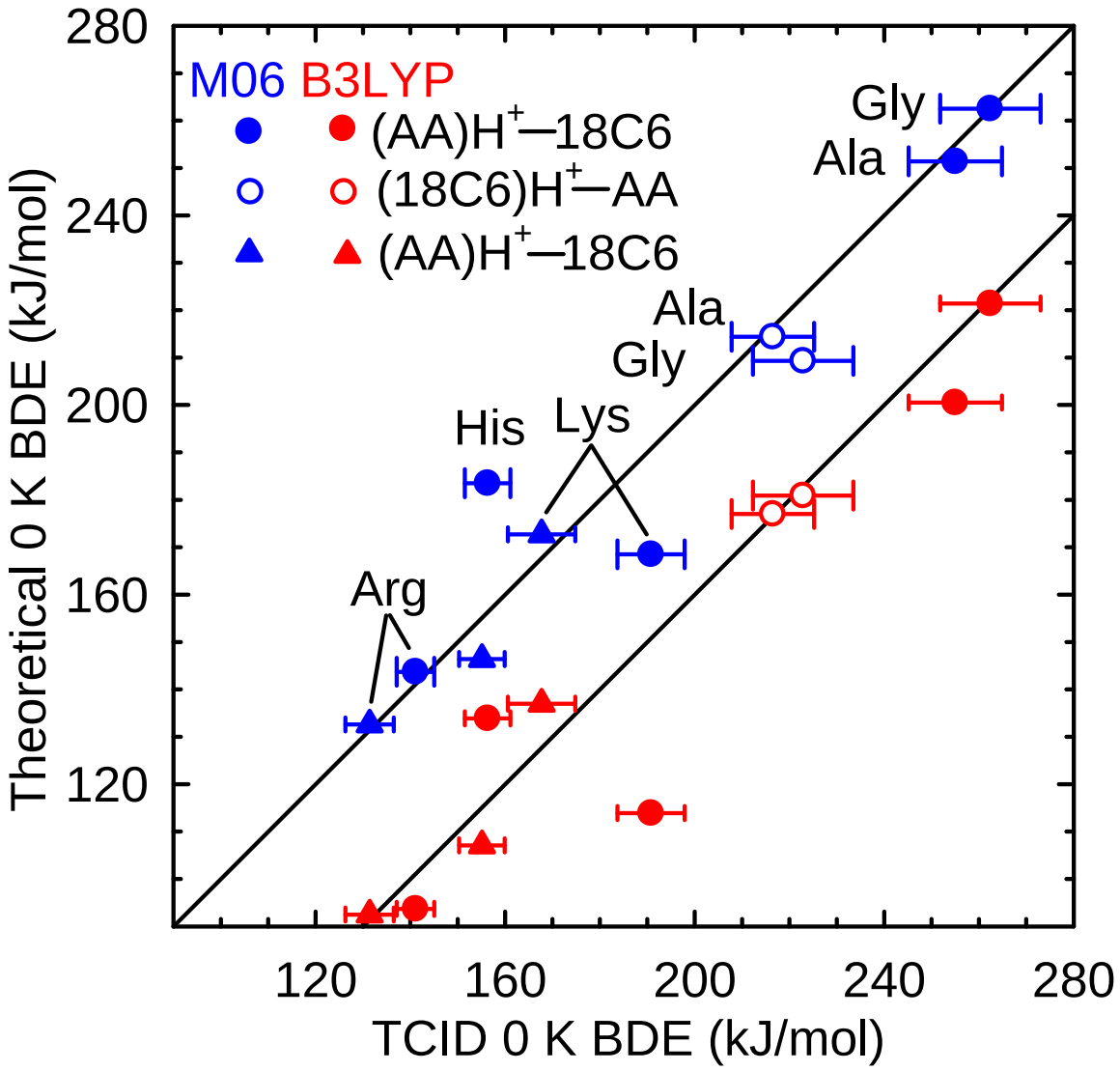
M06 B3LYP
(AA)H+–18C6
(18C6)H+–AA
(AA)H+–18C6
Gly
Ala
Ala
Gly
His
Lys
Arg
Theoretical 0 K BDE (kJ/mol)
TCID 0 K BDE (kJ/mol)
120
160
200
240
280

Figure 4.7.

(a)

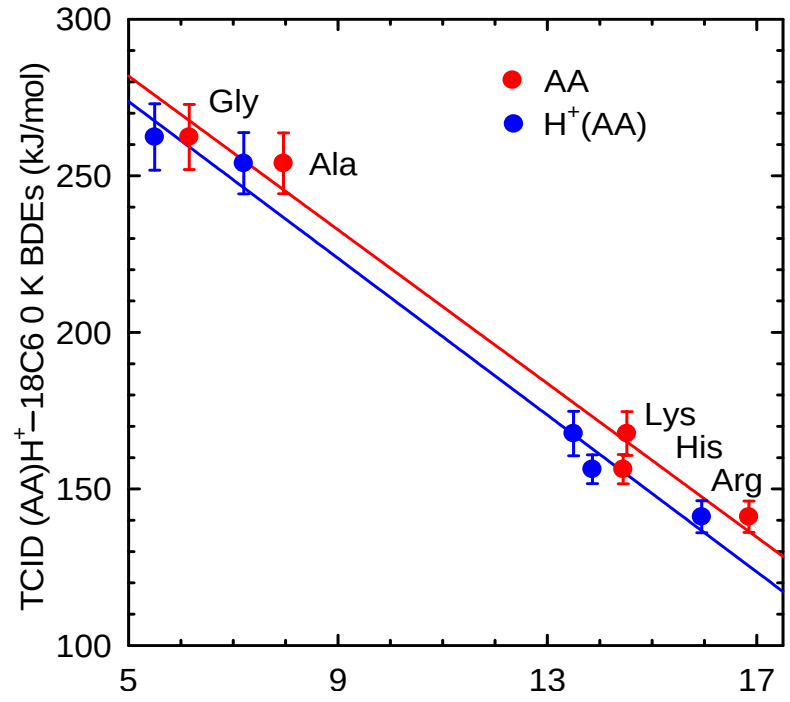
300
250
200
150
100
5
9
13
17
TCID (AA)H+–18C6 0 K BDEs (kJ/mol)
AA
H+(AA)
Gly
Ala
Lys
His
Arg

(b)

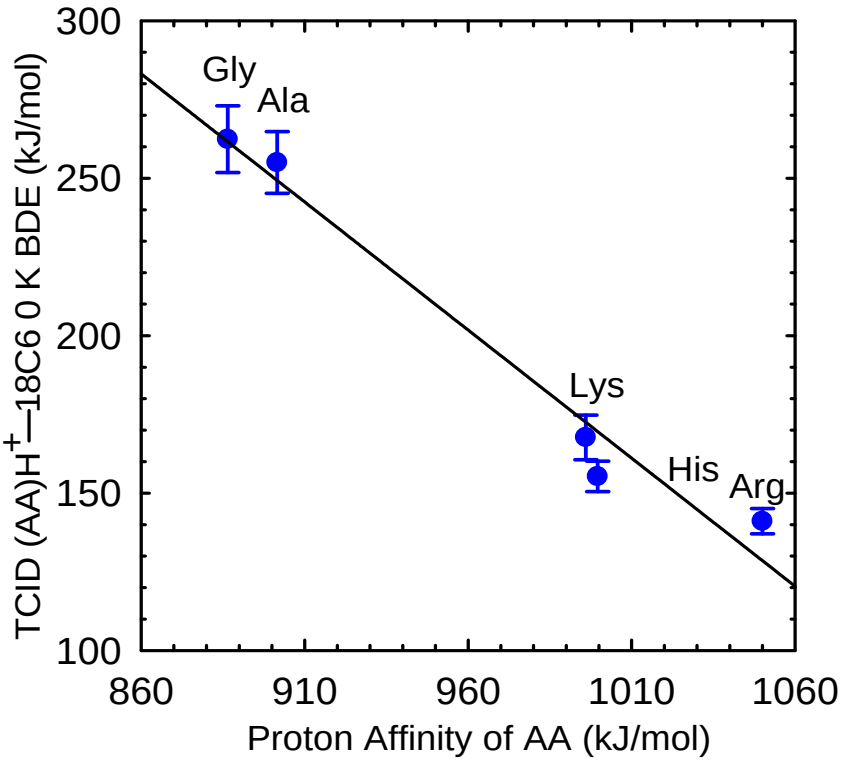
300
250
200
150
100
860
910
960
1010
1060
TCID (AA)H+–18C6 0 K BDE (kJ/mol)
Proton Affinity of AA (kJ/mol)
Gly
Ala
Lys
His
Arg

CHAPTER 5

STRUCTURAL AND ENERGETIC EFFECTS IN THE MOLECULAR RECOGNITION OF ACETYLATED AMINO ACIDS BY 18-CROWN-6

5.1. Introduction

Protein structures and protein-protein interactions play critical roles in all biological processes. As a result, studies aimed at the characterization and improved understanding of the three-dimensional structure of proteins and the intra- and intermolecular interactions that stabilize their structures and complexes abound. These studies provide information that is key to understanding functional behavior in biological systems, and will therefore become increasingly pursued as the field of proteomics matures and evolves.

A variety of MS approaches have been used to characterize protein structure and intra- and inter-molecular protein interactions such as H/D exchange[1-6] chemical cross-linking,[7-15] and selective noncovalent adduct protein probing (SNAPP).[16-25] SNAPP has been developed to exploit protein structure and folding states. The SNAPP method utilizes noncovalent recognition of amino acid residues, and in particular lysine (Lys) residues, to facilitate rapid identification and characterization of protein sequence, structure and conformational changes. In this approach, 18C6 was selected as the protein side chain tag because of its enzyme-like specificity for Lys side chains. The extent of 18C6 adduction to Lys side chains is determined by the number of accessible Lys side chains, i.e., those that are not involved in intramolecular interactions such as hydrogen bonds or salt bridges. Intramolecular interactions generally prevent the attachment of 18C6 and are directly correlated to the structure of the protein. Therefore,

the number of 18C6 ligands that bind is also directly correlated to the protein structure. Because the number of 18C6 ligands that bind to a protein can be easily determined by MS due to the large mass shift (264 Da per 18C6 ligand bound), protein structure and folding under varying solution conditions can be extrapolated.

Although the protonated side chain of Lys has been shown to be the primary binding site for 18C6 complexation, the protonated side chains of His, Arg, and the N-terminal amino group may also compete for 18C6. Therefore, accurate thermochemical information regarding the binding between 18C6 and the basic amino acids may provide insight into the selectivity of the complexation process. However, very limited thermochemical data has thus far been reported in the literature.

We examined the interactions between 18C6 and a series of protonated peptidomimetic bases that serve as mimics of the N-terminal amino group and the side chains of the basic amino acids in **Chapter 3**, as well as five naturally occurring amino acids in **Chapter 4**. Theoretical calculations suggest that in the complexes to His and Arg, the preferred binding site for 18C6 complexation is backbone amino group, instead of the side chain. Therefore, the trend in the 18C6 binding affinities of the side chains of Lys, His, and Arg have yet to be determined. In addition, intramolecular or intermolecular interactions can prevent complexation of 18C6 to the side chains of AA residues in peptides and proteins. Due to the conformation flexibility of peptides and proteins, the backbone may also be involved in the complexation between 18C6 and the protonated AA residue side chains. Therefore, acetylated AAs represent improved models for noncovalent interactions between 18C6 and peptides or proteins.

In order to investigate the 18C6 binding affinities of the side chains of AAs, absolute 18C6 affinities of four acetylated AAs are determined here using guided ion beam tandem mass spectrometry techniques. The acetylated AAs examined here include: N_α–AcLys, N_ε–AcLys, N_α–AcArg, and N_α–AcHis, as shown schematically in the model peptide of **Figure 5.1**. The energy-dependent cross sections for collision-induced dissociation (CID) of the (AcAA)H^+(18C6) complexes are analyzed using methods previously developed that explicitly include the effects of the kinetic and internal energy distributions of the reactants, multiple ion-neutral collisions, and the kinetics of unimolecular dissociation. Absolute (AcAA)H^+–18C6 bond dissociation energies (BDEs) for four (AcAA)H^+(18C6) complexes are derived and compared to theoretical estimates for these BDEs computed here.[26] The effects of acetylation on the 18C6 binding affinities of the AAs are assessed by comparing present results to those for the AAs previously investigated.[27]

5.2. Collision-Induced Dissociation Experiments

Cross sections for CID of four protonated acetylated amino acid-18C6 complexes, (AcAA)H^+(18C6) with Xe, where AcAA = N_α–AcLys, N_ε–AcLys, N_α–AcArg, and N_α–AcHis are measured using a guided ion beam tandem mass spectrometer that has been described in detail previously.[28] The (AcAA)H^+(18C6) complexes are generated by electrospray ionization (ESI).[29] The ions are effusively sampled from the source region, focused, accelerated, and focused into a magnetic sector momentum analyzer for mass analysis. Mass-selected ions are decelerated to a desired kinetic energy and focused into an octopole ion guide. The octopole passes through a static

gas cell containing Xe at low pressure (~0.05–0.20 mTorr) to ensure that multiple ion-neutral collisions are improbable. Products and unreacted beam ions drift to the end of the octopole, are focused into a quadrupole mass filter for mass analysis, and are subsequently detected with a secondary electron scintillation detector and standard pulse counting techniques. Details of the experimental procedures and thermochemical analysis of experimental data are given in **Chapter 2**.

5.3. Theoretical Calculations

A simulated annealing procedure using HyperChem[30] and the AMBER force field was used to generate starting structures of neutral 18C6 and the protonated AcAAs for higher level optimization. All structures determined within 30 kJ/mol of the lowest-energy structure were optimized using the Gaussian 09 [31] suites of programs.

Geometry optimizations for neutral 18C6 and the protonated AcAAs as well as the proton bound (AcAA)H^+(18C6) complexes were performed using density functional theory at the B3LYP/6-31G* level.[32,33] Vibrational analyses of the geometry-optimized structures were performed to determine the vibrational frequencies of the optimized species for use in modeling of the CID data. The frequencies calculated were scaled by a factor of 0.9804.[34] Single-point energy calculations were performed at the B3LYP/6-311+G(2d,2p) and M06/6-311+G(2d,2p) levels of theory using the B3LYP/6-31G* optimized geometries. To obtain accurate energetics, zero-point energy (ZPE) and basis set super position error (BSSE) corrections are included in the computed BDEs using the counterpoise approach.[35, 36] The polarizability of the neutral and protonated AAs are calculated at the Perdew, Burke, and Ernzerhof (PBE1PBE, also known as

PBE0) level of theory, with the 6-311+G(2d,2p) basis set. Details of the theoretical calculations are given in **Chapter 2**.

5.4. Results

5.4.1. Cross Sections for Collision-Induced Dissociation

Experimental cross sections were obtained for the interaction of Xe with four $(AcAA)H^+(18C6)$ complexes, where AcAA = N_α–AcLys, N_ε–AcLys, N_α–AcArg, and N_α–AcHis. **Figure 5.2** shows representative data for the $(N_\alpha\text{–AcLys})H^+(18C6)$ complex. Experimental cross sections for the other $(AcAA)H^+(18C6)$ complexes are shown in **Figure S1** of the Supplemental Information of reference 26. The most favorable process for all complexes is loss of the intact 18C6 ligand in the CID reactions 5.1.

$$(AcAA)H^+(18C6) + Xe \rightarrow H^+(AcAA) + 18C6 + Xe \qquad (5.1)$$

At elevated energies, products arising from the sequential dissociation of the primary $H^+(AcAA)$ CID product were also observed for all complexes as shown in **Figure 5.2** and **Figure S1** of the Supplementary Information of reference 26. Because the fragmentation of $H^+(AcAA)$ is not of specific interest here, these minor sequential fragmentation pathways will not be discussed further.

5.4.2. Theoretical Results

The B3LYP/6-31G* ground-state structures of the $(AcAA)H^+(18C6)$ complexes are shown in **Figure 5.3**. Structures and M06/6-311+G(2d,2p) relative energies of several representative low-energy conformations of the $(AcAA)H^+(18C6)$ complexes computed here are shown in **Figure S2** of the Supplementary Information of reference

26. The ground-state structures of neutral and protonated 18C6 are shown in **Figure 3.4** and in **Chapter 3**. Results for the stable low-energy conformations of neutral and protonated 18C6 and the AcAAs are shown in **Figure S3** of the Supplementary Information of reference 26. The $(AcAA)H^+$–18C6 BDEs at 0 K calculated at the M06/6-311+G(2d,2p)//B3LYP/6-31G* and B3LYP/6-311+G(2d,2p)//B3LYP/6-31G* levels of theory including ZPE and BSSE corrections, are listed in **Table 5.1**. Comparison of the measured and calculated values suggests that the M06 results are most reliable. Therefore, the following discussion will focus on energetics calculated at the M06/6-311+G(2d,2p) level of theory using the B3LYP/6-31G* optimized structures unless otherwise specified.

5.4.2.1. Acetylated Amino Acids

The B3LYP/6-31G* optimized geometries and the M06/6-311+G(2d,2p) relative stabilities of the ground-state and stable low-energy conformations of the neutral and protonated AcAAs are provided in **Figure S2** of the Supplementary Information of reference 26. The preferred site of protonation for N_α–AcLys, N_α–AcArg, and N_α–AcHis is at the side chain substituent. In contrast, protonation of the N–terminal amino group along the backbone is preferred for N_ε–AcLys. The ground-state and low-energy structures of the neutral and protonated AcAAs are stabilized by intramolecular hydrogen bonds between the backbone amino, carboxyl, and acetyl moieties and the side chain substituent.

The ground-state structure of N_α–AcLys is stabilized by two intramolecular hydrogen bonds, one between the backbone carboxyl hydrogen and the side chain

amino nitrogen atoms, the other between the backbone carbonyl oxygen and amino hydrogen atoms. Another conformer that lies 1.5 kJ/mol higher in energy than the ground-state structure is also found that is stabilized by an intramolecular hydrogen bond between the backbone carboxyl hydrogen and the acetyl oxygen atoms. A third conformer lying 5.4 kJ/mol higher in energy than the ground-sate conformer is also found that exhibits an extended conformation with no intramolecular hydrogen bond stabilization.

The ground-state structure of $H^+(N_\alpha$–AcLys) is also stabilized by two intramolecular hydrogen bonds, one between the backbone carbonyl oxygen and amino hydrogen atoms, and the other between the acetyl oxygen and one of the protonated side chain amino hydrogen atoms. A conformer that lies 2.0 kJ/mol higher in energy than the ground-sate conformer also possesses two intramolecular hydrogen bonds, one between the backbone carbonyl oxygen and one of the protonated side chain amino hydrogen atoms, the other between the acetyl oxygen and one of the protonated side chain amino hydrogen atoms. A stable conformer that lies 39.1 kJ/mol higher in energy than the ground-state conformer is also found. This conformer is again stabilized by two intramolecular hydrogen bonds, one between the backbone carbonyl oxygen and one of the pronated side chain amino hydrogen atoms, the other between the backbone amino nitrogen and one of the protonated side chain amino hydrogen atoms.

The ground-state structure of N_ε–AcLys is stabilized by an intramolecular hydrogen bond between the amino hydrogen atom of the acetylated side chain and the backbone amino nitrogen atom. A low-energy conformer that possesses two intramolecular hydrogen bonds, one between a backbone amino hydrogen and the

acetyl oxygen atoms, and the other between a backbone amino hydrogen and the backbone carbonyl oxygen atoms, lies 2.0 kJ/mol higher in energy than the ground-state conformer. A third low-energy conformer that possesses an intramolecular hydrogen bond between the acetyl oxygen and another of the backbone amino hydrogen atoms lies 3.4 kJ/mol higher in energy than the ground-state conformer.

The ground-state structure of $H^+(N_\varepsilon$–AcLys) is also stabilized by two intramolecular hydrogen bonds, one between the backbone carbonyl oxygen and an amino hydrogen atoms of the protonated backbone, the other between the side chain acetyl oxygen atom and an amino hydrogen atom of the protonated backbone. The first-excited conformer, which lies 9.2 kJ/mol higher in energy than the ground-state conformer, possesses two intramolecular hydrogen bonds, one between a backbone amino hydrogen and the acetyl oxygen atoms, and the other between another of the backbone amino hydrogen atoms and the backbone carbonyl oxygen atom. The second-excited conformer found lies 9.3 kJ/mol higher in energy than the ground-state conformer and also possesses two intramolecular hydrogen bonds, one between a backbone amino hydrogen and the acetyl oxygen atoms, and the other between another of the backbone amino hydrogen atoms and the hydroxyl oxygen atom.

The ground-state structure of N_α–AcArg is stabilized by two intramolecular hydrogen bonds, one between the acetyl oxygen atom and one of the side chain primary amino hydrogen atoms, and the other between the backbone amino hydrogen and carbonyl oxygen atoms. The first-excited conformer lies 6.8 kJ/mol higher in energy than the ground-state conformer and possesses three intramolecular hydrogen bonds, another between the backbone hydroxyl hydrogen and amino nitrogen atoms, another

between the backbone amino hydrogen and the side chain imine nitrogen atoms, and the third between a side chain amino hydrogen and the backbone carbonyl oxygen atoms. The second-excited conformer lies 7.0 kJ/mol higher in energy than the ground-state conformer, and is stabilized by two intramolecular hydrogen bonds, one between the backbone amino hydrogen and carbonyl oxygen atoms, and the other between the acetyl oxygen and a side chain amino hydrogen atom.

The ground-state structure of $H^+(N_\alpha$–AcArg) exhibits a similar conformation to that of neutral N_α–AcArg that is also stabilized by the same two intramolecular hydrogen bonds, one between the acetylcarbonyl oxygen and a side chain primary amino hydrogen atom, and the other between the backbone amino hydrogen and carbonyl oxygen atoms. The first-excited conformer is very similar to the ground-state conformer except for the orientation of the alkyl side chain, and lies 8.3 kJ/mol higher in energy. The second-excited conformer lies 9.6 kJ/mol higher in energy than the ground-state conformer and possesses two intramolecular hydrogen bonds, one between the backbone amino hydrogen and hydroxyl oxygen atoms, and the other between the acetyl oxygen and one of the side chain amino hydrogen atoms.

The ground-state structure of N_α–AcHis is stabilized by two intramolecular hydrogen bonds, one between the side chain amino hydrogen and the acetyl oxygen atoms, and the other between the backbone amino hydrogen and carbonyl oxygen atoms. The first-excited conformer exhibits a similar conformation except for the orientation of the backbone carboxyl group. This conformer lies 13.5 kJ/mol higher in energy than the ground-state conformer and possesses two intramolecular hydrogen bonds, one between the side chain amino hydrogen and acetyl oxygen atoms, and the

other between the backbone amino hydrogen and the hydroxyl oxygen atoms. The second-excited conformer lies 18.0 kJ/mol higher in energy than the ground-state conformer, and is stabilized by a single intramolecular hydrogen bond between the side chain amino hydrogen and the backbone carbonyl oxygen atoms.

The ground-state structure of $H^+(N_\alpha$–AcHis) exhibits a similar conformation to that of N_α–AcHis except the side chain is now protonated. The ground-state structure of $H^+(N_\alpha$–AcHis) is also stabilized by two intramolecular hydrogen bonds, one between the side chain amino hydrogen and the acetyl oxygen atoms, and the other between the backbone amino hydrogen and the carbonyl oxygen atoms. The first-excited conformer lies 6.0 kJ/mol higher in energy than the ground-state conformer, and exhibits a conformation similar to the first-excited state conformer of N_α–AcHis except the side chain is again protonated. The second-excited conformer lies 23.7 kJ/mol higher in energy than the ground-state conformer and is stabilized by two intramolecular hydrogen bonds, one between the side chain amino hydrogen and the backbone carbonyl oxygen atoms, and the other between the backbone hydroxyl hydrogen and the acetyl oxygen atoms.

5.4.2.2. (AcAA)H^+(18C6) Complexes

The B3LYP/6-31G* optimized geometries of the ground-state conformations of the (AcAA)H^+(18C6) complexes are shown in **Figure 5.3**. 18C6 binds to the protonated side chain substituent in the complexes to N_α–AcLys, N_α–AcArg, and N_α–AcHis, and to the protonated backbone amino group in the complex to N_ε–AcLys. In all cases, binding occurs via N–H···O hydrogen bonds. The conformation of 18C6 in all of these

complexes bears great similarity to the D_{3d} excited conformer of the neutral crown with a nucleophilic cavity in the center for interaction with the protonated AcAA.

In the ground-state conformation of the $(N_\alpha$–AcLys$)H^+$(18C6) complex (**Figure 5.3**), $H^+(N_\alpha$–AcLys) exhibits an extended conformation, resulting in the protonated side chain amino group interacting with 18C6 via three nearly ideal (i.e., nearly linear) N–H···O hydrogen bonds. Several low-energy excited conformers are found that involve the same N–H···O hydrogen bonding interactions between the protonated side chain amino group and the oxygen atoms of the crown, but differ in the orientation of the amino acid. A stable conformer that lies 18.0 kJ/mol higher in energy than the ground-state conformer was also found. In this conformer, $H^+(N_\alpha$–AcLys) exhibits an extended conformation, with the backbone and side chain nearly perpendicular, as shown in **Figure S3** of the Supplementary Information of reference 26. Another stable conformer that lies 34.0 kJ/mol higher in energy than the ground-state conformer is stabilized by an intramolecular hydrogen bond between the backbone carboxyl hydrogen and amino nitrogen atoms.

In the ground-state structure of the $(N_\varepsilon$–AcLys$)H^+$(18C6) complex (**Figure 5.3**), $H^+(N_\varepsilon$–AcLys) exhibits an extended conformation, resulting in the protonated backbone amino group interacting with 18C6 via three nearly ideal N–H···O hydrogen bonds. A low-energy conformer that lies 4.7 kJ/mol higher in energy than the ground-state structure is also found (**Figure 3S** of reference 26), where the binding interaction remains the same, but the conformation of $H^+(N_\varepsilon$–AcLys) is stabilized by an intramolecular hydrogen bond between the backbone carboxyl hydrogen and the acetyl oxygen atoms. Another stable conformer that lies 6.8 kJ/mol higher in energy than the

ground-state structure is also found. In this conformer, the binding interaction again remains the same, but the $H^+(N_\varepsilon$–AcLys) moiety possesses two intramolecular hydrogen bonds, one between the backbone carboxyl hydrogen and the acetyl oxygen atoms, and another between the side chain amino hydrogen and the backbone carbonyl oxygen atoms.

In the ground-state conformation of the $(N_\alpha$–AcArg)H^+(18C6) complex (**Figure 5.3**), the conformation of $H^+(N_\alpha$–AcArg) is remarkably similar to the conformation of the isolated ground-state species in which the acetyl oxygen atom forms an intramolecular hydrogen bond with one of the protonated side chain amino hydrogen atoms. The protonated side chain interacts with the O1, O2, O4, and O5 atoms of 18C6 via four N–H···O hydrogen bonds. Another stable conformer is found that lies 9.3 kJ/mol higher in energy as shown in **Figure S3** of the Supplementary Information of reference 26. In this excited conformer, $H^+(N_\alpha$–AcArg) also exhibits a similar conformation to the isolated ground-state species, but interacts with the O1, O2, and O4 atoms of 18C6 via four N–H···O hydrogen bonds. Another stable conformer with an extended conformation of $H^+(N_\alpha$–AcArg) such that it does not possess an intramolecular hydrogen bond was also found that lies 44.3 kJ/mol higher in energy than the ground-state conformer.

In the ground-state structure of the $(N_\alpha$–AcHis)H^+(18C6) complex (**Figure 3S** of reference 26), the conformation of $H^+(N_\alpha$–AcHis) is remarkably similar to the conformation of the isolated ground-state species in which the protonated side chain amino group forms a hydrogen bond with the backbone acetyl oxygen atom. In this conformer, $H^+(N_\alpha$–AcHis) binds to the O1 and O4 atoms of a distorted D_{3d} conformer of 18C6 via two N–H···O hydrogen bonds. Another low-energy conformer that lies 1.6

kJ/mol higher in energy is found as shown in **Figure S3** of the Supplementary Information of reference 26. This conformer is very similar to the ground-state conformer except that 18C6 folds slightly towards the protonated N_α–AcHis moiety. Another stable conformer that lies 7.7 kJ/mol higher in energy than the ground-state conformer is also found. This conformer differs from the first excited conformer only in the orientation of the carboxyl group.

5.4.3. Threshold Analysis

The model of equation 2.3 was used to analyze the thresholds for reactions 5.1 in four $(AcAA)H^+(18C6)$ complexes. The results of these analyses are provided in **Table 5.2**. Representative results are shown in **Figure 5.4** for the $(N_\alpha–AcLys)H^+(18C6)$ complex. The analyses for the other three $(AcAA)H^+(18C6)$ complexes are shown in **Figure S4** of the Supplemental Information of reference 26. In all cases, the experimental cross sections for reactions 5.1 are accurately reproduced using a loose PSL TS model.[37] Previous work has shown that this model provides the most accurate assessment of the kinetics shifts for CID process for electrostatically bound ion-molecule complexes.[38-46] Good reproduction of the data is obtained over energy ranges exceeding 3.0 eV and cross section magnitudes of at least a factor of 100. **Table 5.2** also lists E_0 values obtained without including the RRKM lifetime analysis. Comparison of these values with the E_0(PSL) values shows that the kinetic shifts are the largest for the most strongly bound systems, and decrease in the order N_α–AcLys > N_ε–AcLys > N_α–AcArg > N_α–AcHis. This trend in the magnitudes of the kinetic shifts is consistent

with expectations that the observed kinetic shifts should directly correlate with the density of states of the activated complex at the threshold, which increases with energy.

The entropy of activation, $\Delta S^{\dagger}$, is a measure of the looseness of the TS and the complexity of the system. It is determined from the molecular parameters used to model the EM and TS for dissociation as listed in **Table S1** and **S2** of reference 26. The $\Delta S^{\dagger}$(PSL) values at 1000 K are listed in **Table 5.2** and vary between 78 to 120 J/K mol across the these systems. These values are consistent with the noncovalent nature of the binding in these systems. The $\Delta S^{\dagger}$(PSL) values are the smallest for the complex to N_{α}–AcHis, 78 J/K mol, where only two hydrogen bonds are cleaved in the CID process, and larger for the remaining complexes 112 to 120 J/K mol, where three or four hydrogen bonds are broken.

5.5. Discussion

5.5.1. Comparison of Theory and Experiment

The measured and calculated 18C6 binding affinities of N_{α}–AcLys, N_{ε}–AcLys, N_{α}–AcArg, and N_{α}–AcHis at 0 K are summarized in **Table 5.1**. The agreement between M06/6-311+G(2d,2p)//B3LYP/6-31G* theory and experiments is illustrated in **Figure 5.5**. For all systems, M06 theory systematically overestimates the measured (AcAA)H^{+}–18C6 BDEs with a mean absolute deviation (MAD) of 8.9 ± 3.3 kJ/mol. The agreement between B3LYP theory and the measured BDEs is less satisfactory. B3LYP theory systematically underestimates the measured (AcAA)H^{+}–18C6 BDEs by 38.4 ± 11.1 kJ/mol. The average experimental uncertainty (AEU) in the measured (AcAA)H^{+}–18C6 BDEs is 6.0 ± 1.2 kJ/mol, somewhat smaller than the MAD for M06 theory, and

significantly smaller than the MAD for B3LYP theory. Clearly, M06 theory does a much better job of describing the binding in these systems.

5.5.2. Trends in the 18C6 Binding Affinities

The measured $(AcAA)H^+$–18C6 BDEs determined here follow the order: N_α–AcLys > N_ε–AcLys > N_α–AcArg > N_α–AcHis. The interactions of 18C6 with protonated N_α–AcLys and N_ε–AcLys involve three nearly ideal linear N–H···O hydrogen bonds, which results in the strongest noncovalent interactions between 18C6 and the AcAAs investigated here. 18C6 interacts with protonated N_α–AcArg via four less than ideal hydrogen bonds with four oxygen atoms of the crown (O1, O2, O4, and O5) to form a somewhat less strongly bound complex. Protonated N_α–AcHis interacts with 18C6 via two nonideal hydrogen bonds to alternate oxygen atoms (O1 and O4) to form a low symmetry conformer, and exhibits the weakest binding to 18C6. These trends in the $(AcAA)H^+$–18C6 BDEs confirm that the geometry even more importantly than the number of hydrogen bonding interactions, is critical to the strong binding necessary for molecular recognition.

The analogous trend was also observed in our previous study of protonated peptidomimetic base–18C6 complexes in **Chapter 3**. The peptidomimetic bases (B) that bind to 18C6 via three N–H···O hydrogen bonds exhibit the greatest binding affinity for 18C6. The Lys mimic, n-butylamine (NBA), exhibits a higher 18C6 binding affinity than the His mimics, imidazole (IMID) and 4-methylimidazole (4MeIMID), and the Arg mimic, 1-methylguanidine (MGD). The trend in the 18C6 binding affinity between His and Arg is not readily predictable from the peptidomimetic base study because the bases

examined did not mimic the side chain substituents of Lys, His, and Arg in a completely systematic fashion, and the 18C6 binding affinity of the Arg mimic, MGD, is 0.2 kJ/mol lower than His mimic, Imid, but is 8.2 kJ/mol higher than the other His mimic, 4MeImid. The 18C6 binding affinities of Lys, Arg and His were examined in **Chapter 4**. Theoretical calculations suggest that protonated Lys side chain is the preferred binding site for 18C6 complexation. In contrast, the protonated backbone amino group of His and Arg is the preferred binding site for 18C6 complexation. Therefore, the relative 18C6 binding affinities of the side chains of Lys, His, and Arg are not yet determined. However, it is very clear that the 18C6 binding affinity of the side chain of Lys exceeds those of His and Arg.

5.5.3. Amino Acid Side Chain Binding Sites

The 18C6 binding affinity of protonated N_{α}–AcLys is 7.5 kJ/mol higher than that of protonated N_{ε}–AcLys, 42.6 kJ/mol higher than that of protonated N_{α}–AcArg, and 50.0 kJ/mol higher than that of N_{α}–AcHis, indicating that the Lys side chain is the preferred binding site for 18C6 complexation amongst the basic AAs in proteins or peptides. Similar results were also found in our previous study of protonated peptidomimetic bases with 18C6 complexes in **Chapter 3**. The 18C6 binding affinity of the protonated form of the Lys mimic, NBA, is 48.8 kJ/mol higher than that of the His mimic, Imid, and 49.0 kJ/mol higher than that of the Arg mimic, MGD. The same trend was also reported by Julian and Beauchamp[16] when a 1:1:1 mixture of NBA, guanidine (GD) and Imid was sprayed with 18C6. They found that the $(NBA)H^{+}(18C6)$ complex dominates the spectrum, and is the base peak (100% relative abundance), while the relative intensities

of the $(GD)H^+(18C6)$ and $(IMID)H^+(18C6)$ complexes are much smaller, 3.5% and 1%, respectively. These results suggest that backbone effects do not significantly alter the relative binding affinities of the basic amino acids, and that the Lys side chains should remain the preferred binding sites for 18C6 complexation.

5.5.4. Binding Affinities of AcAAs vs AAs

The 18C6 binding affinity of protonated Lys increases by 12.2 kJ/mol upon N_α–acetylation. This is understood by the electron withdrawing effect of the acetyl group, which increases the charge retained by the side chain primary amino hydrogen atoms. The increased charge on the hydrogen atoms of the side chain primary amino group induces higher charge on the oxygen atoms of 18C6 that results in stronger electrostatic interactions between the primary amino hydrogen and ether oxygen atoms. In contrast, N_α acetylation on His decreases the 18C6 binding affinity by 26.4 kJ/mol. This decrease in binding affinity occurs because 18C6 binds to the protonated side chain, instead of the protonated backbone amino group, because the N_α–acetyl group makes binding to this site much less favorable than in free His. In addition, the acetyl carbonyl oxygen atom forms a hydrogen bonding interaction with the protonated amino group of the side chain, providing additional stabilization to the protonated amino acid. However, this interaction stabilizes the isolated AA more than its complexes to 18C6. Thus, the charge on the hydrogen atoms of the protonated side chain decrease and consequently decrease the induced charges on the ether oxygen atoms of 18C6. As a result, the electrostatic interaction between the protonated side chain and 18C6 becomes weaker.

In the ground-state structure of the (N_α–AcArg)H^+(18C6) complex, 18C6 binds to the protonated side chain of Arg. In contrast, 18C6 binds to the protonated backbone of Arg in the ground-state structure of the (Arg)H^+(18C6) complex. As a result, the 18C6 binding affinity of protonated Arg decreases by 3.8 kJ/mol upon N_α–acetylation. The protonated backbone amino group of N_α–AcArg interacts with 18C6 via three ideal N–H···O hydrogen bonds, which results in a stronger binding interaction as compared to that between 18C6 and the protonated side chain of Arg that involves four non-ideal N–H···O hydrogen bonds. In the ground-state structure of (N_α–AcArg)H^+(18C6) complex, the acetyl oxygen atom is hydrogen bonded to an amino hydrogen atom of the protonated side chain. This hydrogen bonding interaction decreases the charge on the hydrogen atoms of the protonated side chain. However, unlike His this hydrogen bond stabilization does not directly involve any of the atoms engaged in the hydrogen bonding interactions with 18C6. Therefore, its effect on the binding is not significant, and thus alters the binding interactions very little.

5.5.5. Side Chain vs N-terminal Binding to Lys

Protonated N_α–AcLys exhibits an 18C6 binding affinity that is 7.5 kJ/mol higher than that of protonated N_ε–AcLys, suggesting that the side chain of Lys residues are the preferred binding sites for 18C6 complexation in peptides or proteins. Theoretical calculations in **Chapter 4** also suggest that the 18C6 affinity of the Lys side chain is 4.2 kJ/mole (M06 theory) more favorable than that of the backbone amino group. The Lys side chain exhibiting a higher 18C6 binding affinity than the N-terminal amino group can be understood based on differences in the steric hindrance of the carboxyl group and

side chain in the complex to N_ε–AcLys, which constrains its complexation to 18C6. The X-ray study of Krestov and coworkers suggests that the steric interaction with the N-terminal amino acid side chain could constrain its complexation to 18C6.[47] They found that the "depth of penetration" of the ammonium group into the 18C6 cavity for complexation exhibits a significant difference between diglycine and dialanine. The ammonium group in diglycine is much closer than that of dialanine during complexation. Steric interactions with the methyl side chain in proximity to the amino group in dialanine do not allow 18C6 to approach as closely and therefore bind as strongly. Thus, the 18C6 binding affinity of the N-terminal amino group should depend on the nature of the side chain. As a result, the Lys side chain constrains the complexation of the N-terminal amino group to a slightly greater extent than the backbone constrains complexation of the side chain amino group and leads to the 18C6 binding affinity of N_α–AcLys being 7.5 kJ/mol greater than that of protonated N_ε–AcLys.

5.5.6. Measured BDEs versus the PA of the Bases

In our previous study of the binding in protonated peptidomimetic base–18C6 complexes, $(B)H^+(18C6)$ in **Chapter 3**, an inverse correlation between the 18C6 binding affinity and the proton affinity (PA) of peptidomimetic base is found as a result of the shorter N–H bonds and the decreased charge retained on the amino protons. In a follow-up study of the binding in protonated amino acid–18C6 complexes in **Chapter 4**, $(AA)H^+(18C6)$, an inverse correlation between the 18C6 binding affinity and the PA of the AA is also found.

Because the AcAAs investigated in this study involve different types and numbers of hydrogen bonding interactions with 18C6, correlations between the PA of the AcAA and the measured BDEs differ depending on the nature of the binding geometries to 18C6. Inverse correlations between the measured 18C6 binding affinity and the PA of the AcAAs are also observed in the systems examined here. The PA of N_α–AcLys is 984.8 kJ/mol and increases to 987.0 kJ/mol for N_ε–AcLys, 996.0 kJ/mol for Lys, 1051.0 kJ/mole for Arg,[48,49] and 1061.0 kJ/mol for N_α–AcArg. Accordingly, the measured (AcAA)H^+–18C6 BDE decreases from 179.9 kJ/mol for N_α–AcLys, to 172.4 kJ/mol for N_ε–AcLys, 167.7 kJ/mol for Lys, 141.1 kJ/mol for Arg (**Chapter 4**), and 137.3 kJ/mol for N_α–AcArg. Again, the inverse correlation between the measured BDEs and the PAs still loosely holds for N_α–AcLys, N_ε–AcLys, His, and N_α–AcHis, although they exhibit different binding interactions with 18C6. The PA of N_α–AcHis is 988.2 kJ/mol, 0.2 kJ/mole higher than that of His,[50] 3.4 kJ/mol higher than that of N_α–AcLys, and 1.2 kJ/mol higher than that of N_ε–AcLys. Accordingly, the measured (N_α–AcHis)H^+–18C6 BDE is 129.9 kJ/mol, 26.4 kJ/mole lower than that of His, (**Chapter 4**) 42.5 kJ/mole lower than that of N_ε–AcLys, and 50.0 kJ/mole lower than that of N_α–AcLys. This inverse correlation was explained based on the N–H bond lengths and the charge retained on the amino protons. AcAAs with higher PAs bind the proton tighter and lead to weaker interactions with 18C6, resulting in lower dissociation thresholds.

5.6. Conclusions

The kinetic energy dependence for CID of four (AcAA)H^+(18C6) complexes, where AcAA = N_α–AcLys, N_ε–AcLys, N_α–AcArg, and N_α–AcHis with Xe is examined by

guided ion beam tandem mass spectrometry techniques. For all four systems, the primary dissociation pathway observed for these noncovalently bound complexes is loss of neutral 18C6. Thresholds for these CID processes are determined after consideration of the effects of the kinetic and internal energy distributions of the reactants, multiple collisions with Xe, and the lifetimes for unimolecular dissociation. The ground-state structures and theoretical estimates for the CID thresholds are determined from density functional theory calculations performed at the B3LYP/6-311+G(2d,2p)//B3LYP/6-31G* and M06/6-311+G(2d,2p)//B3LYP/6-31G* levels of theory. The agreement between M06 theory and experiment is reasonably good with a MAD of 8.9 ± 3.3 kJ/mol. The agreement between B3LYP theory and the measured BDEs is much less satisfactory. B3LYP theory systematically underestimates the measured $(AcAA)H^+$–18C6 BDEs by 38.4 ± 11.1 kJ/mol. Thus, it is clear that M06 theory describes the noncovalent interactions responsible for the binding in these complexes much more effectively than B3LYP theory.

The 18C6 binding affinities determined here combined with structural information obtained from theoretical calculations provides useful insight into the processes that occur in the molecular recognition of peptides and proteins by 18C6 for protein structure and sequence investigation. N_α–AcLys exhibits the highest binding affinity for 18C6, suggesting that the side chains of Lys residues are the preferred binding sites for 18C6 complexation. N_α–AcLys exhibits a higher binding affinity for 18C6 than N_ε–AcLys, again suggesting that the side chain of Lys residues are the preferred binding site for 18C6 as compared to the N-terminal amino group of Lys. N-terminal acetylation increases the 18C6 binding affinity for Lys, and slightly increases the 18C6 binding affinity for Arg. In

contrast, N-acetylation decreases the 18C6 binding affinity of His, again confirming that Lys residues are the preferred binding site for 18C6 complexation, and that competition by Arg and His residues for 18C6 complexation is not significant.

5.7. References

(1) Smith, D. L.; Deng, Y.; Zhang, Z. *J. Mass Spectrom*. **1997**, *32*, 135.

(2) Engen, J. R.; Smith, D. L. *Anal. Chem.* **2001**, *73*, 256A.

(3) Kaltashov, I. A.; Eyles, S. *J. Mass Spectrom. Rev.* **2002**, *21*, 37.

(4) Hoofnagle, A. N.; Resing, K. A.; Ahn, N. G. *Annu. Rev. Biophys. Biomol. Struct.* **2003**, *32*, 1.

(5) Eyles, S. J.; Kaltashov, I. A. *Methods* **2004***, 34*, 88.

(6) Garcia, R. A.; Pantazatos, D.; Villarreal, F. J. *Assay Drug Dev. Technol.* **2004**, *2*, 81.

(7) Sinz, A. *J. Mass Spectrom*. **2003**, *38*, 1225.

(8) Brunner, J. *Annu. Rev. Biochem.* **1993**, *62*, 483.

(9) Kluger, R.; Alagic, A. *Bioorg. Chem.* **2004**, *32*, 451.

(10) Melcher, K. *Curr. Prot. Pept. Sci.* **2004**, *5*, 287.

(11) Kodadek, T.; Duroux-Richard, I.; Bonnafous, J. C. *Trends Pharmacol. Sci.* **2005**, *26*, 210.

(12) Back, J. W.; de Jong, L.; Muijsers, A.O.; de Koster, C. G. *J. Mol. Biol.* **2003**, *331*, 303.

(13) Friedhoff, P. *Anal. Bioanal. Chem.* **2005**, *381*, 78.

(14) Trakselis, M. A.; Alley, S. C.; Ishmael, F. T. *Bioconjug. Chem.* **2005**, *16*, 741.

(15) Petrotchenko, E. V.; Pedersen, L. C.; Borchers, C. H.; Tomer, K. B.; Negishi, M. *FEBS Lett.* **2001**, *490*, 39.

(16) Julian, R. R.; Beauchamp, J. L. *Int. J. Mass Spectrom.* **2001**, *210/211*, 613.

(17) Julian, R. R.; Beauchamp, J. L. *J. Am. Soc. Mass Spectrom.* **2002**, *13*, 493.

(18) Julian, R. R.; Beauchamp, J. L. *J. Am. Soc. Mass Spectrom.* **2004**, *15*, 616.

(19) Julian, R. R.; Akin, M.; May, J. A.; Stoltz, B. M.; Beauchamp, J. L. *Int. J. Mass Spectrom.* **2002**, *220*, 87.

(20) Julian, R. R.; May, J. A.; Stoltz, B. M.; Beauchamp, J. L. *Int. J. Mass Spectrom.* **2003**, *228*, 851.

(21) Ly, T.; Julian, R. R. *J. Am. Soc. Mass Spectrom.* **2006**, *17*, 1209.

(22) Ly, T.; Julian, R. R. *J. Am. Soc. Mass Spectrom.* **2008**, *19*, 1663.

(23) Liu, Z.; Cheng, S.; Gallie, D. R.; Julian, R. R. *Anal. Chem.* **2008**, *80*, 3846.

(24) Ly, T.; Liu, Z.; Pujanauski, B. G.; Sarpong, R.; Julian, R. R. *Anal. Chem.* **2008**, *80*, 5059.

(25) Yeh, G. K.; Sun, Q.; Meneses, C.; Julian, R. R. *J. Am. Soc. Mass Spectrom.* **2009**, *20*, 385.

(26) Chen, Y.; Rodgers, M. T. *J. Am. Soc. Mass Spectrom.* **2012**, submitted.

(27) Chen, Y.; Rodgers, M. T. *J. Am. Chem. Soc*. **2012**, *134*, 5863.

(28) Rodgers, M. T. *J. Phys. Chem. A* **2001**, *105*, 2374.

(29) Moison, R. M.; Armentrout, P. B. *J. Am. Soc. Mass Spectrom.* **2007**, 18, 1124.

(30) *HyperChem Computational Chemistry Software Package*, Version 5.0; Hypercube Inc: Gainsville, FL, 1997.

(31) Frisch, M. J.; et al. *Gaussian 09*, Revision C.01; Gaussian, Inc.: Wallingford, CT, 2009. See **Chapter 2** for full reference.

(32) Becke, A. D. *J. Chem. Phys.* **1993**, *98*, 5648.

(33) Lee, C.; Yang, W.; Parr, R. G. *Phys. Rev. B* **1988**, *37*, 785.

(34) Foresman, J. B.; Frisch, Æ. *Exploring Chemistry with Electronic Structure Methods*, 2nd ed.; Gaussian: Pittsburgh, PA, 1996; p 64.

(35) Boys, S. F.; Bernardi, R. *Mol*. *Phys*. **1979**, *19*, 553.

(36) van Duijneveldt, F. B.; van Duijneveldt-van de Rijdt, J. G. C. M.; van Lenthe, J. H. *Chem. Rev.* **1994**, *94*, 1873.

(37) Rodgers, M. T.; Ervin, K. M.; Armentrout, P. B. *J. Chem. Phys*. **1997**, *106*, 4499.

(38) Rodgers, M. T.; Armentrout, P. B. *J. Phys. Chem. A* **1997**, *101*, 1238.

(39) Rodgers, M. T.; Armentrout, P. B. *J. Phys. Chem. A* **1997**, *101*, 2614.

(40) Rodgers, M. T.; Armentrout, P. B. *Int. J. Mass Spectrom.* **1999**, *185/186/187*, 359.

(41) Rodgers, M. T.; Armentrout, P. B. *J. Phys. Chem. A* **1999,** *103*, 4955.

(42) Armentrout, P. B.; Rodgers, M. T. *J. Phys. Chem. A* **1999,** *104*, 2238.

(43) Amunugama, R.; Rodgers, M. T. *Int. J. Mass Spectrom.* **2000**, *195/196*, 439.

(44) Rodgers, M. T.; Armentrout, P. B. *J. Am. Chem. Soc.* **2000***, 122*, 8548.

(45) Rodgers, M. T.; Armentrout, P. B. *J. Chem. Phys*. **1998**, *109*, 1787.

(46) Rodgers, M. T. *J. Phys. Chem. A*, **2001**, *105*, 8145.

(47) Kulikov, O. V.; Krestov, G. A. *Pure & Appl. Chem*. **1995**, *67*,1103.

(48) Hunter, E. P.; Lias, S. G. *J. Phys. Chem. Ref. Data*, **1998**, *27*, 413.

(49) Cannington, P. H.; Ham, N. S. *J. Electron Spectrosc. Relat. Phenom*. **1983**, *32*, 139.

(50) Bouchoux, G.; Buisson, D. A.; Colas, C.; Sablier, M. *European J. Mass Spectrom*. **2004**, *10*, 977.

Table 5.1. Bond Dissociation Enthalpies of (AcAA)H^+(18C6) at 0 K in kJ/mol[a]

AcAA	TCID	M06[b]			B3LYP[c]		
		D_e	D_0[d]	$D_{0,BSSE}$[e]	D_e	D_0[d]	$D_{0,BSSE}$[e]
N_α-AcLys	179.9 (7.7)	217.3	205.6	192.8	161.5	149.8	139.2
N_ε-AcLys	172.4 (5.8)	204.0	192.0	177.5	144.1	132.1	119.4
N_α-AcArg	137.3 (5.2)	167.3	157.9	146.9	127.5	115.1	106.1
N_α-AcHis	129.9 (5.3)	154.7	148.4	137.8	116.5	110.2	101.3
AEU/MAD	6.0 ± 1.2		21.1 ± 3.2	8.9 ± 3.3		28.3 ± 9.4	38.4 ± 11.1

[a]Present results, uncertainties are listed in parentheses. [b]Calculated at M06/6-311+G(2d,2p)//B3LYP/6-31G* level of theory. [c]Calculated at B3LYP/6-311+G(2d,2p)//B3LYP/6-31G* level of theory. [d]Including ZPE corrections with B3LYP/6-31G* frequencies scaled 0.9804. [e]Also includes BSSE corrections.

Table 5.2. Threshold Dissociation Energies at 0 K and Entropies of Activation at 1000 K of (AcAA)H^+(18C6) Complexes[a]

AcAA	σ_o[b]	n[b]	E_0 (eV)[c]	E_0 (PSL) (eV)[b]	kinetic shift (eV)	ΔS (PSL) (J mol^{-1} K^{-1})
N_α-AcLys	81(11)	1.4 (0.1)	3.71 (0.13)	1.87 (0.08)	1.84	112 (4)
N_ε-AcLys	100 (8)	1.2 (0.1)	3.40 (0.10)	1.79 (0.06)	1.61	120 (4)
N_α-AcArg	47 (2)	1.3 (0.1)	2.61 (0.10)	1.42 (0.05)	1.19	114 (4)
N_α-AcHis	80 (4)	1.3 (0.1)	2.49 (0.09)	1.35 (0.06)	1.14	78 (4)

[a]Present results, uncertainties are listed in parentheses. [b]Average values for loose PSL transition state. [c]No RRKM analysis.

5.8. Figure Captions

Figure 5.1. Multiply protonated model peptide showing the structures of the acetylated amino acids examined here including: N_{ε}–AcLys, N_{α}–AcLys, N_{α}–AcArg, and N_{α}–AcHis.

Figure 5.2. Cross sections for collision-induced dissociation of the $(N_{\alpha}\text{–AcLys})H^+(18C6)$ complex with Xe as a function of collision energy.

Figure 5.3. B3LYP/6-31G* optimized geometries of the ground-state conformers of the $(AcAA)H^+(18C6)$ complexes.

Figure 5.4. Zero-pressure-extrapolated $H^+(N_{\alpha}\text{–AcLys})$ CID product cross section of the $(N_{\alpha}\text{–AcLys})H^+(18C6)$ complex in the threshold region as a function of collision energy.

Figure 5.5. M06/6-311+G(2d,2p) theoretical versus experimental $(AcAA)H^+$–18C6 0 K BDEs. The values for $(AcAA)H^+(18C6)$ complexes are taken from **Table 5.1**. Theoretical values include ZPE and BSSE corrections.

Figure 5.1.

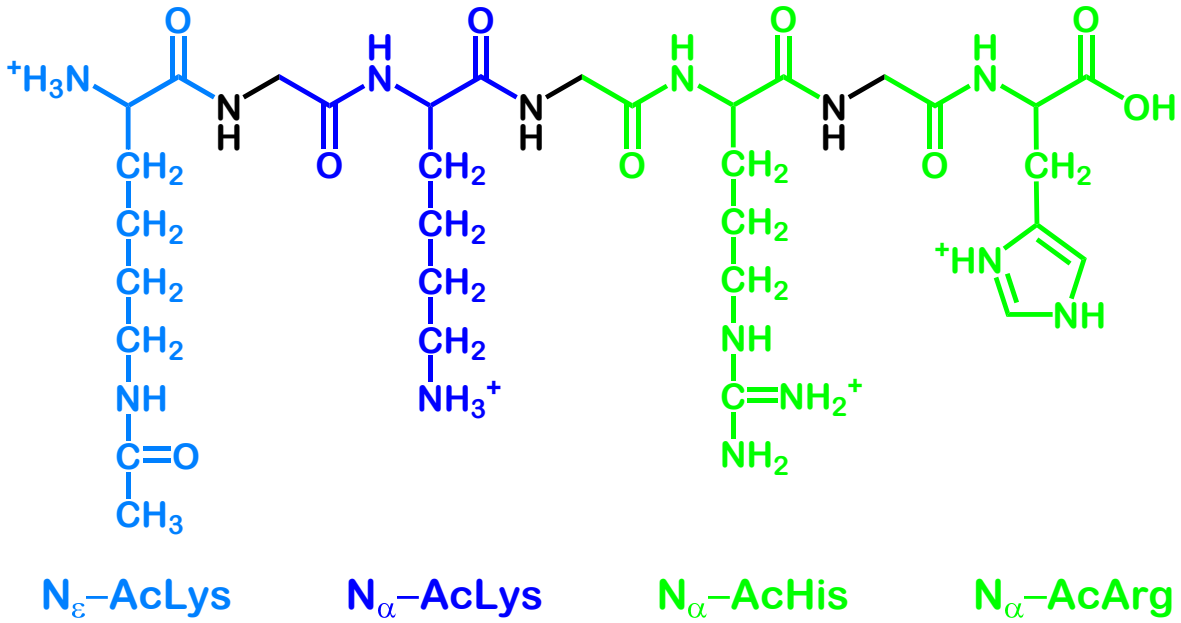
+H3N
O
N
H
CH2
CH2
CH2
CH2
NH
C=O
CH3
Nε–AcLys
H
N
O
CH2
CH2
CH2
CH2
NH3+
Nα–AcLys
H
N
O
CH2
CH2
CH2
NH
C=NH2+
NH2
Nα–AcHis
H
N
O
CH2
+HN
NH
OH
Nα–AcArg

Figure 5.2.

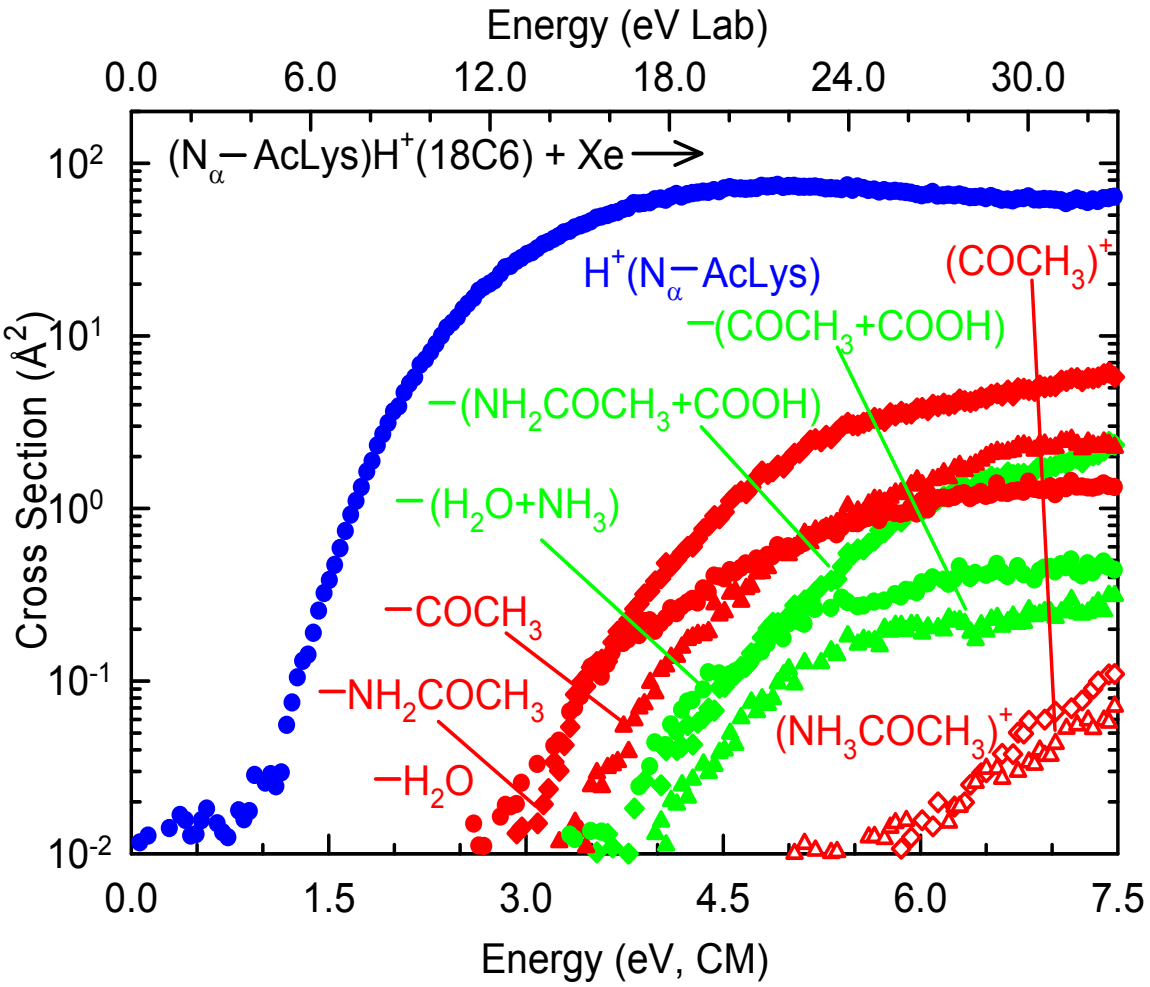
Energy (eV Lab)
0.0
6.0
12.0
18.0
24.0
30.0
(N$_\alpha$−AcLys)H$^+$(18C6) + Xe⟶
H$^+$(N$_\alpha$−AcLys)
(COCH$_3$)$^+$
−(COCH$_3$+COOH)
−(NH$_2$COCH$_3$+COOH)
−(H$_2$O+NH$_3$)
−COCH$_3$
−NH$_2$COCH$_3$
−H$_2$O
(NH$_3$COCH$_3$)$^+$
Cross Section (Å^2)
10^2
10^1
10^0
10^{-1}
10^{-2}
0.0
1.5
3.0
4.5
6.0
7.5
Energy (eV, CM)

Figure 5.3.

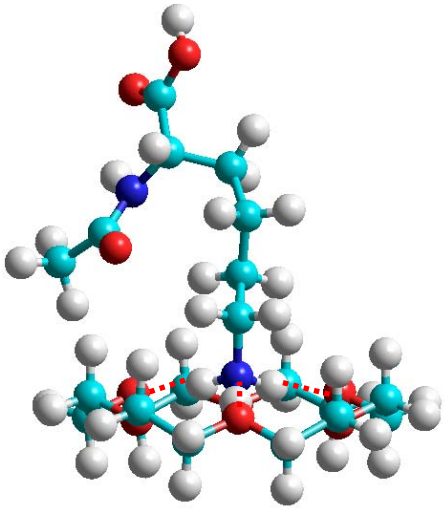

$(N_{\alpha}–AcLys)H^{+}(18C6)$

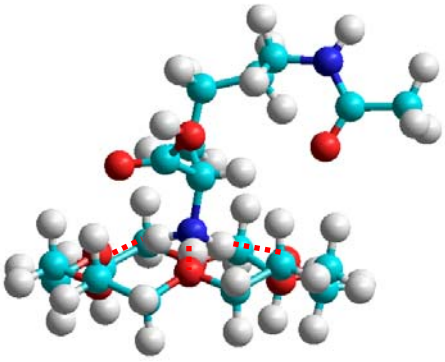

$(N_{\beta}–AcArg)H^{+}(18C6)$

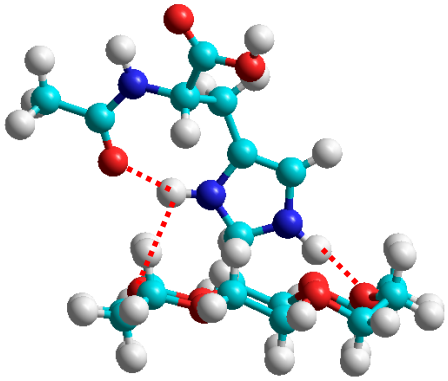

$(N_{\alpha}–AcHis)H^{+}(18C6)$

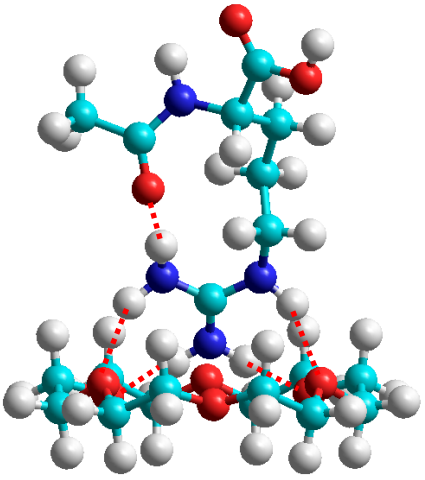

$(N_{\alpha}–AcArg)H^{+}(18C6)$

Figure 5.4.

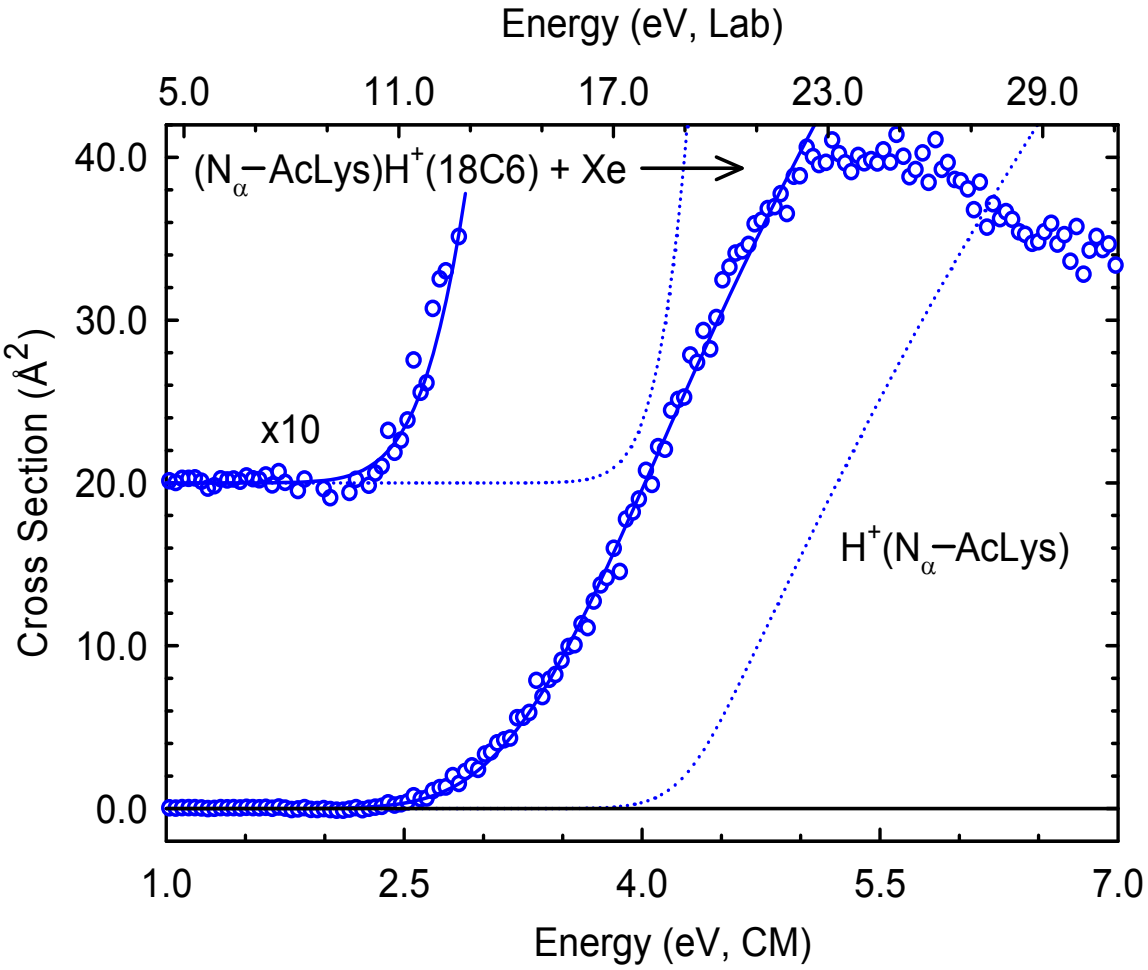
Energy (eV, Lab)
5.0
11.0
17.0
23.0
29.0
40.0
30.0
20.0
10.0
0.0
Cross Section (Å^2)
(N$_\alpha$–AcLys)H$^+$(18C6) + Xe
x10
H$^+$(N$_\alpha$–AcLys)
1.0
2.5
4.0
5.5
7.0
Energy (eV, CM)

Figure 5.5.

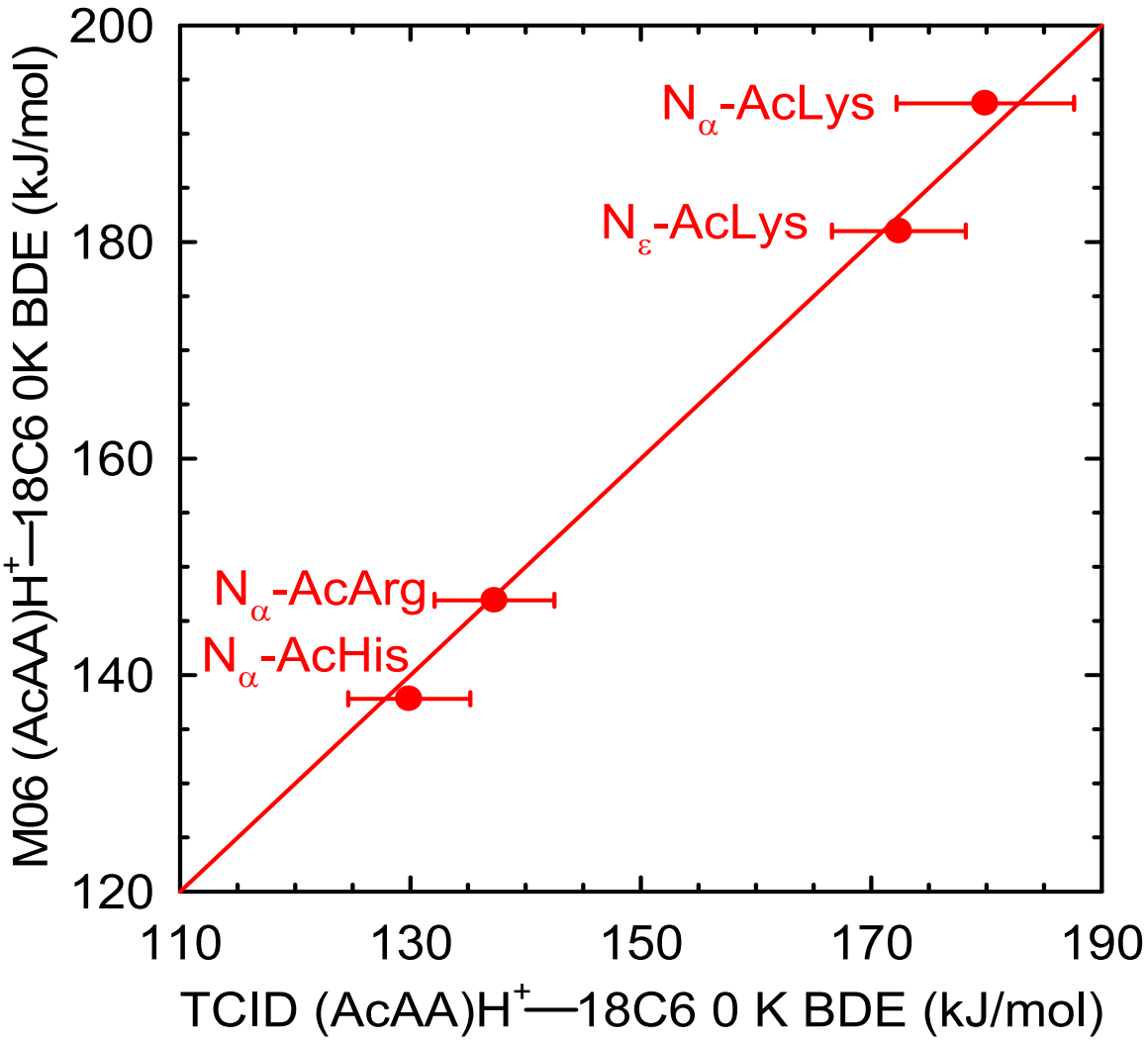
200
180
160
140
120
110
130
150
170
190
M06 (AcAA)H+—18C6 0K BDE (kJ/mol)
TCID (AcAA)H+—18C6 0 K BDE (kJ/mol)
Nα-AcLys
Nε-AcLys
Nα-AcArg
Nα-AcHis

CHAPTER 6

RE-EVALUATION OF THE PROTON AFFINITY OF 18-CROWN-6 USING COMPETITIVE THRESHOLD COLLISION-INDUCED DISSOCIATION TECHNIQUES

6.1. Introduction

Macrocyclic polyethers have gained broad attention since their first characterization by Pedersen in 1967.[1,2] As a result of their ability to bind strongly and selectively to certain cations, macrocyclic polyethers (crown ethers) have found widespread applications. For example, crown ethers are used as carriers to facilitate amino acid and drugs transfer across membranes,[3] and to transport therapeutic radiation to tumor sites.[4] Crown ethers have also been used to design novel materials for isotope separation,[5,6] and as phase transfer catalysts to facilitate dissolution of metals in nonpolar solvents.

In solution, crown ethers exhibit a selectivity for metal cations that is strongly dependent on the relative sizes of the crown ether cavity and the metal cation.[7] In a series of related studies, Armentrout and coworkers determined binding affinities of several crown and acyclic ethers to alkali metal cations in the gas phase.[8-13] In all cases, no size selectivity in the binding was observed. The binding energies were found to increase with the size of the crown ether and fall off with increasing size of the alkali metal cation. Among all crown ethers, 18-crown-6 (18C6) represents the simplest crown ether that exhibits high specificity in its interactions with cations. Apart from high affinities for metal cations, 18C6 and other crown ethers also bind to protonated amines and form very stable complexes in both solution and the gas phase. Binding in such

complexes occurs via hydrogen bonding interactions between the protonated amine hydrogen atoms and the oxygen atoms of the crown ether.

The proton affinity (PA) of 18C6 plays a critical role in the binding and CID behavior of proton bound complexes between 18C6 and guest cations. In our studies of molecular recognition of 18C6 by a series of protonated peptidomimetic bases and amino acids, the magnitudes of the CID product cross sections for production of H^+(B) versus H^+(18C6) are significantly affected by the relative PAs of 18C6 and B. The collision-induced dissociation (CID) behavior of the (B)H^+(18C6) complexes [14,15] differs markedly across these systems as shown in **Chapters 3** and **4**. When the difference in the PA of B and 18C6 is sufficiently small, competition between the two primary CID pathways leading to the formation of H^+(B) or H^+(AA) and H^+(18C6) is observed, and the relative thresholds can be used to determine additional thermochemistry. CID of the proton bound complexes to imidazole (Imid) and 4-methylimidazole (4MeImid) results in the formation of H^+(Imid) or H^+(4MeImid) as the lowest energy CID product. The formation of H^+(18C6) is also observed as a competitive CID pathway at slightly elevated energies. In contrast, for the complexes to Gly and Ala, H^+(18C6) was observed as the lowest energy CID product, whereas the formation of H^+(AA) is observed as a competitive CID product at slightly elevated energies.

The accurate determination of the PA of 18C6 can improve the current understanding and enhance the ability to control molecular recognition between 18C6 and related molecules and guest cations. However, very limited thermochemical data has thus far been reported in the literature. Two separate determinations of the PA of 18C6 have previously been reported. Both Meot-Ner[16] and Kebarle[17] used high

pressure mass spectrometry (HPMS) techniques to determine the PA 18C6. The PA of 18C6 was determined to be 920.5 ± 8.4 kJ/mole by Meot-Ner based on the proton transfer equilibrium reactions between two reference bases, 1,2-diazine and pyridine, and 18C6.[16] The PA of 18C6 determined by Kebarle and coworkers[17] was derived using ammonia as a reference base as 962.3 ± 8.4 kJ/mole. In their PA database evaluation, Hunter and Lias made use of the PA of 18C6 reported by Kebarle and coworkers and adjusted it to 967.0 ± 8.4 kJ/mol based on adjustments and corrections to the PAs of the relevant reference bases.[18,19]

In this chapter, the energy dependences of the CID of four proton bound heterodimers, $(B)H^+(18C6)$ to produce $H^+(B)$ + 18C6 and $H^+(18C6)$ + B in competition are examined. Four bases, Gly, Ala, Imid, and 4MeImid are included in this work to accurately anchor the PA of 18C6. The difference in TCID thresholds for the two CID pathways reflects the relative PAs of B and 18C6. Based on the literature PAs of the reference bases and the measured TCID thresholds, the PA of 18C6 is evaluated. The TCID thresholds for the two CID pathways provide the $(B)H^+$–18C6 and $(18C6)H^+$–B BDEs as well as the PA of 18C6. The measured $(B)H^+$–18C6 and $(18C6)H^+$–B BDEs and evaluated PA of 18C6 are compared to theoretical estimates determined using M06 and B3LYP theories.[20] The PA of 18C6 determined here is compared to measured values reported by Meot-Ner,[16] Kebarle and coworkers,[17] and evaluated by Lias and Hunter for the NIST Webbook.[18,19]

6.2. Collision-Induced Dissociation Experiments

Cross sections for CID of proton bound heterodimers, $(B)H^+(18C6)$ with Xe, where B = Gly, Ala, Imid, and 4MeImid, are measured using a guided ion beam tandem mass spectrometer that has been described in detail previously.[21] The $(B)H^+(18C6)$ complexes are generated by electrospray ionization (ESI) using a home-built ESI source.[22] The ions are effusively sampled from the source region, focused, accelerated, and focused into a magnetic sector momentum analyzer for mass analysis. Mass-selected ions are decelerated to a desired kinetic energy and focused into an octopole ion guide. The octopole passes through a static gas cell containing Xe at low pressure (~0.05–0.20 mTorr) to ensure that multiple ion-neutral collisions are improbable. Products and unreacted beam ions drift to the end of the octopole, are focused into a quadrupole mass filter for mass analysis, and are subsequently detected with a secondary electron scintillation detector and standard pulse counting techniques. Details of the experimental procedures and thermochemical analysis are given in **Chapter 2**.

6.3. Theoretical Calculations

A simulated annealing procedure using HyperChem[23] and the AMBER force field was used to generate starting structures for neutral and protonated 18C6 and the Bs for higher level optimization. All structures determined within 30 kJ/mol of the lowest-energy structure were optimized using the Gaussian 09 [24] suites of programs.

Geometry optimizations for neutral and protonated 18C6 and the Bs as well as the proton bound $(B)H^+(18C6)$ complexes were performed using density functional

theory at the B3LYP/6-31G* level.[25,26] Vibrational analyses of the geometry-optimized structures were performed to determine the vibrational frequencies of the optimized species for use in modeling of the CID data. The frequencies calculated were scaled by a factor of 0.9804.[27] Single-point energy calculations were performed at the B3LYP/6-311+G(2d,2p) and M06/6-311+G(2d,2p) levels of theory using the B3LYP/6-31G* optimized geometries. To obtain accurate energetics, zero-point energy (ZPE) and basis set super position error (BSSE) corrections are included in the computed BDEs using the counterpoise approach.[28, 29] The polarizability of the neutral and protonated AAs are calculated at the Perdew, Burke, and Ernzerhof (PBE1PBE, also known as PBE0) theory, with the 6-311+G(2d,2p) basis set. Details of the theoretical calculations are given in **Chapter 2**.

6.4. Results

6.4.1. Cross Sections for Collision-Induced Dissociation

Experimental cross sections were obtained for the interaction of Xe with four $(B)H^+(18C6)$ complexes, where B = Gly, Ala, Imid, 4MeImid. **Figure 6.1** shows representative data for the $(Imid)H^+(18C6)$ and $(Ala)H^+(18C6)$ complexes. Experimental cross sections for the other $(B)H^+(18C6)$ complexes are shown in **Figure S1** of the Supporting Information of reference 20. Loss of intact neutral B or 18C6 via CID reactions 6.1 and 6.2 is observed for all four $(B)H^+(18C6)$ complexes.

$$(B)H^+(18C6) + Xe \rightarrow H^+(B) + 18C6 + Xe \quad (6.1)$$

$$(B)H^+(18C6) + Xe \rightarrow H^+(18C6) + B + Xe \quad (6.2)$$

The loss of intact 18C6 corresponds to the lowest-energy CID pathway for the (Imid)H^+(18C6) and (4MeImid)H^+(18C6) complexes. In contrast, the loss of intact Gly or Ala corresponds to the lowest-energy CID pathway for the (Gly)H^+(18C6) and (Ala)H^+(18C6) complexes.

Although both enthalpy and entropy favor the formation of H^+(B) in the CID of the (Imid)H^+(18C6) and (4MeImid)H^+(18C6) complexes, H^+(18C6) is still observed in competition as a result of the small differences in the PAs of Imid and 4MeImid versus 18C6. However, the cross section for production of H^+(18C6) occurs at slightly elevated energies as compared to the production of H^+(B), and is two and three orders of magnitude lower than that of H^+(Imid) and H^+(4MeImid), respectively.

At elevated energies, products corresponding to the sequential dissociation of H^+(18C6) were also observed for all of the (B)H^+(18C6) complexes, reactions 6.3.

$$H^+(18C6) + Xe \rightarrow H^+(C_2H_4O)_n + (6\text{-}n)\, C_2H_4O + Xe \qquad n = 1 - 4 \qquad (6.3)$$

6.4.2. Theoretical Results

Theoretical structures for the neutral and protonated Bs and 18C6 as well as the (B)H^+(18C6) complexes were investigated thoroughly in **Chapters 3** and **4**. The ground-state structures of neutral and protonated 18C6 and Bs are shown in **Figure 3.4** in **Chapter 3,** and **Figure 4.4** in **Chapter 4**. **Figure 6.2** shows the ground-state structure of the four (B)H^+(18C6) complexes.

6.4.2.1. Bases

In the ground-state structure of neutral Gly, the N-terminal amino group is rotated away from the CH_2 group, resulting in a 180^o dihedral angle between N–H and C–H bonds. The ground-state structure of Ala exhibits a similar conformation to that of Gly. In the ground-state structure of Imid and 4MeImid, the bases exhibit a planar conformation. In the ground-state structure of H^+(Gly), one of the N-terminal amino hydrogen atoms points toward the carbonyl oxygen atom forming an intramolecular hydrogen bond. The ground-state structure of H^+(Ala) exhibits a similar conformation with the backbone hydrogen atom substituted by a methyl group. In the ground-state structure of H^+(Imid) and H^+(4MeImid), the proton binds at the N3 position of the imidazole ring to form a conformer with C_{2V} and C_s symmetry, respectively.

6.4.2.2. (B)H^+(18C6) Complexes

The ground-state structures of the four (B)H^+(18C6) complexes are shown in **Figure 6.2**. In the ground-state conformations of the (Gly)H^+(18C6) and (Ala)H^+(18C6) complexes, the conformations of H^+(Gly) and H^+(Ala) are remarkably similar to the conformations of the isolated ground-state species. In both cases, the protonated backbone amino group interacts with 18C6 via three nearly ideal N–H···O hydrogen bonds. For the (Imid)H^+(18C6) and (4MeImid)H^+(18C6) complexes, the proton binds to the neutral base to form H^+(Imid) and H^+(4MeImid), which bind to a distorted D_{3d} conformer of 18C6 via 2 N–H···O hydrogen bonds. The O1 and O4 atoms of 18C6 are tilted above the nearly planar ring structure forming hydrogen bonds with the hydrogen atoms of the secondary amines.

6.4.3. Threshold Analysis

The model of equation 2.4 was used to competitively analyze the thresholds for reactions 6.1 and 6.2 in four $(B)H^+(18C6)$ complexes. The results of these analyses are provided in **Table S3** of reference 20, and representative results are shown in **Figure 6.1** for the $(Imid)H^+(18C6)$ and $(Ala)H^+(18C6)$ complexes. The analyses for the other $(B)H^+(18C6)$ complexes are shown in **Figure S2** of the Supporting Information of reference 20. In all cases, the experimental cross sections for reactions 6.1 and 6.2 are accurately reproduced using a loose PSL TS model.[30] Previous work has shown that this model provides the most accurate assessment of the kinetics shifts for CID process for electrostatically bound ion-molecule complexes.[31-39] Good reproduction of the data is obtained over energy ranges exceeding 3.0 eV and cross section magnitudes of at least a factor of 100.

The entropy of activation, $\Delta S^{\ddagger}$, is a measure of the looseness of the TS and the complexity of the system. It is determined from the molecular parameters used to model the EM and TS for dissociation as listed in **Table S1** and **S2** of the Supporting Information of reference 20. The $\Delta S^{\ddagger}$(PSL) values at 1000 K are listed in **Table S3** of reference 20 and vary between 56 to 105 J mol^{-1} K^{-1} for the $H^+(18C6)$ + B CID pathway and 85 to 129 J/K mol for the $H^+(B)$ + 18C6 CID pathway across the these systems. These values are consistent with the noncovalent nature of the binding in these systems. The $\Delta S^{\ddagger}$(PSL) values are the smallest for the complexes to Imid and 4MeImid, 56 and 63 J mol^{-1} K^{-1} (for loss of neutral B), and 85 and 93 J mol^{-1} K^{-1} (for loss of neutral 18C6), where only two hydrogen bonds are cleaved in the CID process, and larger for

the remaining complexes 85 to 105 J mol^{-1} K^{-1} (for loss of neutral B), and 113 to 129 J mol^{-1} K^{-1} (for loss of neutral 18C6), where three hydrogen bonds are broken.

6.5. Discussion

6.5.1. Comparison of Theory and Experiment

The results of threshold analyses for reactions 6.1 and 6.2 in four systems using the model of equation 2.4 are provided in **Table S3** of the Supporting Information of reference 20. The measured and calculated $(B)H^+$–18C6 BDEs at 0 K are summarized in **Table S5** of the Supporting Information of reference 20. The agreement between theory and experiment is illustrated in **Figure 6.3a**. The measured $(B)H^+$–18C6 BDEs exhibit excellent agreement with M06 theory with a mean absolute deviation (MAD) of 3.1 ± 3.4 kJ/mol. The agreement between B3LYP theory and the measured BDEs is less satisfactory. B3LYP theory systematically underestimates the measured $(B)H^+$–18C6 BDEs by 38.7 ± 12.3 kJ/mol. The average experimental uncertainty (AEU) for the measured $(B)H^+$–18C6 BDEs is 8.7 ± 1.7 kJ/mol, is larger than the MAD for M06 theory, but significantly smaller than that of B3LYP theory. The measured and calculated $(18C6)H^+$–B BDEs at 0 K are also compared in **Figure 6.3a** and summarized in **Table S5** of the Supporting Information of reference 20. Excellent agreement between M06 theory and the measured BDEs is also observed with a MAD of 6.4 ± 6.5 kJ/mol. Again, the agreement between B3LYP theory and the measured BDEs is less than satisfactory. B3LYP theory again systematically underestimates the measured $(18C6)H^+$–B BDEs by 28.6 ± 14.5 kJ/mol. The AEU for the measured $(18C6)H^+$–B BDEs is 9.0 ± 1.0 kJ/mol, is slightly larger than the MAD for M06 theory, but significantly

smaller than that of B3LYP theory. Thus, M06 theory is clearly able to describe the energetics associated with the hydrogen bonding interactions in these complexes much more accurately than B3LYP.

The measured and calculated differences in the PAs of 18C6 and B at 0 K are compared in **Figure 6.3b**. The measured ΔPAs exhibit excellent agreement with M06 theory with a mean absolute deviation (MAD) of 6.0 ± 7.6 kJ/mol. The agreement between B3LYP theory and the measured BDEs is somewhat less satisfactory, but is still reasonably good, with a MAD of 11.0 ± 5.3 kJ/mol. The average experimental uncertainty (AEU) in the measured ΔPAs, 4.1 ± 1.8 kJ/mol, is slightly smaller than the MAD for M06 theory, and much smaller than that of B3LYP theory. The major source of error appears to be associated with the value determined for the complex to Gly, suggesting that the competitive CID model may not be performing as well for this system as a result of the relatively large difference in the PAs of 18C6 and Gly such that the statistical assumptions inherent to the competitive CID model begin to break down as the difference in the thresholds increases.

6.5.2. Re-evaluated Proton Affinity of 18C6

The PA of 18C6 is evaluated based on the thermochemical cycles of **Scheme 6.1** for four $(B)H^+(18C6)$ systems. The results for these individual evaluations are summarized in **Table 6.1** and shown pictorially in **Figure 6.4**. For each of these four independent evaluations of the PA of 18C6, the $(B)H^+$–18C6 and $(18C6)H^+$–B BDEs are taken from the thresholds determined from competitive TCID experiments, while the PA of B is taken from the NIST Webbook.

Competitive TCID experiments provide two independent BDEs, $(B)H^+$–18C6 and $(18C6)H^+$–B. Competitive analysis using the modified empirical threshold law, equation 2.4, for the simultaneous analysis of the two TCID pathways provides a more precise determination of the relative thresholds, ΔE_0, for production of $H^+(18C6)$ + B and $H^+(B)$ + 18C6. However, the reliability of the competitive models falls off as the difference in the thresholds increases. Therefore, in our use of the thermochemical cycles of **Scheme 6.1** to evaluate the PA of 18C6, we conservatively use an uncertainty for this value that is three times the standard deviation determined from the competitive analysis. The PA of 18C6 is determined from a weighted linear least squares fit of the PA of B versus the TCID measured ΔPA. The uncertainty is conservatively reported as twice the standard error of the estimate.

The evaluated PA of 18C6 determined by TCID using the four $(B)H^+(18C6)$ complexes examined here is 935.3 ± 11.4 kJ/mol, exhibiting excellent agreement with M06 theory, 928.9 kJ/mol. The agreement between the TCID evaluated PA of 18C6 and the PA calculated using B3LYP theory, 922.5 kJ/mol, is very good. The PA of 18C6 determined in the present study also exhibits good agreement with the PA reported by Meot-Ner,[16] 920.5 kJ/mole, but deviates significantly from the PA reported by Kebarle and coworkers[17] and listed in the NIST Webbook.[18,19] It is not entirely clear why the same HPMS equilibrium method produced such different results. However, Meot-Ner's results are based on comparison to two reference bases instead of one. In addition, the reference bases Meot-Ner chose have PAs that are closer to that of 18C6 than the reference base employed by Kebarle and coworkers such that the systems should compete more effectively and result in ion intensities that differ less and are therefore

more likely to lie within the dynamic range of the instrument. Thus, as for the TCID competitive method, the HPMS equilibrium method appears to be more effective when the differences in the PAs are smaller. Based on theses results, we believe that the PA of 18C6 reported in the NIST Webbook should be adjusted, and that the value reported here based on a least-squares analysis of results from four competitive TCID experiments should be used.

6.5.3 Entropy Effects in the CID of (B)H^+(18C6) Complexes

As seen in the energy resolved CID data of **Figure 6.1** and **Figure S2** of the Supporting Information of reference 20, and elucidated in the threshold analysis of this data (**Table S3** of the Supporting Information of reference 20), entropy effects are clearly influencing the CID of the (B)H^+(18C6) complexes. The differences in the entropies of activation for the H^+(B) + 18C6 and H^+(18C6) + B CID pathways indicate that the kinetics of dissociation are very important in determining the CID branching ratios. The species with the greater PA (B vs 18C6) dominates at low energies, indicating thermodynamic control of the CID process. In contrast, the H^+(B) pathway dominates at elevated energies for all four systems as a result of the greater increase in entropy for this CID pathway, indicating kinetic control of the CID process. As a result, kinetic method measurements would lead to erroneous results in cases where the PA of 18C6 exceeds that of B, i.e., Gly and Ala. Application of the extended kinetic method in these cases may correct for the entropy effects, but has not been tested. In addition to the four (B)H^+(18C6) complexes examined here, we have also examined the CID behavior of five additional complexes to simple primary alkyl amines that exhibit

competition between the H^+(B) + 18C6 and H^+(18C6) + B CID pathways. However, in each of these systems, it is clear that both kinetic and conformational barriers suppress the H^+(18C6) + B pathway such that the difference in the thresholds for the two CID pathways no longer represents the difference in PA of 18C6 and B. These systems are under further investigation, but present results suggest that sterics plays a role. The energy dependence of the CID pathways of these systems provides a clear indication of the entropic effects and ensures proper interpretation of the experimental data. In contrast, even the extended kinetic method would not correct for the entropic effects in these latter systems because the barrier exceeds the endothermicity of dissociation.

6.6. Conclusions

The kinetic energy dependence for CID of four (B)H^+(18C6) complexes, where B = Gly, Ala, Imid, and 4MeImid, with Xe is examined by guided ion beam tandem mass spectrometry techniques. Loss of the intact base, B, and 18C6 are observed in competition for all four complexes. Loss of intact 18C6 corresponds to the lowest-energy CID pathway for the (Imid)H^+(18C6) and (4MeImid)H^+(18C6) complexes, while loss of intact Imid and 4MeImid are observed as a competitive CID pathways in these systems. In contrast, loss of intact Gly or Ala corresponds to the lowest-energy CID pathway for the (Gly)H^+(18C6) and (Ala)H^+(18C6) complexes, while the loss of intact 18C6 is observed as a competitive CID pathway. Thresholds for these CID processes are determined after consideration of the effects of the kinetic and internal energy distributions of the reactants, multiple collisions with Xe, and the lifetimes for unimolecular dissociation. The relative TCID thresholds between the primary and

competitive CID pathways are determined using a modified empirical threshold law that accounts for the competitive dissociation along these two pathways. The ground-state structures and theoretical estimates for the CID thresholds and PAs of the relevant species are determined from density functional theory calculations performed at the B3LYP/6-311+G(2d,2p)//B3LYP/6-31G* and M06/6-311+G(2d,2p)//B3LYP/6-31G* levels of theory. Excellent agreement between the M06 theoretically calculated and experimentally determined (B)H^+–18C6 and (18C6)H^+–B BDEs and the PA of 18C6 was found. In contrast, B3LYP theory systematically underestimates the strength of binding in these systems, but does a reasonable job of estimating the PA of 18C6. Based on the relative TCID thresholds for the primary and competitive CID pathways, as well as the literature PAs of the references bases, the PA of 18C6 is evaluated as 935.3 ± 11.4 kJ/mol. The PA of 18C6 evaluated here exhibits excellent agreement with M06 theory and very good agreement with B3LYP theory and the value measured by Meot-Ner, suggesting that the PA of 18C6 reported in the NIST Webbook and based on the measured value reported by Kebarle and coworkers is overestimated and should be adjusted to the value determined here.

6.7. References

(1) Pedersen, C. J. *J. Am. Chem. Soc* **1967**, *89*, 2495.

(2) Pedersen, C. J. *Angew. Chem., Int. Ed. Engl*. **1988**, *27*, 1021.

(3) Lehn, J.-M. *Angew. Chem., Int. Ed. Engl*. **1988,** *27*, 89.

(4) Kozak, R. W.; Waldmann, T. A.; Atcher, R. W.; Gansow, O. A. *Trends Biotechnol.* **1985**, *4*, 259.

(5) Horwitz, E. P.; Dietz, M. L.; Fisher, D. E. *Solvent Extraction and Ion Exchange* **1991**, *9*, 1.

(6) Chiarizia, R.; Horwitz, E. P.; Dietz, M. L. *Solvent Extraction and Ion Exchange* **1992,** *10*, 337.

(7) De Jong, F.; Reinhoudt, D. N. *Adv. Phys. Org. Chem.* **1980**, *17*, 279.

(8) Ray, D.; Feller, D.; More, M. B.; Glendening, E. D.; Armentrout, P. B. *J. Phys. Chem.* **1996**, *100*, 16116.

(9) More, M. B.; Ray, D.; Armentrout, P. B. *J. Phys. Chem. A* **1997**, *101*, 831.

(10) More, M. B.; Ray, D.; Armentrout, P. B. *J. Phys. Chem. A* **1997**, *101*, 4254.

(11) More, M. B.; Ray, D.; Armentrout, P. B. *J. Phys. Chem. A* **1997**, *101*, 7007.

(12) More, M. B.; Ray, D.; Armentrout, P. B. *J. Am. Chem. Soc.* **1998**, *121*, 417.

(13) Armentrout, P. B. *Int. J. Mass Spectrom.* **1999**, *193*, 227.

(14) Chen, Y.; Rodgers, M. T. *J. Am. Chem. Soc.* **2012**, *134,* 2313.

(15) Chen, Y.; Rodgers, M. T. *J. Am. Chem. Soc.* **2012**, *134*, 5863.

(16) Meot-Ner, M. *J. Am. Chem. Soc.* **1983**, *105*, 4906.

(17) Sharma, R. B.; Blades, A. T.; Kebarle, P. *J. Am. Chem. Soc.* **1984**, *106*, 510.

(18) Hunter, E. P.; Lias, S. G. *J. Phys. Chem. Ref. Data,* **1998**, *27*, 413.

(19) NIST Chemistry Webbook, NIST Standard Reference Database Number 69, http://webbook.nist.gov/chemistry/.

(20) Chen, Y.; Rodgers, M. T. *Anal. Chem.* **2012**, ac-2012-01804j, submitted.

(21) Rodgers, M. T. *J. Phys. Chem. A* **2001**, *105*, 2374.

(22) Moison, R. M.; Armentrout, P. B. *J. Am. Soc. Mass Spectrom.* **2007**, *18*, 1124.

(23) *HyperChem Computational Chemistry Software Package*, Version 5.0; Hypercube Inc: Gainsville, FL, 1997.

(24) Frisch, M. J.; et al. *Gaussian 09*, Revision C.01; Gaussian, Inc.: Wallingford, CT, 2009. See **Chapter 2** for full reference.

(25) Becke, A. D. *J. Chem. Phys.* **1993**, *98*, 5648.

(26) Lee, C.; Yang, W.; Parr, R. G. *Phys. Rev. B* **1988**, *37*, 785.

(27) Foresman, J. B.; Frisch, Æ. *Exploring Chemistry with Electronic Structure Methods*, 2nd ed.; Gaussian: Pittsburgh, PA, 1996; p 64.

(28) Boys, S. F.; Bernardi, R. *Mol. Phys*. **1979**, *19*, 553.

(29) van Duijneveldt, F. B.; van Duijneveldt-van de Rijdt, J. G. C. M.; van Lenthe, J. H. *Chem. Rev.* **1994**, *94*, 1873.

(30) Rodgers, M. T.; Ervin, K. M.; Armentrout, P. B. *J. Chem. Phys*. **1997**, *106*, 4499.

(31) Rodgers, M. T.; Armentrout, P. B. *J. Phys. Chem. A* **1997**, *101*, 1238.

(32) Rodgers, M. T.; Armentrout, P. B. *J. Phys. Chem. A* **1997**, *101*, 2614.

(33) Rodgers, M. T.; Armentrout, P. B. *Int. J. Mass Spectrom.* **1999**, *185/186/187*, 359.

(34) Rodgers, M. T.; Armentrout, P. B. *J. Phys. Chem. A* **1999**, *103*, 4955.

(35) Armentrout, P. B.; Rodgers, M. T. *J. Phys. Chem. A* **1999**, *104*, 2238.

(36) Amunugama, R.; Rodgers, M. T. *Int. J. Mass Spectrom.* **2000**, *195/196*, 439.

(37) Rodgers, M. T.; Armentrout, P. B. *J. Am. Chem. Soc.* **2000**, *122*, 8548.

(38) Rodgers, M. T.; Armentrout, P. B. *J. Chem. Phys*. **1998**, *109*, 1787.

(39) Rodgers, M. T. *J. Phys. Chem. A* **2001**, *105*, 8145.

Table 6.1. Comparison of 18C6 PA Determined by Competitive TCID Methods and Theory

Species	ΔPA TCID	PA of B NIST[18,19]	Evaluated PA of 18C6 TCID
$(Gly)H^+(18C6)$	41.0 (4.2)	886.5 (3.1)	927.5 (5.2)
$(Ala)H^+(18C6)$	40.0 (4.2)	901.6 (4.0)	941.6 (5.8)
$(Imid)H^+(18C6)$	-3.7 (1.8)	942.8 (6.8)	939.1 (7.0)
$(4MeImid)H^+(18C6)$	-21.6 (6.3)	952.8 (6.8)	931.2 (9.3)

Table 6.2. Measured and Calculated PA of 18C6 at 0 K in kJ/mol

TCID	Theory[a]		Literature		
	M06	B3LYP	Meot-Ner[b]	Kebarle[c]	NIST[d]
935.3 ± 11.4	930.6	924.1	920.5 ± 8.4	962.3 ± 8.4	967.0 ± 8.4

[a]Single-point energies are calculated at 6-311+G(2d,2p) basis set using geometries optimized at B3LYP/6-31G* level of theory. [b]Value take from reference 16. [c]Value taken from reference 17. [d]ΔH_0 value taken from the NIST Chemistry Webbook.[18, 19]

6.8. Figure Captions

Figure 6.1. Cross sections for collision-induced dissociation of the (Imid)H^+(18C6) and (Ala)H^+(18C6) complexes with Xe as a function of kinetic energy, parts a-b. Zero-pressure-extrapolated H^+(Imid) and H^+(18C6) CID product cross sections of the (Imid)H^+(18C6) complex and H^+(Ala) and H^+(18C6) CID product cross sections of the (Ala)H^+(18C6) complex in the threshold region as a function of collision energy, parts c-d.

Figure 6.2. B3LYP/6-31G* optimized geometries of the ground-state conformers of the (B)H^+(18C6) complexes.

Figure 6.3. Theoretical versus experimental (B)H^+–18C6 and (18C6)H^+–B 0 K BDEs, part a. Theoretical relative ΔPA versus experimental ΔE_0 (B)H^+–18C6 and (18C6)H^+–B at 0 K. Theoretical values include ZPE and BSSE corrections, part b.

Figure 6.4. Evaluations of the PA of 18C6, ΔPAs are taken from the thresholds determined from competitive TCID experiments, while the PAs of the reference bases, B, are taken from the NIST Chemistry Webbook.[18, 19]

Figure 6.1.

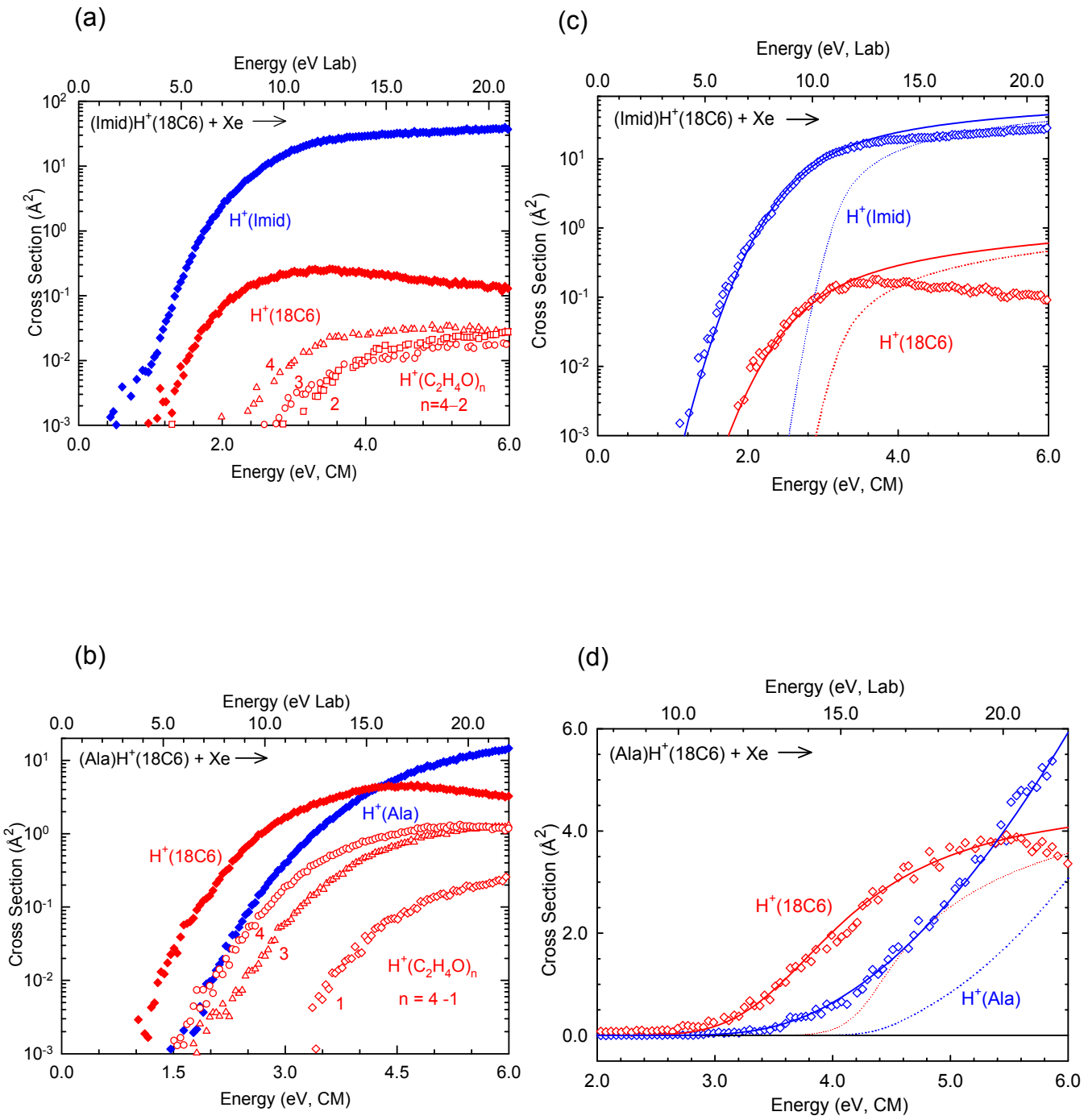
(a)
Energy (eV Lab)
(Imid)H+(18C6) + Xe
H+(Imid)
H+(18C6)
H+(C2H4O)n
n=4–2
Cross Section (Å2)
Energy (eV, CM)
(c)
Energy (eV, Lab)
(Imid)H+(18C6) + Xe
H+(Imid)
H+(18C6)
Cross Section (Å2)
Energy (eV, CM)
(b)
Energy (eV Lab)
(Ala)H+(18C6) + Xe
H+(Ala)
H+(18C6)
H+(C2H4O)n
n = 4 -1
Cross Section (Å2)
Energy (eV, CM)
(d)
Energy (eV, Lab)
(Ala)H+(18C6) + Xe
H+(18C6)
H+(Ala)
Cross Section (Å2)
Energy (eV, CM)

Figure 6.2.

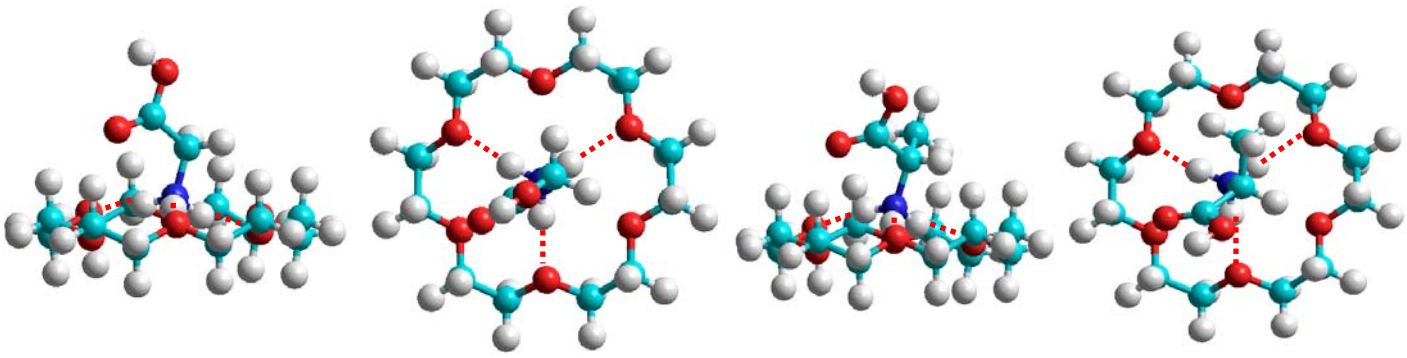

$(Gly)H^+(18C6)$ $(Ala)H^+(18C6)$

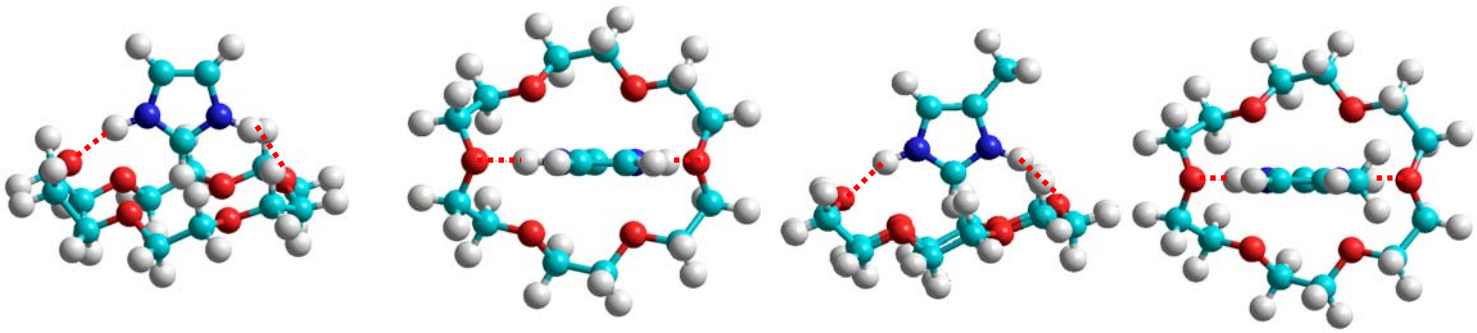

$(Imid)H^+(18C6)$ $(4MeImid)H^+(18C6)$

Figure 6.3.

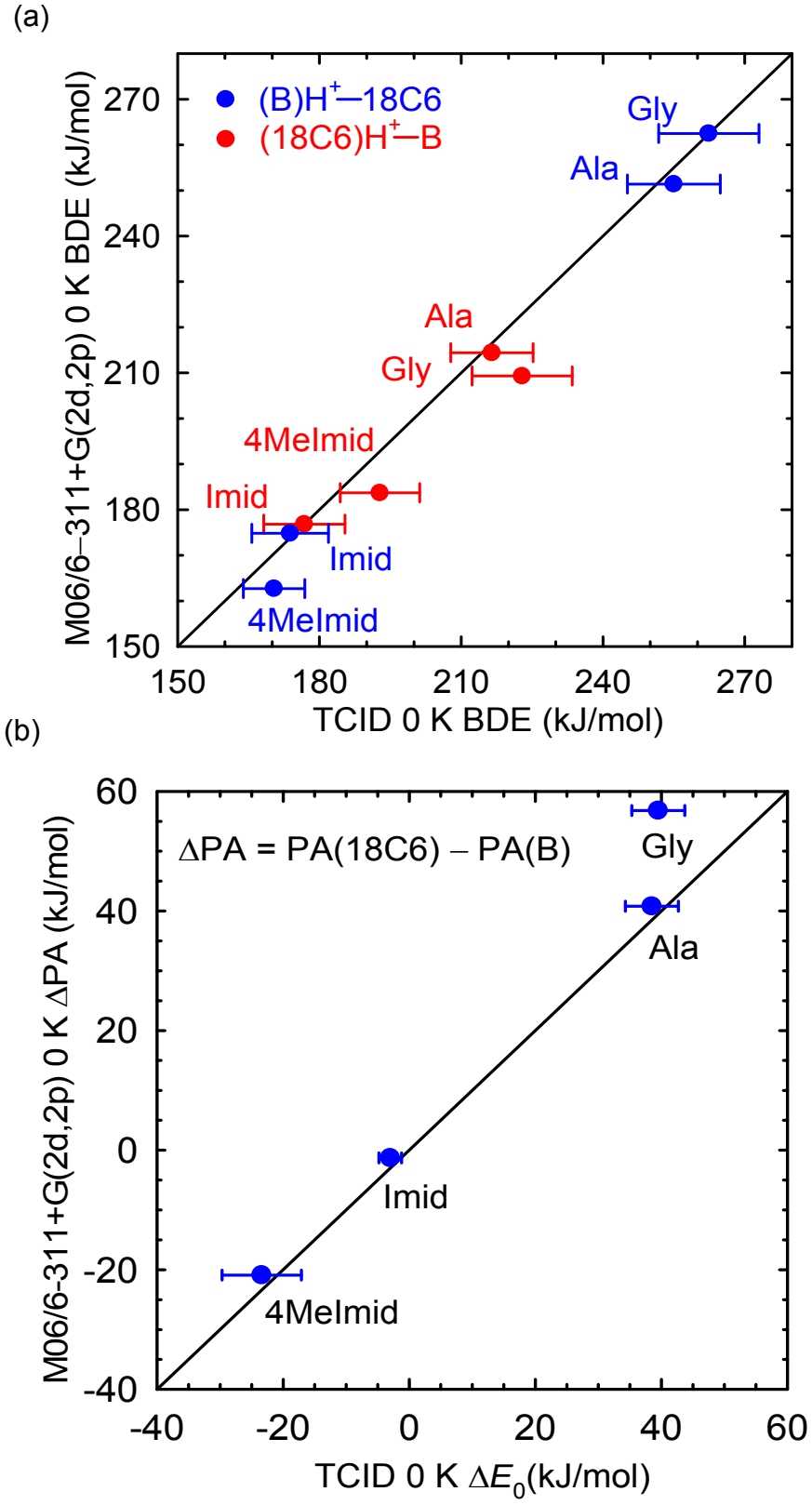
(a)
(B)H+—18C6
(18C6)H+—B
Gly
Ala
Ala
Gly
4MeImid
Imid
Imid
4MeImid
M06/6–311+G(2d,2p) 0 K BDE (kJ/mol)
TCID 0 K BDE (kJ/mol)
150
180
210
240
270
(b)
ΔPA = PA(18C6) – PA(B)
Gly
Ala
Imid
4MeImid
M06/6-311+G(2d,2p) 0 K ΔPA (kJ/mol)
TCID 0 K ΔE0(kJ/mol)
-40
-20
0
20
40
60

Figure 6.4.

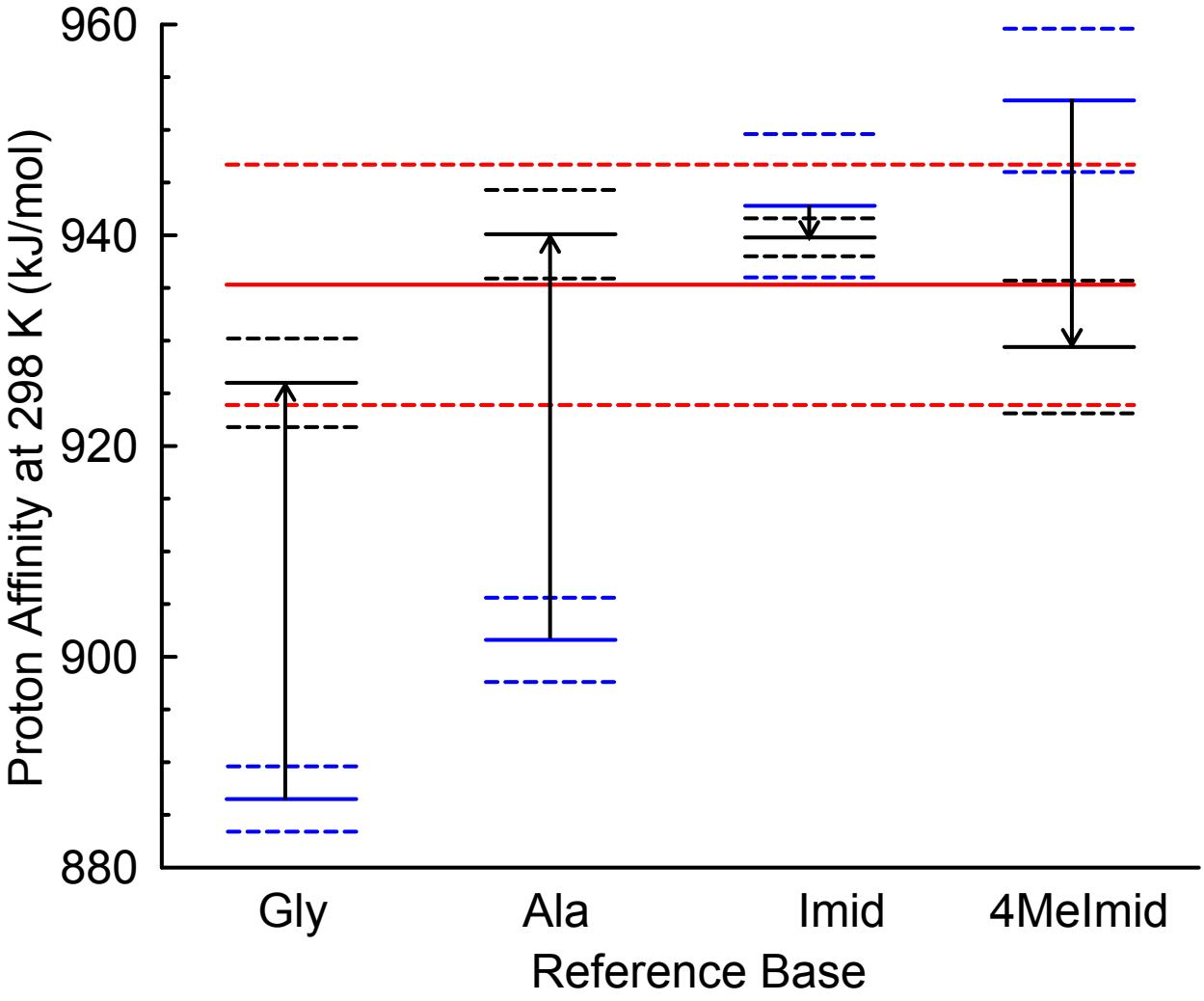
960
940
920
900
880
Proton Affinity at 298 K (kJ/mol)
Gly
Ala
Imid
4MeImid
Reference Base

Scheme 6.1.

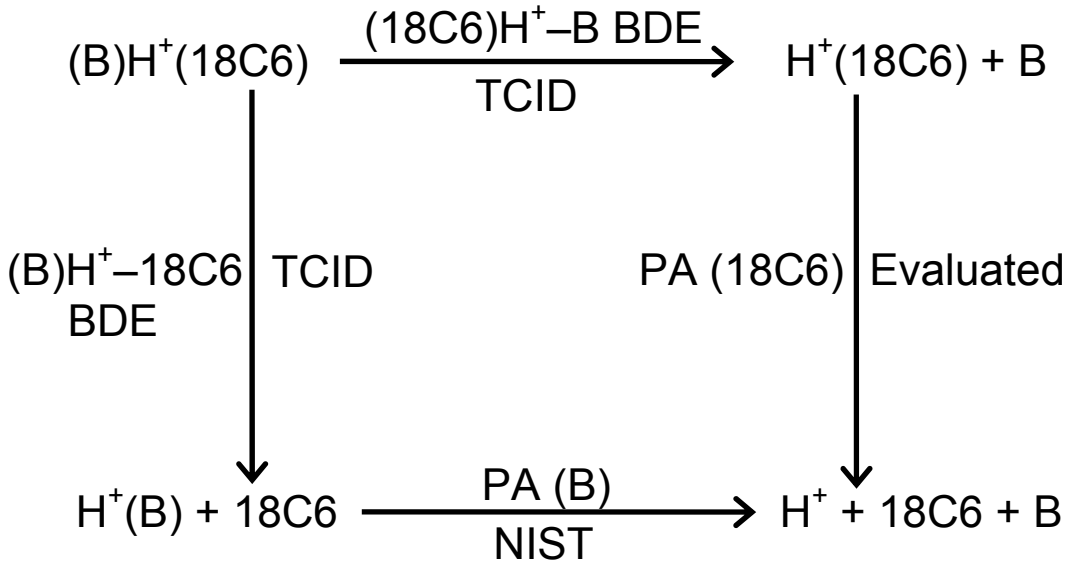
(B)H+(18C6)
(18C6)H+–B BDE
TCID
H+(18C6) + B
(B)H+–18C6
BDE
TCID
PA (18C6)
Evaluated
H+(B) + 18C6
PA (B)
NIST
H+ + 18C6 + B

CHAPTER 7

INFRARED MULTIPLE PHOTON DISSOCIATION ACTION SPECTROSCOPY OF NONCOVALENT COMPLEXES OF PROTONATED PEPTIDOMIMETIC BASES WITH 18-CROWN-6

7.1. Introduction

Crown ethers have been broadly used to investigate molecular recognition, for example, as carriers to facilitate drug transfer across membranes,[1] for the transport of therapeutic radiation to tumor sites,[2] and as phase transfer catalysts to facilitate dissolution of metals in nonpolar solvents.[3] In solution, crown ethers exhibit selectivities for metal cations that are well matched to the size of the crown ether cavity.[4] In a series of related studies, Armentrout and coworkers determined binding affinities of several crown and acyclic ethers to alkali metal cations in the gas phase.[5-10] The measured binding energies were found to increase with the size of the crown ether and fall off with increasing size of the alkali metal cation. In contrast to the solution behavior, no size selectivity in the binding was observed as a result of the spherical shape of alkali metal cations.

Recently infrared multiple photon dissociation (IRMPD) action spectroscopy techniques have been used to address conformational questions regarding metal-crown ether complexes. Martinez-Haya and coworkers have employed IRMPD action spectroscopy and quantum mechanical calculations to elucidate the structures of gas-phase alkali metal cation–18C6 complexes.[11,12] Their study showed that symmetric and chiral arrangements play a dominant role in the conformation of these complexes. The most stable alkali metal cation–18C6 complexes exhibit C_{3v} and C_2 symmetry for Cs^+,

D_{3d} symmetry for K^+, C_1 and D_{3d} symmetry for Na^+, and D_2 symmetry for Li^+. Armentrout and coworkers used IRMPD action spectroscopy techniques to investigate the gas-phase conformations of complexes of the transition-metal cations, Zn^{2+} and Cd^{2+}, with varying sized crown ethers, 12-crown-4, 15-crown-5, and 18-crown-6 (18C6).[13] They reported that the conformation of each transition metal cation-crown ether complex is highly dependent on the size and charge of the metal cation and the flexibility of the crown ether.

The use of molecular recognition of crown ethers has also been employed by other groups. Beauchamp, Julian, and coworkers have developed the selective noncovalent adduct protein probing (SNAPP)[14-23] method using 18C6 because of its specificity for Lys side chains to study protein sequence, structure and conformational changes. Reinhoudt and coworkers reported that the addition of 18C6 to organic solvent significantly enhanced enzyme activity.[24] Their study ruled out the possibility that the crown ether facilitates transport of water molecules from the active site in the bulk organic solvent. They believe that the enhancement in enzyme activity in organic media is a result of the conformational stabilization induced by interaction between the crown ether and protonated amino groups of lysine residues. Kinoshita and coworkers reported the first visual determination of the chain length of linear diamines based on molecular recognition of a functionalized molecule consisting of a phenolphthalein moiety linked to two crown ethers. The interaction between the diamine and crown ether is examined by taking UV-visible spectrum at 571 nm in MeOH at 25 ^oC. Complex formation between diamines and the crown ether results in a dramatic change in color that depends on the length of the diamine.[25]

Structural effects play a critical role in the molecular recognition of peptides or proteins by 18C6. In order to experimentally characterize the ground-state and low-energy conformers of $(B)H^+(18C6)$ complexes, the interaction of 18C6 with five protonated peptidomimetic bases are examined here by infrared multiple photon dissociation (IRMPD) action spectroscopy techniques. Peptidomimetic bases that serve as models for the N-terminal amino group as well as the side chains of Lys, His, and Arg are examined here and include: isopropylamine (IPA) for the N-terminal amino group, n-butylamine (NBA) and 1,5-diamino pentane (DAP) for the side chain of Lys, 4-methylimidazole (4MeImid) for the side chain of His, and 1-methylguanidine (MGD) for the side chain of Arg. A model multiply protonated peptide illustrating the structures of the peptidomimetic nitrogen bases examined is shown in **Figure 7.1**. In order to determine the ground-state and stable low-energy conformers of the $(B)H^+(18C6)$ complexes, the measured IRMPD action spectra of these complexes are compared with linear IR spectra for the stable low-energy conformers of these complexes derived from theoretical calculations performed at B3LYP/6-31G* level of theory.[26]

7.2. Infrared Multiple Photon Dissociation Action Spectroscopy Experiments

IRMPD action spectra of five $(B)H^+(18C6)$ complexes were measure using a 4.7 T Fourier transform ion cyclotron resonance mass spectrometer (FT-ICR MS) coupled to the free electron laser (FEL) that is housed at the FOM Institute for Plasma Physics, Rijnhuizen and has been described in detail elsewhere.[27-29] The protonated complexes were generated using a micromass “Z-spray” electrospray ionization (ESI) and accumulated in a hexapole trap for several seconds followed by pulsed extraction

through a quadrupole bender and injected into the ICR cell via a rf octopole ion guide. The precursor ions were mass selected using stored waveform inverse Fourier transform (SWIFT) techniques and irradiated by the FEL at pulse energies of ~40 mJ per macropulse of 5 μs duration for 3 s at a repetition rate of 5Hz, corresponding to interaction of the $(B)H^+(18C6)$ complexes with 15 macropulses. Details of the experimental procedures and thermochemical analysis of experimental data are given in **Chapter 2**.

7.3. Theoretical Calculations

A simulated annealing procedure using HyperChem[30] and the AMBER force field was used to generate starting structures of neutral and protonated 18C6 and the Bs for higher level optimization. All structures determined within 30 kJ/mol of the lowest-energy structure were optimized using the Gaussian 03[31] and Gaussian 09 [32] suites of programs.

Geometry optimizations of neutral and protonated 18C6 and the Bs as well as the proton bound $(B)H^+(18C6)$ complexes were performed using density functional theory at the B3LYP/6-31G* level.[33,34] Vibrational analyses of the geometry-optimized structures were performed to determine the vibrational frequencies of the optimized species. The frequencies calculated were scaled by a factor of 0.9804 for zero point energy (ZPE) correction.[35] Single-point energy calculations were performed at the B3LYP/6-311+G(2d,2p) and MP2(full)/6-311+G(2d,2p) levels of theory using the B3LYP/6-31G* optimized geometries. To obtain accurate energetics, ZPE corrections are included in the computed relative stabilities.

Theoretical linear IR spectra of five $(B)H^+(18C6)$ complexes, where B = IPA, NBA, DAP, 4MeImid, and MGD were generated using the calculated harmonic vibrational frequencies (scaled by a factor of 0.97) and IR intensities. The theoretical linear IR spectra were broadened using a 20 cm^{-1} fwhm Gaussian line shape to account for the effects of multiple photon excitation and to allow for meaningful comparison to the experimental IRMPD spectra. Details of the theoretical calculations are given in **Chapter 2**.

7.4. Results

7.4.1 IRMPD Action Spectra

Photodissociation of the $(B)H^+(18C6)$ complexes, where B = IPA, NBA, DAP, 4MeImid, and MGD results in the formation of a variety of product ions as listed in **Table 7.1**. Consistent with our CID studies, loss of intact neutral 18C6 is observed upon IRMPD of all five $(B)H^+(18C6)$ complexes, reactions 7.1

$$(B)H^+(18C6) + Xe \rightarrow H^+(B) + 18C6 + Xe \quad (7.1)$$

Loss of the neutral base was also observed in competition with loss of 18C6 for all five $(B)H^+(18C6)$ complexes, reactions 7.2,

$$(B)H^+(18C6) + Xe \rightarrow H^+(18C6) + B + Xe \quad (7.2)$$

This is again consistent with CID results for the complexes to 4MeImid, NBA, and IPA. However, $H^+(18C6)$ was not observed upon CID of the $(MGD)H^+(18C6)$ and $(DAP)H^+(18C6)$ complexes,[36] suggesting that the this channel is relatively low in energy but entropically unfavorable, such that its production is enhanced by the slow heating in

the IRMPD process. Sequential dissociation of the primary H^+(B) and H^+(18C6) was observed for several systems, see **Table 7.1**.

The IRMPD yield was determined from the precursor ion intensity (I_p) and the sum of fragment ion intensities (I_{fi}) after laser irradiation at each frequency as shown in Eq. 7.3

$$\text{IRMPD yield} = \left(\sum_i I_{f_i}\right) \Big/ \left(I_p + \sum_i I_{f_i}\right) \tag{7.3}$$

The IRMPD yield was normalized linearly with laser power to correct for changes in the laser power as a function of the photon energy, i.e., the wavelength of the FEL.

IRMPD spectra were obtained for five (B)H^+(18C6) complexes, where B = IPA, NBA, DAP, 4MeImid, and MGD, over the range extending from ~600 to 1800 cm^{-1} and are compared in **Figure 7.2**. As can be seen in the figures, these complexes exhibit very similar spectral features with modest variations that allow straightforward differentiation of most of the complexes from one another. The measured IRMPD action spectrum of the (IPA)H^+(18C6) complex exhibits a very intense broad band at ~1100 cm^{-1} that is a factor of four more intense than the next most intense band at 950 cm^{-1}. Ten weak bands are visible at ~830, 860, 1210, 1250, 1300, 1350, 1400, 1470, 1530, and 1600 cm^{-1}. The measured IRMPD action spectrum of the (NBA)H^+(18C6) complex is very similar to that of the (IPA)H^+(18C6) complex. The weak bands at 1210 and 1400 cm^{-1} observed for the (IPA)H^+(18C6) complex are not observed in the IRMPD action spectrum of the (NBA)H^+(18C6) complex. Thus, these very minor features are the only bands that can be used to distinguish the (IPA)H^+(18C6) and (NBA)H^+(18C6) complexes. The measured IRMPD action spectrum of the (DAP)H^+(18C6) complex also exhibits similar features as compared to those of the (IPA)H^+(18C6) and (NBA)H^+(18C6)

complexes, except that the weak shoulder at 1050 cm^{-1} is better resolved. An unresolved shoulder at 1385 cm^{-1} also appears in the measured IRMPD action spectrum of the $(DAP)H^+(18C6)$ complex. However, the analogous peak is better resolved in the measured IRMPD action spectrum of the $(IPA)H^+(18C6)$ complex, but is not observed in the measured IRMPD action spectrum of the $(NBA)H^+(18C6)$ complex. Another distinguishing feature for the $(DAP)H^+(18C6)$ complex is the two poorly resolved bands at 1460 and 1475 cm^{-1}, which are observed as a single unresolved band at 1470 cm^{-1} in the measured IRMPD action spectra of the $(IPA)H^+(18C6)$ and $(NBA)H^+(18C6)$ complexes. The measured IRMPD action spectrum of the $(4MeImid)H^+(18C6)$ complex exhibits more complicated features. A sharp peak at 615 cm^{-1} and a partially resolved band at 780 cm^{-1} are observed as characteristic features for the $(4MeImid)H^+(18C6)$ complex. The bands at 830 and 855 cm^{-1} in the measured IRMPD action spectra of the complexes to IPA, NBA and DAP are also observed for the $(4MeImid)H^+(18C6)$ complex, but are less well resolved. In addition, these two bands exhibit similar intensities in the measured IRMPD action spectrum of the $(4MeImid)H^+(18C6)$ complex, whereas in that of the $(IPA)H^+(18C6)$, $(NBA)H^+(18C6)$, and $(DAP)H^+(18C6)$ complexes, the band at 830 cm^{-1} is more intense. An unresolved shoulder at 915 cm^{-1} and a weak band at 1000 cm^{-1} are observed as unique features in the measured IRMPD action spectrum of the $(4MeImid)H^+(18C6)$ complex. The band at 1530 cm^{-1} observed in the measured IRMPD action spectra of the primary amines, IPA, NBA and DAP, is not observed for the $(4MeImid)H^+(18C6)$ complex. The broad band observed at 1600 cm^{-1} in the measured IRMPD action spectra of the complexes to IPA, NBA, and DAP is better resolved and is blue shifted by 20 cm^{-1} in the spectrum of the

(4MeImid)H^+(18C6) complex. The measured IRMPD action spectrum of the (MGD)H^+(18C6) complex exhibits more complicated features. The broad band at 630 cm^{-1} and an unresolved weak shoulder at 715 cm^{-1} are observed as characteristic features. Similar to the (4MeImid)H^+(18C6) complex, the bands at 830 and 855 cm^{-1} exhibit similar intensities. Two additional very weak bands at 1430 and 1570 cm^{-1} are observed in the measured IRMPD action spectrum of the (MGD)H^+(18C6) complex. The broad band observed at 1600 cm^{-1} in the measured IRMPD action spectra of the complexes to IPA, NBA, and DAP is blue shifted by 20 cm^{-1} in the spectrum of the (MGD)H^+(18C6) complex. Another unique feature in the measured IRMPD action spectrum of the (MGD)H^+(18C6) complex is the relatively intense feature at 1690 cm^{-1}.

7.4.2. Theoretical Results

Theoretical structures for the (B)H^+(18C6) complexes were calculated as described in the Theoretical Calculations Section. Enthalpies and Gibbs free energies of the stable structures of the (B)H^+(18C6) complexes found relative to the ground-state structure calculated at the B3LYP/6-311+G(2d,2p) and MP2(full)/6-311+G(2d,2p) levels of theory, including zero-point energy (ZPE) and thermal corrections at 298 K, are listed in **Table 7.2**. The ground-state and stable low-energy conformations of the (B)H^+(18C6) complexes are shown in **Figure S2** of the Supplementary Information of reference 26 along with the MP2(full)/6-311+G(2d,2p) relative free energies at 298 K. Linear IR spectra and the corresponding optimized geometries obtained from theoretical calculations are compared to the experimental IRMPD action spectra for the five (B)H^+(18C6) complexes in **Figures 7.3** through **7.7**. Energetics computed using

MP2(full) theory are expected to be more reliable, therefore, the following discussion will focus on the geometries and energetics calculated at MP2(full)/6-311+G(2d,2p)//B3LYP/6-31G* level of theory unless otherwise specified. In the ground-state conformations of all five (B)H^+(18C6) complexes, the proton binds to the peptidomimetic base, which interacts with 18C6 via multiple N–H···O hydrogen bonds, even when the PA of 18C6 exceeds that of the peptidomimetic base. The conformation of 18C6 in the (IPA)H^+(18C6), (NBA)H^+(18C6), and (DAP)H^+(18C6) complexes bears great similarity to the D_{3d} structure of the neutral crown with a nucleophilic cavity in the center for interaction with the protonated base, whereas in the (4MeImid)H^+(18C6) and (MGD)H^+(18C6) complexes, the conformation of 18C6 is distorted and leads to involvement of different O atoms in the binding.

7.4.2.1. (IPA)H^+(18C6)

In the ground-state **A** conformer of the (IPA)H^+(18C6) complex, the proton binds to the amino nitrogen atom of IPA, and the protonated amino group interacts with 18C6 via three nearly ideal N–H···O hydrogen bonds (see **Figure 7.3**). In conformers **B**, **C**, **D**, and **E**, the H^+(IPA) moiety exhibits a very similar conformation to that found in the ground-state structure, which interacts with 18C6 via three nearly ideal (nearly linear) N–H···O hydrogen bonds. These structures differ primarily in ∠OCCO dihedral angles of the 18C6 moiety. In conformers **F**, **G**, and **H**, the primary amino group of the H^+(IPA) moiety rotates along the N–C bond, interacting with 18C6 via three nearly ideal (nearly linear) N–H···O hydrogen bonds. In conformer **I**, the proton binds between the O1 and O3 atoms of 18C6 to form H^+(18C6), and the neutral amino group of IPA interacts with

the O2 and O4 atoms of 18C6 via two N–H···O hydrogen bonds. Binding of the proton to 18C6 in these complexes is much less favorable than to the base, such that this conformer is calculated to be 197.7 kJ/mol less favorable than the ground-state **A** conformation.

7.4.2.2. (NBA)H^+(18C6)

In the ground-state **A** conformer of the (NBA)H^+(18C6) complex, the proton binds to the amino nitrogen atom of NBA, and the protonated amino group interacts with 18C6 via three nearly ideal (nearly linear) N–H···O hydrogen bonds (see **Figure 7.4**). The H^+(NBA) moiety exhibits an extended zigzag conformation. The excited low-energy conformers, **B** and **C**, differ from the ground-state conformation in the conformation of the H^+(NBA) moiety where the orientations of the CH_2 groups and ∠CCCC dihedral angles differ resulting in unfavorable steric interactions that destabilize the complex, whereas the conformation of 18C6 in these conformers is very similar to that in the ground-state **A** conformer. In contrast, in conformers **D** and **E**, the H^+(NBA) moiety exhibits a extended zigzag conformation similar to that in the ground-state structure, whereas the conformation of 18C6 differs in the ∠OCCO dihedral angles. In the low-energy conformers **F**, **G**, **H**, and **I**, both the H^+(NBA) and 18C6 moieties exhibit different ∠CCCC dihedral angles in the H^+(NBA) moiety and ∠OCCO dihedral angles in the 18C6 moiety. In conformer **J**, which lies 208.9 kJ/mol higher in Gibbs free energy, the proton binds between the O1 and O3 atoms of 18C6 to form H^+(18C6), and the neutral amino group of NBA interacts with the O2 and O4 atoms of 18C6 via two N–H···O

hydrogen bonds. There is clearly a very strong preference for binding of the proton to NBA over 18C6 within this complex.

7.4.2.3. (DAP)H^+(18C6)

In the ground-state **A** conformer of the (DAP)H^+(18C6) complex, the proton binds to one of the amino nitrogen atoms of DAP and the protonated amino group interacts with 18C6 via three nearly ideal N–H···O hydrogen bonds (see **Figure 7.5**). The H^+(DAP) moiety exhibits an extended conformation. Several stable conformers, **B**, **C**, **D**, and **F**, are found that differ in the ∠CCCC and ∠NCCC dihedral angles in the H^+(DAP) moiety and ∠OCCO dihedral angles in the18C6 moiety as compared to the ground-state conformer. In conformers **E** and **G**, the H^+(DAP) moiety bears great similarity to the ground-state ring structure of the isolated form, where the two amino groups share the excess proton. The two primary amino groups interact with the oxygen atoms of 18C6 via four N–H···O hydrogen bonds, as shown in **Figure 7.5** and **Figure S1** of the Supplementary Information of reference 26.

7.4.2.4. (4MeImid)H^+(18C6)

In the ground-state **A** conformer of the (4MeImid)H^+(18C6) complex, the proton binds to the N3 atom of 4Meimid to form the H^+(4MeImid) moiety, which binds to a distorted D_{3d} conformer of 18C6 via two N–H···O hydrogen bonds (see **Figure 7.6**). The O1 and O4 atoms of 18C6 are tilted above the nearly planar ring structure forming hydrogen bonds with the secondary amino hydrogen atoms. Another low-energy conformer, **B**, that lies 2.3 kJ/mol higher in Gibbs free energy, is found for the

(4MeImid)H^+(18C6) complex. Conformer **B** differs from the ground-state in the conformation of 18C6, which is flattened somewhat relative to that of the ground-state **A** conformer. Low-energy conformers, **C** through **J** were also found that exhibit varying degrees of distortion of 18C6 as compared to the ground-state conformer of the (4MeImid)H^+(18C6) complex, which destabilize these complexes by 3.6 to 89.2 kJ/mol as compared to the ground-state **A** conformer. In conformer **K**, which lies 150.0 kJ/mol higher in Gibbs energy than the ground-state conformer, the proton binds between the O1 and O3 atoms of 18C6, similar to the ground-state structure of H^+(18C6), but is flattened somewhat. The imine hydrogen atom of 4MeImid interacts with the O4 atom of H^+(18C6) via a single N–H···O hydrogen bond.

7.4.2.5. (MGD)H^+(18C6)

In the ground-state **A** conformer of the (MGD)H^+(18C6) complex, the proton binds to the imino nitrogen atom of MGD to form the H^+(MGD) moiety, which binds to a distorted D_{3d} conformer of 18C6 in which the O1, O2, O4, and O6 atoms point toward the H^+(MGD) moiety, and bind via four N–H···O hydrogen bonds to the O1, O2, and O4 (2) atoms (see **Figure 7.7**). In conformers **B** through **G**, which lie 2.2 to 8.8 kJ/mol higher in Gibbs free energy than the ground-state conformer, the H^+(MGD) moiety also interacts with 18C6 via four N–H···O hydrogen bonds. However, distortion of the 18C6 moiety leads to binding to different O atoms and results in destabilization of the complex. In conformer **H** of the (MGD)H^+(18C6) complex, the proton is bound to the primary amino group to form the H^+(MGD) moiety, which interacts with 18C6 via three N–H···O hydrogen bonds as shown in **Figure S2** of the Supplementary Information of

reference 26. Clearly, binding to the imino nitrogen of MGD is favored over the amino nitrogen atom as conformer **H** lies 44.0 kJ/mol higher in Gibbs free energy than the ground-state conformer. 18C6 exhibits an approximately D_{3d} conformation where the six oxygen atoms are oriented toward the interior of the ring and interact with the primary amino hydrogen atoms of the protonated H^+(MGD) moiety via three N–H···O hydrogen bonds. Conformer **I**, which lies 46.2 kJ/mol higher in Gibbs free energy than the ground-state conformer, is similar to conformer **H**, but differs in the orientation of one of the amino hydrogen atoms that interact with the oxygen atoms of 18C6. Conformer **J** lies 69.0 kJ/mol higher in Gibbs free energy than the ground-state conformer. In this conformer, the proton also binds to the imino nitrogen atom to form the H^+(MGD) moiety, which interacts with the O1 (2) and O4 atoms of 18C6 via three N–H···O hydrogen bonds. In conformer **K**, which lies 188.3 kJ/mol higher in Gibbs energy than the ground-state conformer, the proton binds between the O1 and O3 atoms of 18C6, similar to the ground-state structure of H^+(18C6), but is flattened somewhat. The amino hydrogen atom of MGD interacts with the O4 atom of H^+(18C6) via a single N–H···O hydrogen bond.

7.5. Discussion

7.5.1. Comparison of Experimental IRMPD and Theoretical IR Spectra of (IPA)H^+(18C6)

The experimental IRMPD action spectrum along with the calculated IR spectra and structures of the ground-state and three select excited stable conformers that exhibit distinguishable IR spectra found for the (IPA)H^+(18C6) complex are compared in

Figure 7.3. The comparison shows excellent agreement between the IRMPD action spectrum and the calculated IR spectrum for the ground-state **A** conformer. All bands match almost perfectly, confirming that the ground-state structure is accessed in the experiments.

The IR spectra of conformers **B**–**F** are very similar to the IR spectrum of conformer **A** and thus cannot be readily differentiated. Conformers **B** trough **F** differ from conformer **A** primarily in the conformation of the 18C6 moiety where distortions of the ∠OCCO dihedral angles destabilize these conformers, but do not significantly alter the frequencies of most of the vibrational modes. Therefore, these conformers may also contribute to the measured IRMPD spectrum. Conformers **G** and **H** differ from conformer **A** by the rotation of the amino group of the H^+(IPA) moiety as well as the ∠OCCO dihedral angles of 18C6 moiety. As a result, the IRMPD spectra of conformers **G** and **H** exhibit moderate differences. The band at 825 cm^{-1} is nicely reproduced in the spectra of conformers **A** and **G,** whereas in the spectrum of conformer **H**, it is predicted as two partially resolved bands. The weak shoulder at 1050 cm^{-1} is reproduced in the spectra of conformers **A**, **G**, and **H** of the (IPA)H^+(18C6) complex. However, in the spectrum of conformer **H**, the band is red shifted by 20 cm^{-1} and becomes more intense, suggesting that conformer **H** is not a significant contributor to the IRMPD action spectrum. The most intense band centered at 1106 cm^{-1} is in good agreement with the IR spectra of conformers **A**, **G**, and **H** in both its position and shape. The bands at 1243 and 1285 cm^{-1} are observed in the spectrum of conformer **A**. The band at 1285 cm^{-1} is broadened in the spectrum of conformer **G** and is blue shifted by 20 cm^{-1}. These two bands are also observed in the spectrum of conformer **G**, but are less resolved. The

band at 1360 cm^{-1} is reproduced nicely in position and shape in the spectra of conformers **A**, **G**, and **H**. The minor band centered at 1475 cm^{-1} is also nicely reproduced in the spectra of conformers **A**, **G**, and **H**, both in shape and position. The band at 1529 cm^{-1} is observed in the spectra of conformers **A**, **G**, and **H**, but is blue shifted by 50 cm^{-1}. The weak band at 1604 cm^{-1} is nicely reproduced in the spectra of conformers **A** and **H** in shape, but is blue shifted by 40 cm^{-1}. It is also observed in the spectrum of conformer **G**, but broadened.

The calculated linear IR spectra of conformers **A**, **B**, **C**, **D**, **E**, **F**, **G**, and **H** match well with the measured IRMPD action spectrum of $(IPA)H^+(18C6)$ complex, suggesting they may all be accessed in the experiments. However, conformers **E, F**, **G**, and **H** lie more than 11 kJ/mol higher in Gibbs free energy as compared to conformer **A**, suggesting that if the computed energetics are reliable, these conformers are not significant contributors to the measured IRMPD action spectrum. Significant differences are observed in the computed IR spectra when the proton is bound to 18C6, conformer **I**, indicating that conformer **I** is not accessed in the experiments. Overall, the mode of binding of the protonated base to 18C6 in the $(IPA)H^+(18C6)$ complex is clearly differentiated, whereas minor distortions of 18C6 cannot be readily distinguished.

The bands at 825, 1243, and 1285 cm^{-1} correspond to the torsions of the CH_2 groups of 18C6. The band at 953 cm^{-1} observed in the spectra of conformers **A**, **G**, and **H** of the $(IPA)H^+(18C6)$ complex is the result of C–C stretching of 18C6. The most intense band centered at 1106 cm^{-1} corresponds to mixed character modes involving C–O stretching. The band at 1360 cm^{-1} corresponds to the CH_2 wagging of 18C6. The minor band centered at 1475 cm^{-1} arises from CH_2 scissoring motions of 18C6. The

band at 1529 cm^{-1} is characteristic of NH_3 wagging. The weak band at 1604 cm^{-1} corresponds to scissoring of the NH_2 group.

7.5.2. Comparison of Experimental IRMPD and Theoretical IR Spectra of (NBA)H^+(18C6)

The experimental IRMPD action spectrum along with the calculated IR spectra and structures of the ground-state and three select excited stable conformers that exhibit distinguishable IR spectra found for the (NBA)H^+(18C6) complex are compared in **Figure 7.4**. The comparison shows excellent agreement between IRMPD action spectrum and the calculated IR spectrum for the ground-state **A** conformer. All bands match almost perfectly, confirming that the ground-state structure is accessed in the experiments.

The IR spectra of conformers **B**, **C**, and **D** are virtually identical to that of **A,** therefore conformers **B**, **C**, and **D** may also be contributing to the measured IRMPD spectrum. The spectra of conformers **F** and **G** are very similar to **E**, except the band at 825 cm^{-1} is observed as two partially resolved bands. In contrast, this band is not observed in the spectrum of conformer **J**, where the proton is bound to 18C6 rather than NBA. The bands at 825, 1050, 1106, and 1475 cm^{-1} are in good agreement with the spectra of **A**, **B**, and **E** in both their position and shape. In contrast, the two semi-resolved bands at 1260 and 1300 cm^{-1} are in good agreement in position, but not in relative intensity. The analogous band at 1542 cm^{-1} of the calculated IR spectra of conformers **A** and **B** is blue shifted by 30 cm^{-1} for conformer **E**, and by 60 cm^{-1} for conformer **J**. The weak band at 1608 cm^{-1} is nicely reproduced in the spectra of

conformers **A** and **B** in shape, but is blue shifted by 50 cm^{-1}. The band in spectra **E** is broadened and arises from coupling of the two NH_2 scissoring motions.

The calculated linear IR spectra of conformers **A**, **B**, **C**, **D**, and **E** match well with the measured IRMPD action spectrum of the $(NBA)H^+(18C6)$ complex, suggesting that conformers **A**, **B**, **C**, **D**, and **E** may be accessed in the experiments. However, conformers **D** and **E** are computed to lie 17.7 and 30.0 kJ/mol higher in Gibbs free energy as compared to conformer **A**, respectively, suggesting that they are not likely to be significant contributors to the measured IRMPD action spectrum. Again, there are significant differences in the calculated IR spectrum of conformer **J**, where the proton binds to 18C6, and the IRMPD action spectrum of $(NBA)H^+(18C6)$, indicating that conformer **J** is not accessed in the experiments. Overall, the $B–H^+\cdots18C6$ binding mode in $(NBA)H^+(18C6)$ complex is clearly differentiated, whereas modest distortions of the backbone of NBA or 18C6 cannot be readily distinguished.

Examining the vibrational information provided for $(NBA)H^+(18C6)$ by DFT calculations, the bands at 825, 1260, and 1350 cm^{-1} correspond to CH_2 torsions of 18C6. The absorption band at 953 cm^{-1} is the result of C–C stretching of 18C6. The small shoulder at 1040 cm^{-1} is due to the wagging of the terminal CH_3 group of $H^+(NBA)$. The weak band at 1050 cm^{-1} corresponds to the C–O stretch. The most intense band at 1106 cm^{-1} arises from mixed character modes involving C–O stretching. The band at 1357 cm^{-1} corresponds to CH_2 wagging of 18C6. The minor band at 1475 cm^{-1} corresponds to CH_2 scissoring motions of 18C6. The band at 1542 cm^{-1} corresponds to NH_3 wagging of the protonated amino group of the $H^+(NBA)$ moiety. The weak band at 1608 cm^{-1} arises from NH_2 scissoring motions.

7.5.3. Comparison of Experimental IRMPD and Theoretical IR Spectra of (DAP)H^+(18C6)

The experimental IRMPD action spectrum along with the calculated IR spectra and structures of the ground-state and three select excited stable conformers that exhibit distinguishable IR spectra found for the (DAP)H^+(18C6) complex are compared in **Figure 7.5**. Excellent agreement between the measured IRMPD action spectrum and the calculated IR spectrum for the ground-state **A** conformer is found. All bands match almost perfectly, confirming that the ground-state structure is accessed in the experiments.

The IR spectra of conformers **B**, **C**, and **D** are virtually identical to that of conformer **A** except that the bands at 838 and 1050 cm^{-1} are slightly less intense. Therefore, these conformers may also be contributing to the measured IRMPD spectrum. The band at 838 cm^{-1} is nicely reproduced in shape in the spectrum of conformer **A**, but is slightly red shifted by 10 cm^{-1}. This band exhibits higher intensity in the spectrum of conformer **A** than **E**, in which the NH_2 group cyclizes to share the excess proton of the protonated amino group. Frequency calculations of such shared proton modes are often unreliable.[37] This band is broadened and red shifted by 250 cm^{-1} in the spectrum of conformer **F**. The absorption band at 960 cm^{-1} is reproduced in shape and position in the spectra of conformers **A**, **E**, and **G**, whereas this band is red shifted by 15 cm^{-1} in the spectrum of conformer **F**. The shoulder at 1050 cm^{-1} is better resolved in the spectra of conformers **A**, **E**, and **G**, as compared to that of conformer **F**. Similar to the other (B)H^+(18C6) systems, the most intense band is observed at 1106 cm^{-1}, and is in good agreement with the spectra of conformers **A** and **E** in both shape

and position, whereas this band is red shifted by 10 cm^{-1} in the spectra of conformers **F** and **G**. The two bands centered at 1252 and 1293 cm^{-1} are in good agreement with the spectra of conformers **A**, **E**, and **G** in both position and relative intensity. These two bands in the calculated IR spectra of conformer **F** are better resolved, but their relative intensities are reversed. The band at 1360 cm^{-1} is in good agreement with the spectra of conformers **A**, **E**, **F**, and **G** both in position and shape. The minor band at 1475 cm^{-1} is also reproduced nicely in shape in the spectra of conformers **A**, **E**, **F**, and **G**. The band at 1547 cm^{-1} is nicely reproduced in the spectrum of conformer **A** in shape, but is blue shifted by 30 cm^{-1}. In contrast, in the spectrum of conformer **E**, where the NH_2 group cyclizes and shares the excess proton with the protonated amino group, this band is red shifted by 10 cm^{-1} and overlaps the band at 1470 cm^{-1}. The characteristic band observed at 1620 cm^{-1} is blue shifted by 40 cm^{-1} in the spectrum of conformer **A**. In the calculated IR spectrum of conformer **E**, two bands are observed at 1650 and 1700 cm^{-1}. The two bands are separated in the spectrum of conformer **E**, where the two amino groups share the excess proton, whereas in the spectrum of conformer **A**, the two bonds merge into a single broad feature. In the spectrum of conformer **G** in which the two amino groups also share the excess proton, this feature is further broadened.

The calculated linear IR spectrum of the ground-state **A** conformer provides an excellent match to the measured IRMPD action spectrum of the $(DAP)H^+(18C6)$ complex, suggesting that conformer **A** is accessed in the experiments. The IR spectra of conformers **B**, **C**, and **D** are very similar to that of conformer **A** and thus are also in good agreement with the measured IRMPD action spectrum, suggesting that conformers **B**, **C**, and **D** may also be accessed to the experiments. The absence of the

two minor bands that appear at 1650 and 1700 cm^{-1} in the IR spectrum of conformer **E** rule out the possibility that it is a significant contributor to the measured IRMPD action spectrum. Although the spectrum of conformer **F** exhibits good agreement with the measured IRMPD action spectrum, its higher relative Gibbs free energy as compared to conformer **A**, 24.0 kJ/mol, suggests that it is probably not an important contributor. The broad unresolved bands in the region from 780 to 880 cm^{-1}, 1220 to 1320 cm^{-1}, and 1620 to 1740 cm^{-1} of the IR spectrum of conformer **G** suggest that this conformer is not accessed in the experiments. Thus, the proton binding site and the conformation of the H^+(DAP) moiety in the (DAP)H^+(18C6) complex is clearly identified, whereas modest distortions of 18C6 cannot be readily distinguished.

Similar to the other (B)H^+(18C6) complexes, the band at 838 cm^{-1} arises from CH_2 torsions of 18C6. However, NH_2 wagging of H^+(DAP) also contributes to the intensity of this band. As a result, this band is of higher intensity in the spectra of conformers **A** than **E**, in which the NH_2 group cyclizes to share the excess proton with the protonated amino group. This band is enhanced only in the spectra of the (DAP)H^+(18C6) complex, which possesses an additional CH_2 group. CH_2 torsions of 18C6 are also minor contributors to this band. As a result, this feature is also observed in other (B)H^+(18C6) complexes, but with much lower intensity. This band in the spectrum of conformer **F** is broadened and red shifted by 20 cm^{-1} as a result of contributions from C–C stretching and CH_2 torsions of the H^+(DAP) moiety. The absorption band at 960 cm^{-1} is the result of C–C stretching of 18C6. The shoulder at 1050 cm^{-1} corresponds to the C–O stretch. The C2–C3 and C3–C4 stretches of the H^+(DAP) moiety also contribute to the intensity of this band. Similar to the other

(B)H^+(18C6) systems, the most intense band appears at 1106 cm^{-1} and arises from mixed character modes involving C–O stretching. The two bands centered at 1252 and 1293 cm^{-1} correspond to CH_2 torsions of 18C6. The band at 1360 cm^{-1} corresponds to CH_2 wagging of 18C6. The minor band at 1475 cm^{-1} arises from CH_2 scissoring motion of 18C6. The band at 1547 cm^{-1} corresponds to wagging of the protonated amino group. The characteristic band observed at 1620 cm^{-1} corresponds to the scissoring of the NH–NH bonds of the NH_2 and NH_3 groups. In the calculated IR spectrum of conformer **E**, two bands are observed at 1650 and 1700 cm^{-1} that correspond to the NH–NH scissoring of the NH_2 and NH_3 groups, respectively.

7.5.4. Comparison of Experimental IRMPD and Theoretical IR Spectra of (4MeImid)H^+(18C6)

The experimental IRMPD action spectrum along with the calculated linear IR spectra and structures of the ground-state and three select excited stable conformers that exhibit distinguishable IR spectra found for the (4MeImid)H^+(18C6) complex are compared in **Figure 7.6**. The calculated IR spectrum of the ground-state conformer of the (4MeImid)H^+(18C6) complex provides the best match to the experimental spectrum. All bands match almost perfectly, confirming that the ground-state structure is accessed in the experiments.

The calculated IR spectra of conformers **B**, **C**, **D**, and **E** are very similar to that of the ground-state conformer **A**, except that the band at 948 cm^{-1} is slightly less well resolved. The band at 615 cm^{-1} is reproduced nicely in shape in the spectrum of conformer **A**, but is red shifted by 10 cm^{-1}. The band at 783 cm^{-1} is only observed in the

spectrum of conformer **A**. The bands at 831 and 854 cm^{-1} are reproduced in position nicely in the spectrum of conformer **A**, but are less well resolved. These bands are also observed in the spectra of conformers **F**, **G**, and **K**, but are not resolved. The absorption band at 948 cm^{-1} is reproduced in the spectra of conformers **A**, **F**, and **G** only in position, but is broadened. The most intense band centered at 1116 cm^{-1} of the IRMPD action spectrum is only reproduced in the calculated IR spectrum of conformer **A** both in shape and position. There are significant differences in the calculated IR spectrum of conformer **F** and the measured IRMPD action spectrum of (4MeImid)H^+(18C6) complex. The calculated IR spectra of conformers **H** and **I** are similar to that of conformers **A** and **G**, respectively, except the band at 1116 cm^{-1} is slightly less resolved. Overall, the (4MeImid)H^+···18C6 binding mode in the (4MeImid)H^+(18C6) complex is clearly differentiated, whereas the distortion of 18C6 cannot be readily distinguished.

The bands at 1255, 1300, 1350, 1467, and 1625 cm^{-1} of the IRMPD action spectrum are matched almost perfectly in position and relative intensity in the spectra of conformers **A**, **B**, **C**, **D**, and **E**, suggesting that these conformers may be experimentally accessed. However, conformer **E** lies 13.5 kJ/mol higher than the ground-state **A** conformer, suggesting that if the computed energetics are reliable that it is unlikely to be a significant contributor to measured IRMPD action spectrum. These bands are reproduced nicely in position in the spectrum of conformer **F**, but not in shape. The broadening of bands between 1040 and 1180 cm^{-1} in the spectra of conformers **F** and **G** rule out the possibility that these conformers are significant contributors to the measured IRMPD spectrum. The calculated IR spectrum of excited conformer **K** exhibits significant differences from the measured IRMPD action spectrum. The

absence of a band at 1050 cm^{-1} in the measured IRMPD action spectrum suggests that conformer **K** is not accessed in the experiments.

The band at 615 cm^{-1} corresponds to the N=C=N wagging. The band at 783 cm^{-1} arises from C–H out-of-plane bending of the imidazole ring. The band at 831 cm^{-1} arises from CH_2 torsions of 18C6, while the band at 854 cm^{-1} corresponds to N–H out-of-plane bending. These bands are also observed in the spectra of conformers **F**, **G**, and **K** as broad unresolved features corresponding to mixed-character modes involving N–H out-plane bending and CH_2 torsions. The absorption band at 948 cm^{-1} is the result of C–C stretching of 18C6. The calculated IR spectrum of conformer **A** suggests that N–H out-plane bending also contributes to the band at 948 cm^{-1} of the IRMPD action spectrum. The band at 1630 cm^{-1} corresponds to C=C stretching of the imidazole ring.

7.5.5. Comparison of Experimental IRMPD and Theoretical IR Spectra of (MGD)H^+(18C6)

The experimental IRMPD action spectrum and the calculated IR spectra of the ground-state and three select excited stable conformers that exhibit distinguishable IR spectra of the (MGD)H^+(18C6) complex are compared in **Figure 7.7**. The comparison shows excellent agreement between the IRMPD action spectrum and the calculated IR spectrum for the ground-state **A** conformer, indicating that it is accessed in the experiments.

The calculated IR spectrum for conformers **B** and **C** are very similar to that of conformer **A**, except that the bands at 613 and 656 cm^{-1} are unresolved. The calculated IR spectrum for conformers **D**, **E**, **F**, and **G** are very similar to that of conformer **A**,

except that the band at 743 cm^{-1} is more intense. The band observed at 643 cm^{-1} in the IRMPD action spectrum is observed in the calculated IR spectrum of the conformer **A**, but is red shifted by 30 cm^{-1}. This band is characteristic for conformer **A**, suggesting that conformer **A** is the experimentally accessed conformer. The bands at 837 and 856 cm^{-1} are observed in the spectrum of conformer **A**, but are unresolved. These bands are also observed in the spectra of conformers **H** and **I**, but are further red shifted by 20 cm^{-1}. The absorption band at 946 cm^{-1} is reproduced in shape and position in the IR spectra of conformers **A**, **H**, and **I**, and red shifted by 10 cm^{-1} in the IR spectrum of conformer **J**. The most intense band centered at 1110 cm^{-1} is observed in the spectra of conformers **A**, **H**, **I**, and **J**. The split of the most abundant band is nicely reproduced in the spectrum of conformer **A** as a shoulder at 1080 cm^{-1}, but is not observed in the calculated IR spectra of other conformers. The bands at 1252, 1297, and 1352 cm^{-1} are in good agreement with the calculated IR spectra of conformers **A**, **H**, **I**, and **J** in position, but the relative intensities are only in good agreement with the spectrum of conformer **A**. The band at 1463 cm^{-1} is reproduced in the spectra of conformers **A**, **H**, and **I** in both shape and position. In the spectra of conformers **H**, and **I**, the band at ~1533–1539 cm^{-1} is observed, but not in the spectrum of conformer **A**. The band at 1629 cm^{-1} is reproduced nicely in the spectra of conformers **A**, **H**, **I**, and **J**. In contrast, the band at 1687 cm^{-1} was only observed in the spectra of conformers **A** and **J**, but not in the spectra of conformers **H** and **I**.

The calculated linear IR spectra of conformers **A, B**, **C**, **D**, **E**, **F**, and **G** provide very good match to the measured IRMPD action spectrum of the $(MGD)H^+(18C6)$ complex, suggesting that these conformers may be accessed in the experiments.

However, conformers **D**, **E**, **F**, and **G** lie more than 7 kJ/mol higher in free energy than the ground-state **A** conformer, suggesting that if the computed energetics are reliable they are not significant contributors to the measured IRMPD action spectrum of the (MGD)H^+(18C6) complex. The band observed at 643 cm^{-1} in the IRMPD action spectrum is characteristic, and is not observed in the spectra of conformers **I** and **J**, indicating that conformers **I** and **J** are probably not accessed in the experiments. The band at 1687 cm^{-1} of the IRMPD action spectrum is not observed in the spectra of conformers **H** and **I**. This is also an indicator that conformers **H** and **I** are not significant contributors to the IRMPD action spectrum. Overall, the proton binding sites and the conformation of the H^+(MGD) moiety in the (MGD)H^+(18C6) complex is clearly identified, whereas minor distortions in the conformation of 18C6 cannot be readily distinguished.

The band observed at 643 cm^{-1} arises from two different motions, NH_2 wagging and twisting at 604 and 657 cm^{-1} of the spectrum of conformer **A**, respectively. The bands at 837 and 856 cm^{-1}, which were also observed for the other complexes, correspond to CH_2 torsions of 18C6. The absorption band at 946 cm^{-1} is the result of C–C stretching of 18C6. The most intense band centered at 1110 cm^{-1} corresponds to mixed character modes involving C–O stretching of 18C6. The bands at 1252, 1297, and 1352 cm^{-1} correspond to CH_2 torsions of 18C6. The band at 1463 cm^{-1} corresponds to CH_2 scissoring of 18C6. In the spectra of conformers **H** and **I**, the band at ~1533–1539 cm^{-1} arises from wagging of the protonated amino group of the H^+(MGD) moiety, which is not observed in the spectrum of conformer **A** because it does not possess a protonated amino group. The band at 1629 cm^{-1} corresponding to C=NH stretching is

reproduced nicely in the spectra of conformers **A**, **H**, **I**, and **J** because all four conformers possess this moiety. In contrast, the band at 1687 cm^{-1} corresponds to the H_2N=C stretching and is only observed in the spectra of conformers **A** and **J**. In the spectra of conformers **H** and **I**, this band is not observed because in conformers **H** and **I** the imino moiety is protonated.

7.6. Conclusions

The IRMPD action spectra of five protonated peptidomimetic base–18-crown-6 complexes, $(B)H^+(18C6)$, were measured over the IR fingerprint region extending from 600 to 1800 cm^{-1}. Comparison of the measured IRMPD spectra with linear IR spectra of the stable low-energy conformers calculated at the B3LYP/6-31G* level of theory allows identification of the experimentally accessed conformations of each system. In all systems, the agreement between the measured IRMPD spectra and the theoretical linear IR spectra of the ground-state conformations is excellent, indicating that these conformers were accessed in the experiments. In the ground-state conformations of the $(B)H^+(18C6)$ complexes, the proton binds to the peptidomimetic base and interacts with 18C6 via two, three, or four N–H···O hydrogen bonds. The calculated IR spectra of the conformers in which the proton binds to 18C6 for all five $(B)H^+(18C6)$ complexes differ markedly from the IRMPD action spectrum, ruling out the possibility that these conformers are accessed in the experiments. Comparison of the calculated IR spectra and measured IRMPD action spectrum of the $(DAP)H^+(18C6)$ complex suggests that the $H^+(DAP)$ moiety exhibits an extended conformation and interacts with 18C6 via three nearly ideal N–H···O hydrogen bonds. Comparison of the calculated IR spectra

and measured IRMPD action spectrum of the (MGD)H^+(18C6) complex suggests that the proton binds to the imino nitrogen and the protonated H^+(MGD) moiety interacts with 18C6 via four non-ideal N–H···O hydrogen bonds. Several low-energy conformers of the (B)H^+(18C6) complexes may be accessed in the experiments, however, the computed relative stabilities as compared to the ground-state conformer suggest that they are unlikely to be significant contributors to the measured IRMPD action spectra of the (B)H^+(18C6) complexes. Overall the proton binding sites and the conformations of the protonated base are clearly identified, whereas minor distortions in the conformation of 18C6 cannot be distinguished in these (B)H^+(18C6) complexes.

7.7. References

(1) Lehn, J.-M. *Angew. Chem., Int. Ed. Engl*. **1988**, *27*, 89.

(2) Kozak, R. W.; Waldmann, T. A.; Atcher, R. W.; Gansow, O. A. *Trends Biotechnol.* **1985**, *4*, 259.

(3) Montanari, F.; Tundo, P. *J. Org. Chem*. **1981**, *46*, 2125.

(4) De Jong, F.; Reinhoudt, D. N. *Adv. Phys. Org. Chem.* **1980**, *17*, 279.

(5) Ray, D.; Feller, D.; More, M. B.; Glendening, E. D.; Armentrout, P. B. *J. Phys. Chem.* **1996**, *100*, 16116.

(6) More, M. B.; Ray, D.; Armentrout, P. B. *J. Phys. Chem. A* **1997**, *101*, 831.

(7) More, M. B.; Ray, D.; Armentrout, P. B. *J. Phys. Chem. A* **1997**, *101*, 4254.

(8) More, M. B.; Ray, D.; Armentrout, P. B. *J. Phys. Chem. A* **1997**, *101*, 7007.

(9) More, M. B.; Ray, D.; Armentrout, P. B. *J. Am. Chem. Soc.* **1998**, *121*, 417.

(10) Armentrout, P. B. *Int. J. Mass Spectrom.* **1999**, *193*, 227.

(11) Martinez-Haya, B.; Hurtado, P.; Hortal, A. R.; Hamad, S.; Steill, J. D.; Oomens, J. *J. Phys. Chem. A* **2010**, *114*, 7048.

(12) Hurtado, P.; Gámez, F.; Hamad, S.; Martínez–Haya1, B.; Steill, J. D.; Oomens, J. *J. Chem. Phys.* **2012**, *136*, 114301.

(13) Cooper, T. E.; Carl, D. R.; Oomens, J.; Steill, J. D.; Armentrout, P. B. *J. Phys. Chem. A* **2011**, *115*, 5408.

(14) Julian, R. R.; Beauchamp, J. L. *Int. J. Mass Spectrom.* **2001**, *210/211*, 613.

(15) Julian, R. R.; Beauchamp, J. L. *J. Am. Soc. Mass Spectrom.* **2002**, *13*, 493.

(16) Julian, R. R.; Beauchamp, J. L. *J. Am. Soc. Mass Spectrom.* **2004**, *15*, 616.

(17) Julian, R. R.; Akin, M.; May, J. A.; Stoltz, B. M.; Beauchamp, J. L. *Int. J. Mass Spectrom.* **2002**, *220*, 87.

(18) Julian, R. R.; May, J. A.; Stoltz, B. M.; Beauchamp, J. L. *Int. J. Mass Spectrom.* **2003**, *228*, 851.

(19) Ly, T.; Julian, R. R. *J. Am. Soc. Mass Spectrom.* **2006**, *17*, 1209.

(20) Ly, T.; Julian, R. R. *J. Am. Soc. Mass Spectrom.* **2008**, *19*, 1663.

(21) Liu, Z.; Cheng, S.; Gallie, D. R.; Julian, R. R. *Anal. Chem.* **2008**, *80*, 3846.

(22) Ly, T.; Liu, Z.; Pujanauski, B. G.; Sarpong, R.; Julian, R. R. *Anal. Chem.* **2008**, *80*, 5059.

(23) Yeh, G. K.; Sun, Q.; Meneses, C.; Julian, R. R. *J. Am. Soc. Mass Spectrom.* **2009**, *20*, 385.

(24) van Unen, D.–J.; Engbersen, J. F. J.; Reinhoudt, D. N. *J. Mol. Catal. B: Enzym.,* **2001**, *11*, 87.

(25) Fuji, K.; Tsubaki, K.; Tanaka, K.; Hayashi, N.; Otsubo, T.; Kinoshita, T. *J. Am. Chem. Soc.* **1999**, *121,* 3807.

(26) Chen, Y; Austin, C. A.; Kaczan, C. M.; Berden, G.; Oomens, J.; Rodgers, M. T. *J. Am. Soc. Mass Spectrom.* **2012**, submitted.

(27) Valle, J. J.; Eyler, J. R.; Oomens, J.; Moore, D. T.; van der Meer, A. F. G.; von Heldon, G.; Meijer, G.; Hendrickson, C. L.; Marshall, A. G.; Blakney, G. T. *Rev. Sci. Instrum*. **2005**, *76*, 023103.

(28) Polfer, N. C.; Oomens, J.; Moore, D. T.; von Helden, G.; Meijer, G.; Dunbar, R. C. *J. Am. Chem. Soc.* **2006**, *128*, 517.

(29) Polfer, N. C.; Oomens, J. *Phys. Chem. Chem. Phys*. **2007**, *9*, 3804.

(30) *HyperChem Computational Chemistry Software Package*, Version 5.0; Hypercube Inc: Gainsville, FL, 1997.

(31) Frisch, M. J.; et al. Gaussian 03, Revision C.02, Gaussian, Inc., Wallingford CT, 2004. See **Chapter 2** for full reference.

(32) Frisch, M. J.; et al. *Gaussian 09*, Revision C.01; Gaussian, Inc.: Wallingford, CT, 2009. See **Chapter 2** for full reference.

(33) Becke, A. D. *J. Chem. Phys.* **1993**, *98*, 5648.

(34) Lee, C.; Yang, W.; Parr, R. G. *Phys. Rev. B* **1988**, *37*, 785.

(35) Foresman, J. B.; Frisch, Æ. *Exploring Chemistry with Electronic Structure Methods*, 2nd ed.; Gaussian: Pittsburgh, PA, 1996; p 64.

(36) Chen, Y; Rodgers, M. T. *J. Am. Chem. Soc*. **2012**, *134*, 2313.

(37) Beran, G. J.; Chronister, E. L.; Daemen, L. L.; Moehlig, A. R.; Mueller, L. J.; Oomens, J.; Rice, A.; Santiago-Dieppa, D. R.; Tham, F. S.; Theel, K.; Yaghmaei, S.; Morton, T. H. *Phys. Chem. Chem. Phys.* **2011**, *13*, 20380.

Table 7.1. Reactant and Product Ions Observed upon IRMPD of (B)H^+(18C6) Complexes

Complex	Reactant ion m/z	Product ion m/z	Fragmentation pathway
(IPA)H^+(18C6)	324.2	60	H^+(IPA) + 18C6
		265	H^+(18C6) + IPA
(NBA)H^+(18C6)	338.2	74	H^+(NBA) + 18C6
		265	H^+(18C6) + NBA
		89	$\rightarrow H^+(C_2H_4O)_2 + (C_2H_4O)_4$
(DAP)H^+(18C6)	367.5	103	H^+(DAP) + 18C6
		60	$\rightarrow H^+$(NPA) + EA
		265	H^+(18C6) + DAP
(4MeImid)H^+(18C6)	347.2	83	H^+(4MeImid) + 18C6
		265	H^+(18C6) 4MeImid
(MGD)H^+(18C6)	338.4	74	H^+(MGD) + 18C6
		265	H^+(18C6) + MGD

Table 7.2. Relative Enthalpies and Gibbs Free Energies at 298 K (in kJ/mol) of Stable Conformers of the $(B)H^+(18C6)$ Complexes.[a]

Complex	Conformer	B3LYP		MP2(full)	
		ΔH_{298}	ΔG_{298}	ΔH_{298}	ΔG_{298}
$(IPA)H^+(18C6)$	A	0	0	0	0
	B	7.2	3.5	9.9	6.1
	C	10.7	5.6	15.5	10.4
	D	13.3	10.6	14.4	11.7
	E	12.1	8.3	16.2	12.4
	F	10.3	15.0	14.6	19.3
	G	17.1	20.4	22.2	25.5
	H	21.3	18.6	29.9	27.2
	I	195.1	184.4	208.3	197.7
$(NBA)H^+(18C6)$	A	0	0	0	0
	B	3.9	5.1	2.5	3.6
	C	7.7	8.1	3.9	4.3
	D	17.0	18.6	16.1	17.7
	E	23.6	25.6	27.9	30.0
	F	26.7	27.7	30.3	31.3
	G	26.9	33.2	24.4	30.6
	H	55.3	52.1	67.0	63.9
	I	103.5	99.4	125.0	115.0
	J	201.7	193.2	217.5	208.9
$(DAP)H^+(18C6)$	A	0	0	0	0
	B	5.4	5.5	2.2	3.7
	C	8.0	9.4	4.0	3.8
	D	15.5	21.0	0.4	5.1
	E	20.3	24.5	9.9	14.1
	F	30.0	30.5	23.5	24.0
	G	30.0	37.4	23.8	31.1
	H	198.1	187.5	213.2	202.5
$(4MeImid)H^+(18C6)$	A	0	0	0	0
	B	4.5	0.8	3.0	2.3
	C	3.5	4.1	3.0	3.6
	D	12.0	15.5	1.6	5.1
	E	16.6	19.1	10.9	13.5
	F	27.0	30.1	22.6	25.7
	G	44.5	43.2	41.6	40.4
	H	43.1	39.9	46.2	43.0
	I	39.9	41.9	41.0	43.1
	J	88.6	82.4	95.3	89.2
	K	152.6	145.9	156.7	150.0

Table 7.2. (cont'd) Relative Enthalpies and Gibbs Free Energies at 298 K (in kJ/mol) of Stable Conformers of the $(B)H^+(18C6)$ Complexes.[a]

Complex	Conformer	B3LYP/(kJ/mole)		MP2(full)/(kJ/mole)	
		ΔH_{298}	ΔG_{298}	ΔH_{298}	ΔG_{298}
$(MGD)H^+(18C6)$	A	0	0	0	0
	B	4.2	2.6	1.0	2.2
	C	4.3	3.2	1.8	3.3
	D	14.2	14.5	2.4	7.7
	E	10.7	16.0	7.4	7.7
	F	14.3	16.7	5.9	8.3
	G	10.9	12.2	7.5	8.8
	H	60.9	64.0	41.0	44.0
	I	64.8	68.9	42.1	46.2
	J	88.1	99.4	57.7	69.0
	K	201.8	196.5	193.5	188.3

[a]Based on single point energy calculations performed at the indicated level of theory using the 6-311+G(2d,2p) basis set and the B3LYP/6-31G* optimized geometries including ZPE and thermal corrections with frequencies scaled by a factor of 0.9804.

7.8. Figure Captions

Figure 7.1. Structures of the peptidomimetic nitrogen bases examined as mimics for the N-terminal amino group and the side chains of the basic amino acids, lysine, histidine, and arginine.

Figure 7.2. Infrared multiple photon dissociation action spectra of $(B)H^+(18C6)$ complexes.

Figure 7.3. Comparison of the measured IRMPD action spectrum of $(IPA)H^+(18C6)$ with linear IR spectra predicted for the ground-state and three select stable excited conformers of $(IPA)H^+(18C6)$ calculated at the B3LYP/6-31G* level of theory. The structures and MP2(full)/6-311+G(2d,2p) relative stabilities of each conformer are also shown.

Figure 7.4. Comparison of the measured IRMPD action spectrum of $(NBA)H^+(18C6)$ with linear IR spectra predicted for the ground-state and three select stable excited conformers of $(NBA)H^+(18C6)$ calculated at the B3LYP/6-31G* level of theory. The structures and MP2(full)/6-311+G(2d,2p) relative stabilities of each conformer are also shown.

Figure 7.5. Comparison of the measured IRMPD action spectrum of $(DAP)H^+(18C6)$ with linear IR spectra predicted for the ground-state and three select stable excited conformers of $(DAP)H^+(18C6)$ calculated at the B3LYP/6-31G* level of theory. The structures and MP2(full)/6-311+G(2d,2p) relative stabilities of each conformer are also shown.

Figure 7.6. Comparison of the measured IRMPD action spectrum of $(4MeImid)H^+(18C6)$ with linear IR spectra predicted for the ground-state and three select stable excited conformers of $(4MeImid)H^+(18C6)$ calculated at the B3LYP/6-31G* level of theory. The structures and MP2(full)/6-311+G(2d,2p) relative stabilities of each conformer are also shown.

Figure 7.7. Comparison of the measured IRMPD action spectrum of $(MGD)H^+(18C6)$ with linear IR spectra predicted for the ground-state and three select stable excited conformers of $(MGD)H^+(18C6)$ calculated at the B3LYP/6-31G* level of theory. The structures and MP2(full)/6-311+G(2d,2p) relative stabilities of each conformer are also shown.

Figure 7.1.

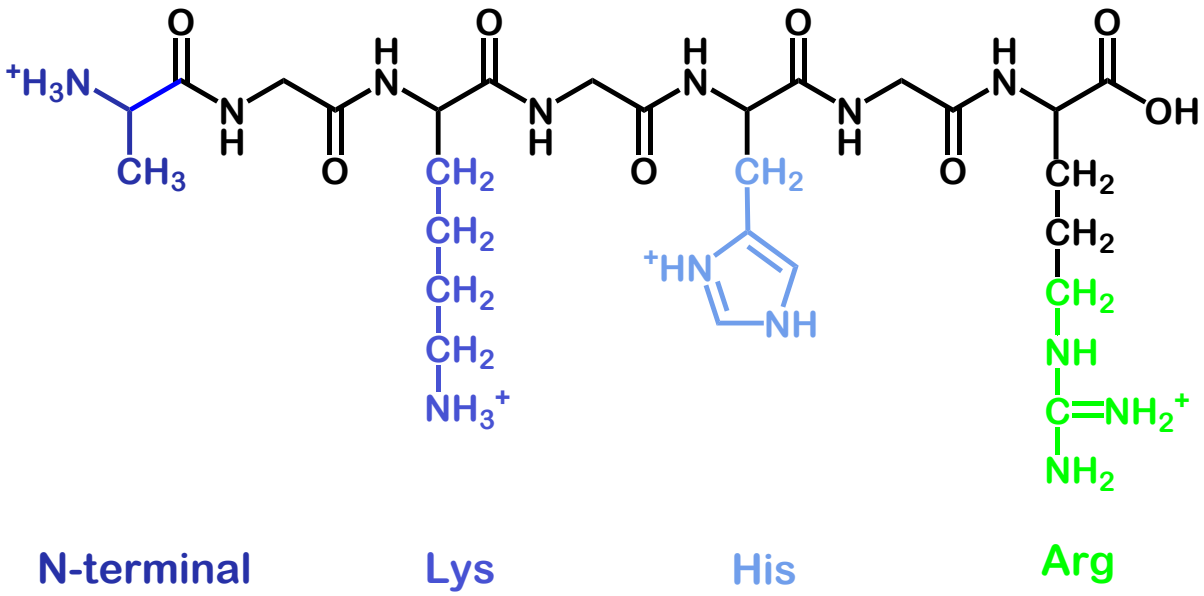

Figure 7.2.

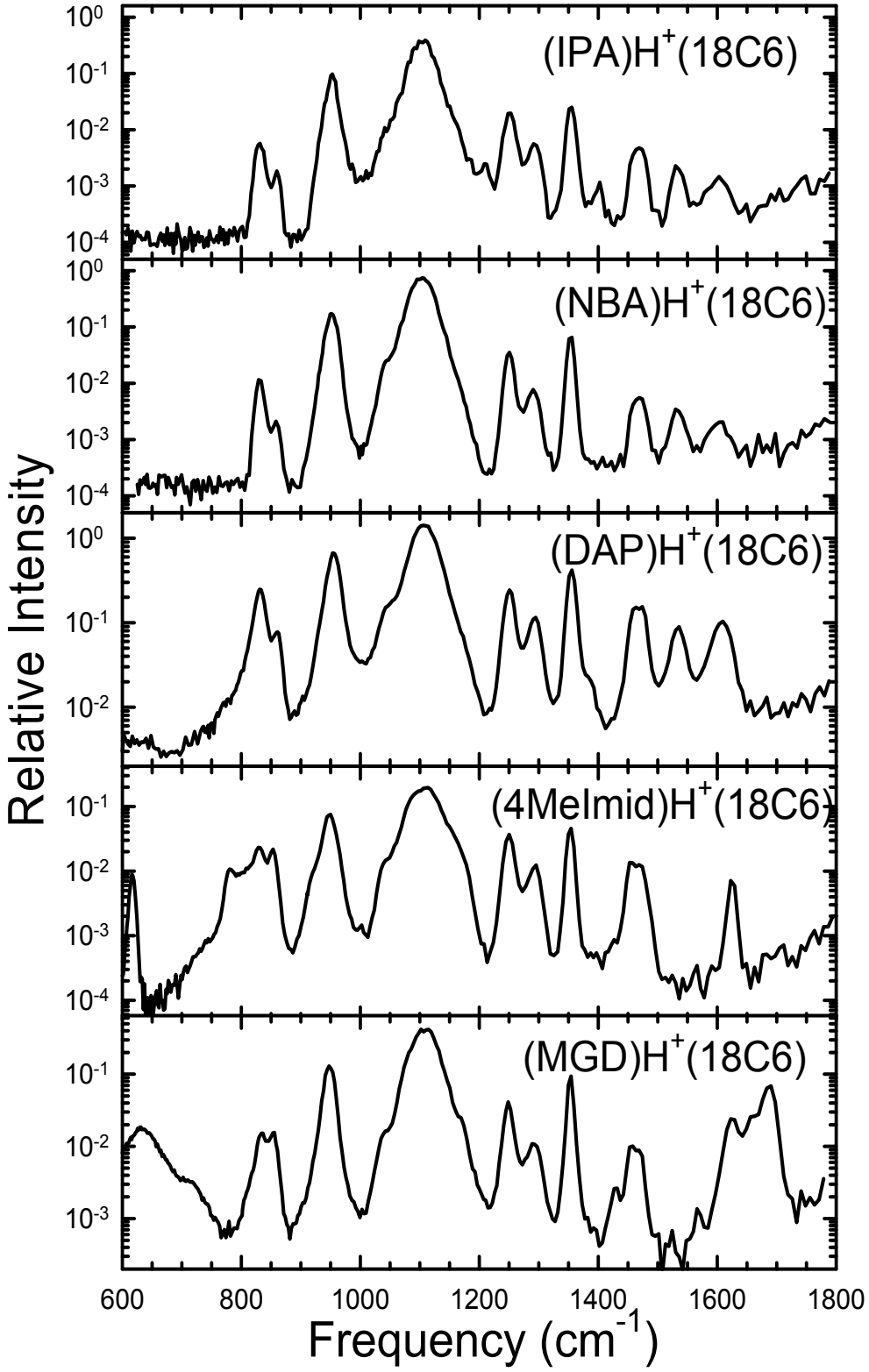
(IPA)H+(18C6)
(NBA)H+(18C6)
(DAP)H+(18C6)
(4MeImid)H+(18C6)
(MGD)H+(18C6)
Relative Intensity
Frequency (cm-1)
600
800
1000
1200
1400
1600
1800

Figure 7.3.

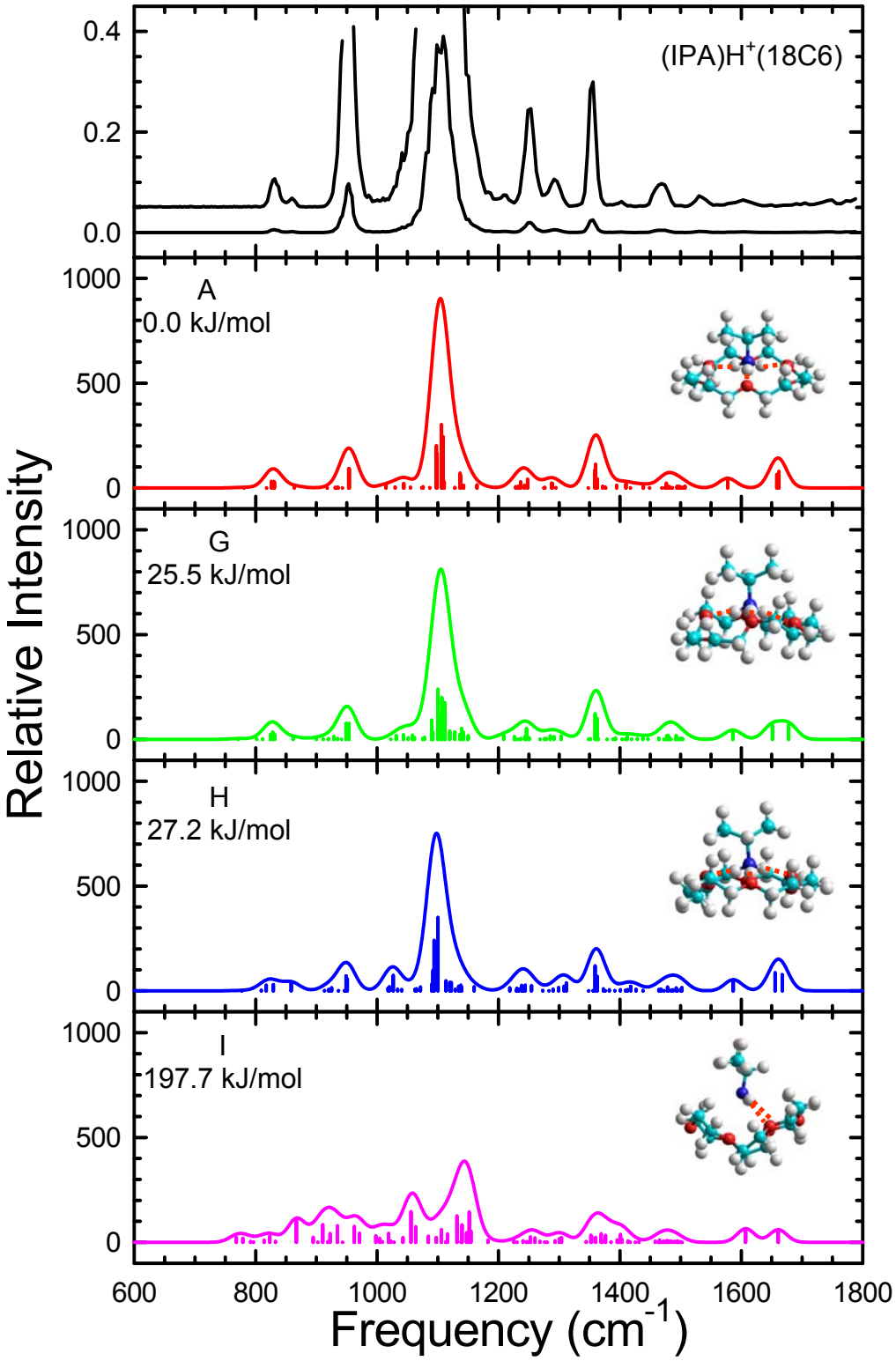
(IPA)H+(18C6)
A
0.0 kJ/mol
G
25.5 kJ/mol
H
27.2 kJ/mol
I
197.7 kJ/mol
Relative Intensity
Frequency (cm-1)

Figure 7.4.

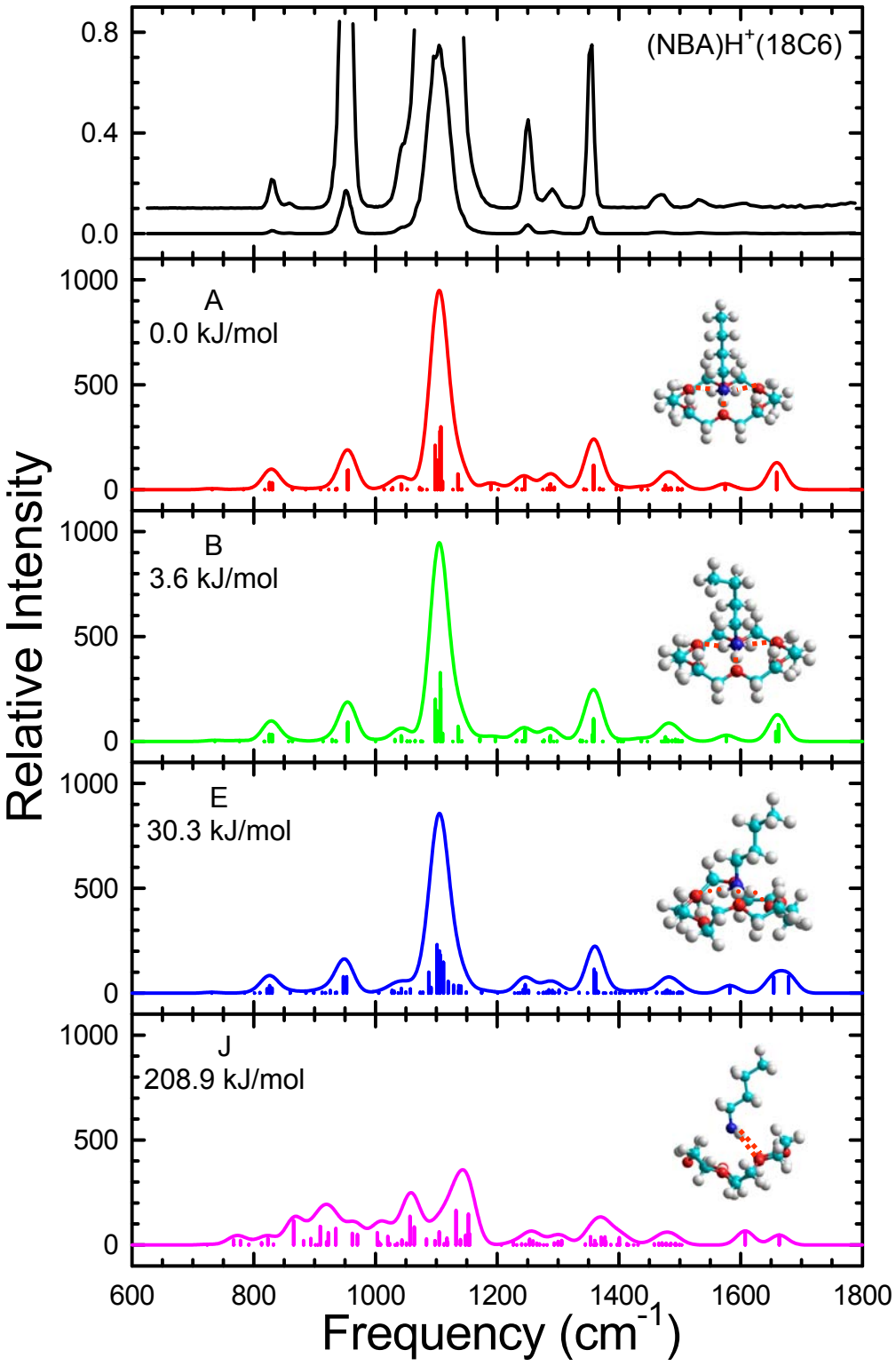
(NBA)H+(18C6)
A
0.0 kJ/mol
B
3.6 kJ/mol
E
30.3 kJ/mol
J
208.9 kJ/mol
Relative Intensity
Frequency (cm-1)

Figure 7.5.

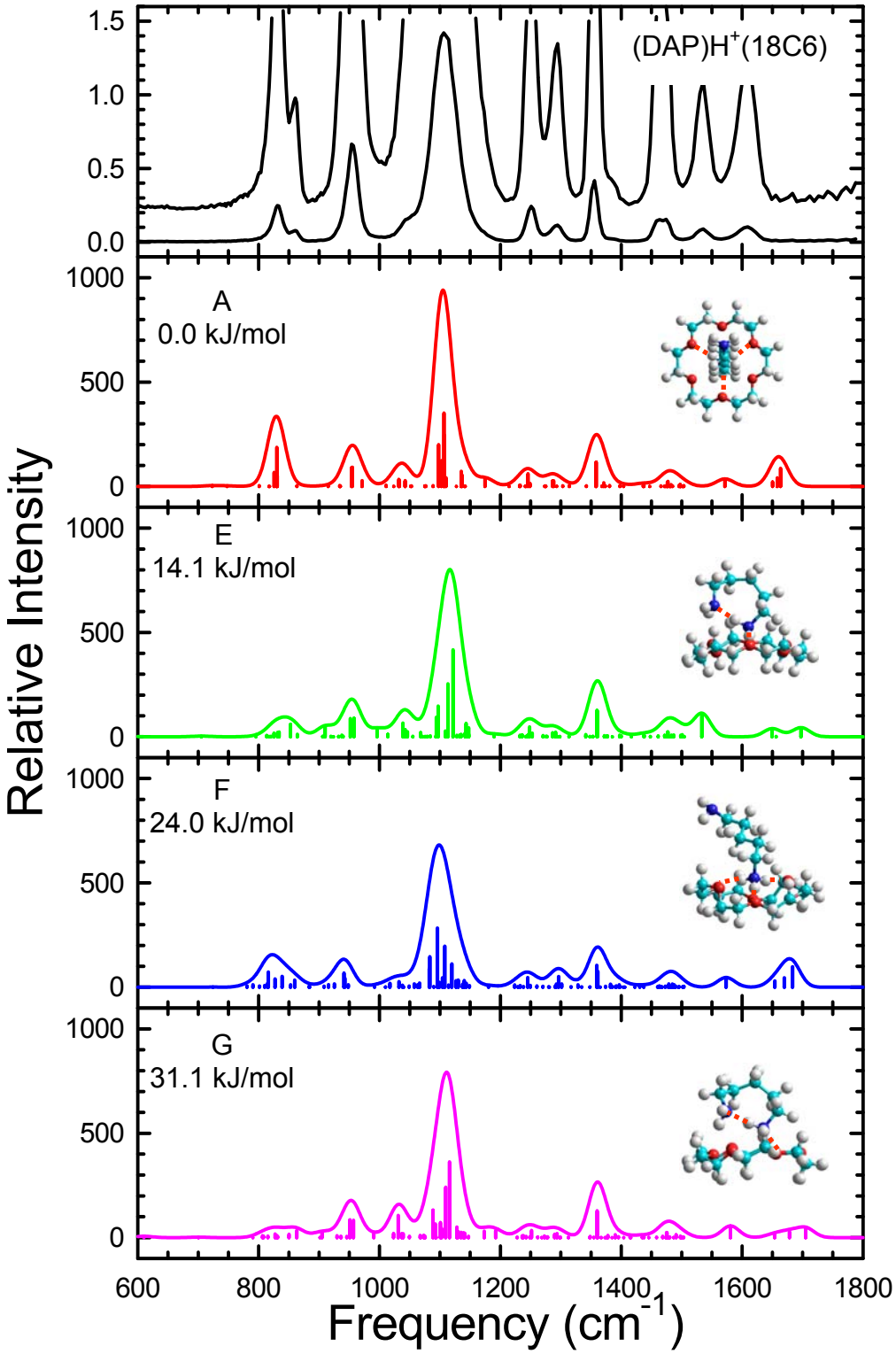
(DAP)H+(18C6)
A
0.0 kJ/mol
E
14.1 kJ/mol
F
24.0 kJ/mol
G
31.1 kJ/mol
Relative Intensity
Frequency (cm-1)

Figure 7.6.

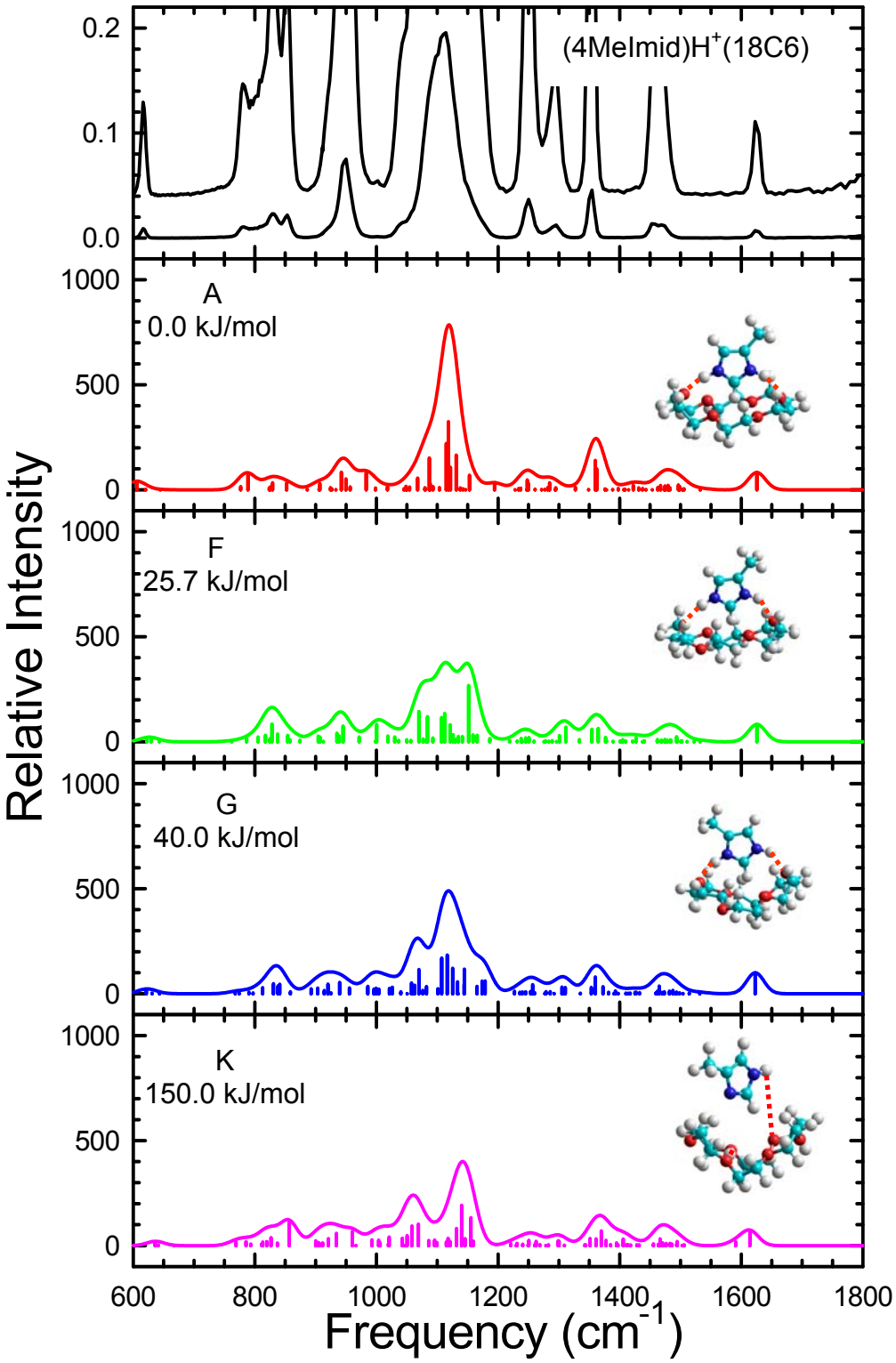
(4MeImid)H+(18C6)
A
0.0 kJ/mol
F
25.7 kJ/mol
G
40.0 kJ/mol
K
150.0 kJ/mol
Relative Intensity
Frequency (cm-1)

Figure 7.7.

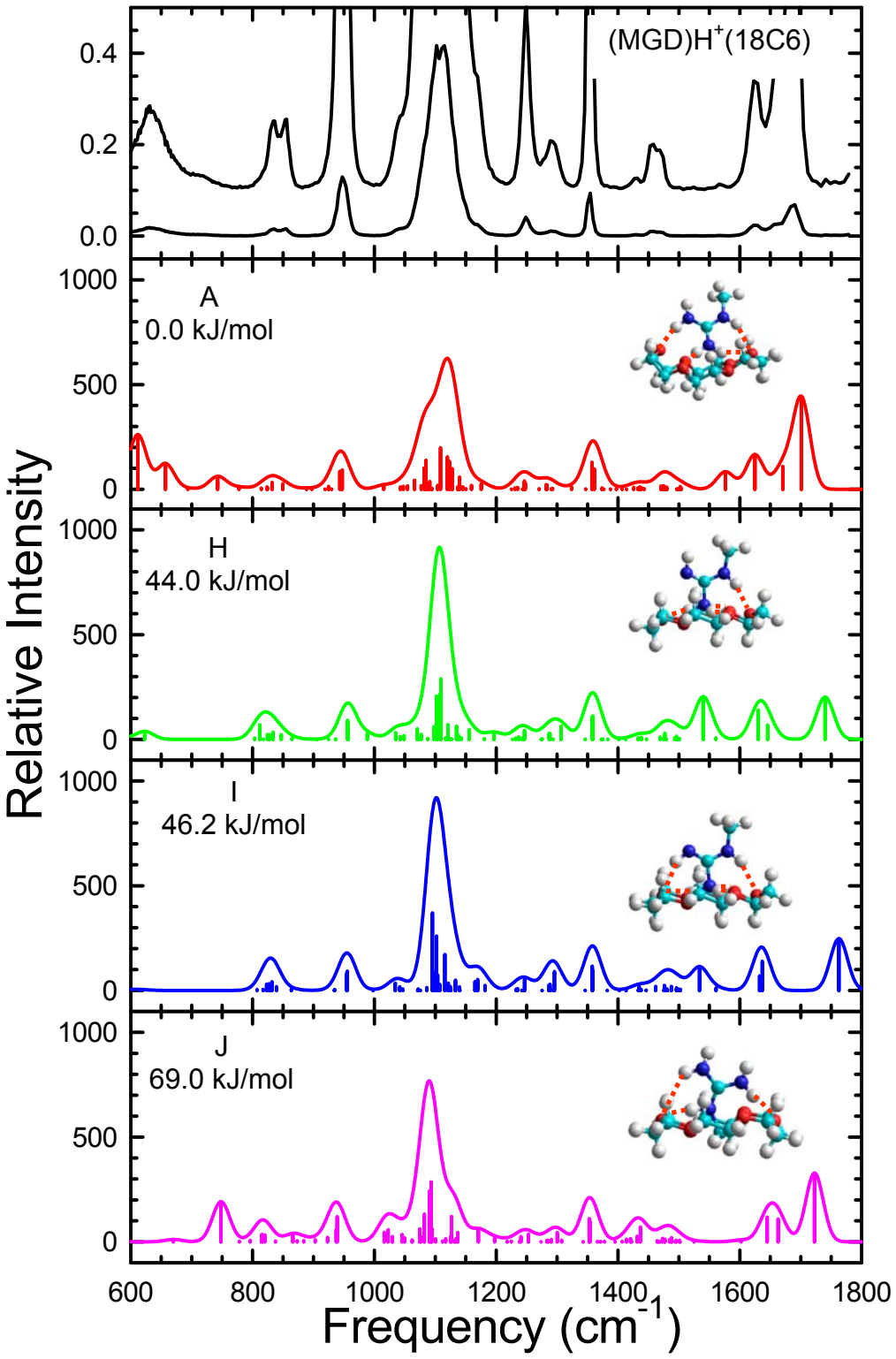
(MGD)H+(18C6)
0.4
0.2
0.0
A
0.0 kJ/mol
H
44.0 kJ/mol
I
46.2 kJ/mol
J
69.0 kJ/mol
1000
500
0
Relative Intensity
600
800
1000
1200
1400
1600
1800
Frequency (cm-1)

CHAPTER 8

CONCLUSIONS AND FUTURE WORK

8.1. Conclusions

In the present work, three major factors that affect the 18C6 selectivity for the side chains of amino acids (AAs) in peptides and proteins are investigated: (1) the 18C6 binding affinities of a series of peptidomimetic bases (Bs), AAs, and acetylated amino acids (AcAAs), where the Bs examined serve as mimics of the N-terminal amino group and the side chains of the basic AAs, the AAs examined include Gly, Ala, Lys, His, and Arg, and the AcAAs include backbone acetylated Lys, His, and Arg, as well as side chain acetylated Lys, (2) the PA of 18C6 was determined, and (3) the binding conformations of protonated peptidomimetic base–18C6 complexes were determined.

Energy-resolved collision-induced dissociation experiments and theoretical electronic structure calculations are used to examine the 18C6 binding affinities of favorable binding sites in peptides and proteins, i.e. the N-terminal amino group and the side chains of the basic amino acids in a pedagogic fashion. First, the 18C6 binding affinities of several peptidomimetic bases (B) that serve as mimics for the side chains of Lys, Arg, His and the N-terminal amino group are examined to determine the intrinsic 18C6 binding affinities of the associated side chain functionalities.[1] The bases (B) included in this work are mimics for the N-terminal amino group and the side chains of the basic amino acids, lysine (Lys), histidine (His), and arginine (Arg). Isopropylamine (IPA) is chosen as a mimic for the N-terminal amino group, imidazole (Imid) and 4-methylimidazole (4MeImid) are chosen as mimics for the side chain of His, 1-methylguanidine (MGD) is chosen as a mimic of the side chain of Arg, and several

primary amines including: methylamine (MA), ethylamine (EA), n-propylamine (NPA), n-butylamine (NBA), and 1,5-diamino pentane (DAP) are chosen as mimics for the side chain of Lys. These studies were extended to include several AAs,[2] including glycine (Gly), alanine (Ala), Lys, His, and Arg, and further extended to acetylated AAs (AcAA)[3] including N-terminal acetylated lysine (N_α–AcLys), arginine (N_α–AcArg), and histidine (N_α–AcHis), as well side chain acetylated lysine (N_ε–AcLys) to determine the binding affinities of the N-terminal amino group and side chains of the basic AAs.

In **Chapter 3**, the mimic for the N-terminal amino group, IPA, is found to exhibit a greater 18C6 binding affinity than the Lys mimic, NBA, suggesting that the N-terminal amino group could serve as an additional favorable binding site for 18C6.[1] Based on correlations between the PA and polarizability of the bases and the measured $(B)H^+$–18C6 BDEs, binding to the N-terminal amino group should be most competitive with the Lys side chains when the N-terminal amino acid is Gly and should become decreasingly less competitive as the size and polarizability of the side chain increases. This conclusion is supported by results presented in **Chapter 4**, where Gly and Ala are shown to exhibit greater 18C6 binding affinities than Lys, again suggesting that the N-terminal amino group could also serve as a favorable binding site for 18C6.[2]

The Lys mimic, NBA, and the smaller primary amine analogs exhibit higher binding affinities for 18C6 than the His mimics, 4MeImid and Imid, and the Arg mimic, MGD, suggesting that amongst all basis amino acids, the side chains of Lys residues are the preferred binding sites for 18C6 complexation. This trend in the 18C6 binding affinity is also observed for the free AAs in **Chapter 4**. Amongst the basic AAs, Lys exhibits the highest binding affinity for 18C6, suggesting that the side chains of Lys

residues are the preferred binding sites for 18C6.[2] The 18C6 binding affinity trend among the basic amino acids is further elucidated in **Chapter 5**. N_α–AcLys exhibits the highest binding affinity for 18C6, confirming that the side chains of Lys residues are the preferred binding sites for 18C6 complexation, and that competition by Arg and His residues for 18C6 complexation is not significant.[3] N_α–AcLys exhibits a higher binding affinity for 18C6 than N_ε–AcLys, again suggesting that the side chain of Lys residues are the preferred binding sites for 18C6 as compared to the N-terminal amino group of Lys.

The proton affinity (PA) of 18C6 plays a critical role in the binding and CID behavior of proton bound complexes between 18C6 and guest cations. Knowledge of an accurate PA of 18C6 can improve the current understanding and control of the molecular recognition between 18C6 and related molecules and guest cations. Based on the relative TCID thresholds for the competitive primary CID pathways, as well as the literature PAs of the references bases, Gly, Ala, Imid, and 4Meimid, the PA of 18C6 is evaluated as 935.3 ± 11.4 kJ/mole.[4] The PA of 18C6 evaluated here exhibits excellent agreement with M06 theory, very good agreement with B3LYP theory, and the value measured by Meot-Ner,[5] suggesting that the PA of 18C6 reported in the NIST Webbook[6,7] and based on the measured value reported by Kebarle and coworkers[8] is overestimated and should be adjusted to the value determined here.

The IRMPD action spectra of five protonated peptidomimetic base–18-crown-6 complexes, $(B)H^+(18C6)$, where B = IPA, NBA, DAP, 4MeImid, and MGD are examined via infrared multiple photon dissociation (IRMPD) action spectroscopy over the region extending from ~600–1800 cm^{-1}.[9] Comparison of the measured IRMPD spectra with the

linear IR spectra of the stable low-energy conformers calculated at the B3LYP/6-31G* level of theory allows identification of the experimentally accessible conformations of each system. In all systems, the agreement between the measured IRMPD spectra and the theoretical linear IR spectra of the ground-state conformations is excellent, indicating that these conformers are accessed in the experiments. In the ground-state conformations of the $(B)H^+(18C6)$ complexes, the proton binds to the peptidomimetic base and interacts with 18C6 via two, three, or four N–H···O hydrogen bonds. The calculated IR spectra of the conformers in which proton binds to 18C6 for all five $(B)H^+(18C6)$ complexes differ markedly from the IRMPD action spectrum, ruling out the possibility that these conformers are accessed in the experiments, even when the PA of 18C6 exceeds that of the base.

Comparison of the calculated IR spectra and measured IRMPD action spectrum of the $(DAP)H^+(18C6)$ complex suggests that the $H^+(DAP)$ moiety exhibits an extended conformation and interacts with 18C6 via three nearly ideal (nearly linear) N–H···O hydrogen bonds. Comparison of the calculated IR spectra and measured IRMPD action spectrum of the $(MGD)H^+(18C6)$ complex suggests that proton binds to the imine nitrogen and the protonated $H^+(MGD)$ moiety interacts with 18C6 via four non-ideal N–H···O hydrogen bonds. Several low-energy conformers of the $(B)H^+(18C6)$ complexes may be accessed in the experiments as they exhibit very similar IR spectra. However, the computed relative stabilities as compared to the ground-state conformer suggests that most of the conformers are unlikely to be significant contributors to the measured IRMPD action spectra of the $(B)H^+(18C6)$ complexes. Overall the proton binding sites and the conformations of the $H^+(B)$ moieties in the $(B)H^+(18C6)$ complexes are clearly

identified, whereas distortions in the conformation of 18C6 cannot be readily distinguished for these $(B)H^+(18C6)$ complexes.[9]

8.2. Future Work

The present work aims to apply quantitative threshold collision-induced dissociation (TCID) methods and electronic structure calculations to obtain accurate thermodynamic information regarding molecular recognition of peptides and proteins by 18C6. There exists a number of projects that could be pursued to further elucidate the structural and energetic effects in the molecular recognition of peptides and proteins by 18C6. The projects are as follows:

1) In **Chapter 3**, the 18C6 binding affinity of protonated peptidomimetic bases that serve as mimics of Lys, Arg, His, and the N-terminal amino group are examined.[1] The bases that involve three N–H···O hydrogen bonds exhibit the highest binding affinity for 18C6. The Lys mimic, NBA, exhibits a higher 18C6 binding affinity than the His mimics, Imid and 4MeImid, and the Arg mimic, MGD. However, the trend between His and Arg is not readily predictable because the 18C6 binding affinity of the Arg mimic lies between that of the two His mimics, Imid and 4MeImid. The 18C6 binding affinity of the Arg mimic, MGD, is 0.2 kJ/mol lower than that of the His mimic, Imid, but is 8.2 kJ/mol higher than the other His mimic, 4MeImid. The peptidomimetic bases employed were not chosen in an entirely consistent fashion. The best mimic for the side chain of Arg would be 1-propylguanidine, rather than 1-methylguanidine. Therefore, the 18C6 binding affinity of 1-propylguanidine may provide insight into the relative 18C6 binding affinities of the mimics of the side chains of Arg and His.

2) Theoretical and experimental study of 18C6 binding to dipeptides will allow determination of polarizability and steric hindrance effects on the 18C6 binding affinities. For example, theoretical calculations and TCID experiments for the (GlyLys)H^+(18C6) complex will provide comparison of 18C6 binding affinities of the N-terminal amino group and the side chain of Lys; theoretical calculations and TCID experiments for the (GlyAA)H^+(18C6) complexes, where AA = Lys, Arg, and His will provide more information regarding the 18C6 selectivity of the N-terminal amino group versus the Lys side chain; theoretical calculations and TCID experiments for the (LysAA)H^+(18C6) complex, where AA = Arg and His will allow comparison of the 18C6 binding sites along the backbone of peptides and proteins.

3) 27-crown-9 (27C9) was found to be the ideally sized host for guanidine. In synthetic chemistry, guanidine has been used as a template for the synthesis of 27C9.[10] Therefore, 27C9 could be used as a tag for the molecular recognition of the Arg side chain. 30-crown-10 exhibits a higher affinity for alkyl-guanidine as compared to 27C9 because of the smaller size of 27C6 that does not afford enough space for the 1-propylguanidine of the side chain of Arg.[11] As a result, 30C10 could serve as a better molecular recognition tag for the side chain of Arg. Therefore, analogous studies of structural and energetic effects of the molecular recognition of Arg side chains by 27C9 and 30C10 may facilitate the application of the selective noncovalent adduct protein probing method for protein structure elucidation.

Other crown ethers are available for molecular recognition of peptides and proteins including: 12-crown-4, 15-crown-5, and 21-crown-7. The sizes of the crown ether cavity and the side chains of the amino acids significantly influence the selectivity

of molecular recognition. Molecular recognition of alkali metal cations and amino acids by a variety of crown ethers have been studied and continues to be of interest of our group. Thus, comparison between the results from the current studies and future work via complementary studies should expand the knowledge database for the molecular recognition of different amino acids by crown ethers, and allow greater control of the selectivity and dissociation mechanism of protonated crown ether–amino acids complexes.

8.3. References

(1) Chen, Y; Rodgers, M. T. *J. Am. Chem. Soc.*. **2012**, *134*, 2313.

(2) Chen, Y; Rodgers, M. T. *J. Am. Chem. Soc.*. **2012**, *134*, 5863.

(3) Chen, Y.; Rodgers, M. T. *J. Am. Soc. Mass Spectrom.* **2012**, submitted.

(4) Chen, Y; Rodgers, M. T. *Anal. Chem.* **2012**, ac-2012-01804j, submitted.

(5) Meot-Ner, M. *J. Am. Chem. Soc.* **1983**, *105*, 4906.

(6) Hunter, E. P.; Lias, S. G. *J. Phys. Chem. Ref. Data,* **1998**, *27*, 413.

(7) NIST Chemistry Webbook, NIST Standard Reference Database Number 69, http://webbook.nist.gov/chemistry/.

(8) Sharma, R. B.; Blades, A. T.; Kebarle, P. *J. Am. Chem. Soc.* **1984**, *106*, 510.

(9) Chen, Y.; Rodgers, M. T. *J. Am. Soc. Mass Spectrom.* **2012**, submitted.

(10) Madan, K. and Cram, D. J. *J. Chem. Soc., Chem. Commun*. **1975**, *11*, 427.

(11) Julian, R. R.; Akin, M.; May, J. A.; Stoltz, B. M.; Beauchamp, J. L. *Int. J. Mass Spectrom*. **2002**, *220*, 87.

ABSTRACT

DEVELOPMENT OF AN ELECTROSPARY IONIZATION SOURCE AND VACUUM INTERFACE FOR GUIDED ION BEAM TANDEM MASS SPECTROMETRY EXPERIMENTS: STRUCTURAL AND ENERGETIC EFFECTS IN THE MOLECULAR RECOGNITION OF AMINO ACIDS BY 18-CROWN-6

by

YU CHEN

August 2012

Advisor: Professor Mary T. Rodgers

Major: Analytical Chemistry

Degree: Doctor of Philosophy

Absolute 18-crown-6 (18C6) binding affinities of the side chains of AAs in peptides and proteins were determined in a pedagogic fashion using guided ion beam tandem mass spectrometry techniques. The 18C6 binding affinities of nine peptidomimetic bases (B) that serve as mimics for the side chains of lysine (Lys), histidine (His), and arginine (Arg), and the N-terminal amino group have been examined to determine the intrinsic 18C6 binding affinities. The Bs were extended to naturally occurring AAs and further extended to acetylated AAs (AcAA) to determine the binding affinities of the side chains of AAs in peptides and proteins. The peptidomimetic bases examined here include: isopropylamine (IPA), imidazole (Imid) and 4-methylimidazole (4MeImid), 1-methylguanidine (MGD), methylamine (MA), ethylamine (EA), n-propylamine (NPA), n-butylamine (NBA), and 1,5-diamino pentane (DAP). This work was extended to include five amino acids (AA), glycine (Gly), alanine (Ala), Lys, His,

and Arg, and further extended to four acetylated amino acids (AcAA), N_{α}–AcLys, N_{ε}–AcLys, N_{α}–AcArg, and N_{α}–AcHis.

The measured 18C6 binding affinities of the Bs, AAs, and AcAAs suggest that the side chains of Lys residues are the preferred binding sites for 18C6 complexation in peptides and proteins. The N-terminal amino group provides another favorable binding site for 18C6. Trends in the 18C6 binding affinities exhibit an inverse correlation with the polarizability and proton affinity of the B and AA. Therefore, the ability of the N-terminal amino group to compete for 18C6 complexation is best for Gly and should become increasingly less favorable as the size of the side chain substituent increases.

The proton affinity (PA) of 18C6 plays a critical role in the binding and CID behavior of proton-bound complexes between 18C6 and guest cations. Therefore, the PA of 18C6 is re-evaluated using competitive threshold collision-induced dissociation techniques. The PA of 18C6 determined here exhibits excellent agreement with M06 theory, very good agreement with B3LYP theory, and very good agreement with the value reported by Meot-Ner determined using high pressure mass spectrometry (HPMS) techniques. Combined these results suggest that the PA of 18C6 reported in the NIST Webbook and based on HPMS measurements by Kebarle and coworkers is overestimated.

The IRMPD action spectroscopy of $(B)H^{+}(18C6)$ complexes are examined using a Fourier transform ion cyclotron resonance mass spectrometer (FT-ICR MS) coupled to a free electron laser. The structural information elucidated here supports the experimental measurements of the absolute 18C6 binding affinities of the basic amino acids and facilitates the understanding of the intrinsic factors that contribute to the

strength and selectivity of binding and thus molecular recognition in selective noncovalent adduct protein probing (SNAPP) and related techniques.

AUTOBIOGRAPHICAL STATEMENT

Yu Chen

EDUCATION

Ph. D. Analytical Chemistry **September 2005 – August 2012**

Wayne State University, Detroit, MI

Ph.D. Mentor: Professor Mary T. Rodgers

M.S. Physical Chemistry **September 2003 – July 2005**

University of Windsor, Windsor, ON, Canada

M.Sc Mentor: Associate Professor Jichang Wang

B.Eng. Applied Chemistry **September 1998 – July 2002**

Dalian University of Technology, Dalian, Liaoning, China

B. Eng Mentor: Professor Jinzong Yang

AWARDS AND HONORS–WAYNE STATE UNIVERSITY

(1) Joseph Jasper Scholarship, WSU, 2006

(2) David F. Boltz Award in Analytical Chemistry, WSU, 2010

(3) Summer Dissertation Fellowship, WSU 2011